Mm-wave photonic-enabled antenna arrays

Álvaro Pascual-Gracia

UNIVERSITÉ DE RENNES 1

THESE DE DOCTORAT DE

L'UNIVERSITE DE RENNES 1

ECOLE DOCTORALE N° 601
Mathématiques et Sciences et Technologies de l'Information et de la Communication
Spécialité : *Électronique*

Par
Álvaro J. PASCUAL-GRACIA

Mm-Wave Photonic-Enabled Antenna Arrays

Thèse présentée et soutenue à Rennes, le 21 Mai 2021
Unité de recherche : IETR – UMR CNRS 6164, Institut d'Électronique et des Technologies du numéRique

Rapporteurs avant soutenance :

Laurent DUSSOPT	Ingénieur de recherche, HDR, CEA-LETI, Grenoble, France
Sascha PREU	Professeur d'université, TU Darmstadt, Darmstadt, Allemagne

Composition du Jury :

Président :	Sascha PREU	Professeur d'université, TU Darmstadt, Darmstadt, Allemagne
Examinateurs :	Stefano MACI	Professeur d'université, Università di Siena, Siena, Italie
	Mathilde GAY	Chercheuse, CNRS, ENSSAT, Lannion, France
	Laurent DUSSOPT	Ingénieur de recherche, HDR, CEA-LETI, Grenoble, France
Dir. de thèse :	Ronan SAULEAU	Professeur d'université, HDR, Université de Rennes 1, France
Co-dir. de thèse :	David GONZÁLEZ-OVEJERO	Chercheur, CNRS, IETR, Rennes, France

Invités :

Guillermo CARPINTERO DEL BARRIO	Professeur d'université, Universidad Carlos III de Madrid, Leganés, Espagne
Luis Enrique GARCÍA-MUÑOZ	Professeur d'université, Universidad Carlos III de Madrid, Leganés, Espagne

Université de Rennes 1

DOCTORAL THESIS

Mm-Wave Photonic-Enabled Antenna Arrays

Submitted in partial fulfillment of the requirements
for the degree of Doctor of Philosophy

at the

Institut d'Électronique et des Technologies du numéRique (IETR)

Author:	Álvaro José Pascual-Gracia
Supervisor:	Ronan Sauleau
Co-supervisor:	David González-Ovejero

Defended on May 2021

"We can only see a short distance ahead,
but we can see plenty there that needs to be done."
— Alan Turing

Dedicated to my family.

Preface

This thesis dissertation comprises the results of the research work carried out by the author over three years and a few months at the Institut d'Électronique et des Technologies du numéRique (IETR) as well as the contents deemed necessary to put them in perspective. As such, the manuscript is largely based on prior dissemination (see List of Publications), although substantial effort has been put into introducing and explaining in detail the methods and techniques used.

The presented results constitute a novel research line at the Institute: the study of antennas for continuous-wave photonic transmitters with enhanced performance at millimeter-waves (mm-waves), more specifically, around 75-150 GHz. The fact that no prior guidelines existed forced us to study the subject from different perspectives, and we have conducted our research on those that offered the highest potential. To this end, we have accomplished various original contributions. The first one is devoted to increasing the radiated power. Compared with classical antenna architectures, our approach achieves more than a tenfold increase using an antenna array efficiently matched to photodiodes. A second contribution is devoted to providing beam steering capabilities to photonic transmitters. In particular, we have reported one of the first leaky-wave antennas integrated with photodiodes for 1-D beam steering at mm-wave frequencies. We have also developed the first-ever implementation, at the same frequency range, of photonic beam switching for flexible communications, along with a demonstration set-up. The last contribution is a theoretical model to calculate the scan impedance in infinite phased arrays of dipoles.

Additionally, this novel research line has also entailed little previous knowledge of the fabrication methods, as well as a a lack of a proper experimental platform to characterize photonic transmitters. It has been therefore customary to rely on collaborations and to develop in parallel an in-house set-up for experimental characterization. As a result, there are a number of people whose direct or indirect assistance has favored the proper development of the research work herein presented, and we are deeply grateful to them. Notably, the collaboration with our partners at Universidad Carlos III de Madrid (UC3M) has allowed photonic characterization of the transmitters as well as accessing the photodiode chips used in the experimental part of this work. Also, collaborating with the Laboratory of Electronics Antennas and Telecommunications (LEAT) has allowed the electronic characterization of the prototypes. As for the set-up developed at IETR, even if it does not constitute per se original

research work, we have devoted to it substantial economical and time effort. It will be also described in the manuscript.

In our research group at the Institute, our expertise is in the field of antennas. This thesis also places the focus on the antenna, and it has been written primarily for engineers familiar with or carrying out research in this field. At least, it is expected that one knows in general terms the contents presented in [1], an introductory text on antennas. Conversely, considerable attention has been given to put into context photonic technologies for the generation of mm- and THz waves. Hence, being familiar with mm-wave and THz science is, a priori, not required. In this respect, the reader should find the text largely self-explanatory.

All in all, this dissertation should be of interest primarily to those seeking to improve the capabilities of photonic transmitters from the antenna point of view. More broadly, this dissertation should also be of interest to those that conduct research on photonic technologies for the generation of mm- and THz waves because the manners in which the antenna influences the other elements that form a photonic transmitter are discussed too.

We hope to have provided a text with enough context and clarity so that the reader best enjoys discovering this research work.

Rennes, April 2021

A. J. P.
D. G.
R. S.

Résumé

Cette thèse constitue le résultat des premiers efforts menés à l'IETR pour consolider une ligne de recherche sur les antennes à ondes millimétriques continues excitées par des photodiodes. En un peu plus de trois ans, nous avons identifié les inconvénients de l'approche photonique, proposé des solutions et démontré expérimentalement certaines d'entre elles. La nouveauté du sujet a également nécessité un effort supplémentaire. En particulier, nous avons développé en parallèle une plateforme de caractérisation d'antennes (voir l'Annexe E).

Au cours des vingt dernières années, les ondes millimétriques (mm) et THz ont fait l'objet d'un grand nombre de publications et de projets de recherche. Ce contexte a favorisé des progrès significatifs des dispositifs utilisés pour générer et détecter de la puissance dans une zone spectrale traditionnellement dénommée "gap THz" (la plage de fréquences comprise entre 0,1 THz et 10 THz) [2]. En particulier, les technologies basées sur le photomixage (photomixing) se sont positionnées comme l'un des principaux candidats pour la génération de puissance dans les fréquences inférieures de cette région spectrale.

Parmi les applications des émetteurs photoniques à ondes continues mm et THz, on peut identifier deux inconvénients : l'absence d'un faisceau orientable associé à une antenne à gain élevé et des niveaux de puissance émis réduits par rapport à leurs homologues électroniques. Surmonter ces limitations sera une étape cruciale pour la consolidation des émetteurs photoniques aux ondes mm et THz, élargissant également leur gamme d'applications.

Les limitations susmentionnées constituent la cible principale des travaux de recherche présentés dans cette thèse. Nous proposerons plusieurs architectures de réseaux d'antennes pour améliorer les performances des émetteurs photoniques pour des applications en télécommunication, spectroscopie et imagerie.

Plan de la Thèse

Au Chapitre 1, nous introduisons le contexte de recherche de cette thèse. Tout d'abord, nous expliquons brièvement les différentes méthodes de génération d'ondes mm et THz. Ensuite, nous identifions plusieurs défis auxquels l'approche photonique est actuellement confrontée et nos objectifs pour les relever. Enfin, nous concluons ce chapitre par un aperçu du contenu de cette thèse.

Au Chapitre 2, nous présentons un modèle analytique pour dériver l'impédance de balayage (scan impedance) de réseaux planaires phasés infinies de dipôles à une interface diélectrique lorsque seul le mode de Floquet (0,0) se propage. Le modèle proposé s'appuie sur les conditions aux limites satisfaites par le mode fondamental de Floquet à l'interface (continuité du champ électrique tangentiel) pour fournir une nouvelle dérivation du circuit équivalent pour l'impédance de balayage. L'analyse est également étendue pour inclure l'effet d'un plan de masse et des formules sont fournies pour calculer le rapport d'intensité rayonnée vers chaque demi-espace d'un réseau interfacial. Dans un second temps, une approximation asymptotique est dérivée pour la distribution du courant dans des réseaux de dipôles avec des terminaisons de charge arbitraires, et la réactance d'un dipôle dans l'environnement du réseau est liée à l'inductance d'une grille de fils. Ce modèle constitue un outil utile pour identifier clairement par des expressions simples et circuits équivalents le rôle des différentes variables du réseau sur l'impédance de balayage, telles que les dimensions des dipôles, permittivité relative du substrat, périodicité, terminaisons de charge aux extrêmes des dipôles et angle de balayage dans les plans principaux. Les prévisions du modèle sont en bon accord avec les simulations pleine onde et avec les travaux publiés antérieurement.

Le modèle a émergé après avoir étudié des réseaux phasés couplés comme méthode pour améliorer l'efficacité d'adaptation d'impédance entre des photodiodes et un réseau d'antennes. Pour plus de clarté, nous avons préféré placer le modèle théorique au début pour inclure ultérieurement tous les contenus liés aux émetteurs photoniques.

Au Chapitre 3, nous retrouvons la voie vers nos objectifs en discutant des applications des ondes mm et THz. Celles-ci se retrouvent principalement dans les télécommunications, l'imagerie et la spectroscopie. Tout d'abord, dans ce chapitre, nous détaillons les caractéristiques pertinentes des ondes mm et THz dans le contexte des champs cités ci-dessus, et mettons en évidence les domaines dans lesquels la génération photonique d'ondes continues joue un rôle notable. Ensuite, nous soulignons les inconvénients : pour les télécommunications, nous identifions le besoin des émetteurs photoniques avec une orientabilité du faisceau et un gain élevé. Un faisceau orientable peut permettre des liaisons reconfigurables ou faciliter l'alignement, alors qu'un gain élevé est nécessaire pour compenser les pertes en espace libre élevées. D'autre part, une puissance émise plus élevée est nécessaire pour réduire le temps d'acquisition des mesures et rendre les systèmes basés sur le photomixage en onde continue plus compétitifs en spectroscopie et en imagerie.

Au Chapitre 4, nous commençons par expliquer les concepts nécessaires pour comprendre un émetteur photonique à ondes mm ou THz. Tout d'abord, nous expliquons la technique du photomixage. Ensuite, nous décrivons des photodiodes, en particulier le type UTC-PD (uni-traveling-carrier). Enfin, nous détaillons les principaux types d'émetteurs photoniques à ondes mm et THz. Ces bases fournissent à un lecteur peu familier avec la science des ondes mm et THz suffisamment de contexte pour comprendre nos choix par la suite.

Au Chapitre 5, nous abordons le premier jalon: l'augmentation de la puissance émise.

En un mot, nous présentons un réseau d'antennes à ondes millimétriques sur puce avec un réflecteur qui permet d'obtenir une adaptation d'impédance efficace avec un UTC-PD. Dans l'hypothèse du réseau infini, il est possible de décrire la cellule unitaire du réseau comme un circuit équivalent, y compris également les pertes ohmiques. En particulier, l'utilisation d'un réflecteur contribue de manière inductive à l'impédance de l'antenne. Le reste des variables du réseau aident en outre à annuler la capacité de la photodiode et à obtenir une adaptation presque conjuguée. La cellule unitaire conçue dans l'environnement de réseau infini est la géométrie de départ pour optimiser un réseau 2×2 fini. Nous discutons également d'aspects tels que l'éclairage efficace de la photodiode et l'assemblage de la structure. L'approche adoptée permet de multiplier la puissance émise: grâce à la combinaison de puissance de plusieurs éléments et à l'amélioration de l'adaptation d'impédance. Nous obtenons une amélioration d'un facteur de 2 à 4 de l'efficacité d'adaptation d'impédance en comparaison avec d'autres méthodes dans la bibliographie tout en conservant une large bande passante relative de 30% en puissance (-3 dB). De plus, la puissance crête émise est supérieure à 11 dB par rapport aux antennes auto-complémentaires.

Au Chapitre 6, nous rapportons le premier réseau d'antennes à ondes de fuite ou "leaky" (LWA) intégré avec des photodiodes à des fréquences mm / sub-mm. Le réseau de LWA conçue est fabriqué dans la technologie des circuits imprimés (PCB) et fonctionne en bande E (de 75 à 85 GHz). L'élément d'antenne consiste en une ligne de micro-rubans chargée périodiquement de talons, et il a été conçu en utilisant une approche hybride combinant des simulations pleine onde et la théorie des lignes de transmission. Cette approche permet une optimisation de la période lorsque la bande d'arrêt ouverte du LWA est largement atténuée ou supprimée. L'antenne fournit un faisceau directif d'environ 18 dBi avec une plage de balayage de 22° avec la fréquence, mais elle a été tronquée après quatre périodes en raison de contraintes expérimentales. Le LWA composé de 19 périodes présente une largeur de faisceau à mi-puissance simulée de 4°. Premièrement, le prototype fabriqué a été testé à l'aide d'une sonde coplanaire de type GSG (ground signal ground), les pertes de retour et les diagrammes de rayonnement mesurés étaient en bon accord avec les simulations pleine onde. Ensuite, le réseau LWA a été intégré avec une pouce des photodiodes. Les mesures de la puissance rayonnée ont donné un maximum de 120 μW à 80,5 GHz pour un photocourant de 9,8 mA. Enfin, l'antenne a été utilisée dans une liaison sans fil de 25 cm, obtenant un débit de données sans erreur de 2,15 Gbps et démontrant la transmission en direct de la vidéo HD entre deux écrans (1,5 Gbps).

Au Chapitre 7, nous présentons un réseau d'antennes photoniquement excité en bande E pour la commutation de faisceau dans les liaisons sans fil. Dans un premier temps, nous discutons des compromis entre la commutation de faisceau et la direction de faisceau avec un réseau phasé pour les émetteurs photoniques à ondes mm. Ensuite, nous présentons l'antenne conçue ; elle se compose de deux sous-réseaux de patchs empilés, avec une photodiode alimentant chaque sous-réseau. Pour valider le montage, des mesures du diagramme de rayonnement et des pertes de retour sont effectuées sur un prototype excité avec une sonde coplanaire GSG. Ensuite, le réseau est combiné avec une lentille pour augmenter la directivité

globale à 27 dBi. En accord avec les simulations pleine onde, les mesures montrent que l'excitation de l'un des deux sous-réseaux permet une commutation de faisceau entre $\pm 2,7°$ avec un croisement de faisceau à -3 dB. Enfin, nous testerons l'émetteur dans une liaison sans fil d'environ 0,6 m. En fonction de la position du détecteur et du sous-réseau excité, nous nous attendons à réaliser une transmission de données en direct sans erreur à plusieurs Gbps. Le système constitue une première preuve de la commutation de faisceau assistée par la photonique pour les émetteurs d'onde mm permettant un fonctionnement à large bande avec un faisceau directif et commutable.

Finalement, nous concluons la thèse en résumant les contributions originales et en commentant les travaux futurs. Notamment, sur la continuation des travaux présentés dans le Chapitre 7.

Pour compléter les chapitres précédents, cinq annexes offrent plus de détails sur les travaux de la thèse. En outre, les contributions originales ont donné lieu à plusieurs papiers rapportés dans des revues et conférences renommées (voir la liste des publications). Nous tenons à mentionner que les articles soumis ou en préparation ciblent les revues à fort impact (SRJ Q1). Enfin, nous tenons à mentionner aussi que nos travaux sur la formation de faisceaux seront inclus dans un chapitre conjoint avec nos collègues de l'UC3M dans un livre édité par des scientifiques de premier plan dans le domaine.

Contents

List of Figures

List of Tables

Acronyms

5G	Fifth Generation
B5G	Beyond Fifth Generation
BER	Bit-Error Rate
BERT	Bit-Error Rate Tester
BFN	BeamForming Network
BWO	Backward-Wave Oscillator
CB	Conduction Band
CMOS	Complementary Metal-Oxide Semiconductor
CPW	Coplanar Waveguide
CST	Computer Simulation Technology
CW	Continuous-Wave
DFB	Distributed FeedBack
DFG	Difference-Frequency Generation
DUT	Device Under Test
EDFA	Erbium-Doped Fiber Amplifier
FD	Frequency Domain
FEM	Finite Element Method
FSL	Free Space Loss
G-CPW	Grounded-Coplanar Waveguide
GSG	Ground Signal Ground
HEMT	High Electron Mobility Transistor
HFSS	High Frequency Structure Simulator
HPBW	Half-Power Beamwidth
IE	Integral Equation
IETR	Institut d'Électronique et des Technologies du numéRique
IL	Insertion Loss
IMPATT	IMPact ionization Avalanche Transient Time (Diode)
IR	Infrared
ITU	International Telecommunication Union
LEAT	Laboratory of Electronics Antennas and Telecommunications
LNA	Low Noise Amplifier
LO	Local Oscillator
LoS	Line-of-Sight
LWA	Leaky-Wave Antenna
Mm-Wave	Millimeter-Wave

MMIC	Millimeter-wave Integrated Circuit
MoM	Method of Moments
NEP	Noise Equivalent Power
NTT	Nippon Telegraph and Telephone
OOK	On-Off Keying
OSA	Optical Spectrum Analyzer
OTD	Optical Time Delay
PC	Polarization Controller
PCB	Printed Circuit Board
PD	Photodiode
PEC	Perfect Electric Conductor
pin-PD	Positive-intrinsic-negative Photodiode
PMC	Perfect Magnetic Conductor
PRBS	Pseudo-Random Binary Sequence
QCL	Quantum Cascade Laser
QO	Quasi-Optical
RF	Radiofrequency
RTD	Resonant Tunneling Diode
Rx	Receiver
SBD	Schottky Barrier Diode
SLL	Sidelobe Level
SNR	Signal-to-Noise Ratio
SotA	State-of-the-Art
SOLT	Short-Open-Load-Through
TD	Time Domain
TDA	Twin Dipole Antenna
TE	Transverse Electric
TEM	Transverse Electromagnetic
TEM-HA	Transverse Electromagnetic Horn Antenna
TL	Transmission Line
TM	Transverse Magnetic
TO	Translated Open
TRL	Thru-Reflect-Line
TS	Translated Short
Tx	Transmitter
UC3M	Universidad Carlos III de Madrid
UTC-PD	Uni-Traveling-Carrier Photodiode
VB	Valence Band
VBA	Visual Basic for Applications
VIA	Vertical Interconnect Access
VNA	Vector Network Analyzer
WG	Waveguide
ZSBD	Zero Bias Schottky Barrier Diode Detector

1

Introduction

In the past twenty years, millimeter- (mm-) and THz waves have been the subject of a large number of publications and research projects. This context has favored significant progress in the devices used to generate and detect radiation in a spectral region traditionally denominated as the THz gap (the range of frequencies comprised between 0.1 THz and 10 THz) [2]. In particular, technologies based on photomixing have positioned themselves as one of the principal candidates for the generation of radiation at the lower end of this spectral region.

In an overview of the applications of mm-wave and THz photonic transmitters for continuous wave (CW) operation, one can identify two main shortcomings: the lack of antennas with simultaneously high-gain and a steerable beam, and the reduced levels of emitted power compared to their electronic counterparts. Overcoming these limitations will be a crucial milestone for the consolidation of photonic transmitters at mm- and THz waves, possibly boosting as well the number of scenarios where photonic transmitters will be applied.

The aforementioned limitations constitute the primary target of the research work hereafter presented. We will propose several architectures of antenna arrays to enhance the performance of photonic transmitters with application in telecommunications, spectroscopy, and imaging. In this introductory chapter, we first broadly discuss CW photomixing within the field of mm-wave/THz science. Then, we describe in more detail our goals and give a glimpse of how we will try to accomplish them. Finally, we conclude this introductory chapter with the outline of this document. Even if our antenna conceptions will be for the 75-150 GHz range, we have preferred to introduce mm- and THz waves since both are often merged, sharing technology, approaches, and applications.

1.1 Scientific Context

One of the principal causes that obstructed the advancements of mm-wave and THz science in the past was the lack of efficient emitters [3]–[5]. Among the existing ones, one could find sources as gyrotrons, klystrons or free-electron lasers [6], none of which are suited for applications where small volumes or portable devices are required [2]. Table-top backward

wave oscillators (BWO) can produce power in the range of mW at 1 THz to 100 mW at ≈ 100 GHz [2]. However, BWO require high voltages, have short lifetimes, and are not easily available [2]. As a result, only a few niche applications used mm- and THz waves, mostly devoted to science [7]. Consequently, this region of the spectrum did not develop the same level of sophistication as microwaves up to ≈ 60 GHz or optics. Indeed, mm-waves (30-300 GHz) and THz waves (0.1-10 THz or 0.3-10 THz, depending on the author) lie at the frontier between traditional electronics and optics. Neither of them offers a paradigm solution.

Nevertheless, over the last twenty years, the number of scientific works related to this region of the spectrum has skyrocketed, as reported in [4], [8], [9]. For instance, from 2002 to 2019, around 23 surveys were published [9]. Such reviews have been necessarily a consequence of improvements in mm-wave and THz technology. Indeed, nowadays a sufficient number of generation and detection methods exist [10], and the term THz gap is now considered outdated by some authors [2], [4], [11]. For instance, [12] provides a comprehensive comparison of mm-wave and THz sources, they are illustrated in Fig. 1.1. Although the values of output power are slightly outdated, the figure provides a good overview of the different sources. Below, we comment on those most pertinent to our subject.

Traditionally, the oscillation period of mm-wave and THz frequencies was shorter than the response time of semiconductor devices, so that their response was largely filtered out. Ultra-fast electronics, with response times of a fraction of a nanosecond have been ever since developed [9], [13]–[15]. The solutions existing nowadays work predominantly at the lower region of the THz spectrum, up to 1-2 THz approximately. Among the sources (oscillators), one can find Gunn diodes, resonant tunneling diodes (RTDs), or impact ionization avalanche transit time (IMPATT) diodes [2]. Besides, the improvements in fabrication methods and transistor scaling have led to the development of amplifiers based on heterojunction bipolar transistors (HBT) and high electron mobility transistors (HEMT), with demonstrations featuring cut-off frequencies around one THz [15], [16]. These developments have favored the advancement of Monolithic Microwave Integrated Circuits (MMIC), where GaAs, InP, and GaN are the usual workhorses, the latter for high-power applications [16]. Some implementations of MMIC and applications in wireless communications can be found in [17]–[19]. Besides, CMOS technology has progressed in device down-scaling, and it is attractive due to a low manufacturing cost and a high level of integration, but at the expense of lower output powers. In [9] the output power of some solid-state electronic devices is compared (RTD, MMIC, and CMOS-based). It lies in the milliwatt range around 300 GHz.

Still pertaining to solid-state electronics, one also finds Schottky diodes [20]. Rather than frequency generation or amplification, they allow frequency multiplication when used in conjunction with oscillators such as Gunn or IMPATT diodes. Schottky multipliers generally take the form of doublers or triplers where an input tone (typically < 150 GHz) is multiplied by 2 or 3, respectively [2]. However, to obtain higher frequencies, they can be cascaded to achieve, for instance, a ×216 multiplication factor and 5 μW power at 2.7 THz [20]. Around 300 GHz, Schottky diodes reach output powers in the order of one milliwatt (broadband) or

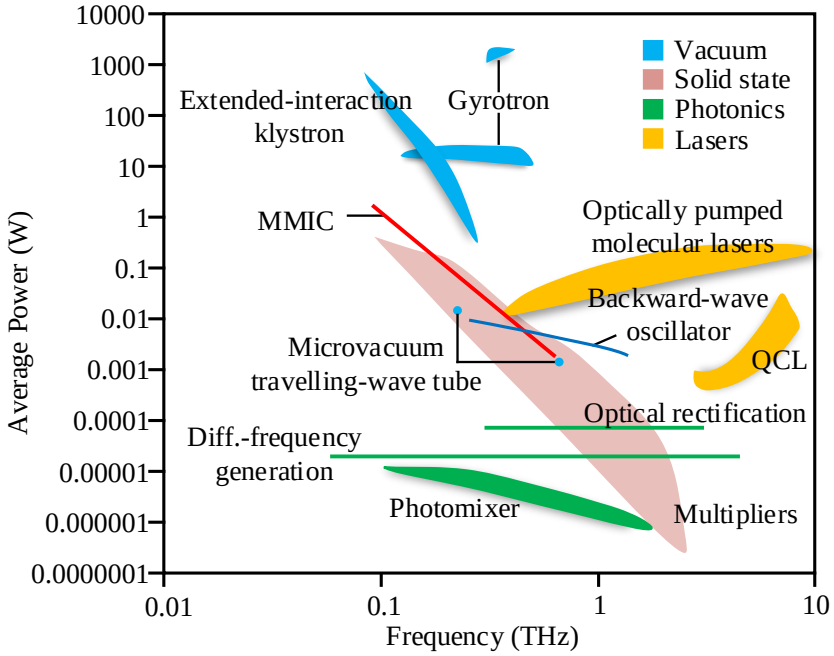

Figure 1.1 A general overview of the sources in the mm-wave and THz region. Reprinted from [23].

tens of milliwatts (narrowband) [2].

Conversely, approaches from optics include p-Ge, gas, and quantum cascade lasers (QCLs). Even if there is no fundamental limit to operate QCLs at THz frequencies [21], the fact that the photon energy (4.1 meV for 1 THz) is comparable to the thermal energy ($k_B T = 25.9$ meV at 300 K) has obstructed room temperature operation. Carriers in excited levels relax thermally instead of through stimulated emission of photons, as is required for laser operation. Therefore, they must be cooled, regularly at cryogenic temperatures [2]. This is also the case for p-Ge lasers [2]. Regarding THz gas lasers, they use the same concepts as typical lasers systems. The active medium is composed of polar molecules featuring transitions in the THz range. They are limited to operate at frequencies where appropriate transitions exist, for instance, 1.073 THz for NH_3 or 2.52 THz for CH_3OH [22]. Usually, gas lasers are optically pumped by a bulky $C0_2$ laser, but they feature output powers in range of tens of milliwatts [5], [22]. Generally, optical sources dominate generation beyond approximately 2 THz [23], [24].

Frequency down-conversion is the last generation approach. It can be accomplished through nonlinear optical processes such as optical rectification, difference-frequency generation (DFG), or optical parametric oscillation [8]. All these methods have in common the use of a nonlinear crystal (GaAs, ZnTe or $LiNbO_3$, among others [8]) to down-convert optical frequencies to the mm-wave/THz domain. The process can use, for instance, the second-order electrical susceptibility, $\chi^{(2)}$, as explained in [22] for DFG. Since they rely on nonlinear effects, they are more efficient under high electric fields, where the nonlinear interaction is stronger. Consequently, nonlinear methods are generally used under pulsed operation where

the crystals are illuminated by nano/femtosecond pulsed lasers [2], [22]. They constitute valuable sources for the generation of pulses spanning several THz [25] with peak powers of several Watts [22] and have favored the development of THz-Time domain spectroscopy [26].

An alternative for frequency down-conversion is photomixing. Both CW and pulsed operation modes are possible [2]. For CW operation, two optical wavelengths illuminate a fast photodetector, such as a photoconductor or a photodiode [24], [27]. They are also denominated as a photomixers. These devices output a photocurrent proportional to the input optical power, such that $I \propto |E|^2$. Since the output is quadratic with the electric field, it contains a beat note equal to the frequency difference of the two optical wavelengths, chosen to be in the mm-wave or THz range (we will explain this in more detail in a future chapter). When the photomixer is coupled to a suitable system (like an antenna), the output signal can be radiated. This constitutes the most basic realization of what we denote as photonic transmitter. Nowadays, state of the art photodiodes feature an output power in the range of tens to hundreds of μW at 300 GHz [3], [28], [29], and this figure is even lower for photoconductors [3].

Compared to the rest of the generation methods, the output power in CW photomixing is among the lowest [4], [23]. Even so, this approach is one of the preferred alternatives for CW signal generation starting as low as tens of GHz, up to approximately 2 THz [2], [9], [30]–[33]. The reason is that photomixing features key advantages in some applications. The most relevant ones are [2]:

- Most semiconductor lasers are tunable by several to tens of nanometers, so it is straightforward to tune a laser by 1 THz. It corresponds to a 0.5% tuning of the emission frequency of a 1550 nm laser (or a wavelength offset of 8 nm). Therefore, the beat note can span over a wide frequency range. For instance, the system of [34] provides a tuning range between ~ DC to 1.1 THz using two temperature-controlled distributed feedback (DFB) lasers and a broadband antenna. This aspect is particularly relevant for spectroscopic applications.
- The lasers linewidth determines the radiation linewidth of a CW photomixer. Typical values are a few MHz to a few tens of MHz for standard DFB lasers, and this suffices for applications such as telecommunications with direct detection or standard-resolution spectroscopy. Nevertheless, the use of long cavity lasers and stabilization techniques can achieve linewidths as low as a few kHz [35]. Narrow laser linewidths are of utmost importance when a signal with a long coherence length is required, and a relevant example is the Atacama large millimeter array (ALMA) local oscillator [36].
- A photonic transmitter illuminated at 1.55 μm makes use of widely employed telecommunications equipment. In particular, it is possible to feed it remotely with an optical fiber to reduce the free space propagation distance. It is also possible to use flexible modulation formats that has no electronic equivalent, or ultra-broadband optical communication devices such as switches, amplifiers, or true-time delays [37].

- Finally, photomixers are small footprint devices that operate at room temperature, avoiding dedicated cooling equipment, and making them apt for widespread use [38].

1.2 Challenges

Nowadays, mm-wave and THz science offer some maturity; research advances carried out over the previous decades have come into fruition, with the main concepts generally well established. Certainly, one can find a variety of books on the subject where the principles, applications, and research lines are in general coincident, e.g., [10], [39]–[41]. This is also the case for CW photomixing, where photonic transmitters and its applications (to which we will dedicate a whole chapter later) have been widely investigated.

Numerous examples of CW photomixing for spectroscopy can be found in the literature [24], [42]–[44], and even a commercial system is already on the market [45]. CW photomixing has been used as well in imaging [43], [46]–[49]. All the spectroscopy and imaging systems in the bibliography use lock-in detection to reduce the noise that masks the detected signal. Nevertheless, lock-in detection requires some integration time, with typical values between a few to hundreds of ms per measurement point [45]. It is worth pointing out that, to achieve 99% of the measured signal value, one has to average over 5-7 T, with T the integration time [50], as occurs similarly for an RC filter.

Therefore, data acquisition in these CW photomixing-based systems is slow, in the order of several minutes [44]. The acquisition time becomes even longer for imaging when the pixels are measured sequentially. This limitation stems from the low emitted power from photomixing, as we have shown before (see Fig. 1.1). This is caused in part by the difficulty from the circuit point of view to conjugate match an antenna to a source (photodiode) that presents an input impedance mainly capacitive with a low value of the real part ($\approx$ 3-15 Ω) [51], [52]. An improvement in the emitted power would lead to a lower measurement time. In turn, a reduction of the measurement time would make photomixing compatible with production time-scales, which could result in a more widespread use of CW photomixing not only in research but also in industrial applications such as plastic or package inspection, spectroscopic imaging, or humidity control, among others [10].

Wireless communications is probably the other application most widely targeted by demonstrations of photonic transmitters. Successive mobile generations have used higher and higher frequency bands that offer more bandwidth to accommodate the ever-increasing amount of wireless data traffic [53]. 5G and beyond 5G (B5G) networks will include mm- and THz frequencies where typical application scenarios include indoor communications, wireless backhauling, and reconfigurable links in data centers, e.g., [9], [54], [55]. These frequencies, however, generally require line-of-sight (LoS) links to overcome free-space propagation loss [31]. At the same time, it is widely acknowledged that beam steering would be an attractive, and even necessary feature for 5G and beyond [4], [31], [56]. Applications of beam steering include fine beam alignment in point-to-point links [19], the compensation of twist and sways of

mounting structures [57], point to multipoint communications, and user tracking in last-mile applications [54].

However, despite the previous demonstrations of photonic transmitters for wireless communications [37], [58]–[60], to cite a few, beam steering has received little attention so far [61]. Indeed, examples of photonic transmitters with beam steering are relatively uncommon, and they all make use of phased arrays [61]–[65]. The limited number of beam steering demonstrations is caused by the challenging integration of an antenna array with several photodiodes efficiently illuminated, where, besides, the amplitude and phase of the optical illumination must be controlled. As a result, only arrays with a few active elements are reported (approximately between 2 to 4), and the performance of the transmitter needs to be improved. To the best of our knowledge, a photonic transmitter with a directive (> 25 dBi), steerable beam has not been demonstrated yet for wireless communications at mm-waves or THz frequencies.

1.3 Goals

To overcome the previous challenges, we have conducted two main lines of research. In the first one, we propose an innovative antenna array concept featuring improved matching efficiency with the goal of substantially increasing the emitted power. First, an array with several elements increases the emitted power proportionally. Second, since the antenna array presents improved impedance matching, most of the available power from the photodiode is extracted (or radiated). In this way, we demonstrate more than a tenfold increase in the radiated power with respect to classical antennas. Fig. 1.2 illustrates the concept.

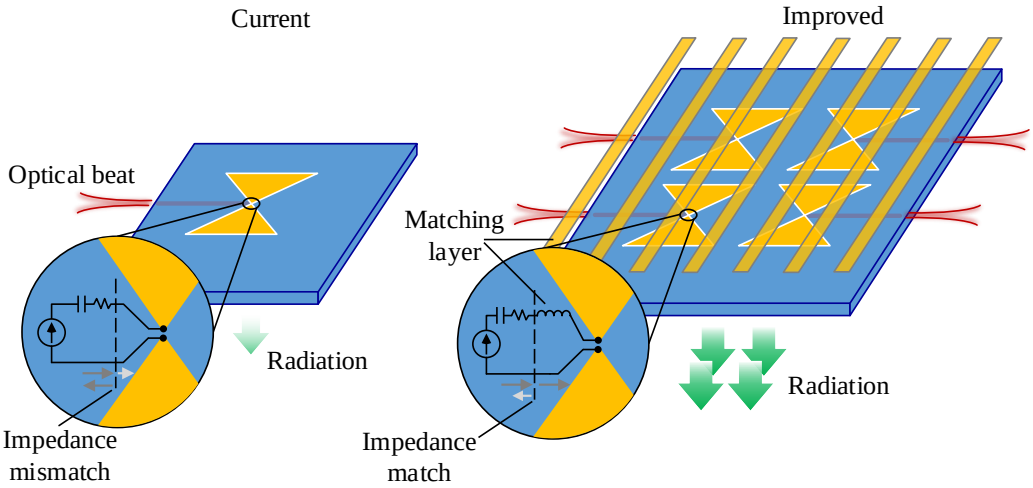

Figure 1.2 Antenna array with improved matching efficiency and emitted power for applications in spectroscopy and imaging.

Additionally, for telecommunications we have targeted novel photonically-excited arrays to tackle the lack of transmitters with a directive and steerable beam. To that end, we have proposed a leaky-wave antenna (LWA) array for 1-D beam steering in indoor reconfigurable

links. Besides, we have demonstrated photonic beam switching as an alternative to a phased array to obtain simultaneously a directive and steerable beam, while integrating a reduced number of antenna elements. Fig. 1.3 illustrates both concepts.

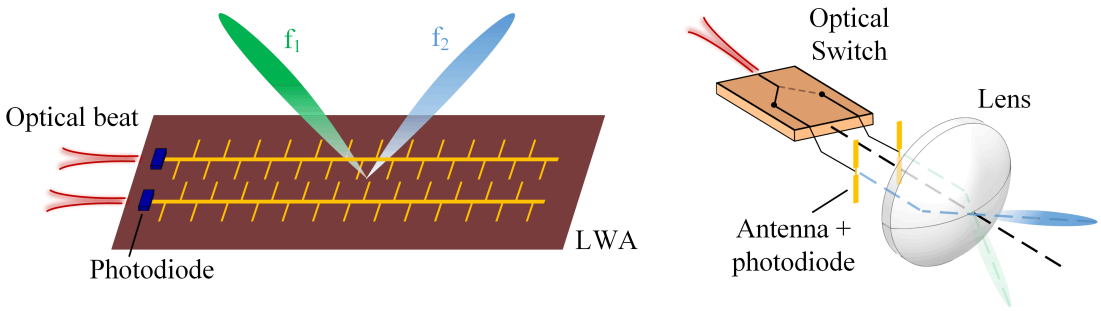

Figure 1.3 For telecommunications we present an antenna architecture with a directive and steerable beam using a LWA (left), and propose photonic beam switching (right).

1.4 Outline

In detail, we have organized this manuscript as follows: Chapter 2, together with Appendices A and B, includes a theoretical model for the scan impedance in infinite phased arrays of dipoles. We use equivalent circuits and a novel formulation to emphasize the aspects that affect the dipole impedance in the array environment. The model came about after studying tightly coupled phased arrays as a method to improve the matching efficiency between a photodiode source and an antenna array. Such a matching method is explained in a subsequent chapter. For clarity, we have preferred to place the theoretical model at the beginning to include later all the contents related to photonic transmitters.

After, we recover the path towards our goals by discussing in Chapter 3 applications of CW photonic transmitters at mm-wave and THz frequencies. We have emphasized those where our contributions would favor the consolidation of photonic transmitters.

Next, and before describing the research results on photonic transmitters, Chapter 4 introduces the method of photomixing and the different constituents of a transmitter. Together with Appendix C, these basics provide a reader not necessarily familiar with mm-wave and THz science with enough context to understand our choices after.

Chapter 5 tackles the first milestone, namely, to increase the emitted power. It presents a technique to increase the power emitted by an array of photodiodes efficiently coupled to the antennas, using some of the results from the model on infinite phased arrays in Chapter 2. Subsequently, we discuss a practical realization.

Finally, in Chapters 6 and 7, together with Appendices D and E, we address the second hurdle: the development of beam steering with directive antennas. In particular, we describe the design, assembly, measurements, and application of two novel photonic transmitters: a leaky-wave antenna that allows scanning the beam in 1-D for reconfigurable wireless links

(Chapter 6) and a patch array for beam switching in mm-wave wireless communications (Chapter 7).

In general lines, the chapters with original contributions follow the same structure: preface and summary, introduction, contents, and conclusions. As for the state-of-the-art on photonic transmitters, we have judged more convenient to split it. A substantial part of it is found in the chapter devoted to the basics (Chapter 4). The rest has been distributed among the consecutive chapters.

The appendices include material that is relevant to the contents but would have otherwise interrupted the lecture flow. They include extensions or detailed explanations of specific subjects treated within the main text, and the reader is encouraged to review them too.

We have tried to make clear what was done directly by the author, or in collaboration with colleagues during the experimental stages. This information is found at the conclusions section of each chapter, if pertinent. In this section, one may find as well a summary of the novel contributions. The novel contributions are again reviewed in broad terms in the Concluding Remarks of the manuscript, together with future research lines.

Last but not least, we will finish this document expressing our gratitude to the many actors that, directly or indirectly, helped us sail through the sea of the unknown to make this work possible.

2

An Asymptotic Approach to Analyze the Scan Impedance in Infinite Phased Arrays of Dipoles

The first contribution of this thesis deals with a theoretical model for infinite phased arrays of dipoles. The contents of the chapter, completed by appendices A and B, constitute an extension of [ii] from the List of Publications. Phased arrays are an important part of this thesis, since integration with photodiodes allows one to increase the total radiated power and to steer the beam. In the analysis and design of phased arrays, one can resort to the infinite array approach because it enables the study of the array elements as an equivalent network, more prone for interpretation with simple mathematical expressions, hence the importance of this chapter for subsequent analysis. In Chapter 5, we use some of the results obtained here to design the unit-cell of an array with improved matching efficiency between the photodiode source and the antenna. For convenience, approaches to design antenna arrays fed by photodiodes are introduced in Chapter 5 in order to cover here array theory only.

To some extent, the contents of this chapter are not in line with the main research objective of this thesis: to develop photonic transmitters with enhanced performance at mm-waves. Hence, we have opted for a succinct introduction to infinite phased array theory that suffices to put into context the model. We will not cover introductory contents that would deviate the focus from our main target. Furthermore, the model builds on fundamental concepts such as the radiation pattern of a Hertzian dipole or transmission line theory, so that little prior knowledge on antenna arrays is required. In addition, to provide a better perspective, we have put special emphasis on highlighting the novelties with respect to other works on infinite phased arrays. We hope that even the experienced antenna array designer will appreciate this chapter, where we work out novel perspectives, formulas, and developments for infinite phased arrays of dipoles.

In summary, the original contribution of this chapter consists in an analytic model to derive the scan impedance of planar infinite phased arrays of dipoles at a dielectric interface

when only the (0,0) Floquet mode propagates. The proposed model builds on the boundary conditions satisfied by the fundamental Floquet mode at the interface to provide a novel derivation of the equivalent circuit for the scan impedance. The analysis is also extended to include the effect of a sufficiently thick grounded substrate that does not affect the elements current distribution and does not interact with the evanescent fields. Next, formulas for the ratio of intensity radiated towards each half-space for an interfacial array are provided. In a consecutive step, an asymptotic approximation is derived for the current distribution in arrays of dipoles with arbitrary load terminations, and the reactance of a dipole in the array environment is related to the inductance of a grid of wires. This model constitutes a useful tool to clearly identify the role of the different array variables (dipole dimensions, relative permittivity of the substrate, periodicity, end-load, and scan angle in the principal planes) on the scan impedance by simple expressions and equivalent circuits. The model predictions are in good agreement with full-wave simulations and with previously published works.

2.1 Introduction

Phased arrays represent a broad class of antennas to which extensive research efforts have been dedicated [66]–[68]. In particular, planar phased arrays of printed elements, such as dipoles or slots, have received most of the attention. The substrate in which the elements are printed offers a relatively simple, low-cost, and low-profile framework for monolithic or hybrid integration with active elements. Wide-band, dual-linear, and wide-scan performance have been reported for connected or tightly coupled arrays of dipoles [69]–[71].

As the number of elements in the array increases for a fixed element spacing, the central elements behave like those within an infinite array [72], [66, Ch. 7]. Thus, the infinite array approach is an analysis method suitable for large arrays where edge elements and edge-related effects do not substantially affect the overall performance.

Previous studies on infinite phased arrays of dipoles are numerous. Indeed, the periodicity of the array enables the expansion of the fields in a discrete set of plane waves or Floquet modes (spectral approach). This approach generally leads to simplified mathematical expressions that can be readily evaluated numerically or even analytically in some cases. In [73], the current sheet model was presented as the simplest infinite phased array in the limiting case of closely spaced Hertzian dipoles. This model led to simple expressions for the scan resistance, and the concept was later extended in [74] for printed elements on a semi-infinite dielectric interface. Arrays of disconnected dipoles in free space were considered either assuming a current distribution [75], [76], [77, Ch. 3], or by an integral equation technique [78]. Later on, the study was extended to solve disconnected dipoles printed on semi-infinite substrates or on a grounded dielectric slab using a Method of Moments (MoM) [79]. Since then, extensive numerical studies, implementations, and theoretical modeling of connected or tightly coupled arrays have been carried out, for instance in [80]–[86].

Of special relevance are the works by Munk and collaborators [87], [88], in which capaci-

tive coupling among colinear dipoles was introduced to increase the impedance bandwidth. In [87], a periodic MoM approach was used to determine expressions for the dipole scan impedance; the summation in the spectral domain of the magnetic vector potential from a Hertzian dipole was combined with a mutual impedance approach. However, in the aforementioned studies, the arrays in multilayered media were always embedded in a homogeneous region, and never at the interfaces, as it is usually the case in practical realizations.

Despite the extensive efforts devoted in the past to the analysis of infinite phased arrays of dipoles, to date, there is no model to readily interpret the impact of the array variables on the scan impedance, especially on the reactance. The numerical methods such as those in [79], [87], [89] or the description in [84], are rigorous and computationally powerful but mask the fundamental impedance features of the array. Therefore, one is forced to carry out exhaustive computation and parametric sweeps to gain physical insight into the array operation for different configurations. For instance, the spectral expansion approach by [87] yields a double infinite sum to calculate the scan reactance. From this, general conclusions can be hardly inferred. However, an approximate analytic method is more appropriate to evaluate in a simple manner how the different phenomena affect the scan impedance for diverse array configurations. We provide in this chapter a novel and insightful circuit approach that readily shows the role of the main variables of a phased array of dipoles on the scan impedance as defined in [66, Ch. 1]. These variables include the dipole dimensions and type of end-load, the array periodicity, the relative permittivity of the substrate for a printed array, and the scan angle in the principal planes. Although the Green's function approach was used in [83] to derive equivalent circuits for interfacial arrays of connected dipoles, the circuits and expressions in this work stem instead from the boundary conditions met by the fundamental Floquet mode and an asymptotic approximation of the current, which can handle arbitrary loads.

The remainder of the chapter is organized as follows: In Section 2.2, we exploit the far-field plane wave expansion of a dipole array on an interface to obtain boundary conditions at the interface for the radiated fundamental Floquet mode. In Section 2.3, the boundary conditions are used to obtain equivalent networks and expressions for the scan resistance when the array lies at a dielectric interface. The ratio of intensity radiated towards each half-space is also derived. In Section 2.4, the analysis is extended to cases where a ground plane backs the interfacial array. We assume a thick substrate so that the ground plane does not affect the elements current distribution and it does not interact with the evanescent fields. Such assumptions are fulfilled by a typical substrate thickness of $\lambda/4$. Section 2.5 is devoted to the derivation of the current along the dipole and an equivalent network for the scan reactance at broadside. The results obtained with the proposed model are compared to full-wave simulations in Section 2.6, followed by the results for the principal scan planes in Section 2.7. We conclude the analysis with remarks on the scan impedance and general conclusions in Sections 2.8 and 2.9, respectively.

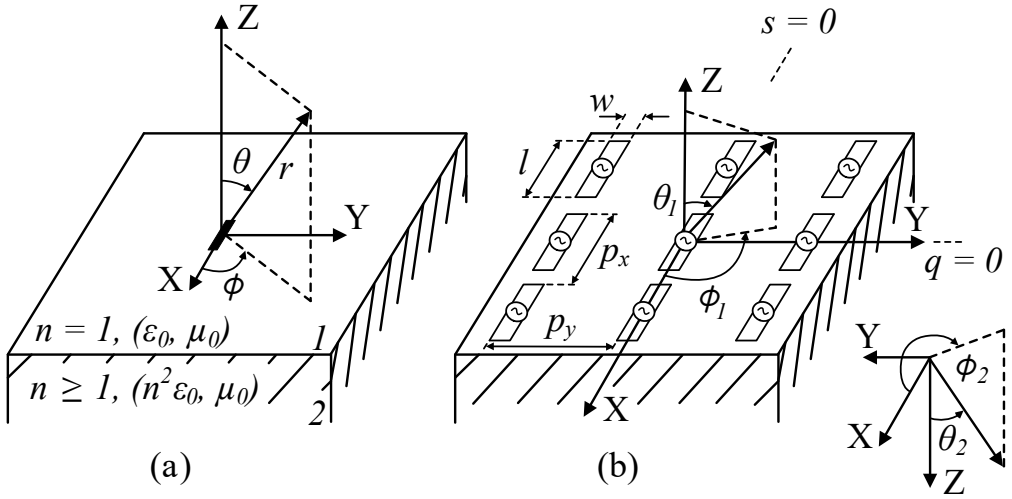

Figure 2.1 (a) Hertzian dipole printed on the interface between two lossless dielectrics. Medium 1 ($z > 0$) is characterized by $n = 1$ and medium 2 ($z < 0$) is characterized by $n \geq 1$. (b) Cut of the infinite interfacial array of dipoles in a rectangular lattice, relevant geometrical parameters, and the respective coordinate system for each half-space.

2.2 Plane Wave Expansion on the Radiated Fields

In order to derive the electric field radiated by an infinite phased array of dipoles lying on a dielectric interface, first we add the individual contributions of interfacial Hertzian dipoles. Then, this sum is written in the spectral domain as a discrete set of plane waves or Floquet modes. We will show that the tangential electric field is equal at both sides of the interface for the fundamental Floquet mode. This result will constitute the basis of the subsequent discussion.

The electric field of a Hertzian dipole in a homogeneous medium admits a closed-form expression both in the near- and far-field regions. This is not the case for a dipole placed parallel, and at the interface between two different dielectrics. This hurdle, however, can be conveniently overcome using the far-field of the interfacial Hertzian dipole in [90]. The Hertzian dipole is of length Δl, its current I, and the interface is composed of two lossless dielectrics as shown in Fig. 2.1a. The upper dielectric is characterized by $n_1 = 1$ and the lower one by $n_2 = n \geq 1$. That is, the ratio of dielectric index is n. For a harmonic time dependence $\mathrm{e}^{\mathrm{j}\omega t}$, the expression is written as

$$dE_i^{\theta,\phi} = \frac{\mathrm{j}k_0 n_i I \Delta l}{2\pi} Z_0 f_i^{\theta,\phi}(\theta,\phi) \frac{\mathrm{e}^{-\mathrm{j}n_i k_0 r}}{r}, \tag{2.1}$$

where i denotes the medium, and Z_0 is the impedance of a TEM wave in free-space. Expression (2.1) is valid when $k_0 r \to \infty$ and $0 \leq \theta \leq \pi/2$ in medium 1, and when $nk_0 r \to \infty$ and $\pi - \theta_c \leq \theta \leq \pi$ in medium 2. The angle θ_c is obtained from $\sin\theta_c = 1/n$, and it will be the

maximum scan angle allowed in medium 2. The pattern functions in (2.1) are defined as

$$f_1^\theta = \left\{ \frac{\cos^2\theta}{\cos\theta + (n^2 - \sin^2\theta)^{1/2}} - \sin^2\theta\cos\theta \frac{\cos\theta - (n^2 - \sin^2\theta)^{1/2}}{n^2\cos\theta + (n^2 - \sin^2\theta)^{1/2}} \right\} \cos\phi \tag{2.2a}$$

$$f_1^\phi = -\frac{\cos\theta\sin\phi}{\cos\theta + (n^2 - \sin^2\theta)^{1/2}} \tag{2.2b}$$

$$f_2^\theta = \left\{ \sin^2\theta\cos\theta \frac{(1 - n^2\sin^2\theta)^{1/2} + n\cos\theta}{n(1 - n^2\sin^2\theta)^{1/2} - \cos\theta} - \frac{\cos^2\theta}{(1 - n^2\sin^2\theta)^{1/2} - n\cos\theta} \right\} \cos\phi \tag{2.2c}$$

$$f_2^\phi = \frac{\cos\theta\sin\phi}{(1 - n^2\sin^2\theta)^{1/2} - n\cos\theta}, \tag{2.2d}$$

where the subscript and superscript in f refer to the corresponding medium and polarization, respectively.

The Hertzian element is now replicated to form a double infinite array of dipoles in a rectangular lattice. The element periodicity is given by p_x and p_y, as shown in Fig. 2.1b. The dipoles of length l and width w are center-fed by ideal δ-gap generators with uniform current amplitude and linear phase progression, defined for the (q,s) element as $I_{qs} = I_{00}\mathrm{e}^{-\mathrm{j}q\Delta\alpha}\mathrm{e}^{-\mathrm{j}s\Delta\beta}$. I_{00} is the current of the $(0,0)$ element, located at the origin of coordinates, and the phase progression is defined (recall $n_1 = 1$):

$$\Delta\alpha = p_x k_1 \sin\theta\cos\phi = p_x k_0 s_x, \tag{2.3a}$$

$$\Delta\beta = p_y k_1 \sin\theta\sin\phi = p_y k_0 s_y. \tag{2.3b}$$

The electric far-field of the array is obtained by summation of all individual contributions of the Hertzian elements and double application of Poisson's sum formula. Following a procedure similar to that in [87, Ch. 4], we have

$$E_i = \frac{Z_0}{p_x p_y} \sum_{u=-\infty}^{+\infty} \sum_{v=-\infty}^{+\infty} \frac{f_i(\theta,\phi)}{s_z} \mathrm{e}^{\pm\mathrm{j}k_i z s_z} \mathrm{e}^{-\mathrm{j}k_0 x\left(s_x + u\left(\frac{\lambda_0}{p_x}\right)\right)} \mathrm{e}^{-\mathrm{j}k_0 y\left(s_y + v\left(\frac{\lambda_0}{p_y}\right)\right)} \int_{-l/2}^{l/2} I(x') \mathrm{e}^{\mathrm{j}k_0 x'\left(s_x + u\left(\frac{\lambda_0}{p_x}\right)\right)} dx', \tag{2.4}$$

with

$$s_z = \sqrt{1 - \left(\frac{s_x}{n_i} + u\left(\frac{\lambda_i}{p_x}\right)\right)^2 - \left(\frac{s_y}{n_i} + v\left(\frac{\lambda_i}{p_y}\right)\right)^2}. \tag{2.5}$$

The steps to obtain (2.4) from (2.1) have been described in detail in Appendix A. In (2.4), $z \lessgtr 0$, and the sign in the exponential is taken accordingly for propagation away from the interface. The polarization superscripts in E and in the pattern functions have been omitted, and we have assumed that the current flows along the longitudinal axis of the dipole.

Equation (2.4) is the electric field resultant from the addition of the far-fields of Hertzian dipoles. It yields a discrete sum of plane waves or Floquet modes with wavevector components at a discrete set of directions in space. For s_z real, the (u,v) mode propagates and decays

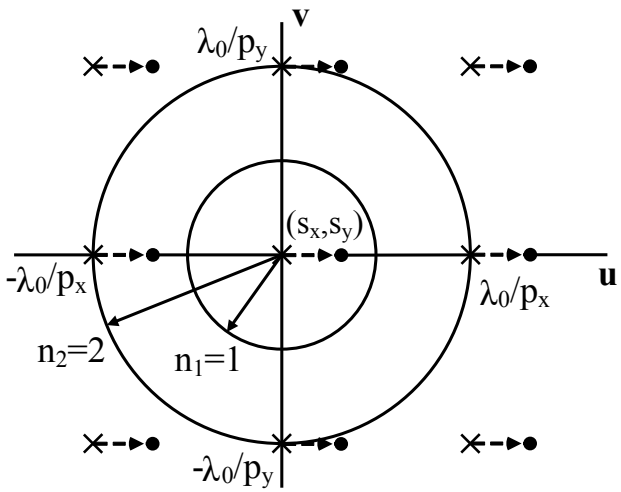

Figure 2.2 Reciprocal plane diagram to determine the presence of grating lobes, for $p_x = p_y = \lambda_0/2$. The crosses indicate the modes when the dipoles radiate in phase, whereas the solid circles represent the modes for $(s_x = 1/\sqrt{2}, s_y = 0)$. For the circles there is only one mode falling within the circle of radius 1 but there are two modes within the circle of radius 2.

exponentially otherwise. Note the total electric field is weighed by the dipole pattern function, according to the principle of pattern multiplication.

2.2.1 The (0, 0) Floquet Mode

For a single propagating term in (2.4), or equivalently, for no grating lobes, the following condition is to be fulfilled:

$$\left(s_x + u\left(\frac{\lambda_0}{p_x}\right)\right)^2 + \left(s_y + v\left(\frac{\lambda_0}{p_y}\right)\right)^2 > n_i^2 \tag{2.6}$$

for all (u, v) modes except for the $(0,0)$. The $(0,0)$ mode always propagates if the scan angle θ is limited below 90° in medium 1 ($s_x^2 + s_y^2 < 1$). Equation (2.6) is best interpreted on the basis of Fig. 2.2: in the reciprocal plane, the (u, v) vectors representing the modes constitute points arranged in a regular grid with a periodicity given by λ_0/p_x and λ_0/p_y for u and v directions, respectively. The points are displaced (s_x, s_y) from the broadside positions (marked with crosses), which corresponds to $(s_x = 1/\sqrt{2}, s_y = 0)$ in the example shown. In particular, one can note that the excitation, as defined in (2.3), determines the wavevector components, (s_x, s_y) of the $(0,0)$ Floquet mode. For a mode to decay, it must fulfill the condition that its distance to the origin is $> n_i$, therefore, the points other than the $(0,0)$ falling within the circle of radius n_i, represent other modes that contribute to radiation (grating lobes). For a given phase progression that determines (s_x, s_y), it evidently suffices with the examination of medium 2 to determine the presence of grating lobes. Besides, it can happen that a mode propagates in medium 2 but not in 1, as shown in the example for the $(-1,0)$ mode. Finally, for a homogeneous medium, both circles in Fig. 2.2 would collapse into a single one and the diagram would be equivalent to that widely discussed in classic antenna texts, such as [77].

2.2.2 The Boundary Conditions

In the absence of grating lobes, the $(0,0)$ term in (2.4) corresponds to the electric field of the radiated plane wave, and is the only term contributing to the scan resistance. The remainder of terms represent the contribution of the Hertzian dipole far-field to the scan reactance in the array environment. At this point, it is convenient to use a different reference system for each half-space, as shown in Fig. 2.1b, to obtain a simpler expression for the radiated field. To that end, we apply the following transformations: $\theta_1 = \theta$, $\phi_1 = \phi$ in medium 1, and $\theta_2 = \pi - \theta$, $\phi_2 = -\phi$ in medium 2. The angles of propagation of the $(0,0)$ mode in each medium are related by $\phi_2 = -\phi_1$ and $n\sin\theta_2 = \sin\theta_1$. In view of the previous discussion, the radiated electric field in each half-space is expressed as

$$E_i = \frac{Z_0}{p_x p_y} f_i(\theta_i, \phi_i) \frac{\mathrm{e}^{-\mathrm{j}\vec{k}_i\cdot\vec{r}_i}}{\cos\theta_i} \int_{-l/2}^{l/2} I(x') \mathrm{e}^{\mathrm{j}k_0 x' s_x} dx', \tag{2.7}$$

where $\vec{r}_i$ is the observation point in each coordinate system, $\vec{k}_1 = k_0(s_x, s_y, \cos\theta_1)$, and $\vec{k}_2 = k_0(s_x, -s_y, n\cos\theta_2)$. At broadside, it is not difficult to see that $E_1 = E_2$ at the interface plane ($z_i \to 0^+$). Similarly, comparing in (2.7) for both media, after some algebra, one finds the following relations

$$E_{1\theta}\cos\theta_1 = E_{2\theta}\cos\theta_2, \qquad E_{1\phi} = -E_{2\phi}. \tag{2.8}$$

The relations are valid for any scan angle (recall $0 \le \theta_2 < \theta_c$, or equivalently, $0 \le \theta_1 < \pi/2$). Therefore, the tangential component of the electric field is equal at both sides of the interface for the fundamental Floquet mode, analogously to the classical boundary condition. We will also refer to (2.8) as boundary condition even if this expression is true in the far-field. In general, (2.8) is valid for any two loss-less dielectrics characterized by n_1 and $n_2 \ge n_1$, with θ_1 and θ_2 related by the Snell's law. The minus sign for $E_{2\phi}$ in (2.8) appears given that $\hat{\phi}_i$ are reversed as measured from system of reference 2 with respect to system of reference 1.

Equation (2.8) will be used in the next section to derive expressions and equivalent networks for the scan resistance of dipoles in an infinite phased array, and also to calculate the intensity radiated towards each half-space.

The boundary conditions in (2.8) have been derived for the fundamental mode that concerns our present study. However, it is not difficult to demonstrate that the continuity of the tangential component of the electric field across the interface is fulfilled by all modes individually, except for a $-\mathrm{j}$ factor if the mode decays in medium 1 but not in 2. This stems from the fact that the plane wave decomposition results in the fields being expressed as a sum of propagating or evanescent plane waves fulfilling the classical boundary condition. Indeed, the boundary conditions will be used in Appendix B to examine the scan resistance when a second mode propagates.

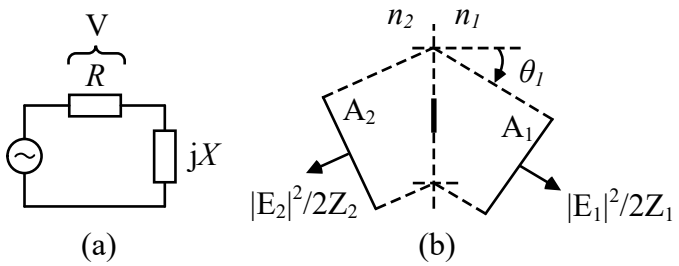

Figure 2.3 The power dissipated in the scan resistance of the dipole (a), corresponds to the power carried away by the radiated mode in the apparent area allocated for the element (b).

2.3 Array on a Dielectric Interface

In this section, the structure depicted in Fig. 2.1b is studied. The generators excite the array impressing a fixed voltage, or current, at the dipole input terminals. Ohmic losses are neglected, and the dielectric half-spaces are generally characterized by n_1 and $n_2 \geq n_1$. The corresponding impedances for a TEM wave are Z_1 and Z_2. The periodicity is such that grating lobes are precluded, and the allocated area for each element is $p_x p_y$.

2.3.1 Scan Resistance at Broadside

The scan resistance at broadside can be derived through (2.8). For the radiated plane wave, we have $E_{1\theta} = E_{2\theta} = E$. Let V be the voltage drop in the scan resistance of a reference dipole, R_r, as in the Thevenin equivalent of Fig. 2.3a. The power dissipated in the resistance equals the total Poynting vector times the element allocated area (Fig. 2.3b for $\theta_1 = 0$). Omitting the factor 1/2 from time average, we have

$$\frac{|V|^2}{R_r}\frac{1}{p_x p_y} = \frac{|E|^2}{Z_1} + \frac{|E|^2}{Z_2}. \tag{2.9}$$

For an emitted plane wave, the electric field is related to the voltage at the dipole terminals by $V = P_f E$ [87, eq. 4.45], where E is the electric field parallel to the dipole ($\hat{x}$-directed). Since the tangential component is continuous across the interface, there is no ambiguity in the choice of E. P_f is defined as

$$P_f = \frac{1}{I(0)}\int_{-l/2}^{l/2} I(x')\mathrm{e}^{\mathrm{j}k_1 x' s_x}\,dx'. \tag{2.10}$$

Bear in mind that k_1 appears in the expression above because medium 1 is chosen to define the phase progression (in turn defining s_x). The integral is performed over any element of the array, with $I(0)$ the current at the feed point. Relating E and V in (2.9) gives

$$R_r = (Z_1 \parallel Z_2)\frac{|P_f|^2}{p_x p_y}. \tag{2.11}$$

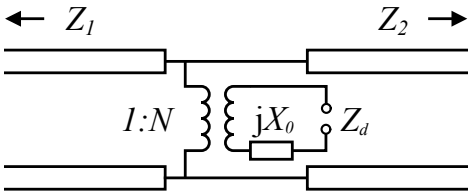

Figure 2.4 Equivalent network for the scan impedance of an infinite interfacial phased array of dipoles.

2.3.2 Scan Resistance for Principal Scan Planes

Let us now examine how the scan resistance varies at the principal scan planes. As explained above, the power delivered to R_r in the Thevenin equivalent equals the total Poynting vector times the apparent or projected area allocated for the element. Thus we have

$$R_r = \frac{|P_f|^2}{p_x p_y} \frac{Z_0}{\dfrac{n_1}{\cos\theta_1} + \dfrac{n_2}{\cos\theta_2}} = N^2 (Z_1 \cos\theta_1 \parallel Z_2 \cos\theta_2), \tag{2.12a}$$

$$R_r = \frac{|P_f|^2}{p_x p_y} \frac{Z_0}{n_1 \cos\theta_1 + n_2 \cos\theta_2} = N^2 \left(\frac{Z_1}{\cos\theta_1} \parallel \frac{Z_2}{\cos\theta_2} \right), \tag{2.12b}$$

where (2.12a) and (2.12b) stand for E- and H-plane scan respectively. Arbitrary scan angles shall be treated similarly, and noting that $E_{1\theta}/E_{1\phi} = f_{1\theta}/f_{1\phi}$, which is known analytically. The shunt impedance in (2.11) indicates that the scan resistance can be expressed in terms of an equivalent network composed of two shunt infinite transmission lines (TLs), while the factor $|P_f|^2/p_x p_y = N^2$ is accounted for by a transformer. At broadside, the scan impedance, Z_d, corresponds to the equivalent network of Fig. 2.4, and by transforming $Z_i \to Z_i \cos\theta_i$, $Z_i \to Z_i/\cos\theta_i$, analog networks follow for E- and H-plane scan respectively. For a homogeneous medium, this is in agreement with the results from [77], [87]. X_0 in the equivalent network accounts for the scan reactance, and depends in general on n_1 and n_2, the array geometry, the scan angle, and the frequency. Note that the current distribution is also required to calculate P_f and in turn the scan resistance. These two aspects will be studied in Section 2.5. Finally, the analysis is extended in Appendix B for the case when a second propagating mode is present.

2.3.3 The Intensity Radiated Toward Each Half-Space

Let us now examine the ratio of intensity (S) radiated toward each half space. For H-plane scan, using (2.8) one can easily obtain $S_1 = n_1|E_{1\phi}|^2/Z_0$, and $S_2 = n_2|E_{1\phi}|^2/Z_0$. Hence:

$$\frac{S_2}{S_1} = \frac{n_2}{n_1}. \tag{2.13}$$

In this plane, the ratio is constant with the scan angle. For an air-dielectric interface, it equals $\epsilon_r^{1/2}$, with ϵ_r the relative permittivity of the dielectric. For E-plane scan, $S_1 = n_1|E_{1\theta}|^2/Z_0$, and

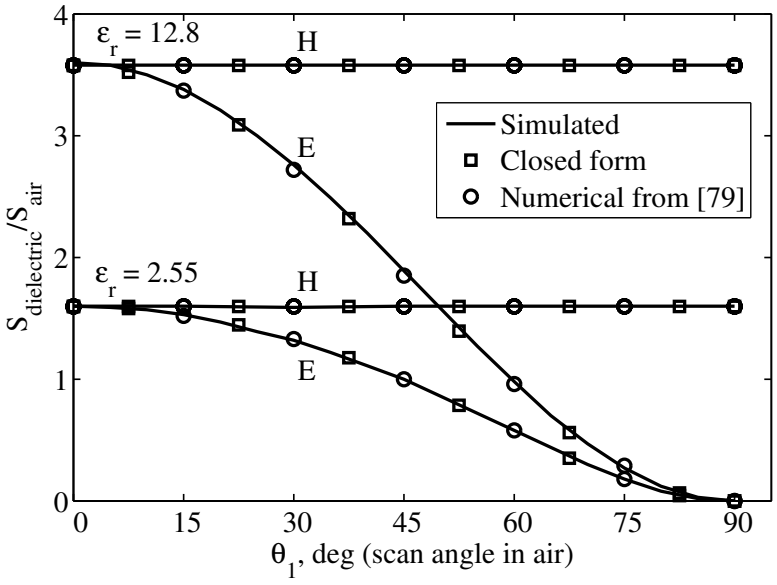

Figure 2.5 Ratio of Poynting vector modulus in the principal planes for the mode radiated by an infinite phased array of dipoles. We consider two different air-dielectric interfaces: Duroid ($\epsilon_r = 2.55$) and GaAs ($\epsilon_r = 12.8$). Full-wave simulations with ANSYS HFSS [91] (solid lines), present model (squares), and numerical calculation from [79] (circles). The dimensions are $p_x = p_y = 0.2184\lambda_0$, $l = 0.182\lambda_0$, $w = 0.01\lambda_0$.

$S_2 = n_2|E_{2\theta}|^2/Z_0$. Then, using (2.8):

$$\frac{S_2}{S_1} = \frac{n_2 \cos^2\theta_1}{n_1 \cos^2\theta_2}. \tag{2.14}$$

The ratio of intensity is in general different from that of a single dipole, which equals $\epsilon_r^{3/2}$ at broadside for an air-dielectric interface, as can be inferred from (2.1)-(2.2), and also noted in [79]. Fig. 2.5 shows the intensity ratio calculated by (2.13)-(2.14) for two different air-dielectric interfaces. Results practically overlap with full-wave simulations and are in good agreement with those calculated in [79, Fig. 9]. The power ratio would be obtained by multiplying S times the projected area allocated for each element in the direction of the scan angle. In particular, at broadside both projected areas coincide and the power ratio also equals $\epsilon_r^{1/2}$ for an air-dielectric interface. Since at broadside $E_1 = E_2$, the ratio must be the same for any planar antenna regardless of its current distribution, even if the antenna is not linear.

2.4 Array on a Dielectric Interface Backed by a Ground Plane

Since the initial radiated fields are known by the boundary conditions, it is possible to account for the effect of a ground plane reflector by computing the multiple reflections. Calculation of the real and complex power leads to expressions for the scan impedance for broadside and for the principal scan planes. It is assumed that the reflector is placed at a distance d from the

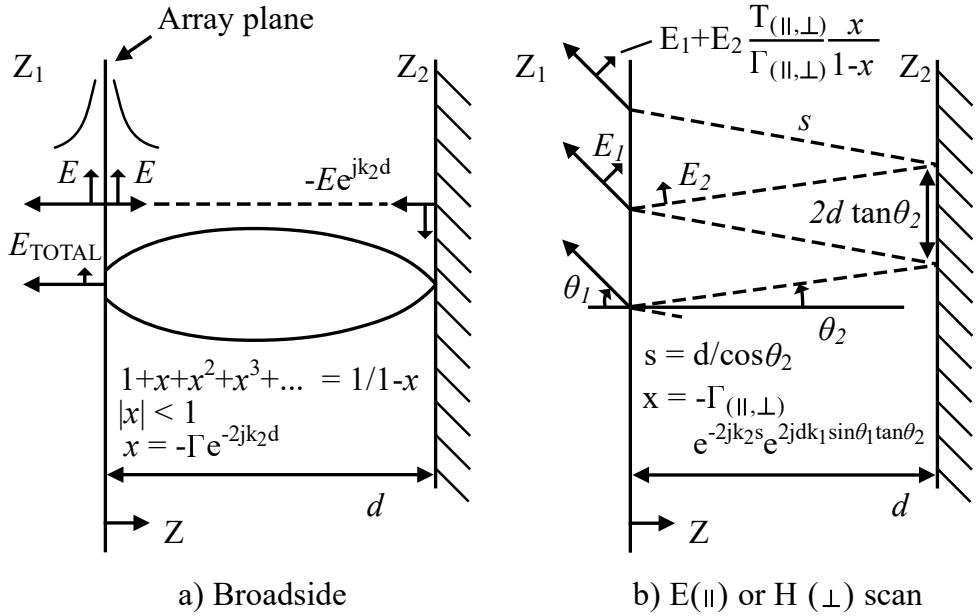

Figure 2.6 Longitudinal cut of the infinite dipole array backed by a groundplane at a distance d. (a) Broadside emission (top-bottom): evanescent fields in z-direction do not interact with the groundplane, initially radiated fields, resultant electric field from the partially standing wave, and sum formula for multiple reflections. (b) E- or H-scan (top-bottom): emerging field at the interface plane after multiple reflections, initially radiated fields, and directions of propagation.

interface in any medium, say medium 2, such that the evanescent modes do not interact with it and that its presence does not alter the current distribution of the elements. For the sake of simplicity, the broadside case is treated first and the expressions for E- and H-plane scan are derived next by analogy. Under the previous assumptions, the scan impedance is written as the sum of three terms: X_0, the initial reactive part, R_r^{GP} , a term related to the amplitude of the plane wave emerging from the structure and, X^{GP}, related to the reactive energy stored due to the presence of the ground plane:

$$Z_d = R_r^{\mathrm{GP}} + \mathrm{j}X^{\mathrm{GP}} + \mathrm{j}X_0. \tag{2.15}$$

2.4.1 Scan Impedance at Broadside

The situation where the array radiates at broadside is depicted in Fig. 2.6a.

Real Power and Resistance

The resultant electric field emerging from the structure at the interface plane, after consideration of the multiple reflections, is given by

$$E_{\mathrm{total}} = E\left(\frac{1-\mathrm{e}^{-2\mathrm{j}k_2 d}}{1+\Gamma\mathrm{e}^{-2\mathrm{j}k_2 d}}\right), \tag{2.16}$$

where Γ is the Fresnel's reflection coefficient from medium 2 to 1 for normal incidence:

$$\Gamma = \frac{n_2 - n_1}{n_2 + n_1}. \tag{2.17}$$

The power radiated per allocated element area is

$$\frac{|I(0)|^2}{p_x p_y} R_r^{\mathrm{GP}} = \frac{|E|^2}{Z_1} \left| \frac{1 - \mathrm{e}^{-2\mathrm{j}k_2 d}}{1 + \Gamma \mathrm{e}^{-2\mathrm{j}k_2 d}} \right|^2. \tag{2.18}$$

The power delivered to each element per allocated area when there is no ground plane is given by

$$\frac{|I(0)|^2}{p_x p_y} R_r = \frac{|E|^2}{Z_1 \parallel Z_2}, \tag{2.19}$$

combining (2.18) and (2.19), one obtains

$$R_r^{\mathrm{GP}} = R_r \frac{n_2/n_1 + 1}{1 + \left(\dfrac{n_2}{n_1 \tan(k_2 d)} \right)^2}. \tag{2.20}$$

For a homogeneous medium, (2.20) reduces to $R_r^{\mathrm{GP}} = 2R_r \sin^2(k_2 d)$. Examination of (2.20) indicates that for $k_2 d = m\pi$, with $m = 0, 1, 2...$, the ground plane short-circuits the array and the scan resistance equals 0. The positions of maximum scan resistance occur at $k_2 d = (2m+1)\pi/2$ and yield $R_r^{\mathrm{GP}} = R_r(1 + n_2/n_1)$. Finally, for $\tan^2(k_2 d) = n_2/n_1$, the ground plane leaves the scan resistance of the array untouched, $R_r^{\mathrm{GP}} = R_r$. The first position occurs at $d = \lambda/8$ for a homogeneous medium (radiated field to the left and reflected add in quadrature), but the position deviates when the array is at an interface.

Complex Power and Reactance

To calculate the reactive part associated with the presence of the ground plane, first, the resulting fields inside the structure are computed:

$$E_{\mathrm{total}} = \frac{E}{1 + \Gamma \mathrm{e}^{-2\mathrm{j}k_2 d}} \left(\mathrm{e}^{-\mathrm{j}k_2 z} - \mathrm{e}^{-\mathrm{j}k_2 d} \mathrm{e}^{\mathrm{j}k_2 (z-d)} \right), \tag{2.21a}$$

$$H_{\mathrm{total}} = \frac{E}{Z_2 \left(1 + \Gamma \mathrm{e}^{-2\mathrm{j}k_2 d}\right)} \left(\mathrm{e}^{-\mathrm{j}k_2 z} + \mathrm{e}^{-\mathrm{j}k_2 d} \mathrm{e}^{\mathrm{j}k_2 (z-d)} \right), \tag{2.21b}$$

where $0 \le z \le d$. The calculation of the reactive power, P_X, per allocated area yields

$$\frac{P_X}{p_x p_y} = \frac{\partial \left(\int_0^d (W_e - W_m) dx \right)}{\partial t} = \mathrm{j} \frac{|E|^2}{Z_2 |1 + \Gamma \mathrm{e}^{-2\mathrm{j}k_2 d}|^2} \sin(2k_2 d). \tag{2.22}$$

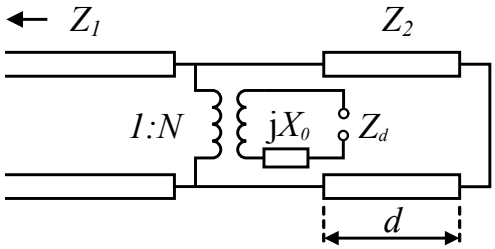

Figure 2.7 Equivalent network for the scan impedance of an infinite interfacial phased array of dipoles backed by a ground plane.

W_e and W_m are, respectively, the electric and magnetic energy densities. Comparing the reactive power delivered to the reactance X^{GP} by the ideal current generator and the power delivered to the scan resistance when there is no reflector (2.19), yields

$$X^{\mathrm{GP}} = R_r \frac{n_1 + n_2}{2\left(n_2 \cos^2(k_2 d) + \dfrac{n_1^2}{n_2}\sin^2(k_2 d)\right)} \sin(2k_2 d). \tag{2.23}$$

When the initially radiated field adds in phase with the reflections, the scan resistance is maximum and X^{GP} equals 0. X^{GP} takes this value again when the ground plane short-circuits the antenna; then the zeros of X^{GP} occur for $k_2 d = m\pi/2$. X^{GP} takes extreme values larger than $\pm R_r$ when $Z_2 < Z_1$ and lower otherwise. For a homogeneous medium, (2.23) reduces to $X^{\mathrm{GP}} = R_r \sin(2k_2 d)$, and X^{GP} takes values between $\pm R_r$. In particular, when R_r^{GP} equals R_r, so does $|X^{\mathrm{GP}}|$.

Finally, it can be seen that (2.15), where R_r^{GP} is given by (2.20), and X^{GP} is given by (2.23), corresponds to the input impedance of the equivalent network of Fig. 2.7.

2.4.2 Scan Impedance for Principal Scan Planes

Let the array now scan in a principal plane that corresponds to an angle θ_1 in medium 1.

Real Power and Resistance

The resultant electric field emerging from the structure at the interface plane, after addition of the multiple reflections (see Fig. 2.6b) is

$$E_{\mathrm{total}} = E_1 \left(\frac{1 - \mathrm{e}^{-2\mathrm{j}k_2 d\cos\theta_2}}{1 + \Gamma_{\parallel,\perp}\mathrm{e}^{-2\mathrm{j}k_2 d\cos\theta_2}}\right), \tag{2.24}$$

where the relation $\Gamma_\perp - T_\perp = \Gamma_\parallel - T_\parallel \cos\theta_1/\cos\theta_2 = -1$ has been used to compute the sum, with T being the electric field transmission coefficient from medium 2 to 1. The subscripts $\perp, \parallel$ denote TE and TM polarization for the H- and E-plane respectively. In turn, the Fresnel

reflection coefficients are given by

$$\Gamma_{\perp} = \frac{n_2 \cos\theta_2 - n_1 \cos\theta_1}{n_2 \cos\theta_2 + n_1 \cos\theta_1}, \tag{2.25a}$$

$$\Gamma_{\parallel} = \frac{n_2/\cos\theta_2 - n_1/\cos\theta_1}{n_2/\cos\theta_2 + n_1/\cos\theta_1}. \tag{2.25b}$$

By substituting $d \to d\cos\theta_2$, $Z_i \to Z_i \cos\theta_i$ (E-plane), $Z_i \to Z_i/\cos\theta_i$ (H-plane) in (2.16) and (2.17), one retrieves (2.24) and (2.25a). Then, applying these transformations in (2.20) suffices to obtain R_r^{GP} in the principal scan planes.

Complex Power and Reactance

The electric field within the structure can be written as

$$E_{\mathrm{total}} = \frac{E_2}{1+\Gamma_{\parallel,\perp} \mathrm{e}^{-\mathrm{j}2k_2 d\cos\theta_2}} \left(\mathrm{e}^{-\mathrm{j}k_2 z\cos\theta_2} \hat{u}_+ - \mathrm{e}^{-\mathrm{j}k_2(z-d)\cos\theta_2} \mathrm{e}^{\mathrm{j}k_2(z-d)\cos\theta_2} \hat{u}_- \right), \tag{2.26}$$

where $\hat{u}_{\pm} = \hat{y}\cos\theta_2 \mp \hat{z}\sin\theta_2$, and $\hat{u}_{\pm} = \hat{x}$ for E- and H-plane scan respectively. In turn, the reactive power per allocated element area is given by

$$\frac{P_X}{p_x p_y} = \mathrm{j} \frac{|E_2|^2 \cos\theta_2}{Z_2 \left| 1+\Gamma_{\parallel,\perp} \mathrm{e}^{-\mathrm{j}2k_2 d\cos\theta_2} \right|^2} \sin(2k_2 d\cos\theta_2). \tag{2.27}$$

After comparing (2.27) with (2.22) and the Fresnel's reflection coefficients, it is found that X^{GP} in the principal scan planes can be also obtained applying in (2.23) the transformations: $d \to d\cos\theta_2$, $Z_i \to Z_i \cos\theta_i$ (E-plane), $Z_i \to Z_i/\cos\theta_i$ (H-plane). Since both the real and imaginary parts transform the same for either E- or H-plane scan, the equivalent networks and conclusions are analog to those drawn for the broadside case in Section 2.4.1.

Although we have treated here the case of an array backed by a ground plane reflector, a similar treatment can be developed for other structures (i.e. grids [92] or an arbitrary impedance sheet) where the reflection coefficients are known for TE and TM polarization. In particular, one can observe that the radiated plane wave propagates across the layers of the structure much like a TEM wave does in a TL with different segments and loads. Then, it is possible to extend the equivalent networks presented here to multilayered structures as long as their equivalent network is known in terms of plane wave propagation with the corresponding polarization.

Finally, note that a grounded dielectric slab may introduce additional solutions of propagation in the form of surface waves, potentially causing scan blindness [93]. A condition for this to occur is that the k-vector component of a radiated mode along the interface, k_t, matches the propagation constant of the surface wave, β_{SW}. Nevertheless, the scan angle in the medium 1 (recall $n_1 \leq n_2$) is limited below 90°, so $k_t < k_1$ for the fundamental Floquet

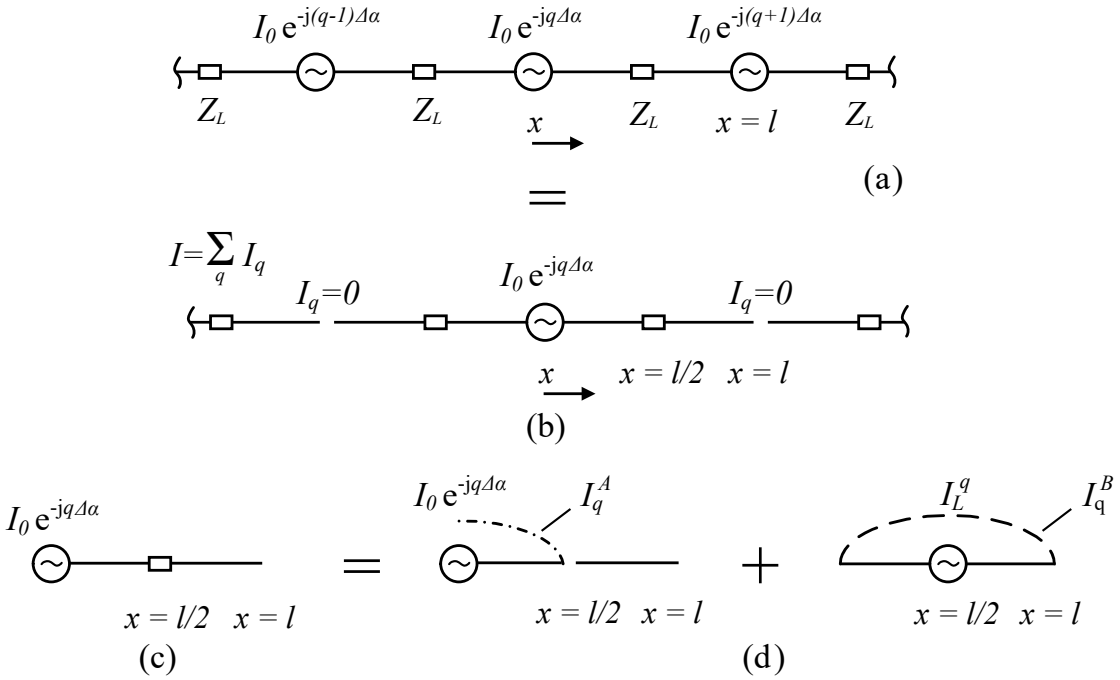

Figure 2.8 Derivation of the current distribution: (a) whole row, (b) solution by superposition. (c) and (d) derivation of the current along the dipole by superposition of the generator q and the load equivalent generator.

mode, with $k_1 \leq \beta_{\mathrm{SW}}$. Hence, it cannot excite a surface wave and it is necessary that at least a grating lobe exists. The assumption that only the $(0,0)$ Floquet mode propagates precludes the appearance of this phenomenon.

2.5 Asymptotic Current Approximation

The plane wave expansion in (2.7) has enabled the derivation of expressions and equivalent networks for the scan resistance and the reactance term due to a ground plane, if present. To compute them, however, the dipole current distribution must be known, so that it can be inserted in (2.10). In addition, only the far-field from the Hertzian dipole has been accounted for in the plane wave expansion. Hence, the decaying terms in the sum of (2.4) do not represent the total evanescent fields, and the Poynting theorem [75] cannot be used to calculate X_0. This section is devoted to the analysis of the scan reactance in an alternative way, and to derive the current distribution along the dipoles.

Let us start by examining the current distribution along one row of the array presented in Fig. 2.1b. In the most general case, the dipoles can be connected through lumped loads of impedance Z_L. The load can be an open circuit (disconnected arms with moderate gap), a short-circuit (connected arms) or an interdigitated capacitor [94]. For convenience, we assume the q element centered at the origin of coordinates as shown in Fig. 2.8a.

In the source-free regions of a linear antenna, it was demonstrated in [95, Ch. 8] that

the current satisfies ordinary TL equations when the dipole width $w \to 0$, and the effect of radiation resistance on the current is neglected. Under these assumptions, hereinafter referred to as asymptotic approximation, one can write

$$\frac{\mathrm{d}^2 I_q(x)}{\mathrm{d}x^2} + \beta^2 I_q(x) = 0. \tag{2.28}$$

$I_q(x)$ denotes the current along the row due to the q generator, with all others disconnected, and β is the propagation constant in the medium in which the array is located [95, Ch. 8]. The interface can be simply treated as an homogeneous medium of effective dielectric constant [79] $\epsilon_{\text{eff}} = (\epsilon_1 + \epsilon_2)/2$. We define the source-free domain as $\Omega := x \in \mathbb{R} - \{ml\}$, $m \in \mathbb{Z}$. That is, the length of the row except the points where the sources are located. The corresponding boundary consists of the positions of the generators ($x = ml$).

To solve for the total current along the row, $I(x)$, it suffices to solve (2.28) and later apply superposition with the proper phased excitation, as shown schematically in Fig. 2.8b. Equation (2.28) is a homogeneous Helmholtz equation which general solution is well known. To solve it we apply Dirichlet boundary conditions such that $\forall x \in \partial\Omega - \{0\}$, $I_q(x) = 0$ and $I_q(0) = I(0)\mathrm{e}^{-\mathrm{j}q\Delta\alpha}$. We also enforce the continuity of the current. It is not difficult to see that $I_q(x) = 0$ for $|x| \geq l$. In addition, by symmetry, $I_q(x) = I_q(-x)$, so actually we only need to solve for $0 \leq x \leq l$, as in Fig. 2.8c. This region corresponds to the right arm of dipole q and left arm of dipole $q+1$.

To determine $I_q(x)$ in $0 \leq x \leq l$, we also substitute the load by an equivalent generator whose value is the current in the load when only the q generator is connected, I_L^q. Then, $I_q(x)$ in this region is given by the superposition of currents from the generator q, denoted as I_q^A, and the load equivalent generator, denoted as I_q^B, both fulfilling (2.28). Thus, $I_q(x) = I_q^A(x) + I_q^B(x)$ as schematically shown in Fig. 2.8d. They are expressed as

$$I_q^A(x) = \begin{cases} \dfrac{I(0)\mathrm{e}^{-\mathrm{j}q\Delta\alpha}}{1-\mathrm{e}^{-\mathrm{j}\beta l}}\left(\mathrm{e}^{-\mathrm{j}\beta x} - \mathrm{e}^{\mathrm{j}\beta(x-l)}\right), & 0 \leq x < l/2 \\ 0, & l/2 \leq x \leq l. \end{cases} \tag{2.29}$$

$$I_q^B(x) = \begin{cases} I_L^q \dfrac{\mathrm{e}^{-\mathrm{j}\beta x} - \mathrm{e}^{\mathrm{j}\beta x}}{\mathrm{e}^{-\mathrm{j}\beta l/2} - \mathrm{e}^{\mathrm{j}\beta l/2}}, & 0 \leq x < l/2 \\ I_L^q \dfrac{\mathrm{e}^{\mathrm{j}\beta(x-l)} - \mathrm{e}^{-\mathrm{j}\beta(x-l)}}{\mathrm{e}^{-\mathrm{j}\beta l/2} - \mathrm{e}^{\mathrm{j}\beta l/2}}, & l/2 \leq x \leq l. \end{cases} \tag{2.30}$$

To determine I_L^q we use the telegrapher's equation for the current derivative:

$$\left(\left.\frac{\mathrm{d}I_q}{\mathrm{d}x}\right|_{l/2^-} - \left.\frac{\mathrm{d}I_q}{\mathrm{d}x}\right|_{l/2^+} \right) = \mathrm{j}\omega C I_L^q Z_L, \tag{2.31}$$

where $I_L^q Z_L = (V_{l/2^-} - V_{l/2+})$. Combining (2.29)-(2.31):

$$I_L^q = \frac{I(0)\mathrm{e}^{-\mathrm{j}q\Delta\alpha}}{(z_L+1)\mathrm{e}^{\mathrm{j}\beta l/2} - (z_L-1)\mathrm{e}^{-\mathrm{j}\beta l/2}}, \tag{2.32}$$

we have defined $z_L = Z_L/(2Z_c)$, and $\omega C = \beta/Z_c$ has been used. Z_c is the characteristic impedance of the wire. The current along the row due to generator q is then given by (2.29), (2.30) and (2.32), and it vanishes for $|x| \geq l$.

Let us solve now for the total current I, along the q element: the contributions to the right arm are given by I_q^A, I_q^B, and I_{q+1}^B. Similarly, for the left arm I_q^A, I_q^B, and I_{q-1}^B contribute. Note also the current due to the $q \pm 1$ generator takes the same form, only centered around $x' = x \mp l$. Hence, the current along the dipole q reads

$$I(x) = I(0)\mathrm{e}^{-\mathrm{j}q\Delta\alpha}\left[\frac{\mathrm{e}^{-\mathrm{j}\beta|x|} - \mathrm{e}^{\mathrm{j}\beta(|x|-l)}}{1-\mathrm{e}^{-\mathrm{j}\beta l}} + \frac{1+\Gamma_I}{2\left(\mathrm{e}^{\mathrm{j}\beta l/2} + \Gamma_I \mathrm{e}^{-\mathrm{j}\beta l/2}\right)} \frac{\mathrm{e}^{-\mathrm{j}\beta|x|} - \mathrm{e}^{\mathrm{j}\beta|x|}}{\mathrm{e}^{-\mathrm{j}\beta l/2} - \mathrm{e}^{\mathrm{j}\beta l/2}} \left(1 + \mathrm{e}^{\pm\mathrm{j}\Delta\alpha}\right)\right]. \tag{2.33}$$

The minus sign in the exponential of (2.33) corresponds to the right arm and the plus sign to the left arm. Analogously to a transmission line, we have defined the current-wave reflection coefficient in the load as $\Gamma_I = (1-z_L)/(1+z_L)$. Note that, by superposition, $I(x)$ is also solution of (2.28). The current is quasi-periodic, forced by the excitation, and it is symmetric if $\Delta\alpha = 0$, as expected.

For an array composed of infinite rows, we will assume that the current along the row maintains the same shape. Coupling among the rows will be taken into account through Z_c, determined after. Under this assumption, it is clear that for H-plane scan the current along the row is the same as for broadside.

2.5.1 Special Cases

There are several important cases where $I(x)$ adopts a simple form. The first is broadside emission, where the current is symmetric. We can write ($q = 0$ element)

$$I(x) = I(0)\frac{\mathrm{e}^{\mathrm{j}\beta(l/2-|x|)} + \Gamma_I \mathrm{e}^{-\mathrm{j}\beta(l/2-|x|)}}{\mathrm{e}^{\mathrm{j}\beta l/2} + \Gamma_I \mathrm{e}^{-\mathrm{j}\beta l/2}}. \tag{2.34}$$

Then, at broadside (or H-plane scan), the asymptotic current distribution along the dipoles is that of a TL. In particular, for a disconnected array, assuming $\Gamma_I = -1$, it takes the familiar form $I(x) = I(0)\sin\beta(l/2-|x|)/\sin(\beta l/2)$. For a connected array $\Gamma_I = 1$, and it takes the form $I(x) = I(0)\cos\beta(l/2-|x|)/\cos(\beta l/2)$. In addition, for a disconnected array the current distribution is also independent of E-plane scan as it can be seen from (2.34). This is not the case for connected arrays, where the current takes the form:

$$I(x) = \frac{I(0)}{\mathrm{e}^{-\mathrm{j}\beta l} - \mathrm{e}^{\mathrm{j}\beta l}}\left[\mathrm{e}^{\mathrm{j}\beta|x|}\left(\mathrm{e}^{-\mathrm{j}\beta l} - \mathrm{e}^{\pm\mathrm{j}\Delta\alpha}\right) + \mathrm{e}^{-\mathrm{j}\beta|x|}\left(\mathrm{e}^{\pm\mathrm{j}\Delta\alpha} - \mathrm{e}^{\mathrm{j}\beta l}\right)\right]. \tag{2.35}$$

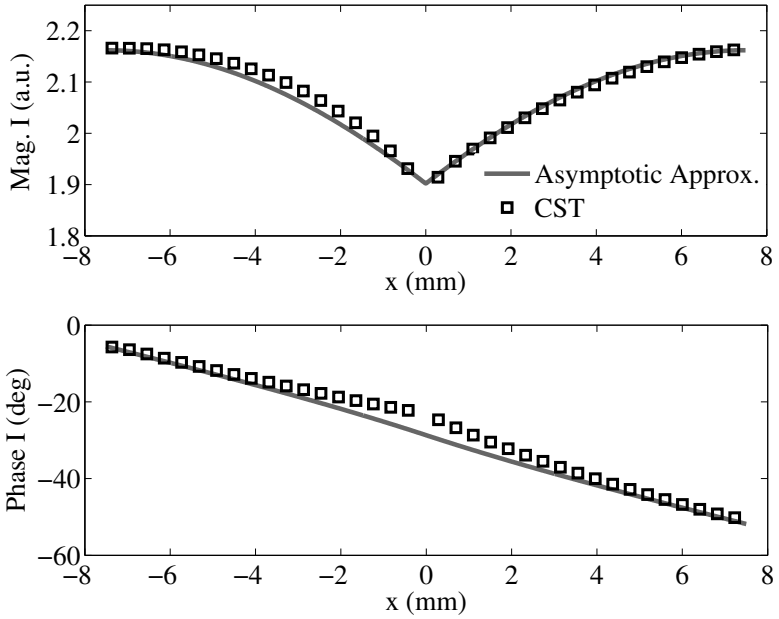

Figure 2.9 Current distribution for an infinite phased array of connected dipoles in free-space scanning in E-plane at 40°. $p_x = p_y = l = \lambda/5$, and $w = \lambda/1000$.

The solid line in Fig. 2.9 shows the current distribution obtained from (2.35) for an array of connected dipoles scanning in the E-plane at 40°. The total phase change along the dipole equals $\Delta\alpha$, forced by the excitation, and can be easily noted in (2.34). For comparison, full-wave simulation results obtained for the same configuration by CST Studio Suite [96] are also plotted. As it can be seen, both curves are in good agreement. Near the dipole feed, where the current is minimum, the effect of the radiation resistance causes some discrepancy in the phase as discussed in Section 2.8. Finally, the results shown are also in agreement with the MoM analysis in [97].

2.5.2 The Asymptotic Equivalent Network at Broadside

In (2.34) we have seen that at broadside the current along the dipole is analogous to that of a TL. Therefore, X_0 can be retrieved from the network shown in Fig. 2.10a. It is composed of a TL of length $l/2$ (as the dipole arm) terminated in Z_L. However, the characteristic impedance of the TL remains unknown.

Assuming TEM wave propagation, Z_c can be calculated from the inductance per unit length of the structure, L, using $Z_c = Lc/\sqrt{\epsilon_{\text{eff}}}$. The value of L is retrieved as follows: let a grid of vertical and parallel strips of width w and period p_y be illuminated by a plane wave at normal incidence, such that a uniform current distribution is excited along the strips, the electric field being parallel to the strips. The impedance of this structure has been studied in e.g., [92], [98], [99]. In particular, as discussed in [100], the inductance of the grid per strip and

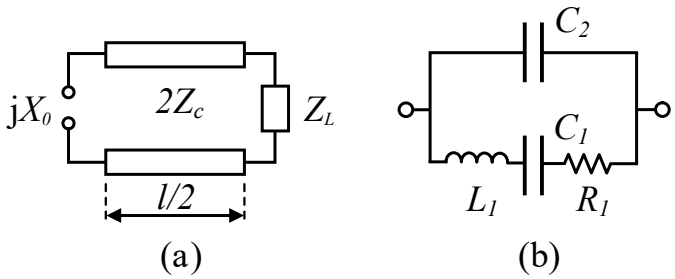

Figure 2.10 (a) Equivalent network representing the scan reactance. (b) Equivalent lossy lumped element circuit that represents the scan impedance.

per unit length is given by

$$L = \frac{Z_0}{2\pi c} \ln\left(\frac{1}{\sin\left(\frac{\pi w}{2p_y}\right)}\right). \tag{2.36}$$

For the interface case, it is assumed that $\mu \approx \mu_0$ for both dielectrics, so L remains unaltered [92]. Finally, to account for the two arms of the dipole, the characteristic impedance of the network is given by $2Z_c$, twice that of the wire. This definition is also in agreement with the definition of z_L for Γ_I above.

Once the characteristic impedance of the TL is determined, it is worth mentioning that X_0 calculated with the equivalent network of Fig. 2.10a takes automatically into account the dipole end load, including disconnected dipoles ($Z_L \to \infty$).

Now, it is possible to calculate the impedance for broadside emission (principal scan planes will be dealt with in Section 2.7). The current distribution for broadside given by (2.34) can be inserted in (2.10) to obtain the transformer relation, N, in the equivalent networks of Fig. 2.4 (interface) or Fig. 2.7 (interface and backing ground plane). Besides, X_0 can be obtained from the network of Fig. 2.10a, where the inductance per unit length in (2.36) is used to calculate $2Z_c$.

Nevertheless, the asymptotic current approximation is only valid when w approaches 0 so that the scan impedance is mainly dominated by a reactance and the effect of the radiation resistance on the current distribution can be neglected. This approximation gives in general accurate results for thin dipoles except in the regions where the current at the dipole feed approaches zero (anti-resonance). In the latter case, (2.34) diverges at all times, independently of the dipole width, which is clearly wrong. To overcome this issue, and for more precise calculations, we have derived a lumped element circuit that accounts for variations in the stored energy and finite radiation losses in the impedance curves, as shown in Fig. 2.10b, whereas we can rely on the simple networks to extract qualitative conclusions. For simplicity, we will restrict the analysis of the scan impedance when there is no ground plane in the cases of connected and disconnected dipoles.

To derive the lumped element circuit one can reason as follows: when losses are absent, it

Table 2.1 Lumped Element Circuit Parameters.

Parameter	Connected	Disconnected
L_1	Ll	$(C_1\omega_R^2)^{-1}$
C_1	∞	$(3/16)ln_{\text{eff}}^2/(Lc^2)$
C_2	$(L_1\omega_{AR}^2)^{-1}$	$C_1/3$
R_1	$R_{r,f\to 0}$	$(16/9)R_{r,f\to 0}$
ω_{AR}	$\pi c/(n_{\text{eff}}l)$	$2\pi c/(n_{\text{eff}}l)$
ω_R	0	$\pi c/(n_{\text{eff}}l)$

follows the curve of X_0 given by the network of Fig. 2.10a. L_1 and C_1 determine the resonance frequency as predicted by the TL ($X_0 = 0$). Besides, L_1, C_1, and C_2 determine anti-resonance ($X_0 \to \pm\infty$). The third condition is to guarantee that the circuit yields the input reactance of the network model at low frequencies. Last, losses are included in the circuit by a lumped resistor R_1 so that the input resistance of the lumped element circuit is that of the network model when $f \to 0$. The values relating the different lumped elements with the network model are summarized in Table 2.1 for connected and disconnected dipoles. This circuit equivalent is valid up to, approximately, anti-resonance. An alternative circuit was developed in [101] but it utilizes the dipole auto-inductance. Furthermore, it is only valid for tightly coupled and connected arrays, and does not arise from a physical explanation of the scan impedance.

2.6 Results for Broadside Emission

To test the validity of the proposed model, it is compared with full-wave simulations carried out with ANSYS HFSS [91]. The geometry of the unit-cell used for the simulations is shown in Fig. 2.11. For a central frequency of $f = 1$ cycle per unit-time that determines λ_c, the nominal parameters are: $p_x = p_y = \lambda_{c,\text{eff}}/2$, $l = 1.0p_x$ (connected) or $0.9p_x$ (disconnected), $w = \lambda_{c,\text{eff}}/1000$, and feed port length $\lambda_{c,\text{eff}}/100$. The array is freestanding or lies on a vacuum-dielectric interface. In the following, results are presented for a variation of one nominal parameter at a time. The calculated curves in Figs. 2.12-2.14 have been obtained using the lumped element circuit in Fig. 2.10b explained in the preceding section.

2.6.1 Varying End Load

The resonant behavior of dipole arrays is highly dependent on the load and can be simply examined by inspection of the input reactance in the equivalent network of Fig. 2.10a. For connected dipoles $X_0 = 2Z_c\tan(\beta l/2)$, therefore resonances occur at $l/\lambda = n$ with n a natural number, whereas anti-resonances occur at $l/\lambda = n + 1/2$. In the latter, the open circuit condition is effectively achieved and $I(0) = 0$, consequently, R_r will diverge too. Conversely, for disconnected arrays of dipoles, $X_0 = -2Z_c/\tan(\beta l/2)$ and the resonant/anti-resonant

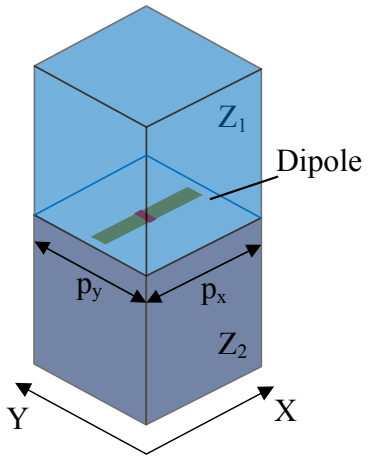

Figure 2.11 Schematic of the unit-cell used to simulate the infinite array of dipoles. The top and bottom surfaces are considered as radiation boundaries, whereas for the four lateral sides periodic boundary conditions are used. The dipole is centered-fed by a lumped port (depicted in red), and two perfect electric conductor (PEC) sheets depicted in dark yellow constitute the dipole arms.

frequencies will be swapped with respect to connected dipoles of the same length (see for instance Fig. 2.12). This fundamental difference between connected and disconnected dipoles stems from the fact that in the former the maximum current occurs at the dipole end ($\Gamma_I = 1$) whereas, for disconnected dipoles, the current at the edge is always minimum ($\Gamma_I = -1$). The π phase difference in the reflection coefficient is responsible for the $\lambda/2$ shift of the resonances. In the usual case of capacitively loaded dipoles, the phase of the reflection coefficient for the current-wave lies between the previous cases, then the resonances lie between the aforementioned limiting cases. Furthermore, the fact that connected dipoles show resonant response at low frequencies makes them amenable to array design with large scan angles. In this case, the lattice can be kept $< \lambda/2$, whereas for disconnected dipoles $p_x > \lambda/2$ limited by the resonant length of the dipole. This is even more evident for a dielectric interface, where the required spacing to avoid grating lobes is $\lambda/(2n_2)$ but the dipole length scales down only as n_{eff}.

2.6.2 Varying ϵ_r

Practical array designs require printing the antennas on an interface, for mechanical support or to diminish the effect of a ground plane. In the latter case, it is more convenient to position the ground plane in the medium with lower dielectric index for a broadband design, since it renders the impedance less dependent on frequency. Also, it is to be observed that the short-circuit will occur at DC and certain frequencies regardless of the interface, hence, imposing a fundamental limit in the absolute impedance bandwidth of the array.

As shown in the previous subsection, X_0 is proportional to Z_c and in turn to $1/\sqrt{\epsilon_{\text{eff}}}$ for connected or disconnected dipoles. Thus, a high permittivity dielectric substrate flattens the dipole reactance. Fig. 2.12 shows the variation of the simulated and calculated broadside impedance with ϵ_r for connected (a), and disconnected (b) dipoles. ϵ_r corresponds to the

relative permittivity of the substrate when the array is printed in an air-dielectric interface as shown in Fig. 2.1b. It is important to note that p_x, and p_y are scaled by $\lambda_{c,\text{eff}}$ and so the dipole electrical length remains fixed as seen in Fig. 2.12.

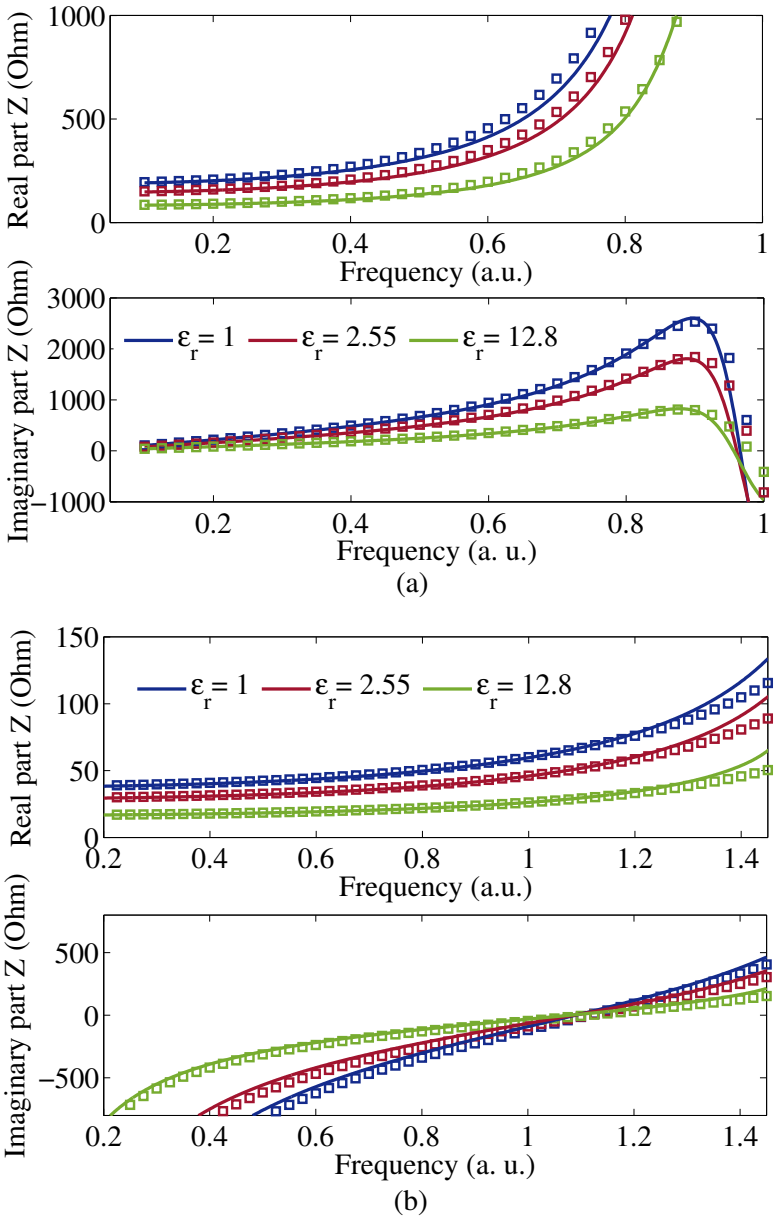

Figure 2.12 Real and imaginary parts of the broadside impedance: simulated (solid lines), and calculated (squares) for three different relative permittivities of the substrate. (a) connected dipoles, (b) disconnected dipoles.

2.6.3 Varying Dipole Width

Fig. 2.13 shows the simulated and calculated broadside impedance for different dipole widths for connected (a), and disconnected (b) dipoles. If we calculated the scan resistance from

the asymptotic current approximation in (2.34), where Γ_I does not depend on w, it would yield a result also independent on w. In practice, this is true only for regions far away from anti-resonance. As w increases, the resonance quality factor decreases, and the impedance curves are affected. The lossy lumped element circuit predicts this behavior reasonably well for connected dipoles, as shown in Fig. 2.13a. However, for disconnected dipoles the model loses validity. In particular, variations of effective dipole length with dipole width are not taken into account. We will discuss it in more detail in Section 2.8. Finally, note a wider dipole yields a flatter reactance, as can be inferred from (2.36).

2.6.4 Varying Lattice (p_x, p_y)

The dipole length has been defined as 100% or 90% of p_x, therefore, variations in p_x will scale the curves accordingly. Conversely, variations in p_y influence the coupling among neighboring rows, and can be used to modify the impedance.

From the network model we can observe that the factor N^2 is inversely proportional to p_y. Since within this approximation the current distribution does not change with p_y for connected or disconnected dipoles, R_r scales inversely proportional to p_y. Besides, from (2.36), L decreases with p_y, so narrower spacing decreases X_0 and flattens the dipole reactance. Coupling, as is clear from the network model, can be used to obtain broadband arrays. Fig. 2.14 shows the broadside impedance for a connected array and different values of p_y relative to p_x. The latter is maintained to the nominal value of $\lambda_c/2$. When $p_y \ll p_x$, R_r becomes too large and the lossy lumped element circuit is no longer accurate. However, this is not a case of general importance.

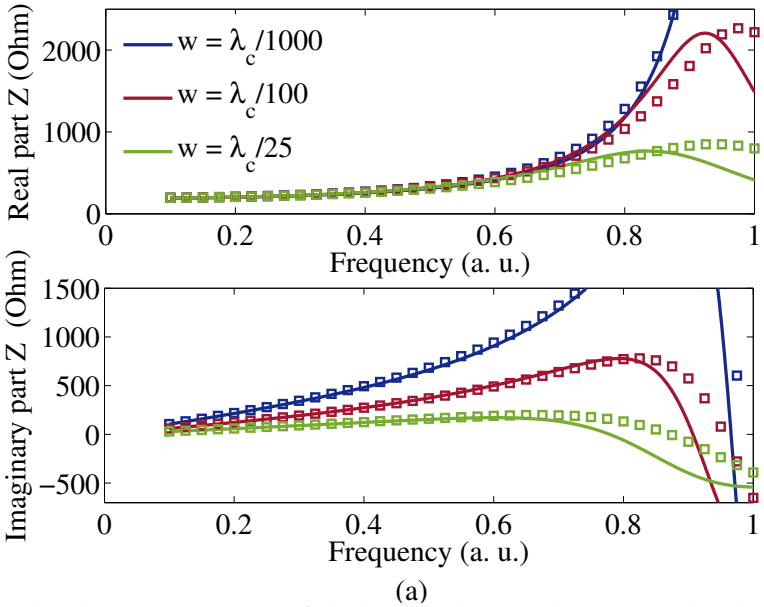

(a)

Figure 2.13 Real and imaginary parts of the broadside impedance: simulated (solid lines), and calculated (squares) for three different dipole widths. (a) connected dipoles.

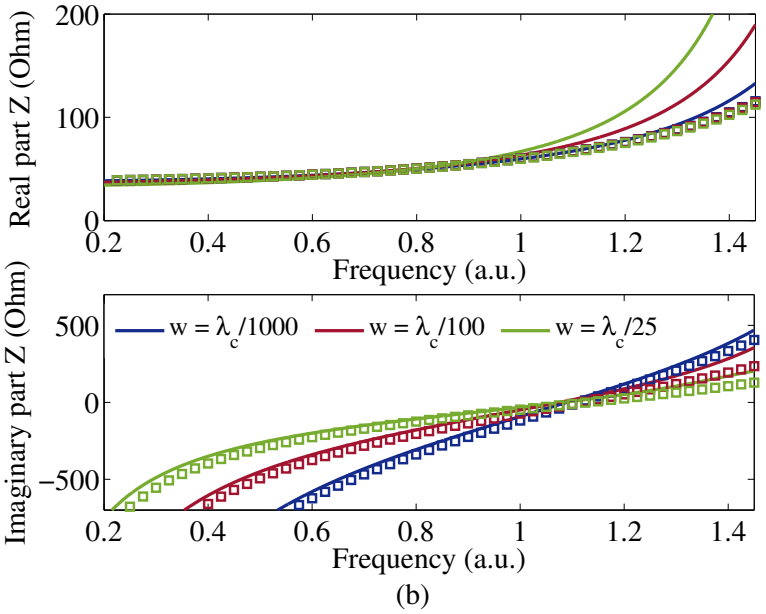

(b)

Figure 2.13 (Cont.) Real and imaginary parts of the broadside impedance: simulated (solid lines), and calculated (squares) for three different dipole widths. (b) disconnected dipoles.

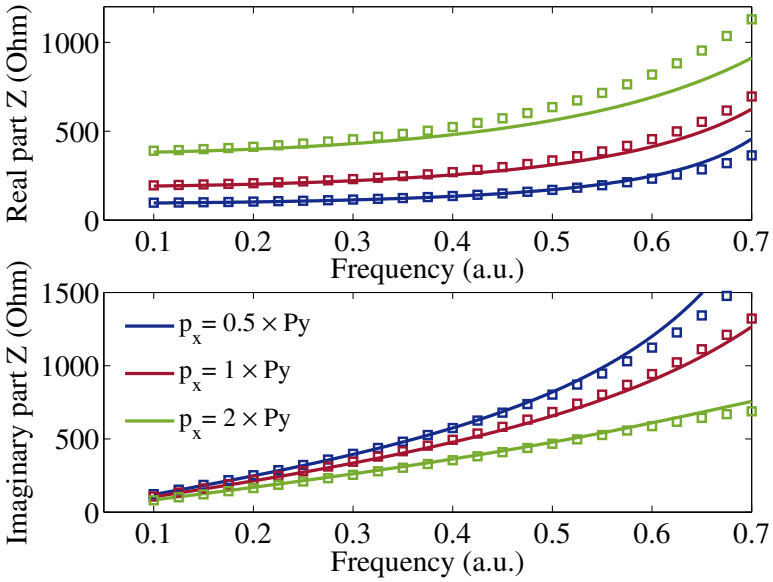

Figure 2.14 Real and imaginary parts of the broadside impedance: simulated (solid lines), and calculated (squares) for a connected array of dipoles and different values of p_y.

2.7 Extension for Principal Scan Planes

In section 2.5, we have seen that at broadside emission the current distribution along the dipole in asymptotic approximation is that of a transmission line. Therefore, it was possible to identify X_0 with the equivalent network of Fig. 2.10a, and ultimately compute the scan impedance at broadside using a lossy lumped element circuit. For scan in the principal planes,

we need to examine the variations of the inductance per unit length on the equivalent TL and of the current distribution, if any.

The inductance of a grid of strips for a plane wave in oblique incidence with the tangent electric field parallel to the wires was calculated in [99, Ch. 4]. We can express the grid inductance per unit length as

$$L = \frac{Z_0}{2\pi c} \ln\left(\frac{1}{\sin\left(\frac{\pi w}{2p_y}\right)}\right)\left(1-\cos^2\phi\sin^2\theta\right). \tag{2.37}$$

For H-plane scan, $\phi = 90°$, and L does not change. Also, according to our model, the current is the same as for broadside. Therefore, it is still possible to compute the impedance with the lossy lumped element circuit and extract conclusions from the network model. Results calculated using the lossy lumped element circuit for an array of connected dipoles are shown in Fig. 2.15a for different scan angles and nominal array parameters. As radiation losses increase while L is maintained, anti-resonance becomes wider and flatter, and this behavior is well captured. Conversely, the equivalent network would predict that X_0 is maintained and R_r is scaled by $1/\cos\theta$ because it does not capture the consequences of a lower quality factor in the resonance. This is specially clear at large scan angles. Finally, for scan at 80° near $f = 1$ a.u. the curve deviates from simulation as the onset of a grating lobe is approached.

For E-plane scan, we need to distinguish between connected and disconnected dipoles. In the latter case, the current in (2.33) is the same as for broadside emission, so X_0 remains the same and R_r scales with $\cos\theta$. Note that, even if in (2.37) L varies, this is for a plane wave in oblique incidence that generates a linear phase progression along the wires of the grid. For the array of disconnected dipoles, there is no linear phase progression, and the expression for L at broadside has to be used.

Nevertheless, for connected dipoles, the scan impedance can be obtained as follows: the current at the dipole feed is $I(0)$, whereas the voltage is the superposition of the voltages impressed by all generators in $x = 0$. As we have seen before, for the q element, only $q-1$, q, $q+1$ contribute to the current. When only the q generator is active, we use the fact that the current along the dipole is that of an open-ended transmission line of length l. The dipole self-reactance is then $Z_{q,q} = V^q(0)/I(0) = -\mathrm{j}2Z_c/\tan(\beta l)$. When only one of the $q\pm1$ generators is on, the voltage at the dipole feed corresponds to that of the open-ended transmission line of length l at the position of the load, so $Z_{q\pm1,q} = V^{q\pm1}(x=0)/I(0) = \mathrm{j}Z_c e^{\pm\Delta\alpha}/\sin(\beta l)$. Thus, the scan reactance is given by the sum of the three terms:

$$X_0 = 2Z_c\left(\frac{\cos\Delta\alpha}{\sin(\beta l)} - \frac{1}{\tan(\beta l)}\right). \tag{2.38}$$

It is interesting to note that (2.38) reduces to $2Z_c\tan(\beta l/2)$ when $\Delta\alpha = 0$ and is an alternative way to calculate the scan reactance based on mutual impedances. Fig. 2.15b shows

the results for an array of connected dipoles and nominal array configuration. Calculations are performed inserting the current distribution given by (2.35) in (2.10) to calculate R_r from the network of Fig. 2.4. X_0 is calculated using (2.38). In this case, the current distribution no longer follows that of a TL, and it is not possible to map the impedance curves with the lossy lumped element circuit used before, causing the model to deviate close to anti-resonance.

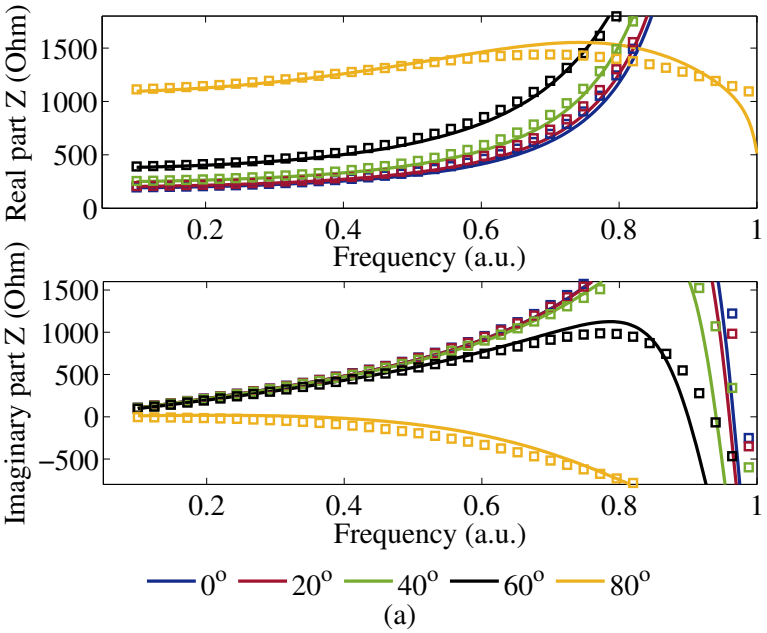

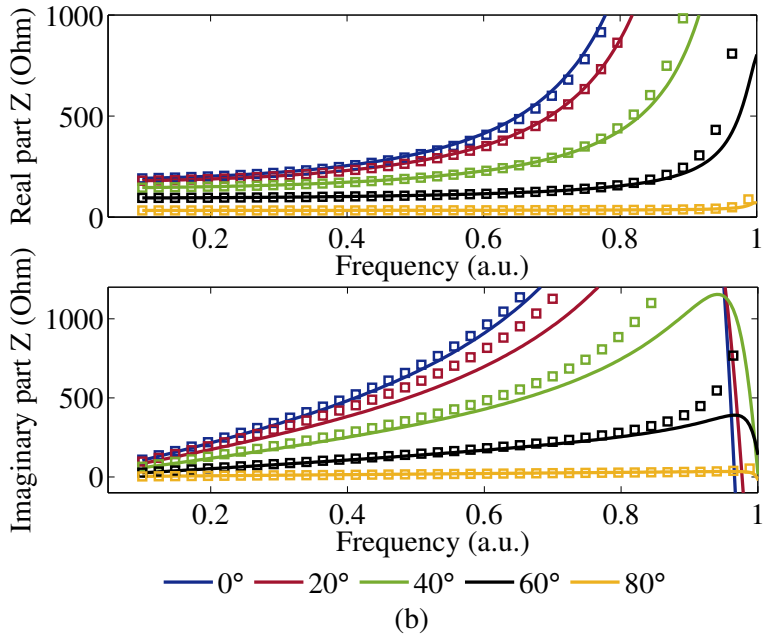

Figure 2.15 Real and imaginary parts of the scan impedance: simulated (solid lines), and calculated (squares) for a connected array of dipoles at different scan angles in (a) H-plane, and (b) E-plane.

2.8 Model Limitations

As already mentioned, the asymptotic current approximation neglects the effect on the current due to the radiation resistance. It constitutes a term in quadrature with the current impressed by the generator and the distribution is that of a reflecting antenna, as noted by [95]. Since $R_r \neq 0$, this term is present even when $w \to 0$ and it dominates the current at the dipole input terminals at anti-resonance when the asymptotic current distribution approaches zero and the impedance takes a maximum value. Thus, in this region, the TL model loses validity. This limitation can be overcome for the interfacial array by using a lossy lumped element except for E-plane scan with connected dipoles. In general, multilayered media or a ground plane will affect R_r and so, the associated term in the current distribution. In addition, following the discussion of [95], the asymptotic current distribution stems from a TEM wave that propagates along a linear antenna. When discontinuities exist, such as at the ends of disconnected dipoles, a TEM wave cannot match the boundary conditions and higher-order waves must exist. They will have an impact on the current distribution. In particular, it results in the model being more accurate for connected dipoles than for disconnected ones. Similarly, it is known that as a grating lobe is close to its onset, it affects the scan impedance [66, Ch. 7], then, in this case, some deviation from the model should be expected. Last, the expression for L becomes invalid if the spacing is comparable to the wavelength [92]. In this case, it is invalid when grating lobes appear and the inductance of the grid can no longer be expressed by a single lumped element.

Finally, to validate the assumption that the ground plane does not interact with the evanescent modes and that it does not modify the elements current distribution, we have compared the network model (Figs. 2.4 and 2.7) with full-wave simulations. When there is no ground plane, the model gives $Z_d = 55.7 - \mathrm{j}109.4\ \Omega$ versus $Z_d = 59.7 - \mathrm{j}91.0\ \Omega$ for the full-wave solver. When a ground plane is present at $d = \lambda/4$, $Z_d = 111.4 - \mathrm{j}109.4\ \Omega$ and $Z_d = 118.6 - \mathrm{j}98.6\ \Omega$ for the model and full-wave solver, respectively. The values correspond to an array of nominal parameters (as detailed in Section 2.6), $f = 1$, and disconnected dipoles, and they indicate that the model is in this case still approximately valid.

2.9 Conclusions of the Chapter

A model has been presented to determine the scan impedance of infinite phased arrays of dipoles at a dielectric interface. First, equivalent circuits and expressions for the scan resistance in the principal scan planes are derived using the boundary conditions for the fundamental Floquet mode. This derivation provides a straightforward interpretation of the role played on the scan impedance by the pattern of the Hertzian dipole, apparent allocated area, or partially stationary waves formed by the presence of a ground plane or interface. Using such boundary conditions, closed-form expressions have also been derived for the ratio of intensity radiated towards each half-space of the interfacial array. Second, an asymptotic approximation is introduced to determine the current along the array. Besides, the scan

reactance has been related to the inductance per unit length of an inductive grid of strips. To perform the calculations of the scan impedance, a lossy lumped element circuit is generally preferred because it conveniently removes the divergence of the impedance at anti-resonance of the asymptotic approximation, and it also accounts for variations in the impedance curves associated with the quality factor of the resonance. The model shows how fundamental differences in the current distribution between connected and disconnected dipoles relate to different impedance curves at broadside and in the principal scan planes. Indeed, the derivation of a model based on physical grounds has permitted us to illustrate with equivalent circuits and simple expressions how the principal array variables affect the scan impedance. In the next chapter, we will make use of some of the obtained results to develop a method for enhanced matching efficiency between photodiodes (sources) and the antenna array.

Original Contribution

The contribution of this chapter consists in the model itself as well as the approach to derive it. Although the scan impedance of infinite phased arrays of dipoles can be investigated by numerical methods (e.g., the MoM in [79]) or just with a full-wave simulator, the originality of the proposed approach lies in an insightful analysis of the scan impedance by means of a novel formulation and equivalent circuits that can be readily interpreted and related to the different array parameters. The analytic expressions provided for the intensity radiated towards each half-space in (2.13) and (2.14), for the current distribution in (2.33) (which accounts for arbitrary dipole end load and scan angle in the principal planes), or for the scan reactance in E-plane for connected dipoles in (2.38), to cite a few, are original and throw some new light on the understanding of this important class of antenna.

3

Applications of CW Photonic Transmitters at Mm- and THz Frequencies

Mm- and THz waves have found application in telecommunications, imaging, and spectroscopy. It is the case, for instance, of time-of-flight techniques in imaging, time-domain systems in spectroscopy, or ultra-high data rates in wireless communications. Although mm-wave and THz technology often share concepts and methods used in other regions of the spectrum, the uniqueness of this spectral region requires a different hardware approach for the generation and detection of radiation. The short wavelength, diffraction and interference effects, and the propagation and absorption properties with several media confer mm- and THz waves unique features. In this chapter, we detail relevant characteristics of mm- and THz waves in the context of the fields cited above, highlighting where continuous-wave photonic transmitters at room temperature play a notable role.

3.1 Applications in Telecommunications

Telecommunications is probably the application of mm- and THz waves receiving most of the attention nowadays. This interest is driven by an ever-increasing amount of data exchange in the ongoing digital revolution. On average, 1.5 review papers on the status of THz communications have been published yearly since 2010 [9]. Only under the European program Horizon 2020, eight projects have been funded. Mm-wave and THz wireless communications also constitute a quite heterogeneous field, since it involves standardization, hardware development, system demonstrations, and novel approaches to accommodate more and more demanding needs. In this section, we focus on the needs and solutions proposed for the physical layer in 5G and beyond 5G (B5G) communications systems. We also discuss the characteristics of a link budget at these frequencies to illustrate the need for high-gain antennas. Next, we present different application scenarios of THz and mm-waves, detailing two cases where photonic Tx play a particularly important role. Although all-electronic approaches are also a relevant hardware option for mm-wave and THz communications, for the sake of brevity, we will refer to [10] and to the figures provided in Chapter 1. To conclude the section, the need for directive

and beam-steerable antennas is justified. Finally, regarding wireless link demonstrations and architectures at mm-wave and THz frequencies, the reader is referred to the numerous works compared in [102]. In Chapters 6 and 7, and Appendix E, we will also provide a detailed explanation of the wireless link developed in this thesis to test the Tx performance.

3.1.1 Next Generation Wireless Communications

The global amount of data traffic exchanged by mobile users experienced an eightfold increase from 2014 to 2018, and a ×6 increase has been forecast during the 2018-2024 period [103]. This data growth will be driven by many emerging applications, like intelligent transportation systems and autonomous vehicles, connected utilities and amenities in smart cities, 4K and 8K video resolution for entertainment, education or medical applications, or industrial automation [104]. It is generally accepted that 5G and B5G networks will constitute a paradigm shift [56]. On the one hand, B5G networks are expected to handle massive connectivity motivated by the rise of the Internet of Things (IoT) and, on the other hand, to offer enhanced quality services such as 8K video.

The previous applications will impose stringent requirements on B5G networks: robustness to interference, low latency, massive multiple access, ultra-reliability, low energy consumption per link for greener networks [56], and fast and flexible spectrum reallocation with high data rates available to the user. All these demands do not have to be met simultaneously through the network, and some of them may be relaxed under particular circumstances.

Tackling these necessities will require considering many different solutions. Device to device communication or non-orthogonal multiple access deal with massive access [59]. Software-defined networks improve efficient resource management and energy efficiency. Multiple-input multiple-output techniques increase spectral efficiency and reliability. Besides, the use of carriers at frequencies higher than those used in traditional sub-6 GHz bands offers larger bandwidths. Finally, the trend of network densification with frequency reuse in nano/picocells, covering areas of a tenth of a km^2, has been identified as the largest contributor to the increase of wireless capacity over the past three decades [56], [104], [105].

3.1.2 Frequency Bands at Mm- and THz Waves

It is estimated that wireless backhaul links will soon require a capacity > 10 Gbps [105], and even 100 Gbps [9]. Assuming a realistic spectral efficiency of ~ 5 bps/Hz, the bandwidths required to fulfill such demands exist only at mm-waves and beyond. IR and optical frequencies could provide the required bandwidths. However, they interfere with ambient light, are susceptible to scintillation (as shown in Appendix C), require extremely low alignment tolerances, and are more attenuated in adverse atmospheric conditions (fog, dust) than mm- and THz waves [9]. Therefore, the latter are preferred for wireless communications. Table 3.1 summarizes the frequency ranges with an available bandwidth larger than 5 GHz.

Frequency range (GHz)	Bandwidth (GHz)	Range (km)	Licensing	Example
60	7	< 1	No	[106]
71-76 and 81-86	2×5	$\gtrsim 1$	Light	[107]
120	18	$\gtrsim 1$	Reg. in Japan	[108]
252-325	40	≤ 1	No	[109]
325 < f < 1000	Several windows	$\ll 1$	No	[110]
	25 to 110			

Table 3.1 Relevant frequency bands for 5G and B5G wireless systems. Exact figures depend upon author or geographical location.

The 60 GHz band is characterized by a high oxygen absorption peak, so it is appropriate only for frequency reuse in small communication cells and secure communications [111]. For instance, this band has been used in the Terragraph project [112]. It uses a high density of nodes (spaced 200-250 m) for high-speed internet in urban areas. The E-band (71-76 GHz and 81-86 GHz), which is the one selected to develop our photonic Tx in Chapters 6 and 7, benefits from worldwide allocation of two 5 GHz windows generally light licensed [113]. Light licensing is associated with cheaper and faster deployment. Furthermore, the E-band is already in use for wireless backhauling [107]. Similar to the E-band, the 120 GHz band offers a moderate bandwidth and free space loss (see Appendix C) and it is intended for tens of Gbps links at km-distances. Following the successful live retransmission of the 2008 Olympic Games in Beijing (10 Gbps for a 1 km distance), it was regulated in Japan in 2014 for wireless broadcasting [19], [114].

The 300 GHz band is currently under study, but it can offer higher data rates than the aforementioned bands for shorter distances. Recently, a 100 Gbps point-to-point communication standard has been developed (IEEE Std 802.15.3d-2017), and transmission of 56 Gbps at 1 km has been demonstrated [115]. Finally, bands beyond 325 GHz are still at an early experimental investigation stage. They can potentially provide enough bandwidth for > 100 Gbps, but the current low powers emitted have made it possible to only demonstrate data rates of tens of Gbps at link distances of around 1 m [37].

3.1.3 Link Budget

Fig. 3.1 shows the architecture of a photonic Tx in a wireless link. The optical signal travels through the fiber until it reaches the photodiode, where it is converted to the RF domain and is subsequently radiated. To illustrate the data capacity and antenna gain requirements of a mm-/THz wave link, we provide a simplified link budget calculation summarized in[116]. Table 3.2 lists the link parameters used in the calculation.

The received power (P_{rec}), is calculated as a function of the antenna gain (G) from a modified Friis equation that accounts for atmospheric attenuation, as given by (C.4). For

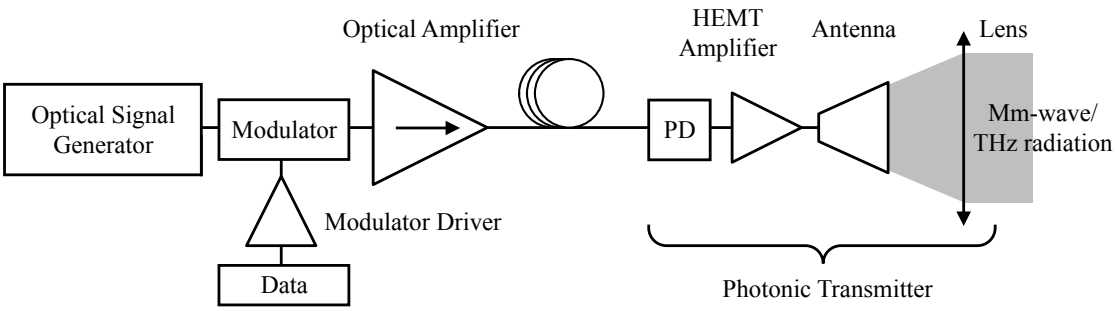

Figure 3.1 Schematic of a photonic transmitter in a wireless link.

Parameter	Value
Power transmitted, P_t	0 dBm
Carrier frequency, f_c	300 GHz
Link distance, r	5 m
Atmospheric Attenuation, α	0.01 dB/m @f_c
Noise spectral density, N_0	-174 dBm/Hz
Spectral efficiency, η	1 bps/Hz
Noise bandwidth, B	Data rate $\times\eta$
Rx total noise figure, NF	15 dB
System margin, M	10 dB

Table 3.2 Parameters for the link budget calculation.

simplicity, $G_{\mathrm{Rx}} = G_{\mathrm{Tx}} = G$ is assumed. The signal-to-noise ratio (SNR) can be expressed in dB as [116]

$$\mathrm{SNR} = P_{\mathrm{rec}} - \left(N_0 + 10\log_{10}(B) + \mathrm{NF} + M\right). \tag{3.1}$$

N_0 is the noise spectral density, NF is the detector total noise figure, M is the system margin, and B is the system bandwidth, which we assume equal to the link capacity (spectral efficiency equals 1 bps/Hz). First, we obtain $P_{\mathrm{rec}}(G)$ from (C.4). Next, we insert $P_{\mathrm{rec}}(G)$ into (3.1), and for a given value of SNR, we obtain B (or link capacity). For Shannon's maximum transmission capacity, when the bandwidth equals the capacity, the value of SNR corresponds to 1. For ASK and BPSK modulation formats, the values of SNR correspond to 13.54 dB and 16.54 dB, respectively for a bit-error-rate (BER) of 1×10^{-6} (assuming shot noise). Fig. 3.2a shows the curves of data capacity as a function of G.

Besides, to highlight the necessity of LoS links and the stringent alignment requirements, Fig. 3.2b shows the half-power beamwidth (HPBW) versus antenna gain for a uniformly illuminated circular aperture [117]. The vertical error bars indicate the alignment tolerance for a 3 dB loss.

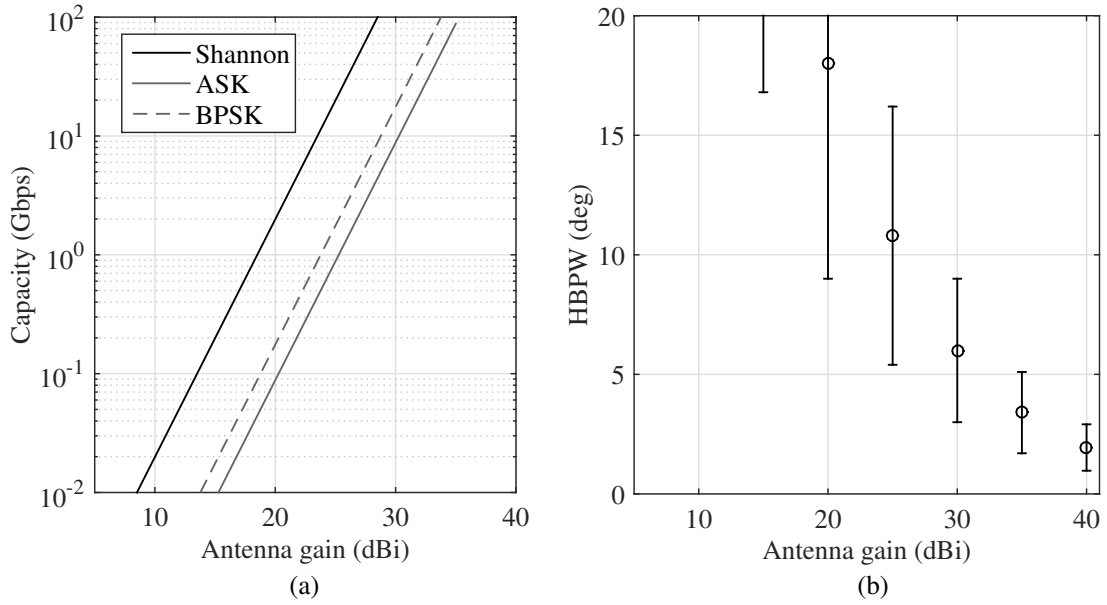

Figure 3.2 (a) Link capacity versus antenna gain, and (b) HPBW versus antenna gain. The error bars correspond to the alignment tolerance for a 3 dB misalignment loss.

3.1.4 Application Scenarios

Applications of mm- and THz waves include indoor communications (wireless local and personal area networks), near-field communications (kiosk downloading and chip- to-chip), vehicular communications, last-mile access, reconfigurable wireless interconnections in data centers, and wireless backhauling [9], [55], [109], [118]. Photonic solutions are in general more costly than MMIC or CMOS technology. However, they are well suited for data centers and backhauling due to the compatibility with the fiber optic network. Hence, we will limit the discussion to potential uses of photonic Tx in these two applications.

Keeping up with the demanded capacities will lead to a massive deployment of base stations. Backhauling in such high density networks implies a clear trade-off between network performance and installation costs. Macro-cells widely use fiber links [105], but it is estimated that most of the smaller cells in 5G and B5G networks will be connected wirelessly. Fig. 3.3a illustrates this scenario. Compared to a fiber link, a wireless link reduces deployment costs while offering > 10 Gbps data rates [105]. The advantages of photonic Tx with respect electronic ones include antenna remoting, seamless integration with the fiber link, and ability to handle multi-carrier and multi-format channels, which to date has no equivalent in electronics-based solutions [37], [108].

In another potential scenario, we discuss a mm-wave photonic Tx for beam alignment in wireless data centers. The application of wireless links in data centers has been considered by several authors [55], [118], [119]. It could provide scalability and reconfigurability, difficult to achieve by fiber interconnected nodes as the number of servers increases. These are critical

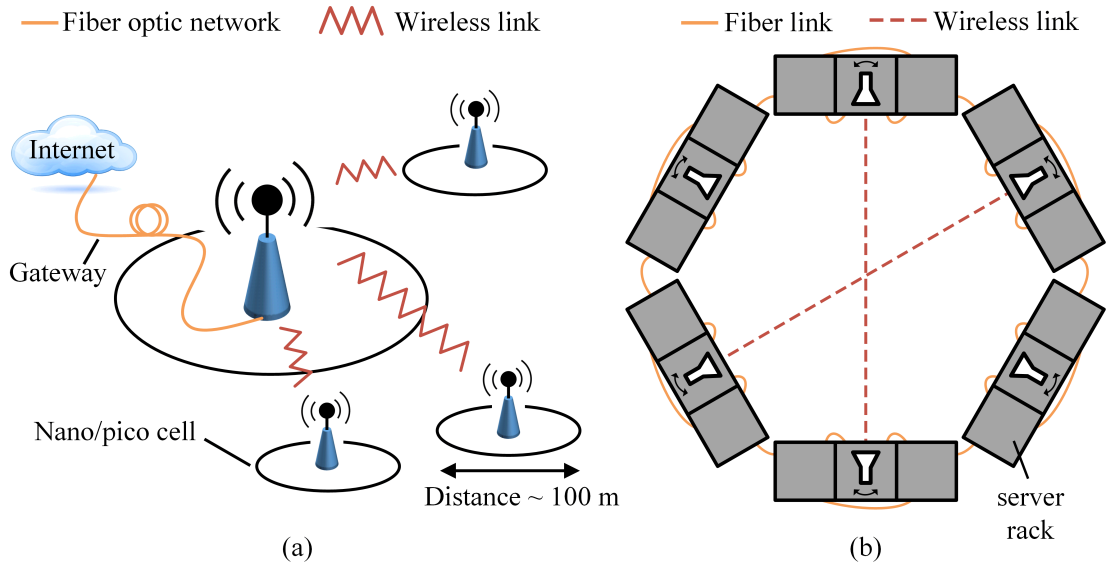

Figure 3.3 Application scenarios of mm-waves: (a) Wireless backhauling in high-density network with nano/picocells, (b) reconfigurable wireless links in data centers.

aspects of modular data centers [119]. Mm-wave links at 60 GHz, based on the IEEE 802.15.3c wireless standard or E-band frequencies, suited for tens of Gbps data rates, could provide a flexible alternative to fiber. Fig. 3.3b depicts a simplified data center structure with server racks distributed in a hexagonal lattice. The servers form subgroups interconnected by fiber, whereas the wireless links provide flexible interconnection between them, forming a hybrid architecture. Further details on hybrid architectures can be found in [119].

3.1.5 The Need for Beam-Steering

Beam-steerable antennas are required for reconfigurable links, such as in wireless connections in data centers. Similarly, beamsteering has been widely identified as a necessity to ease alignment during link set-up and to correct twists and sways of posts [19], [37], [107], [108], [120]. Current antennas for backhaul links are installed in large telecommunication towers, but a massive deployment of base stations will force the use of structures with a low visual impact that fit to the space available in rooftops and urban furniture. These structures will be more susceptible to misalignment [57]. For instance, we refer to the conclusions of one of the most successful demonstrations of a mm-wave wireless link at Beijing Olympics [19]: "On the technical side, we will accelerate development of automatic antenna-axis alignment technology to help reduce the time required for equipment positioning, which was one of the problems identified by broadcast technicians in the trial."

Therefore, antennas featuring a directive, steerable beam are required even in the use cases featuring point-to-point links. However, as the review of the SotA in the incoming chapters will reveal, this is still technologically challenging for photonic Tx. The research results in

Chapter 6 and 7, are intended to develop photomixing antennas with beamsteering to fulfill the previous needs.

3.2 Applications in Spectroscopy

A large number of chemical compounds feature absorption at mm-wave and THz frequencies. Examples include gas molecules (Ammonia, CO_2, water vapor, O_2), where the energy between quantized rotational states of the molecules correspond to photons in the microwave to THz regions [121]. For instance, the absorption spectrum due to atmospheric gases is shown in Figure C.1. Non-polar solids such as explosives (e.g., RDX), or organic solids (e.g., α-lactose monohydrate), also feature absorption at THz frequencies, which is associated with molecular vibrational modes or with interaction among molecules [122]. Numerous examples of molecular absorption can be found in the HITRAN database [123].

Similar to atoms, each molecular species presents a unique set of energy levels, enabling unambiguous identification [121]. Furthermore, mm- and THz waves are not absorbed by some materials that are otherwise opaque to visible light. The most relevant ones are plastics, clothing materials, or semiconductors [124], [125] (Table C.3 lists absorption properties for general media).

The unique spectral signatures of different molecules and chemical compounds, and the ability to penetrate certain materials, make mm-wave and THz spectroscopy well suited for a diverse range of applications. Examples include the assessment of water content in leaves for biological studies [126], determination of the refractive index of semiconductors [127], and remote sensing for monitoring the ozone depletion zone in Antarctica [121], or fire detection [128]. A comprehensive review of industrial applications for mm-wave and THz sensing can be found in [129]. Space observations also rely on spectral measurements for molecule detection (H_2O, O_2, CO, N_2, etc.). A dated but interesting review on THz waves for space science is found in [7].

Aside from passive spectroscopic systems, such as in space applications, spectroscopic systems can use also active illumination by mm- and THz waves. Depending to the type of excitation, we can distinguish between two types: time-domain (TD), working in pulsed operation, and frequency-domain (FD), working in CW operation. A TD system based on photomixing employs an ultra-short pulsed laser (ps-fs) to illuminate two photoconductive antennas, one acting as a transmitter and the other as a receiver. A pulse covering mm-wave and THz frequencies is generated in the transmitter. After passing through a sample, it is mapped on the receiver using a delayed optical pulse. Details on the operation principle can be found in [26]. On an FD system based on photomixing, the outputs of two single-mode laser diodes whose frequency difference equals the desired THz frequency are first combined. Then, similar to a TD system, the signal is divided to illuminate two photomixing antennas, one acting as a transmitter, and one as a receiver. The principle of photomixing will be described in detail in the next chapter. In both cases, coherent detection is possible. Initially, FD and

TD systems based on photomixing used Ti:Sapphire lasers ($\lambda \approx 800$ nm). Nowadays, more compact and lower cost fiber lasers (for pulsed operation) or laser diodes (for CW operation) are available, and spectroscopic systems based on photomixing at 1.55 μm are offered by several vendors [32], [130], [131]. It is worth mentioning that commercialization has been only possible about ten years ago, after intensive research efforts and the challenging development of fast photoconductors for 1.55 μm illumination [44], [132].

Even if TD spectroscopy is more widely used, FD systems are better suited to high-resolution measurements, resolving spectral features as narrow as a few MHz, as in [42], [129]. Among FD system sources, one finds backward-wave oscillators, gyrotrons or free-electron lasers, classical microwave sources such as Gunn, Impatt, or resonant tunneling diodes, as well as photonic-based: QCL or through generation in non-linear crystals [133]. Several devices can be used as detectors: bolometers, Golay cells, pyroelectric detectors, or Schottky barrier diodes [134]. The first three detect power, and the latter can be used in either direct or coherent detection. Finally, one also finds FD systems based on photomixing. The main advantages concerning other approaches are a decade-spanning bandwidth, a compact and relatively cheaper set-up, coherent detection, and room temperature operation without the need for bulky cooling equipment. The previous makes photomixing especially well suited for widespread use in FD spectroscopy outside a laboratory environment. In [24], no less than half a dozen references of spectroscopy with CW photomixers are provided.

To illustrate their performance, we compare a TD and FD commercial systems based on photomixing [32]. The TD system benefits from a bandwidth spanning around 5 THz, whereas the FD system offers a 2.7 THz bandwidth. Alternatively, a CW system enables a better resolution, < 10 MHz, compared to the 1-10 GHz achieved in pulsed operation. For instance, in [42], in a window of 96.1 MHz around 312.5 GHz, five gas resonances were resolved using a relatively simple laser stabilization scheme in an FD system. Finally, regarding the set-up, the TD system requires a pulsed laser and a mechanical delay line with free-space optics or another synchronized pulsed laser [32]. The FD equivalent is less complex and less expensive, because it uses simpler CW laser diodes and does not require any mechanical delay [129].

Figure 3.4 shows a typical FD spectroscopy system using photomixing. The tones of two single-mode laser diodes offset by f_{RF} are combined and split on a 2×2 coupler. After, the split signals are fed to the Tx and Rx photomixing antennas. It suffices with two lasers to achieve f_{RF} between DC to 1.1 THz, and it can be extended to 2.7 THz using a third laser [135]. At telecommunication wavelengths, the transmitter uses a photodiode (PD). For the receiver, even if it is still possible to use a PD [122], photoconductors are preferred. The reason for this is that, unlike PDs, photoconductors do not present a built-in electric field. Thus, in the absence of a detected voltage, the current in a photoconductor will be zero even under illumination.

It can be shown that the photocurrent at the Rx of Fig. 3.4 after averaging variations at

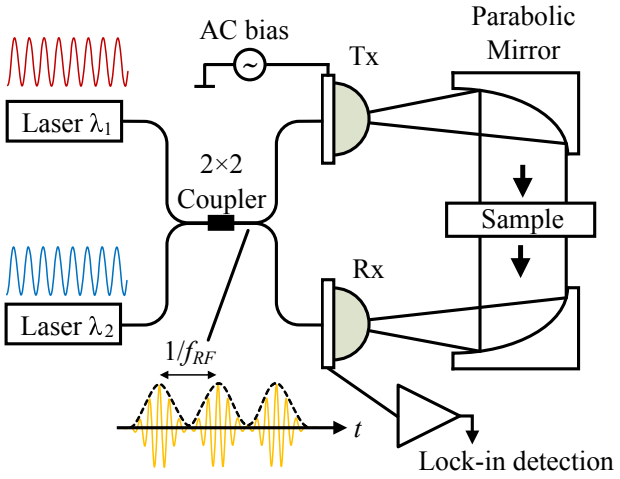

Figure 3.4 CW mm- and THz wave spectroscopy set-up based on photomixing. Adapted from [32].

$1/f_{RF}$ timescales is [122]:

$$I \propto |E_{RF}| \cos\left(2\pi f_{RF} L/c\right). \tag{3.2}$$

$|E_{RF}|$ is the amplitude of an incoming electric field captured in the receiving antenna. L is the additional optical path followed by the transmitted signal, and it includes mismatches in the optical fiber lengths, the quasi-optical propagation, and the sample.

This current is in the order of pA-nA [136], so it can be amplified and measured. In the set-up, the Tx bias is modulated (which modulates the amplitude of the emitted electric field), and lock-in detection is used. The same RF frequency is used to transmit and receive, being an example of homodyne detection. If L is constant in a short frequency interval, from (3.2) the current will oscillate with a period c/L as f_{RF} is swept. For instance, for $L = 30\,\text{cm}$, the period is 1 GHz. Typical traces of photocurrent versus f_{RF} with and without sample can be found in [129, Figure 3a]. In (3.2), the envelope gives information of amplitude transmission, whereas the zero-crossing positions provide phase information. Sub-period resolution is still possible [137], but sufficient points to retrieve data reliably are required, so f_{RF} is swept in small frequency steps of around several to tens of MHz. Finally, the retrieved data is compared by a measurement without a sample to remove the system contribution.

Overall, the main advantage of a CW spectroscopy system based on photomixing is a relatively simple, cheap, and compact set-up that enables high resolution and broadband measurements with both phase and amplitude information. Nevertheless, such a resolution results in a large density of data points, with a subsequent increase in the measurement time. Typical measurement times range from 30 s to even 3 h depending on the frequency window and lock-in integration time, which is around tens to hundreds of ms [132]. For faster measurements, integration times in the order of a single-ms are required [122], indicating a

need to improve the transmitted power or the photoconductor sensitivity.

3.3 Applications in Imaging

Mm- or THz waves feature a relatively small wavelength, which enable an imaging resolution in the mm range [46]. Also, mm- and THz waves enable non-destructive and non-ionizing testing with very low or even non-existent exposure health risks [138] (the photon energy equals 4 meV at 1 THz, much lower than the 4 eV for UV-A radiation). They can penetrate non-polar and non-metallic materials, such as paper, textiles, and other common packaging materials [139], whereas they are reflected by metals and absorbed by water.

The ability to penetrate materials that are otherwise opaque to visible light has resulted in the application of mm- and THz waves for inspection in industrial applications, including plastic composites [140] or sealed packages [139]. Penetration on clothing materials plus a stark contrast characteristic of metallic objects is also advantageous in imaging for security screening [124]. Likewise, in the framework of security, the characteristic spectral fingerprint featured by numerous chemical compounds makes mm- and THz waves attractive for spectroscopic imaging [141] to detect concealed explosives or chemical or biological agents [139], [142]. Spectroscopic imaging has also been proposed for chemical mapping in the pharmaceutical industry [141]. Finally, other applications in imaging benefit from non-hazardous radiation as well as being highly absorbed by water. This makes mm- and THz waves well suited to imaging in agricultural or biomedical studies (see references 20 to 24 in [143]).

The first 2-D image in the THz range was demonstrated in 1995 in [144] using a TD spectroscopy system with photoconductive antennas to transmit and receive. The image was raster-scanned using a two-axis motorized stage, as schematically shown in Figure 3.5a. Since then, imaging in this frequency range has become a truly heterogeneous field. Currently, there is not a single technology or technique fitting all problem requirements: spatial resolution, image acquisition time, system size and cost, among others [143]. For the sake of briefness, we will limit ourselves to cover the application of CW photonic Tx in imaging and refer to [124], [138], [143], [145] for comprehensive reviews on techniques and methods of imaging in the mm- and THz wave ranges.

Examples of the application of photonic Tx in imaging can be found in [43], [46]–[49]. In particular, [46], [48], [49] employ a UTC-PD in the transmitter illuminated at 1.55 μm, whereas the rest use a photoconductor illuminated at 800 nm. They all benefit from room temperature operation and are actively illuminated. In all cases, the image is pixel-by-pixel raster-scanned in transmission, and lock-in detection is employed. The typical set-up is similar to that used in spectroscopy, except that the QO system focuses the radiation onto the sample, as shown in Figure 3.5b. As for the receiver, a photoconductive antenna or an SBD are used. In principle, both enable phase and amplitude spectroscopic imaging (the SBD requiring an additional local oscillator) [48], [49], but often there is no need for complete sample information, and direct detection is used [43], [46].

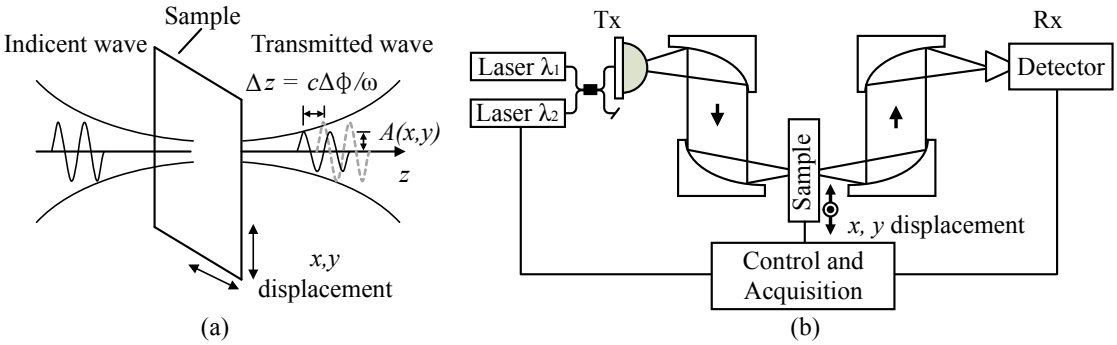

Figure 3.5 (a) Schematic of raster imaging in transmission. Adapted from [139]. (b) Typical imaging set-up employing a CW photomixer.

In contrast to THz cameras that produce real-time images at tens of frames per second [143], CW imaging systems based on photomixing are slow and not compatible with production timescales [133]. The development of a camera sensor based on an array of photomixers with hundreds of pixels is ruled out due to the optical power that would be necessary to illuminate the array, being currently tens of mW for a single device. For instance, [43] reports a 450 × 173 pixel image where the sample is mounted on a motorized XY translation stage. The pixel size is 0.3 mm × 0.3 mm, and it is captured at 450 GHz with a lock-in integration time of 300 ms. The image is taken on an overnight measurement, and the speed limits arise from the translation stage and lock-in detection time. The authors of [43] estimate that for a continuously moving stage together with lock-in integration times of 1 ms, the measurement would take around 10 s. CW photomixing imaging systems offer a compact and simple set-up for room temperature operation with dynamic ranges above 50 dB at around 350 GHz [46], [48], [49]. This is comparable to the fastest TD systems: 50 dB in < 1 ms and 80 dB in 1 s [45], albeit the latter provide a faster image acquisition.

From the previous discussion, it is clear that CW systems based on photomixing for imaging must decrease integration time. Their performance in terms of dynamic range is comparable to TD systems, but the latter can be faster. In particular, and similarly to spectroscopy, research improvements in the emitted power would make them more competitive with other technologies.

3.4 Conclusions of the Chapter

In this chapter, we have shown the challenges of photonic Tx at mm- and THz waves. For telecommunications, we have seen the need for photonic Tx featuring beamsteering and a high gain. Beam steering can enable reconfigurable links and/or ease alignment, whereas a high gain is needed to compensate for the high FSL. Besides, a higher emitted power is required to reduce measurement acquisition time and make CW photomixing-based systems more competitive in spectroscopy and imaging. In the next chapter, we will provide the introductory contents necessary to understand CW photonic Tx. After, in Chapters 5 to 7, we

will show our research results.

4

Basic Concepts for Photonic Transmitters

In this introductory chapter, we review the concepts required to understand a mm-/THz wave photonic Tx. First, we explain the photomixing technique. Next, we describe pin-based photodiodes used in photomixing, particularly uni-traveling-carrier photodiodes (UTC-PDs). Finally, we detail the main types of photonic Tx for the emission of mm- and THz waves.

4.1 Generation of Continuous-Wave Radiation by Photomixing

Photomixing is sometimes denoted as optical heterodyne down-conversion. In its most basic realization, a detector, with an output current proportional to the incident optical power, is illuminated by two optical tones producing a beat signal equal to the tones' difference frequency. Broadly speaking, photoconductors and photodiodes are used for photomixing. Their operation principle, materials, and structure are explained in the next section after the photomixing technique is introduced.

4.1.1 Operation Principle

Let us assume two monochromatic optical beams of frequencies f_1 and f_2 with the same polarization and spatially superimposed to maximize interference between the two electric fields. Under these assumptions, a scalar treatment of photomixing can be developed. The schematic is shown in Fig. 4.1, and the resultant electric field reads

$$E = E_1 \cos(2\pi f_1 t) + E_2 \cos(2\pi f_2 t + \phi), \tag{4.1}$$

where E_i is the amplitude of the electric field incoming from beam i, and ϕ is the phase of the oscillation of beam 2 referenced to that of beam 1. Let us assume now that the two beams are combined in a photomixer that generates a current proportional to the optical power. The

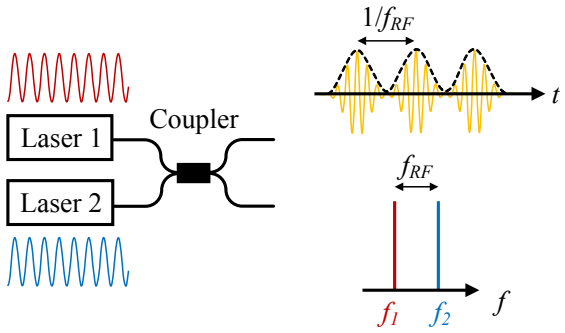

Figure 4.1 Schematic of the photomixing process.

photomixer response time is $\gg 1/f_1, 1/f_2$. The photocurrent reads as

$$I = \frac{e}{h\nu}\left(P_1 + P_2 + 2\sqrt{P_1 P_2}\cos(2\pi f_{RF} t + \phi)\right). \tag{4.2}$$

$f_{\mathrm{RF}} = |f_1 - f_2|$, $f_{RF} \ll f_1, f_2$ ($f_1 \approx f_2 = \nu$), and $e/(h\nu)$ is the conversion factor from optical power to electrical current assuming each photon generates an e-h pair. The term RF denotes a radio-frequency. In our case, f_{RF} is a frequency located in the mm-wave or THz range. If the power of both optical sources is equal, $P_1 = P_2 = P_0/2$, the oscillation term is maximized and I is expressed as:

$$I = \frac{eP_0}{h\nu}\left(1 + \cos(2\pi f_{RF} t + \phi)\right), \tag{4.3}$$

with P_0 the incident average optical power. From (4.3), it is clear that the mixing process of the two optical tones yields a DC term plus an AC term at the frequency difference f_{RF}. For radiation purposes, one is interested in the AC term.

If the tones feature a non-zero linewidth, the beat note will exhibit a non-zero linewidth too. Laser emission linewidth is associated with variations in amplitude or phase produced by noise and with broadening effects between the levels of the gain medium (e. g., Doppler or time-energy uncertainty). In particular, the emission linewidth in semiconductor lasers is usually mostly affected by phase noise, and they present a Lorentzian intensity spectrum [146]. Assuming two free-running semiconductor lasers with equal linewidth and uncorrelated phase noise, the beat note features a linewidth twice that of one laser when combined in a photomixer [147].

Another relevant aspect in photomixing is the frequency stability of the optical source. It is associated with effects that determine the emission frequency in a much longer timescale (μm – ms), such as a temperature change in the laser cavity. Therefore, the quality of the beat note of photomixing depends on the optical sources, which are explained in the following section.

4.1.2 Optical Sources

The two main wavelength ranges used to illuminate photomixers for CW (sub-)THz generation are around 800 nm and 1550 nm. These wavelengths correspond to the first and third optical communication windows, respectively, and benefit from the re-use of cost-effective and reliable optical communication devices (amplifiers, laser diodes, splitters, optical delays, etc.). The absorption layer for the first range is made of GaAs-based materials ($\lambda_g \approx 870\,\text{nm}$, where λ_g is the semiconductor cutoff wavelength), whereas for the second range $In_xGa_{1-x}As$, $x \sim 0.5$ based materials are used ($\lambda_g \approx 1580\,\text{nm}$) [2]. Due to the earlier development of low temperature grown GaAs (LT-GaAs) photoconductors, 800 nm laser sources were employed first, such as Ti:Sapphire lasers. Nowadays, CW photomixers based on photodiodes illuminated at 1550 nm feature more than an order of magnitude higher output power compared to photoconductors illuminated at 800 nm [45], and they are prevalent in telecommunications applications.

The most straightforward photomixing configuration uses two independent free-running distributed feedback (DFB) laser diodes. Each laser integrates a thermo-electric cooler to tune the emission wavelength thermally [27]. They are compact, inexpensive, and care-free. Table 4.1 shows the main characteristics of the lasers used in this work.

Specification	Value
Output power	> 30 mW combined
Tuning coefficient	~ 12 GHz/K
Tuning range	DC to ~ 1.1 THz (Up to 2.7 THz with three lasers)
Tuning speed	~ 0.5 K/s/laser Up to 100 GHz/s
Beat linewidth	1 MHz
Frequency precision	< 10 MHz (relative)
Frequency stability	20 MHz RMS (5 h)

Table 4.1 Relevant laser parameters for photomixing, from [45], [135].

The characteristics listed in Table 4.1 suffice for many applications including spectroscopic experiments [148] and wireless communications links with direct detection [149]. Other applications are more demanding, such as coherent wireless links, more sensitive to phase fluctuations in the carrier frequency [110]. Indeed, phase and frequency stabilization are imperative for error-free transmission with coherent detection [110]. More details on the optical sources for photomixing used in coherent wireless links are given in [31], [102]. Noteworthy are the advances in laser integration to reduce the phase noise associated with fluctuations in the optical path length difference between both lasers [150].

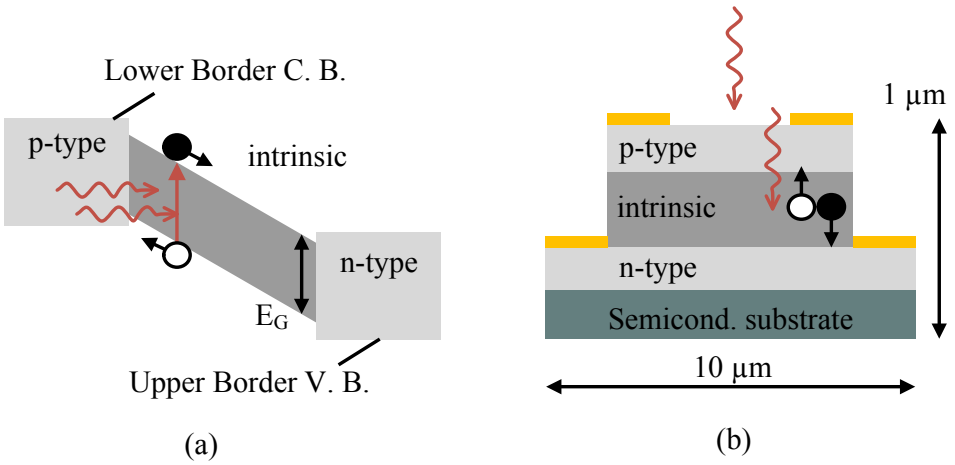

Figure 4.2 Band structure and schematic of a pin-PD.

4.2 Photomixers

In this section, we describe the photomixer devices and detail the type used in this thesis: a pin-based photodiode (in particular, a UTC-PD). As discussed before, photodiodes are preferred over photoconductors for CW mm-wave generation under 1.5 μm illumination.

There are two types of photomixers for mm- or THz wave generation: pin-based photodiodes, such as a UTC-PD, and photoconductive mixers. A photoconductive mixer is based on photoconductivity, where a semiconductor material increases its conductivity due to the generation of e-h pairs by absorbed light. The e-h pairs can be collected by electrodes under an external bias, creating a photocurrent. Conversely, an ultra-fast photodiode is based on a pin structure [2], as shown in Fig. 4.2 (in the example, it is top illuminated). It consists of three semiconductor regions: p-doped, intrinsic, and n-doped. The p-n junction produces a built-in electric field in the intrinsic layer (seen as a tilt in the band structure), where photogenerated e and h are accelerated towards the n and p regions respectively, producing a photocurrent. In the field-free n and p regions, the slow carrier contribution due to diffusion is avoided using materials with a bandgap exceeding the photon energy. In general, an external bias up to $3-5$ V further assists in carrier transport, increasing the responsivity. Photodiodes are reverse biased to enhance the built-in electric field in the depleted intrinsic region and to operate in a regime where the current is proportional to the incident optical power. In a pin-based photodiode, the intrinsic region also decreases the device capacitance, which is approximately given by that of the parallel-plate capacitor:

$$C \approx \epsilon_0 \epsilon_r \frac{A}{d_i}, \tag{4.4}$$

where ϵ_r, d_i are the relative permittivity and thickness of the intrinsic material, respectively, and A is the device cross-sectional area.

4.2.1 Photodiode Metrics and Design Trade-Offs

The performance of a photodiode (and in general of a photomixer) is evaluated attending the maximum available power and the effects limiting its efficiency.

The maximum available power is related to the maximum optical power tolerated by the photodiode, with Joule heating of lesser importance [2]. The calculation carried out in [2] for a UTC-PD with typical dimensions showed that current saturation limits the optical power to $\approx 70\,\text{mW}$, whereas thermal constraints limit the maximum optical power to about 70-100 mW. The previous is in good agreement with typical values reported in the bibliography [151], [152].

For the efficiency, it is necessary to consider the responsivity, $\Re$, defined as the ratio of photocurrent to incident optical power, and effects limiting the bandwidth. We will deal with the responsivity first. When an optical beam illuminates the photodiode, as shown in Fig. 4.2, part of the light will be reflected at the interface. Besides, due to the finite thickness of d_i, only a fraction of light will be absorbed. For instance, for a monochromatic plane-wave in normal incidence from air ($n = 1$) to InP ($n = 3.2$), 27% of the power is reflected, but anti-reflection coatings [153] or structures with enhanced optical transmission [29] can mitigate the reflection. Taking the previous into account, one can write

$$I = (1-R)\left[1-\exp\left(-\alpha d_i\right)\right]\frac{eP}{h\nu} = \Re P. \tag{4.5}$$

R is the fraction of optical power reflected, α is the absorption coefficient in the absorption region, P is the incident optical power, and ν is the light frequency. The maximum responsivity is given by $e/(h\nu)$ and equals 1.25 A/W for 1.55 μm illumination. Sometimes, the term external quantum efficiency is used instead of $\Re$, and it is defined as follows

$$I = \eta_q \frac{eP}{h\nu} \Rightarrow \eta_q = \Re\frac{h\nu}{e}. \tag{4.6}$$

Both terms are interchangeable, η_q is dimensionless and denotes an efficiency. When it equals 1, every photogenerated e-h pair contributes to the current and $\Re$ is maximum. In general, in addition to reflection, misalignment in the illumination, or a larger light spot than the active area of the photodiode also influence the fraction of power absorbed. These effects are incorporated through $\Re$. Including $\Re$ in the photomixing equation given by (4.3), one gets

$$I = \Re P_0\left(1+\cos(2\pi f_{RF}\,t+\phi)\right). \tag{4.7}$$

Since $f_{RF} \ll f_1, f_2$, $\lambda_1 \approx \lambda_2$ and the effects determining the responsivity are considered equal for both optical wavelengths. Since the average value of the AC term is zero, $\Re$ can be extracted from a DC measurement.

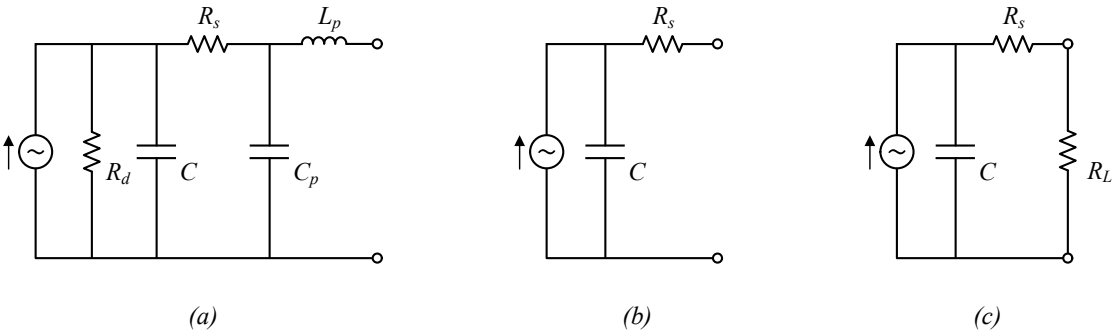

Figure 4.3 (a) Equivalent circuit of a reverse-biased photodiode, (b) simplified circuit, and (c) simplified circuit loaded with a real impedance.

In addition, one finds effects that impact the PD bandwidth. They are the RC and transit time roll-offs. To understand the RC roll-off, it is necessary to examine first the equivalent circuit of a reverse-biased photodiode, as in Fig. 4.3a. A more accurate representation is discussed in [52]. The circuit consists of a current source, in parallel with the resistance across the intrinsic layer, R_d, and with the parallel-plate capacitance created by the p-n regions, C. The expression for C is given by (4.4). For a photodiode with a circular cross-section of $64\,\mu\text{m}^2$, $d_i = 300\,\text{nm}$, and $\epsilon_r = 13$ [2], $C = 24.6\,\text{fF}$. Since the intrinsic region is depleted, values of R_d are expected high, typically in the range of hundreds of kΩ [52]. R_s denotes a series resistance, arising from the finite conductivity of the p, n regions, as well as the ohmic contact with the metal connection. Its value is usually of a few Ω [51], [154]. Finally, L_p and C_p denote a parasitic inductor and capacitor, respectively, introduced by the metallic contacts between the photodiode and the external structure. The circuit in Fig. 4.3a may be simplified to that shown in Fig. 4.3b. When the photodiode is connected to a real load, R_L, as in Fig. 4.3c, the AC current trough the load (I_L) reads

$$I_{RF}^L = \frac{I_{RF}}{1 + \text{j}\omega_{RF}(R_L + R_s)C} \Rightarrow |I_{RF}^L| = \frac{|I_{RF}|}{\sqrt{1 + (\omega_{RF}(R_L + R_s)C)^2}}. \tag{4.8}$$

I_{RF} is given by the AC term of (4.7). We define the RC roll-off as:

$$\eta_{RC} = \frac{1}{\sqrt{1 + \left(f_{RF}/f_{RC}\right)^2}}, \tag{4.9}$$

with $f_{RC} = 1/(2\pi(R_s + R_L)C)$ denoting a cutoff frequency. The RC roll-off is equivalent to that of an RC filter. The average RF power dissipated in the load is:

$$P_L = \frac{1}{2}\left|I_{RF}^L\right|^2 R_L = \frac{1}{2}\Re^2 P_0^2 \eta_{RC}^2 R_L. \tag{4.10}$$

For $f = f_{RC}$, the power dissipated on the load drops −3 dB with respect to a sufficiently

low frequency ($f \approx 0.1 f_{RC}$). For an antenna with a real impedance of 72 Ω, $R_s \ll R_L$, and the capacitance value computed before (24.6 fF), the cutoff frequency is 90 GHz.

The RC roll-off is a simplification valid for real loads. It is commonly used with broadband self-complementary antennas developed on GaAs or InP substrates whose impedance is real and approximately equal to 72 Ω. In Chapter 5, we will discuss more generally the RF power delivered to an arbitrary load where the RC roll-off will be substituted by the matching efficiency.

Similar to the RC roll-off, a finite transit time of the carriers, τ_{tr}, limits the photodiode maximum operating frequency. Assuming all carriers are instantly accelerated and undergo the same transit time, it can be demonstrated that it modifies the RF photocurrent term approximately as [2]

$$|I_{RF}^{L}| = \frac{|I_{RF|}}{\sqrt{1+\left(f_{RF}/f_{tr}\right)^2}}, \tag{4.11}$$

where $f_{tr} = 1/(2\tau_{tr})$ denotes the transit time cutoff frequency. For $In_{0.53}Ga_{0.47}As$ under optimum electric field, the electron velocity is $v \sim 4 \times 10^7$ cm/s, whereas for holes, $v \sim 5 \times 10^6$ cm/s [155]. Assuming the carriers are instantly accelerated to v, for a 300 nm transport length, the e and h contributions to the photocurrent feature a cutoff of $f_{tr} = 670$ GHz and $f_{tr} = 84$ GHz, respectively. The exact value of f_{tr} is more complicated to determine than f_{RC} and is often derived from experimental measurements or Monte Carlo simulations [2].

When the photodiode roll-offs are taken into account in photomixing, the photocurrent reads as

$$I_L = \Re P_0 \left(1 + \eta_{RC}\eta_{\mathrm{tr}} \cos(2\pi f_{\mathrm{RF}} t + \phi)\right). \tag{4.12}$$

To be completely rigorous, ϕ includes now, in addition to the optical tones phase difference, the effects of transit time and RC roll-offs in the phase. Optimization of the photodiode bandwidth requires the optimization of both roll-offs simultaneously. Since both have the same functional form, optimum bandwidth occurs when $f_{\mathrm{RC}} = f_{\mathrm{tr}}$. In practice, values are similar since the responsivity and maximum available power must also be taken into account for optimization. For instance, $f_{\mathrm{RC}} = 210$ GHz, and $f_{\mathrm{tr}} = 170$ GHz were reported in [153]. These roll-offs produce a 40 dB/decade (12 dB/octave) decrease in the RF output power. Hence, extending the photodiode bandwidth, even at the cost of lower $\Re$ or maximum output power at lower frequencies, is essential for ultra-fast operation.

The very distinct transit time cutoff frequencies for e and h in the highly simplified example above indicates that the photodiode performance can be improved by enhancing contribution of electrons to the photocurrent compared to that of holes. This is exactly what the design of a

UTC-PD pursues. A closer look at the semiconductor properties of $In_{0.53}Ga_{0.47}As$ allows one to better understand the benefits of electron transport in a UTC-PD.

4.2.2 Material Characteristics of $In_{0.53}Ga_{0.47}As$

$In_{0.53}Ga_{0.47}As$ is the material primarily used in the absorption region of pin-based photodiodes for 1.55 μm illumination. Attractive characteristics include a direct bandgap (required for efficient absorption of photons) and a cutoff wavelength of 1.68 μm. Among other semiconductors with energy bandgap $E_G > 0.5$ eV, it features the highest electron mobility and the largest absorption coefficient [156]. It can be grown on InP because they are lattice-matched. Since InP features larger E_G and thermal conductivity, it is used as substrate to grow $In_{0.53}Ga_{0.47}As$, and for the $p-n$ regions of the photodiode. Table 4.2 summarizes relevant semiconductor characteristics of both materials.

Specification	$In_{0.53}Ga_{0.47}As$	InP
E_G	0.75 eV	1.34 eV
Cutoff wavelength	1.68 μm	0.96 μm
Lattice constant	5.87 Å	5.87 Å
Thermal conductivity	0.05 $W cm^{-1} K^{-1}$	0.68 $W cm^{-1} K^{-1}$
h mobility	250 $cm^2 V^{-1} s^{-1}$	-
e mobility	10^4 $cm^2 V^{-1} s^{-1}$	-
Absorption at band edge	0.8×10^4 cm^{-1}	-
$E_{\Gamma-L}$	0.46 eV	0.59 eV

Table 4.2 Semiconductor properties of $In_{0.53}Ga_{0.47}As$ and InP at room temperature [2], [157].

4.2.3 Band Structure and Operation Principle of a UTC-PD

Fig. 4.4 shows the band structure of a UTC-PD. It was initially proposed around 1997 by researchers at Nippon Telegraph and Telephone (NTT) to extend the bandwidth of pin-PDs [158]. The band structure is similar to that of a pin-PD with p-, n- contacts, and an absorption layer, including additional blocking and collection layers.

In a UTC-PD, absorption occurs on a thin layer (p-doped $In_{0.53}Ga_{0.47}As$, typical thickness 120-200 nm [52], [155]), where p-doping causes holes being the majority carrier. As a consequence, photogenerated holes relax quickly with a relaxation time as low as 33 fs for sufficiently high doping [52]. Thus, holes do not drift towards the p-contact, and their contribution to the photocurrent is removed [155]. Diffusion of photogenerated electrons towards the p-contact is obstructed by the block layer, so they diffuse towards the transport layer (also called the collection layer). In the field-free absorption region, electrons move by diffusion, which is slower than drift. It is then necessary to maintain this region as thin as possible. A thin layer also helps to tolerate higher optical powers since the thermal conductivity of $In_{0.53}Ga_{0.47}As$

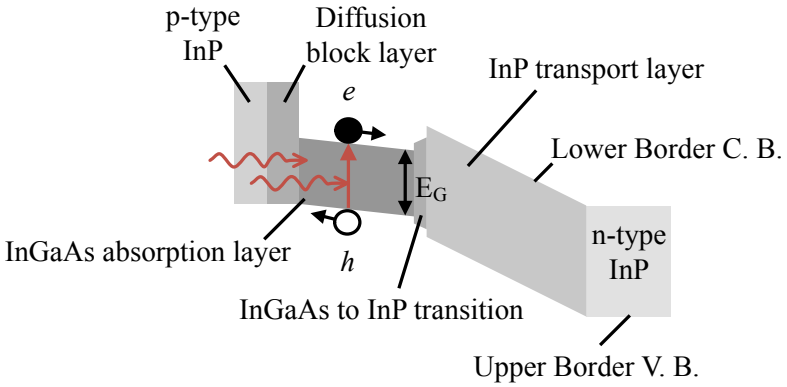

Figure 4.4 Band structure of a UTC-PD (C. B.= Conduction Band, V. B.= Valence Band).

is ×13 smaller than that of InP (see Table 4.2). Once the electrons enter the collection layer (intrinsic or slightly n-doped InP with a thickness around 300 nm [52], [155]), they drift towards the n-contact due to the electric field. Maintaining the collection layer is necessary to reduce the parallel-plate capacitance of the PD. Finally, to avoid the step in the conduction band of the InP-InGaAs heterointerface, which could produce current blocking, a stepped transition of InGaAsP with different weights of GaAs and P is grown [155].

The band structure depicted in Fig. 4.4 implies that electrons are the only carriers contributing to the photocurrent. For collection and absorption regions of similar thickness, the electron traveling time in the absorption region dominates because diffusion velocity is smaller than drift velocity with a sufficiently high electric field [155]. To compensate for this, bandgap or doping grading the absorption region create a quasi-field (seen as a slight tilt in the absorption layer of Fig. 4.4), which is highly effective in reducing electron transit time. As discussed in [52], a quasi-field equivalent to 50 mV can extend the transit time 3 dB bandwidth from 160 GHz to almost 400 GHz for 120 nm thick absorption and collection layers.

Another significant feature in a UTC-PD is electron velocity overshoot in the collection layer [155]. The effect is explained in [2]. For a high electric field in the transport layer, electrons will scatter early to other valleys in the conduction band, and they will move at saturation velocity $v_s \sim 10^7$ cm/s. However, a low electric field will cause reduced acceleration and will increase transit time. For an intermediate field, electrons benefit from a velocity overshoot (os) where the average velocity is higher, $v_{os} \sim 4 \times 10^7$ cm/s. The effect depends on the thickness of the transport layer, in practice hundreds of nm thick. For thicker layers, the electrons would travel most of the time at saturation velocity, and overshoot would be unnoticed. Nevertheless, in GaAs devices $E_{\Gamma L} = 0.3$ eV [2] (lower than $E_{\Gamma L} = 0.59$ eV for InP), and they benefit less from velocity overshoot. Therefore, UTC-PD realizations are developed for 1.55 μm, with few exceptions at 800 nm [159].

As the input optical power increases, photogenerated carriers accumulate in the collection layer of the PD. This charge buildup (space charge effect) causes the band to bend so that the zone close to the absorption layer becomes more horizontal [3]. Then, it decreases the built-in

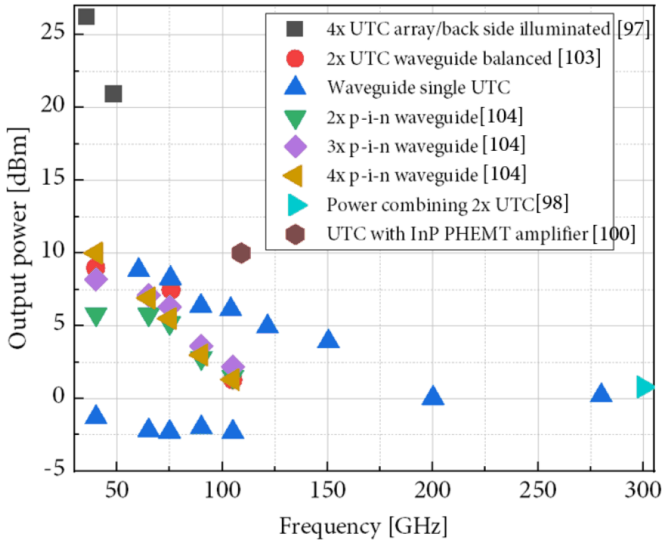

Figure 4.5 Output power of pin- and UTC-PDs, reprinted from [160].

electric field in the intrinsic region, increasing transit time. This can only be moderately relieved by an external bias (where an external field increases carrier velocity and avoids charge accumulation). The space charge effect arises in both pin- and UTC-PDs, but the effect is different between them [155]. In a UTC-PD, *e* benefit from velocity overshoot, which is much higher than the drift velocity of holes in a pin-PD. Therefore, carriers in a UTC-PD tend to accumulate less, and saturation occurs at higher current densities than in a pin-PD. Overall, one can obtain a saturation current density ~ 3 times higher in a UTC-PD than in a pin-PD [155]. Detailed analysis as in [155] requires an in-depth examination of the photodiode properties, which is beyond the scope of this introduction. Since UTC-PDs saturate at higher current densities, they also feature higher RF power. Fig. 4.5 shows a comparison between the output power of UTC-PDs and pin-PDs.

It is worth mentioning a recent paper that compares the output power of a pin-PD and a UTC-PD for the same optical power [28]. This is a fair comparison when the optical power is limited or is a relevant parameter, as in telecommunications. In the comparison, it is shown that the pin-PD outperforms the UTC-PD in terms of output power up to approximately 200 GHz, and after, both devices provide a comparable output power. The reason for this behavior is that $\Re = 0.35\,\mathrm{A/W}$ in the pin-PD whereas it is around half this value (0.18 A/W) for the UTC-PD. Of course, at higher optical powers, the UTC-PD features a higher RF output power than the pin-PD, in line with the improved saturation characteristics commented before.

We have seen how a narrow absorption region in a UTC-PD helps reduce the electron transit time with respect to a pin-PD. It must be around 200 nm so that the slow diffusion of electrons does not rise transit time substantially (for a thick absorption region of 400 nm and 100 mV equivalent quasi-field, the transit time surpasses that of a pin-PD! [155]). However, for

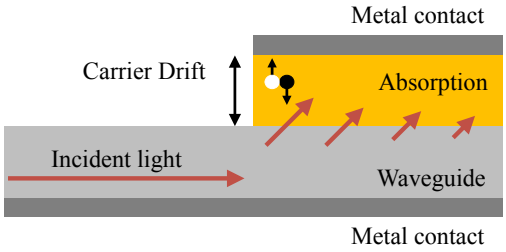

Figure 4.6 Structure of a waveguide-fed, evanescently coupled photodiode.

a 200 nm-thick $In_{0.53}Ga_{0.47}As$ absorption layer, absorption is 15% only, not even accounting for reflection at the interface. The light not absorbed in the UTC-PD does not contribute to device heating. One can use higher optical powers to compensate, but the efficiency decreases. For instance, in [153], an absorption layer of 100 nm is used, and they measure $\Re = 0.03\,A/W$ (2.5% of the maximum).

Despite the simpler structure of a top-illuminated PD, designs often employ alternative configurations where the PD is illuminated from the edge to improve $\Re$. In this case, light absorption and layer thickness are decoupled to some extent, enabling optimization of both responsivity and transit time. Fig. 4.6 shows one instance of a waveguide-fed, evanescently coupled structure illuminated from the edge. This is also the structure of the UTC-PD used in this thesis [161]. Light evanescently penetrates the absorption layer through a dielectric waveguide grown on the substrate. For instance, in [162], the PD length is 15 μm to absorb 90% of the incident optical power. Its width is reduced to about 3 μm to obtain an RC cutoff frequency at 350 GHz (for a 50 Ω load), with a transit-time cutoff frequency of 340 GHz. A $\Re = 0.2\,A/W$ is achieved (the authors do not include the optical loss between the optical fiber and the PD chip, estimated at 40%). Other similar edge-illumined structures have been reported in [163].

The UTC-PD explained in the section is a common type of PD used for ultra-fast operation, but not the only one. Some alternatives include UTC variations such as the modified UTC (MUTC) or the triple transit region photodiode (TTR-PD). One also finds variations of the pin diode, e.g., the nip-nip PD. Their discussion is beyond the scope of this chapter, and we refer the interested reader to [2] for an overview.

4.3 Photonic Transmitters

In the context of this work, a photonic transmitter comprises a photomixer, optical means to couple light, a DC connection to bias the device, and an antenna to radiate. It is sometimes directly denoted as a photomixer, but we have preferred to use different terms.

Fig. 4.7 shows the commercial versions of the two main types of photonic transmitters [34], [164]. We will provide more examples later when we discuss the state-of-the-art in Chapters 5 to 7. In Fig. 4.7a-b, the photomixer is developed on a semiconductor substrate (in green)

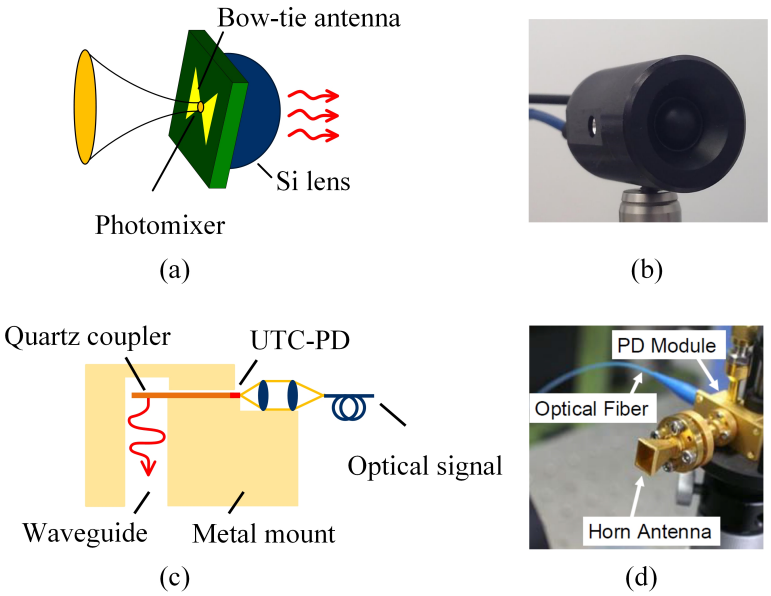

Figure 4.7 Two commercial types of photonic transmitters: (a) and (b) on-chip antenna with silicon lens from TOPTICA [34]. (c) and(d) waveguide module from NTT [164]. Artist views from [38], [167].

together with the antenna, and it is located at the antenna feed point. We will denote this type as the on-chip antenna transmitter. In the example shown, the antenna corresponds to a self-complementary bow-tie. The radiation from the antenna, directed mainly towards the semiconductor substrate [165], is coupled to free space by a high-resistivity silicon lens, depicted in blue and not to scale. The high dielectric index of the semiconductor substrate ($n_{\mathrm{InP}} = 3.2$ at $1.55\,\mu$m) requires in practice the use of the substrate lens. In Fig. 4.7b, the packaged device is shown. It corresponds to a CAN-type package [166], where the optical fiber (in blue) illuminates the photomixer, and the black cable serves to bias it. The package aperture occupied the silicon lens is about 10 mm in diameter.

Differently, Fig. 4.7c-d correspond to a photonic transmitter with a waveguide output. We will refer to it as the waveguide type photonic transmitter. Similar to the other type, a fiber plus lens system focuses light into a photomixer, a UTC-PD in this case. The PD output is coupled to a quartz substrate that eventually radiates into the waveguide, using, for instance, a tapered slot antenna (TSA) printed on the quartz. Details of the interconnection are given in [168]. It is worth mentioning that to extend the operation bandwidth, the coupling structure can be designed to suppress higher-order modes in the output waveguide [169]. The packaged device is shown in Fig. 4.7d, where a horn antenna has been connected to radiate the generated power. The output waveguide dimensions can be adapted to cover different frequency bands, and the concept has been proved from frequencies ranging from W-band (75 to 110 GHz) to beyond 600 GHz [169].

For on-chip antenna transmitters, broadband self-complementary antennas are generally used. Due to the large bandwidth of self-complementary antennas, they are more appropriate

for spectroscopy to cover large frequency windows. Besides, the modular characteristic of the waveguide output type is advantageous for telecommunications. For instance, the module can be combined with a horn and a dielectric lens to achieve a high gain of 37 dBi or 52 dBi [168] and compensate for propagation loss in wireless links.

4.3.1 Photomixer Illumination

The mode field area of a standard single-mode fiber (SMF-28) is around $78\,\mu m^2$, and it diverges on a cleaved facet. Conversely, the active area of photodiodes reported in the literature ranges approximately between $9-60\,\mu m^2$ [29], [64], [170]. For evanescently coupled photodiodes illuminated by an optical waveguide, the input dimensions are $< 4\,\mu m$ in width and $\sim 300\,nm$ in height [154]. Therefore, some additional optical means are in general required for PD illumination. Since the RF power scales as $\Re^2$ (see (4.10)), efficient photomixer illumination is a critical assembly aspect.

For single device illumination, a lensed fiber can be used, either adding a focusing/collimating lens system (see Fig. 4.7c) or tapering the fiber tip for a spot diameter of $2.5-5\,\mu m$ [171]. For two PDs, it is also possible to integrate the fibers as reported in [172], [173].

Multiple device illumination requires microlens arrays or fiber bundles (either 1-D or 2-D) [64], [174]. The former solution uses an expanded, collimated beam to illuminate the microlenses, which in turn focus the light onto the photomixers. Consequently, a fraction of optical power is lost. Furthermore, the diffraction-limited spot diameter is tens of μm [175], so it does not represent an efficient illumination option. As for fiber bundles, they have been used in [63], [64]. They require careful alignment and can lead to an uneven coupling efficiency due to alignment errors and pitch mismatch between the photomixer array and the fiber array [63]. The difficulty to illuminate efficiently simultaneously several photodiodes (> 4) will be more evident when examples of photonic Tx with antenna arrays are reviewed in the following chapters.

4.4 Conclusions of the Chapter

In this chapter, we have explained the fundamentals of photomixing for CW generation and the impact of the optical sources on the generated RF signal. Next, we have described relevant metrics and the structure of pin- and UTC-PDs, the preferred sources for CW generation of mm- and THz waves under $1.55\,\mu m$ illumination. Finally, we have reviewed the main types of mm-wave and THz photonic transmitters and the optical means to illuminate them.

We have tried to provide a brief but complete overview of the required concepts to understand a mm-wave or THz photonic Tx for CW operation, especially the aspects more related to photonics. Once the applications, operation principles, and limitations of photonic Tx have been clarified, in the rest of the chapters of this thesis, we will present the antenna conceptions

aiming at improving the performance of such Tx.

5

A Method for On-Chip Antenna Arrays Efficiently Matched to UTC-PD

In this chapter, we address one of the main drawbacks of photonic transmitters: the low values of emitted power. As we have pointed out in Chapter 3, the available power is a crucial aspect for applications such as spectroscopy or imaging. To overcome this issue, we have designed an array of antennas efficiently matched to UTC-PDs. We note that henceforward we will simply denote the scan impedance as impedance. It is clear from Chapter 2 that we refer to the antenna impedance when all of the array elements are excited with the same amplitude with a linear phase progression. The material presented here constitutes an extension of reference [iv] from the List of Publications.

In a nutshell, we present a mm-wave array of on-chip antennas with a backing reflector that allows one to obtain efficient impedance matching to a UTC-PD. In the infinite array limit, it is possible to describe the array unit-cell as an equivalent circuit, including also ohmic losses. In particular, the use of a backing reflector contributes inductively to the antenna impedance. The rest of the array variables further help to cancel out the photodiode capacitance and to obtain near conjugate matching. The unit-cell designed in the infinite array environment is the starting geometry to optimize a finite 2×2 array. We also discuss aspects such as efficient photodiode illumination and the assembly of the structure. The adopted approach provides a twofold increase in the emitted power: through power combining of several elements, and through the improvement of the impedance match. We obtain a 2-4 enhancement in the matching efficiency concerning other matching methods in the bibliography while preserving a wide -3 dB power relative bandwidth of 30%. Furthermore, the peak increase in the emitted power is larger than 11 dB compared to the power radiated by a self-complementary antenna with the same UTC-PD source.

5.1 Introduction

Photodiode-fed antenna designs have become more and more common due to the advent of photonic solutions for the generation of mm- and THz waves. The relatively low radiated power is one of the main drawbacks of photonic generation. Therefore, solutions to increase the radiated power are actively sought. The limitation in the emitted power arises from the maximum optical power admitted by the photodiode before breakdown. From (4.10), it is clear that the higher the optical power, the higher the photocurrent and the power dissipated on a load. This aspect solely depends on the PD design if the transmitter enables efficient illumination and good heat dissipation. Another limitation concerns how well the power is extracted from the PD, and eventually radiated. The latter aspect involves the design of the transmitter, and is related to the impedance matching efficiency between the antenna and the PD and other losses in the transmitter.

In general, there are two strategies to increase the emitted power in photonic transmitters. The first strategy consists in power combining using antenna arrays fed by multiple PDs. However, we will see that practical limitations preclude the use of more than, approximately, four active elements. The second strategy relies in increasing the matching efficiency using matching networks or resonant antennas. We will detail these two approaches after.

The solution proposed in this chapter combines the two strategies above. It makes use of an antenna array integrated with PDs and efficiently illuminated. Besides, the array geometry is optimized so that the antennas feature increased impedance matching to the PD over a relative bandwidth broader than that provided by resonant antennas ($\approx 15\%$). Equally important, we take into account aspects such as ohmic losses and manufacturing considerations. It is important to note that, even if the method is used for photodiodes, it could also be used to enhance the matching efficiency (and in turn the detected power) in an antenna array integrated with Schottky Barrier Diode (SBD) detectors. The reason is because, similar to a photodiode, an SBD features a capacitive impedance with low values for the real part [176].

The remainder of the chapter is organized as follows: in the rest of the introduction, we analyze the metrics used to evaluate the output power in a photonic transmitter. Subsequently, we study relevant realizations in the bibliography. In Section 5.2, we present the infinite array approach that allows us to analyze the antenna impedance using an equivalent circuit approach. Next, we optimize a preliminary layout using the equivalent circuit. In Section 5.3, we study a finite 2×2 array and proceed with a full-wave optimization. In Section 5.4, we discuss manufacturing considerations. Finally, Section 5.5 includes the concluding remarks of the chapter.

5.1.1 Power and Efficiency Considerations

The most relevant metrics of photonic transmitters include the output power and the fraction of optical power converted to RF power. The latter is referred to in some contexts as optical-to-

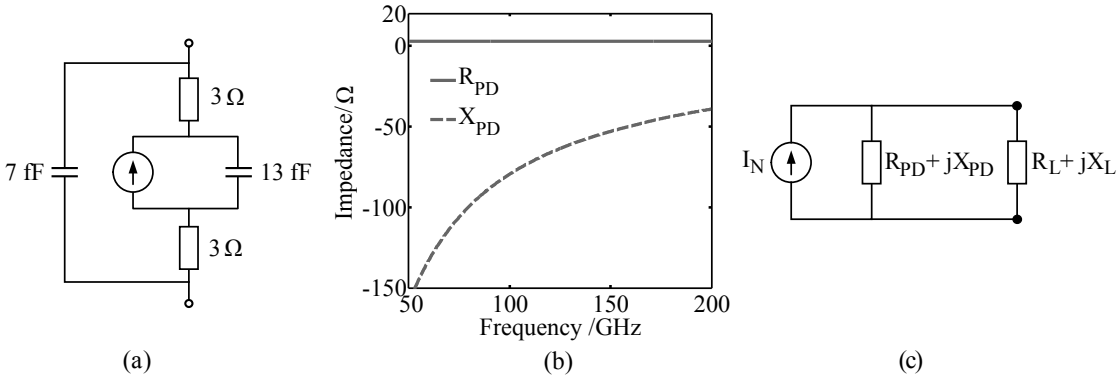

Figure 5.1 (a) Photodiode equivalent circuit from [51], (b) computed impedance, and (c) equivalent circuit of the photonic transmitter at the RF frequency.

terahertz conversion efficiency. Let us examine next the different aspects that come into play to calculate the radiated power in photonic transmitters:

In Section 4.2, we have seen the processes that reduce the photocurrent and depend only on the photodiode. When the responsivity ($\Re$) and transit-time roll-off (η_{tr}) are considered, the photodiode generates a current given by $I = \Re P\left(1+\eta_{\text{tr}}\cos(2\pi f_{\text{RF}} t+\phi)\right)$. P is the average optical power, f_{RF} and ϕ are the differences in frequency and phase, respectively, of the two optical tones used for photomixing.

Another factor that determines the overall efficiency is the impedance matching efficiency, η_M. It accounts for the fraction of the available power dissipated in the load. In turn, the available power corresponds to the power dissipated in the load under conjugate match. In addition, the radiation efficiency (η_R) defined in [1, Ch. 2], accounts for the fraction of power delivered to the load that is radiated by the antenna.

There are other factors that impact the radiated power. For instance, how well the radiated pattern fits a Gaussian beam (Gaussian efficiency), losses due to a substrate lens, or the fraction of power emitted with a particular polarization (polarization efficiency). However, these aspects are more important at the system level, such as during the design of a quasi-optical link, and will not be considered for the time being.

Let us now provide a mathematical framework for the systematic analysis of the different efficiencies. In particular, we will focus on η_M, which is best examined using the circuit equivalents for the photodiode and the load in Fig. 5.1. The equivalent circuit of the photodiode presented in [51] is shown in Fig. 5.1a, and Fig. 5.1b shows the computed impedance. For other photodiode realizations, similar values are obtained too [52]. Fig. 5.1c shows the Norton equivalent of the photodiode connected to a load. From the circuit, the power dissipated in

the load reads as

$$P_L = \frac{1}{2}\left|I_N\right|^2 \frac{R_{PD}^2 + X_{PD}^2}{(R_{PD}+R_L)^2 + (X_{PD}+X_L)^2} R_L, \tag{5.1}$$

where I_N is the Norton current, and it depends only on I and on the photodiode impedance, $Z_{\mathrm{PD}} = R_{\mathrm{PD}} + \mathrm{j}X_{\mathrm{PD}}$. The load is represented by $Z_L = R_{\mathrm{L}} + \mathrm{j}X_{\mathrm{L}}$. Under conjugate matching (M), the power dissipated in the load is:

$$P_L^M = \frac{1}{2}\left|I_N\right|^2 \frac{R_{PD}^2 + X_{PD}^2}{4R_{PD}}. \tag{5.2}$$

For an arbitrary load we can define $\eta_M = P_L / P_L^M$, which results in:

$$\eta_M = \frac{4R_{PD}R_L}{(R_{PD}+R_L)^2 + (X_{PD}+X_L)^2}, \tag{5.3}$$

where $0 \leq \eta_M \leq 1$. Obviously, conjugate matching yields $\eta_M = 1$. It this case, the power dissipated in R_L is maximized and is equal to the power dissipated in R_{PD}. Equation (5.1) may be written as a function of η_M as

$$P_L = \frac{1}{2}\left|I_N\right|^2 \frac{R_{\mathrm{PD}}^2 + X_{\mathrm{PD}}^2}{4R_{\mathrm{PD}}} \eta_M. \tag{5.4}$$

First, the equation above tells us that the power on the load, and eventually the power radiated, scales with $|I_N|^2$. Hence, increasing the maximum current withstood by the photodiode is a critical aspect in the design of the device. One of the main advantages of the UTC-PD is that it saturates at higher current densities than a pin-PD, ultimately resulting in higher output power [155], [177]. Second, for fixed photodiode parameters, the power dissipated in the load depends exclusively on the matching efficiency. For instance, using (5.3) and the values of Fig. 5.1b at 100 GHz for Z_{PD}, the matching efficiency for $Z_L = 72\ \Omega$ and $Z_L = 50\ \Omega$ is:

$$\eta_M = 6.1\%\ (72\ \Omega),$$

$$\eta_M = 5.6\%\ (50\ \Omega).$$

The first case represents the impedance of a self-complementary antenna printed on an InP substrate ($\epsilon_r = 12.5$ [52]). It is calculated from Mushikae's relation $Z = Z_{\mathrm{eff}}/2$ [178], with $Z_{\mathrm{eff}} = Z_0/\sqrt{(1+12.5)/2}$. The second case corresponds to the characteristic impedance of common transmission lines. Approaches to improve matching efficiency include matching circuits [51] or resonant antennas [179], and will be discussed later in this chapter.

From the previous values, it is evident that there is room for improvement in the matching

efficiency to enhance the emitted power. Since the PD resistance is only a few Ω, exact conjugate matching would require an antenna with a low input resistance. In that case, ohmic losses could compromise the radiation efficiency, η_R. Therefore, we need to consider the total radiated power, P_R, using the expression:

$$P_R = \frac{1}{2}\Re^2 P_0^2 \eta_{\mathrm{tr}}^2 \frac{1}{|1+\mathrm{j}\omega_{\mathrm{RF}} CR|^2} \frac{R_{PD}^2 + X_{PD}^2}{4R_{PD}} \eta_M \eta_R, \tag{5.5}$$

where $I_N = I/(1+\mathrm{j}\omega_{RF}CR)$ is the Norton current, with $C = 13\,\mathrm{fF}$, and $R = 6\ \Omega$ as given by the equivalent circuit of Fig. 5.1a. Besides, we have assumed $f_{\mathrm{tr}} = 220\,\mathrm{GHz}$ [51] for the transit-time roll-off. In the subsequent calculations, the factor $\Re^2 P_0^2/2$ is normalized to 1 A^2, and the power will be given in arbitrary units.

5.1.2 Photonic Transmitters Based on On-Chip Antennas

Common on-chip antenna realizations fed by photodiodes include broadband antennas [132], [151], [170], resonant antennas [152], [179], or antenna arrays [62]–[64], among others [180]. Some examples are shown in Fig. 5.2.

Broadband antennas usually consists in self-complementary structures, where the antenna plus the antenna rotated θ around its normal (usually 90°) equals a ground plane. In this case, the antenna presents a constant input impedance that follows Mushikae's relation [178]. For an antenna printed on InP, the corresponding input impedance is 72 Ω, as calculated above to illustrate the matching efficiency. In practice, the input impedance is not constant for all frequencies, but it can cover more than a decade. For instance, from 150 GHz to 1.7 THz [170]. The lower frequency bound is due to the finite size of the antenna. When the electrical size of the antenna is comparable to the wavelength, it presents a resonant behavior. The upper-frequency limit is determined by the smallest antenna detail and the feed gap. Integrating an amplifier or a matching circuit at the antenna feed is not interesting for broadband antennas because it would limit the bandwidth. Therefore, this type of antenna exhibits a limited output power with a 40 dB roll-off per decade (12 dB per octave), of which 20(6) dB correspond to the roll-off caused by the transit-time, and another 20(6) dB correspond to the RC roll-off, as shown in Section 4.2. Circular or linear polarization can be accomplished using spiral or log-periodic toothed, and bow-tie shapes, respectively. Sufficiently far from the lower frequency bound, the current at the rim of the antenna has decayed [181]. Therefore, DC bias pads can be conveniently connected at the antenna periphery without requiring additional circuitry, such as an RF choke, as one can observe in Fig. 5.2c,d.

Among the realizations that use resonant antennas, one can find the folded dipole shown at the bottom of Fig. 5.2a or the twin dipole antenna (TDA), as shown in Fig. 5.2b. Near and below anti-resonance, dipole antennas feature an impedance mainly inductive [182], so that the RC roll-off of broadband antennas can be compensated [179]. Nevertheless, as in a

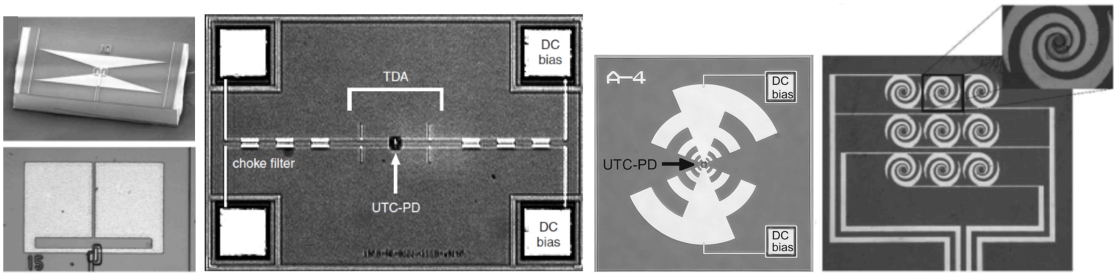

Figure 5.2 Examples of on-chip antennas: (a) bow-tie (top) and folded dipole (bottom) [152], (b) twin dipole antenna (TDA) [179], (c) log-periodic toothed antenna [151], and (d) an array of log-periodic spiral antennas [64].

resonant parallel RLC circuit (that resembles the input impedance of a dipole antenna [182]), a high inductance implies having simultaneously a high value of the resistance. Therefore, the real parts of the photodiode and antenna impedance will not be matched, and only a partial compensation can be achieved [179]. Besides, resonant antennas require an RF choke to polarize the antenna, which can be also used to tune the antenna impedance. However, the final antenna footprint can become significantly larger, as in the TDA shown in Fig. 5.2b. In [179], the output power of a log-periodic toothed antenna was compared with the output powers (for the same photocurrent) of three TDAs designed at 0.75 THz, 1.05 THz, and 1.5 THz. Although 4 different resonant TDAs would be necessary to cover the same band provided by the log-periodic broadband antenna, the peak power emitted by the resonant antennas was from 3 to 4 times higher than the corresponding power emitted by the broadband one at those frequencies. Nevertheless, the TDA presented a narrowband impedance matching, estimated to be around 15% (3 dB power drop).

Another relevant demonstration of on-chip antenna is the TEM horn antenna (TEM-HA) presented in [180] and shown in Fig. 5.3a. The TEM-HA allows wideband operation. In principle, it could be also possible to integrate a matching circuit, amplifier, or bias circuitry on the photodiode side. The antenna radiation is mainly directed parallel to the air-substrate interface, and not towards the substrate. Thus, it avoids substrate modes present in typical on-chip antennas, and it does not require the use of a substrate lens. However, since the TEM-HA aperture is several wavelengths wide, scaling this antenna to an array can be challenging, and in the best case scenario, it would be possible in one direction only.

Arrays of on-chip antennas have been presented in [62]–[65]. In [62], the array was formed using several individual transmitters focused on a plane for a transmission distance of 4.2 m. Packaging the individual transmitters enabled optimum integration of the fiber with the photodiode. In total, the combination of 4 transmitters resulted in a spot with a peak intensity 16 times higher than for the single element. A factor of about 4 was due to the reduction of the spot size from the coherent beam superposition, and another 4 factor came from power combining. However, due to the size of the individual emitters, they were separated 17.5 cm,

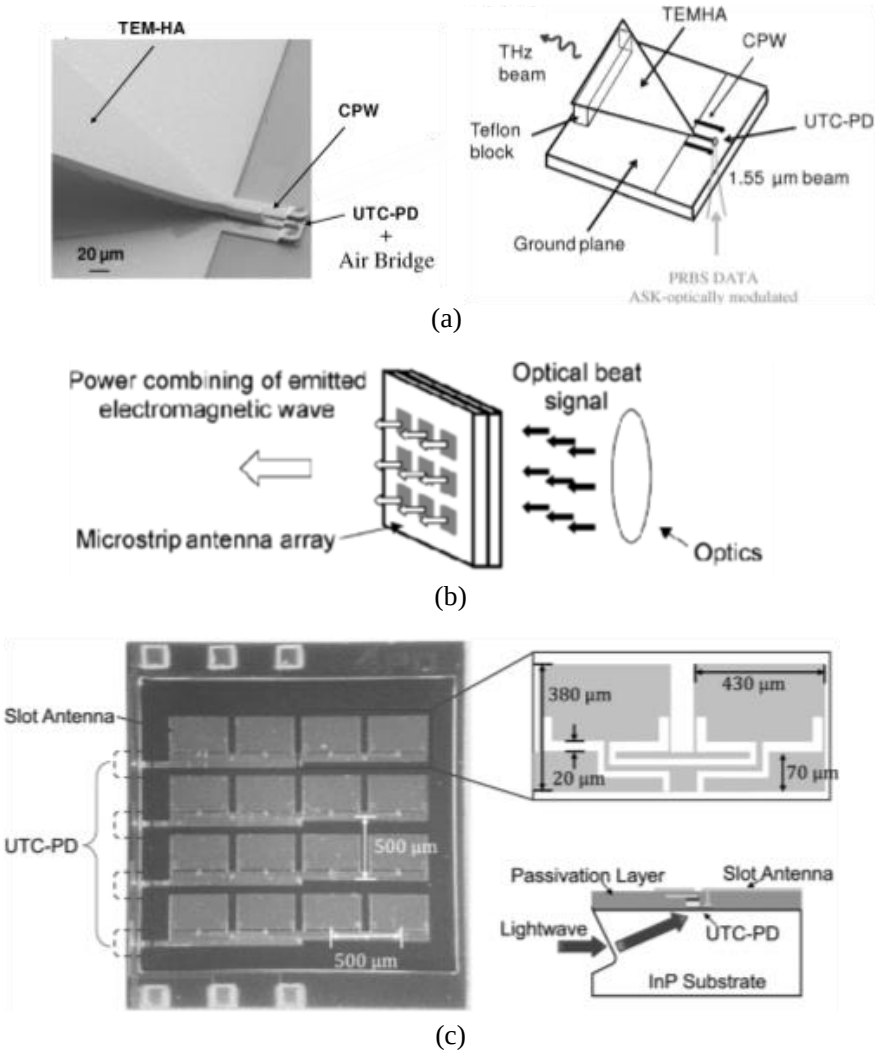

Figure 5.3 Examples of on-chip antennas: (a) TEM- horn antenna [180], (b) 3×3 microstrip array [63], and (c) 4×4 slot antenna array [65].

and it is clear from the array factor that the superposition of the beams will create many lobes. Indeed, in the reported patterns, the sidelobe level was only -6 dB. As the authors of [62] later commented, individually packaged elements featured poor scalability [64]. To overcome this issue, they presented in [64] an array of log-periodic spirals printed on a single chip, shown in Fig. 5.2d. A fiber bundle fed the array, and four elements were active. The work accomplished power combining and spot size reduction as before, but without improving the matching efficiency. In addition, the use of electrically large broadband spirals and a collimating substrate lens made it complicated to achieve good beam steering performance ($\pm 5.2°$ before the sidelobes became more powerful than the main beam).

In [63], the authors presented a microstrip antenna array shown in Fig. 5.3b. Each microstrip antenna included a matching circuit to cancel out the PD capacitance. Unfortunately,

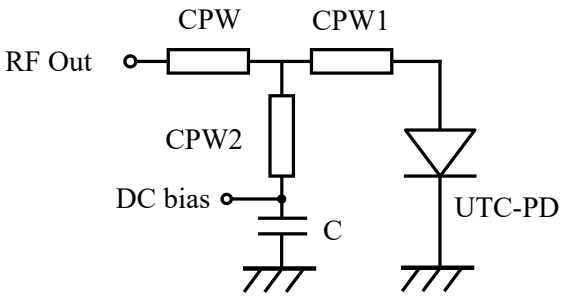

Figure 5.4 Matching circuit from [51] used to improve the emitted power.

no information was reported about the increase in the emitted power. Nevertheless, the authors did stress the difficulty of using a fiber bundle to illuminate efficiency each photodiode on the array, despite only one row being active. Finally, [65], [183] present a recent demonstration of a phased array composed of slot elements. Fig. 5.3c shows the fabricated array, a detail of the slot element, and the scheme used to illuminate the UTC-PDs. The slots feature an impedance bandwidth of 13% matched to 50 Ω (i.e., without any technique to increase impedance matching). Again, practical constraints resulted only in two active rows out of the four fabricated.

Finally, we will comment on the method reported in [51] that, even if it does not fall in the category of on-chip transmitters, seeks to improve the radiated power using a matching circuit. The matching circuit is shown in Fig. 5.4. It consists of a stub that tunes out the capacitive part of the PD impedance. The stub includes a shorting capacitor that serves simultaneously as a bias-tee to polarize the photodiode. By modifying the length of the stub (CPW2), as well as its distance from the photodiode (CPW1), the matching efficiency can be optimized. The authors present calculated results where the matching efficiency can be improved between 50-90% compared to a 50 Ω load, with 3 dB compression bandwidths of 50% and 25%, respectively.

5.2 Infinite Array Approach

Infinite phased arrays have been used extensively as an analysis tool to obtain impedance matching over a large bandwidth [69], [70]. For instance, [87] introduced capacitive coupling between consecutive dipoles in a row to compensate for the inductance introduced by a ground plane that backed the array. Other examples include modeling ultrawideband coupled spiral antennas [184], and more recently, they have also been used to design photodiode-fed antenna arrays [185]–[187] for frequencies between 5 GHz and 20 GHz. Even [185]–[187] constitute a valuable contribution, it is important to note that the proposed integration technology is not compatible with our approach for on-chip antennas where the PDs are developed in the same substrate.

The importance of the infinite phased arrays relies on the fact that equivalent circuits can provide an accurate description of the scan impedance. In turn, the equivalent circuits are

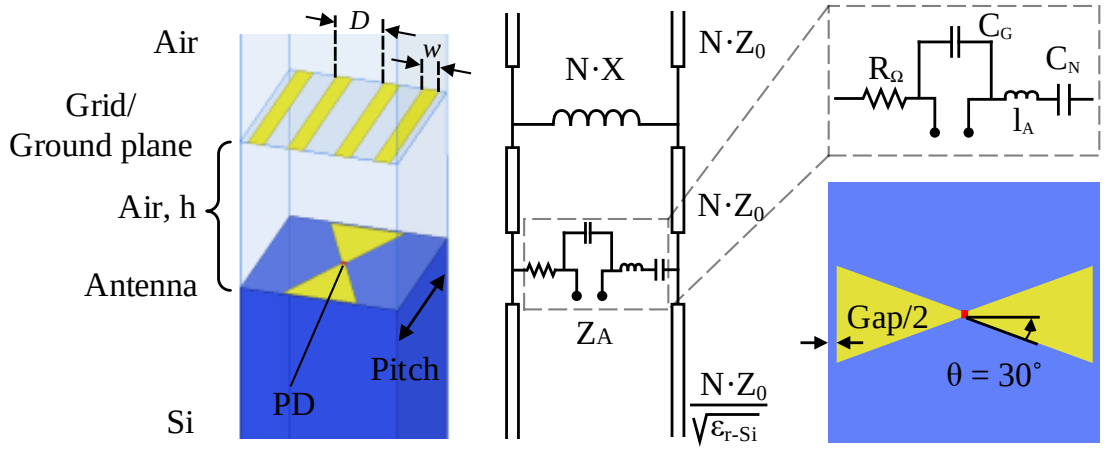

Figure 5.5 Left: geometry of the array unit-cell with the antenna at the interface and the reflector on the air side. Center-right: corresponding equivalent circuit, and antenna geometry.

useful for optimization [85], [184], or to develop insight on the nature of mutual coupling, as we have emphasized in Chapter 2. Generally, the equivalent circuits enable preliminary design parameters, whereas an accurate analysis of finite structures requires full-wave simulations [88, Ch. 2]. In this section, we explain the selected array geometry and the corresponding equivalent circuit. Next, we illustrate the impedance matching enhancement and the optimization of the unit-cell.

5.2.1 Array Geometry

Fig. 5.5 left shows the proposed unit-cell geometry. It is square with the antenna lying at the interface between air and silicon ($\epsilon_r = 11.9$ [188]) half-spaces. At a distance h from the interface, a conductive grid or ground plane reflector is introduced to assist in conjugate matching the antenna and PD impedance. We will consider the cases where the reflector is either on the air or on the Si side. The pitch of the unit-cell equals $\lambda_{Si}/2 = 0.439\,\text{mm}$ (100 GHz), but other criteria are also possible. In this way, the onset of grating lobes occurs at 200 GHz for broadside emission, as can be verified using the grating lobe diagram of Fig. 2.2.

Fig. 5.5 right shows the antenna geometry. It is defined by the semi-bow angle, $\theta = 30°$ in this case, and by the gap with the neighbor antenna. In Section 2.5, we have shown that the current distribution is drastically different for arrays of connected and disconnected dipoles, and so is the impedance. In a practical array realization, we can expect around four elements, so we have opted for a gap that produces a current similar to disconnected dipoles. In this manner, the predictions of the infinite array will resemble more the finite case. Conversely, given that the antenna resonant length is $\lesssim \lambda_{\text{eff}}/2$, with $\lambda_{\text{eff}}/2 = 0.59\,\text{mm}$ (100 GHz) (see Fig. 2.12 and Fig. 2.13), for matching purposes, it is convenient to design the antenna longer, with the smallest gap possible, to push to the lower frequencies the capacitive behavior.

We have selected a $10\,\mu$m gap, which provides a good trade-off between the two aspects discussed above. We have verified that this gap yields the desired behavior by simulating a dipole antenna ($\theta = 0°$). At resonance, the current at the extreme is 1/30 that of the feed point, which approaches substantially to the isolated case.

The antenna is processed in $0.6\,\mu$m-thick gold, whose conductivity is $\sigma = 2 \times 10^7$ S/m [189]. This value is lower than the conductivity of bulk gold ($\sigma = 4.1 \times 10^7$ S/m) due to the deposition of a thin-film and to the lower conductivity of the Ti layer used to bond the gold to the semiconductor substrate [189] (not considered in the simulation). Standard deposition thicknesses usually range between $0.15\,\mu$m and $0.35\,\mu$m. However, since gold depositions of up to $1\,\mu$m thickness have been also demonstrated [190], the chosen thickness is somewhat higher than the standard to reduce ohmic losses. Last, the antenna is fed by an ideal lumped port with identical amplitude and phase (for broadside radiation) with dimensions $10\,\mu\text{m} \times 10\,\mu$m, which is comparable to the footprint of a UTC-PD [63].

For actual implementation, the antenna and the PD would be grown on an InP substrate ($\epsilon_r = 12.5$) [52]. Since the thickness of such a layer is unknown, we have not included it in the simulation. However, the relative permittivities of InP and Si are only slightly different, and changes on the unit-cell geometry would be small.

Finally, it is worth mentioning that we have carried out all simulations of the unit-cell with ANSYS HFSS [91] on a similar set-up to that presented in Section 2.6. Master/slave boundary conditions are enforced to the lateral walls, and radiation boundaries truncate the top and bottom half-spaces.

5.2.2 Equivalent Circuit

Fig. 5.5 center-right shows the equivalent circuit. The authors of [85] presented a similar one, but it was intended for short antennas ($\lambda/10$) that are well described by lumped circuit elements. Nevertheless, in Chapter 2, we have seen that a lumped element circuit composed of a series RLC in parallel with a capacitor can still model distributed effects in the dipole impedance (Fig. 2.10b). The parallel capacitance is represented in the circuit of Fig. 5.5 by C_G, the series LC elements are represented by l_A and C_N respectively, and R_Ω has been included to account for ohmic losses. In addition, in the equivalent circuit of Fig. 2.10b, it can be seen that R is proportional to $Z_1||Z_2$ for a semi-infinite interface. Then, the two half-spaces are modeled in the circuit of Fig. 5.5 by the shunt of semi-infinite transmission lines where N is the proportionality factor, and the shunt is connected in series with l_A and C_N to give the series RLC. Finally, since the radiated plane wave propagates along the multilayer structure as a TEM wave on equivalent segments of TL, we have included X in the circuit to model the reflector impedance. It is important to note that we assume that the half-space not backed by the reflector extends to infinity and produces no reflections.

In general, the reflector is a grid defined by its period, D, strip width, w, and orientation.

For dipole-like antennas that radiate in linear polarization, X is capacitive if the grid is cross-oriented with the antenna. Conversely, the grid is inductive for a co-oriented dipole, and it takes the value [98]:

$$L = \frac{Z_0}{2\pi c D} \ln\left(\frac{1}{\sin\left(\frac{\pi w}{2D}\right)}\right). \tag{5.6}$$

The reason for introducing the grid is because it is a generalization of a ground plane and it can also be used to fine-tune the impedance matching efficiency. Besides, from a practical point of view, the fact that parts of the grid are optically transparent would ease alignment, PD inspection, or even enable photodiode top-illumination. In the following, we will consider the limiting case where $w = D$ and the grid becomes a ground plane.

To better understand the effect and optimum position of the reflector, we have used the equivalent network in Fig. 5.5 to compute the contribution of a ground plane to the antenna impedance, Z_A. Neglecting the parameters within the dashed box of Fig. 5.5, one can write for the reflector on air:

$$\frac{Z_A}{N} = Z_{\mathrm{Si}} || \mathrm{j} Z_0 \tan(\beta h) = \frac{Z_0 n_{\mathrm{Si}} \tan^2(\beta h) + \mathrm{j} Z_0 \tan(\beta h)}{1 + \epsilon_{r-\mathrm{Si}} \tan^2(\beta h)}, \tag{5.7}$$

where β is the propagation constant of a plane wave in free space. Equation (5.7) is plotted in Fig. 5.6a for $N = 1$, whereas Fig. 5.6b presents Z_A when $N = 1$ and the ground plane is on the Si side. The curves indicate that the ground plane contributes inductively to the antenna impedance if placed at a distance $h < \lambda/4$, where λ is the wavelength in air or Si, depending on which side the ground plane is located. Thus, it can be used to compensate the capacitive reactance of the UTC-PD for conjugate matching. Furthermore, for a close distance to the interface ($h/\lambda < 0.07$ or $h/\lambda < 0.17$ for air and Si respectively), the radiation resistance is lower than without a backing reflector. This feature also contributes to a more efficient impedance matching since the PD resistance is typically a few Ohms, as we have indicated in the introduction. Lastly, at the interface, the ground plane impedance is seen as $\mathrm{j} Z_0 \tan(2\pi h/\lambda)$, a periodic function of h. Even if multiple (infinite) equivalent positions exist for a given frequency, wideband operation requires to reduce impedance variations with frequency, and the lowest period is taken.

5.2.3 Array Synthesis

To calculate Z_A using the equivalent circuit in Fig. 5.5, one must determine first the values of the rest of the elements, namely: C_A, C_G, l_A, R_Ω, and N. In Chapter 2, we have seen that it is possible to retrieve them analytically for a thin dipole. However, the model fails to predict them accurately for wide dipoles ($> \lambda/25$). Then, the simplest is to obtain them running a full-wave simulation when the antenna lies in the interface without the reflector. Afterwards,

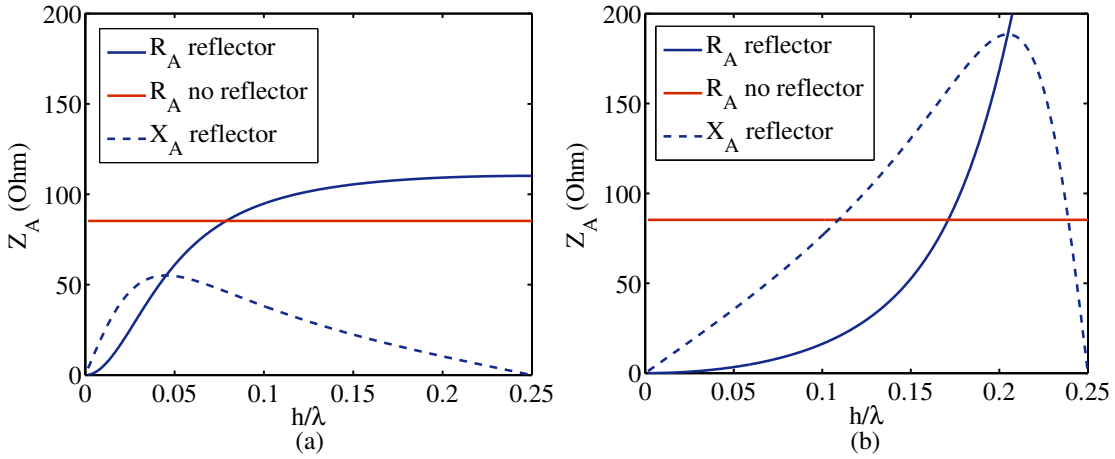

Figure 5.6 Contribution of the reflector to the antenna impedance versus reflector height in wavelengths for $N = 1$. (a) reflector on air, and (b) reflector on Si.

their values are adjusted so that the equivalent circuit impedance fits the simulation results. In addition, R_Ω is adjusted to fit the radiation efficiency at 100 GHz. Table 5.1 shows the optimal values for a gap = 10 μm, and $\theta = 30°$, valid between 50 GHz and 150 GHz.

Table 5.1 Equivalent circuit parameters for the antenna defined by semi-bow angle $\theta = 30°$ and gap = 10 μm at a silicon-air interface.

C_N (pF)	C_G (pF)	l_A (nH)	$R_\Omega(\Omega)$	N
5.19×10^{-2}	5.54×10^{-3}	0.0692	2.75	0.669

After determining the values for the discrete circuit elements, it is simple to calculate Z_A, the radiation efficiency, and ultimately the radiated power when the reflector is included the structure. We maximize the radiated power at 100 GHz sweeping the ground plane position along h. The radiated power (per antenna) is calculated using (5.5), and the PD impedance used in the computation is that represented in Fig. 5.1. Fig. 5.7 and Fig. 5.8 show the optimum results for the reflector on the air and on the silicon side, respectively.

The optimum position of the reflector on the air side is $h = 95\,\mu$m, which corresponds to $h/\lambda = 0.032$. The inductive contribution of the reflector is limited, and conjugate matching the reactance is only possible around 117 GHz. Therefore, the optimum position occurs near the maximum inductive contribution (see Fig. 5.6a). As a consequence, the improvement in the matching efficiency with respect to a 72 Ω antenna is limited to ×2.6. The improvement in the radiated power is ×2.3 per antenna at the target frequency, with a 3 dB bandwidth of 42% (using the simulated curve).

In general, the calculated results are in agreement with full-wave simulations (Fig. 5.7b-d). It is important to note that we have neglected the interaction of the reflector with the reactive

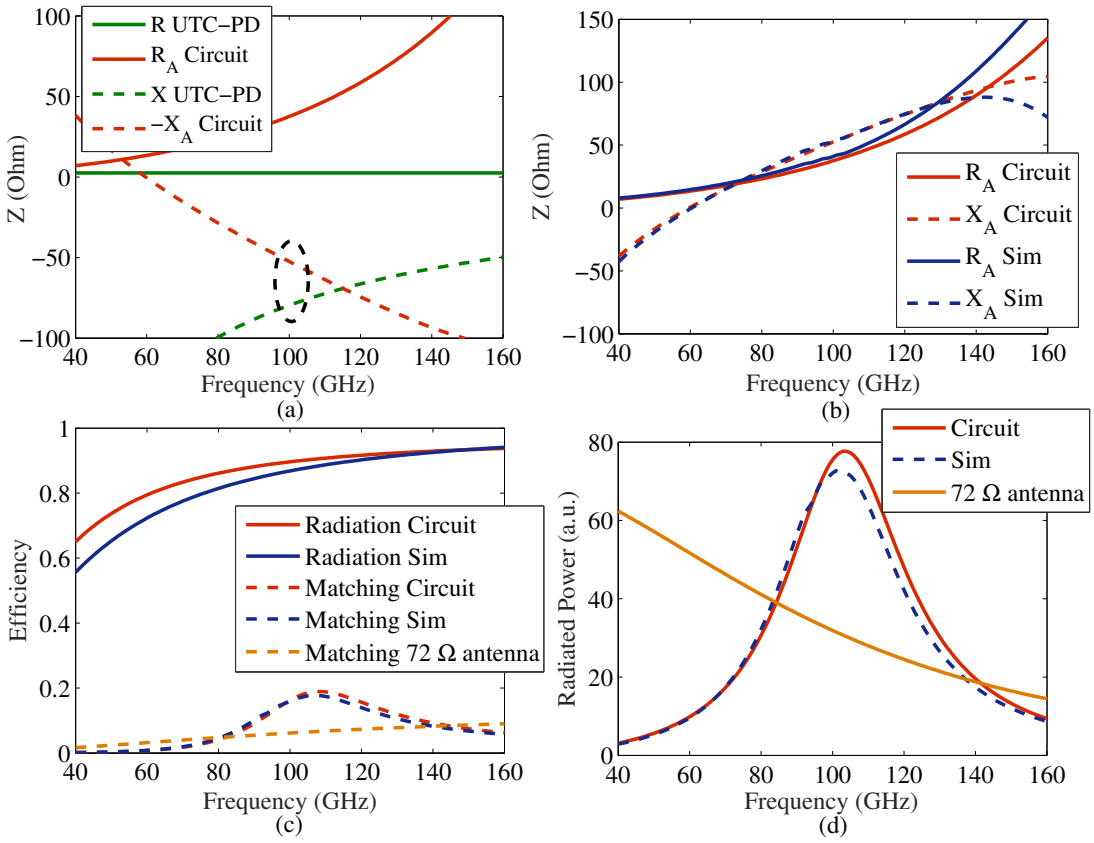

Figure 5.7 Optimal solution for the reflector on air. (a) impedance of the UTC-PD and of the antenna, (b) simulated and calculated antenna impedance, (c) matching and radiation efficiency, and (d) optimum power radiated and compared to a 72 Ω antenna.

fields of the antenna. We have also assumed that the current distribution is not modified by the presence of the reflector. These two aspects cause some deviation between simulated and calculated results. In particular, they cause the antenna anti-resonance to shift towards lower frequencies.

Fig. 5.8 shows the optimum results when the reflector is on the silicon side. In this case, the inductive contribution of the ground plane is higher than in the air case (observe Fig. 5.6a,b), but at the cost of a steeper reactance curve and consequently a narrower impedance matching. Also, Fig. 5.8 shows that ohmic losses can compromise the radiated power if the radiation resistance is low $\lesssim 10\ \Omega$, hence opting for the thicker gold before. The optimum position occurs for $h = 85\,\mu$m ($h/\lambda = 0.1$), with a matching improvement of $\times 5.78$. The emitted power per antenna is 4.38 times higher at 100 GHz than a reference 72 Ω antenna for the same photodiode current, and the 3 dB relative impedance matching bandwidth is 15%. All the previous values have been extracted from the simulated curves.

In principle, other dipole-like antenna shapes could be considered in the method above to further optimize the emitted power and bandwidth. Thin dipoles have been ruled out

because they present a pronounced resonant impedance curve that would be largely affected by the inclusion of bias lines to polarize the PDs and by manufacturing tolerances. Besides, the equivalent circuit was demonstrated rigorously for linear antennas. It can still be used for moderate semi-bow angles ($\theta \approx 30°$), but antennas defined by larger angles present an impedance curve that cannot be followed by the circuit, and the predictions are less and less accurate.

Last, it is worth pointing out that previous works have analyzed the limits of impedance matching [191] and matching limits for infinite arrays over a ground plane [192]. Since we deal with a trade-off between matching and radiation efficiency, such works have not been considered in the analysis.

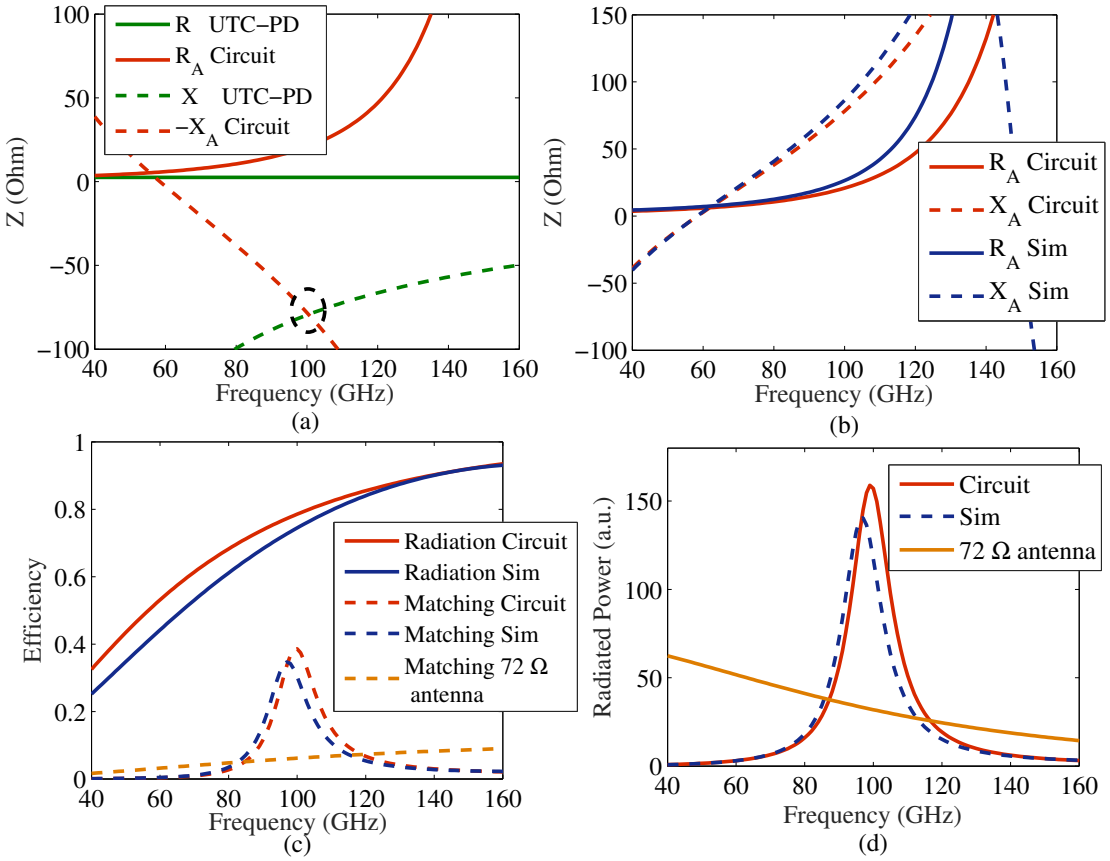

Figure 5.8 Optimal solution for the reflector on silicon. (a) impedance of the UTC-PD and of the antenna, (b) simulated and calculated antenna impedance, (c) matching and radiation efficiency, and (d) optimum power radiated and compared to a 72 Ω antenna.

5.3 Finite Array

In this section, we present the design of a finite array using the preliminary layout obtained in the previous section with the equivalent circuit. The bibliography indicates that it is

challenging to illuminate more than a few elements efficiently. Therefore, we have selected a 2×2 array as a feasible solution.

In the previous section, we have seen that an infinite array printed on a grounded silicon slab can increase more than four times the power radiated by each antenna element compared to a self-complementary antenna, for the same UTC-PD as source. For an infinite broadside array, the radiation pattern is a plane wave propagating in the direction normal to the interface, as we saw in Chapter 2. In this case, no power would be lost to surface waves in the grounded silicon slab. However, a 2×2 array with an electrical size of $\approx \lambda_{\mathrm{Si}} \times \lambda_{\mathrm{Si}}$, will not radiate a plane wave, and it is necessary to examine how much power could be lost to surface waves [193]. Curves representing the fraction of radiated power lost to surface waves versus substrate thickness were given in [194, Fig. 37(d)] for an infinitesimal dipole on a grounded slab of $\epsilon_r = 12$. When the slab is of infinite thickness, the problem becomes a Hertzian dipole on a semi-infinite interface. In this case, the ratio of power radiated towards the silicon to air is approximately $\epsilon_r^{3/2}$ [165], [193]. However, for a thin slab, as in our case ($h/\lambda_0 = 0.03$), where only the fundamental TM_0 surface wave mode can propagate, the power coupled to this mode is negligible. This encouraging result justifies the method with arrays of finite size as long as the ground plane is close to the interface. This approach would remove the silicon lens that is lossy and can produce high reflections at the silicon-air interface, unless an anti-reflection coating is used. Nevertheless, our target is to compare the proposed solution to classical antennas, such as those in [151], [179]. Hence, we will continue our investigation for the case where the ground plane is on air and a silicon substrate lens will remove unwanted surface waves [193].

In the infinite array optimal solution with the ground plane on the air side (Fig. 5.7), one observes the antenna reactance does not compensate for the PD capacitance at 100 GHz. In this case, the ground plane inductive contribution is smaller than in the case where it is on the silicon side, for which compensation is possible and a better impedance matching efficiency is achieved. In addition, one can observe that the antenna is electrically small: the array pitch is $\lambda_{\mathrm{Si}}/2$, whereas the resonance for a thin dipole occurs approximately at $\lambda_{\mathrm{eff}}/2$. That is, there is a factor $n_{\mathrm{Si}}/n_{\mathrm{eff}} = 1.36$ of difference. If the resonance occurred at lower frequencies, the dipole would present a higher radiation resistance, which, in turn, would increase the inductive contribution of the ground plane, as can be deduced from (5.7). By proceeding in this way, it will be possible to compensate to a larger extent the PD reactance.

To decrease the resonance frequency, the inner arms of the dipoles are connected, as shown in Fig. 5.9. Resorting to the asymptotic current approximation of Chapter 2, one can derive the reactance of two centered-fed, thin dipoles of length l each, where their inner arms are connected. The reactance reads:

$$X \propto -\frac{1}{\tan(\beta l)}. \tag{5.8}$$

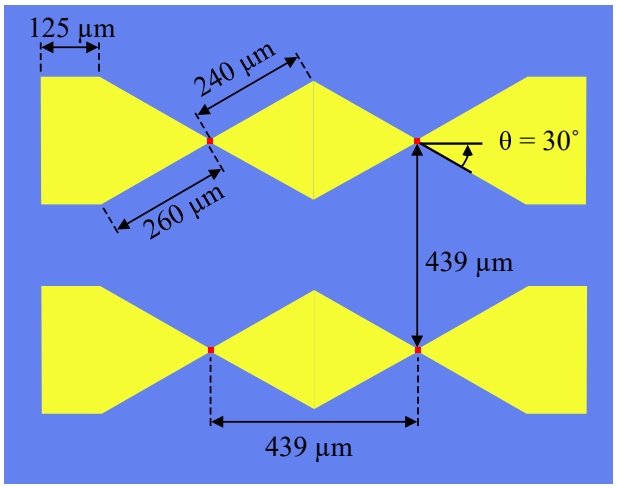

Figure 5.9 Optimal geometry for the array on a semi-infinite interface, with the ground plane at $h = 60\,\mu$m from the interface.

Interestingly, when one arm is connected with the other disconnected, the resonant frequency occurs for a dipole length $l = \lambda/4$, which lies just in the middle between the resonant frequency for both arms disconnected (dipole length equals $\lambda/2$) and for both arms connected ($l = 0$).

To synthesize the 2×2 array from the infinite array unit-cell, we first connect the inner dipole arms in the finite array. In line with lowering the resonance frequency, the outer arm is made also longer, whereas the array pitch and θ are maintained. Fig. 5.9 shows the optimal geometry that maximizes the radiated power at 100 GHz while keeping a 3 dB bandwidth $> 30\%$. For the optimization, we have swept the following variables: the oblique length of the outer arm between $240 - 280\,\mu$m ($240\,\mu$m was the value for the unit-cell), the horizontal length added between $0 - 200\,\mu$m in $25\,\mu$m steps, and the height of the ground plane between $50 - 95\,\mu$m with $5\,\mu$m steps ($85\,\mu$m was the initial value).

Fig. 5.10c shows the power radiated by one of the antennas of the array as calculated from (5.5). The curves correspond to the ground plane nominal height ($60\,\mu$m) and to deviations of $\pm 5\,\mu$m to assess the robustness of the solution against manufacturing tolerances. Fig. 5.10c shows also the radiated power for a self-complementary 72 Ω antenna, and the matching method in [51]. In Fig. 5.10a, it is important to note that, unlike for the infinite case, the modified antenna shape achieves compensation of the PD capacitance very close to 100 GHz. As for the radiation efficiency, it is still close to 1. Then, there is room for improvement to increase impedance matching with a lower radiation resistance. Noteworthy, compared to the case of a self-complementary antenna, each antenna in the array radiates power that is a factor 3.67 (5.7 dB) higher at 100 GHz. Combining the power of the four antennas, the total increase would be more than 11 dB, with a 30% −3 dB bandwidth. The improvement of radiated power per antenna is comparable to that obtained with resonant antennas (three to four times) [179], but in this case, we double the −3 dB power bandwidth, not to account

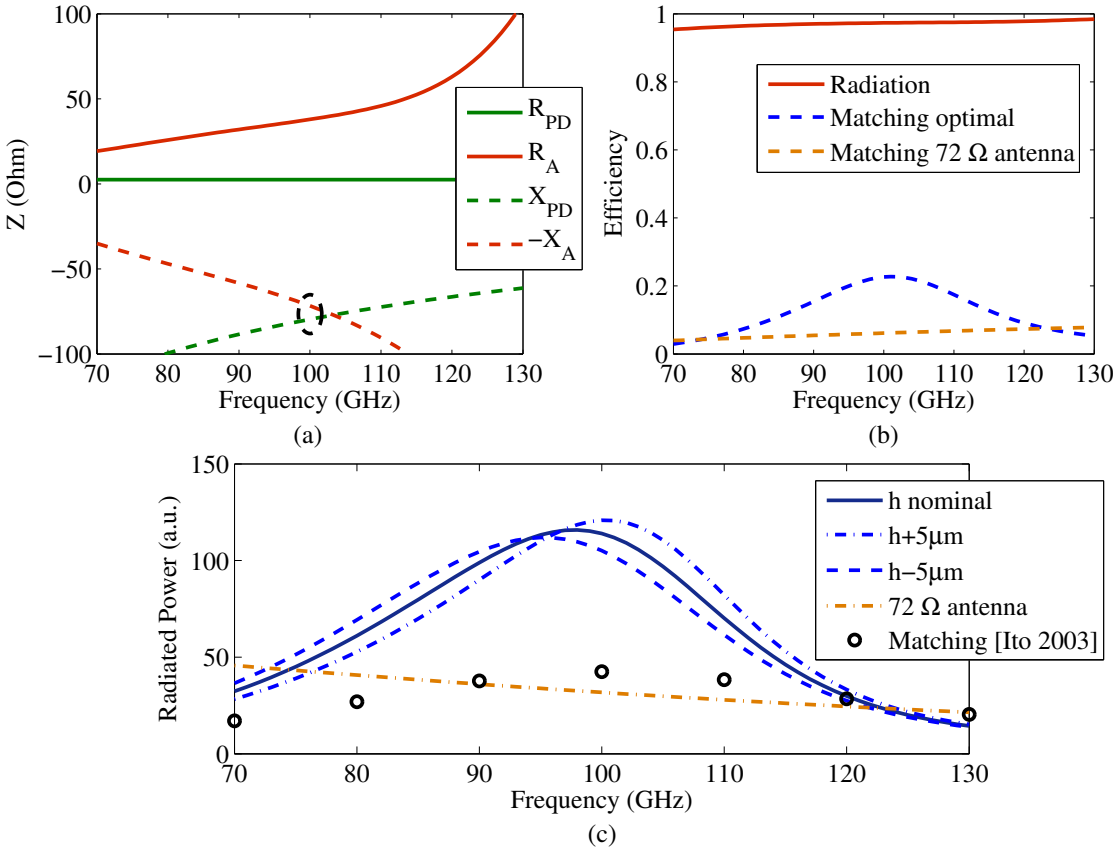

Figure 5.10 Curves calculated with the optimal geometry: (a) antenna and UTC-PD impedance. (b) matching and radiation efficiency, and matching efficiency for an ideal 72 Ω antenna. (c) radiated power at the nominal h of the ground plane, at $h \pm 5\,\mu$m, radiated power of an ideal 72 Ω antenna at the same photocurrent, and calculated for the matched solution in [51].

for the 6 dB extra due to the 2×2 array configuration. Also, compared to highest increase calculated in [51, Fig. 3], the improvement is 2.0 times larger, and the solution of [51] also features a slightly lower bandwidth (25%).

Finally, it is worth mentioning that bias lines to polarize the PDs have not been included in the design. Indeed, reverse-biasing the PDs is necessary to obtain a photocurrent proportional to the incident optical power. For antennas whose arms are electrically connected, a biasing scheme similar to that presented in [174, Fig. 9] could be used. An inductive choke should be included in the design to polarize the PDs, and to avoid the RF signal leaking through the bias lines. The choke design would be used as a design variable as in [179], [189] to optimize further the antenna impedance and, for instance, increase the impedance bandwidth.

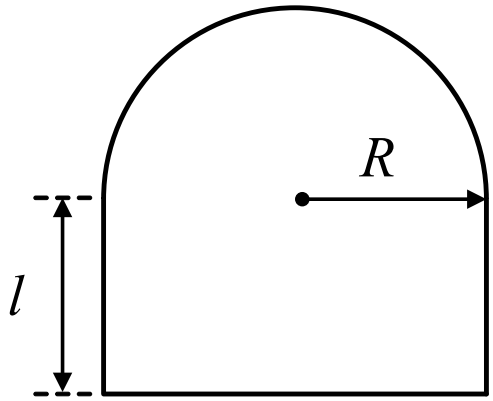

Figure 5.11 Schematic of an extended hemispherical lens.

5.3.1 Far Field

After showing in the previous section the potential enhancement of radiated power by the array, in this section, we will examine the primary array pattern (the radiation pattern at each half-space) and the pattern when a silicon substrate lens is included.

It is well known that printed antennas on semiconductor substrates of finite thickness suffer from power lost to substrate modes. Indeed, it can be estimated from [165] that, for a resonant dipole at an air-$\epsilon_r = 12$ interface, more than 50% of power is radiated towards the substrate beyond the critical angle ($\theta_c = 17°$). This power would be trapped in the semiconductor substrate due to total internal reflection. Therefore, it is customary to terminate the semiconductor substrate in an extended hemispherical lens to preclude this effect [194], [195]. Such a lens is composed of a hemisphere of radius R and a cylinder of the same radius and length l, as shown in Fig. 5.11.

Fig. 5.12 shows the primary array patterns for the proposed structure in the E- and H-planes together with the patterns of a resonant dipole and of a self-complementary bow-tie, all at 100 GHz. To obtain these patterns, we need to recall that the Finite Element Method (FEM), as implemented in HFSS, calculates radiation patterns only for a homogeneous medium, so it is not possible to retrieve them accurately when the antenna lies at an interface [196]. Instead, we have used the Integral Equation (IE) solver to obtain the patterns for the resonant dipole and for the bow-tie. The IE solver solves the currents on the model surfaces with a MoM using the Green's function of the dielectric half-space. Conversely, for the array backed by an infinite ground plane, we keep the FEM solver because the radiation is towards a homogeneous medium.

For the sake of validation, in Fig. 5.12a, one can note that the shape of the radiation patterns in the principal planes of a resonant dipole is in good agreement with the results reported in [165]. The slope discontinuities at the critical angle in both cuts of the radiation pattern are a mathematical artifact resulting from the stationary phase method used to compute the

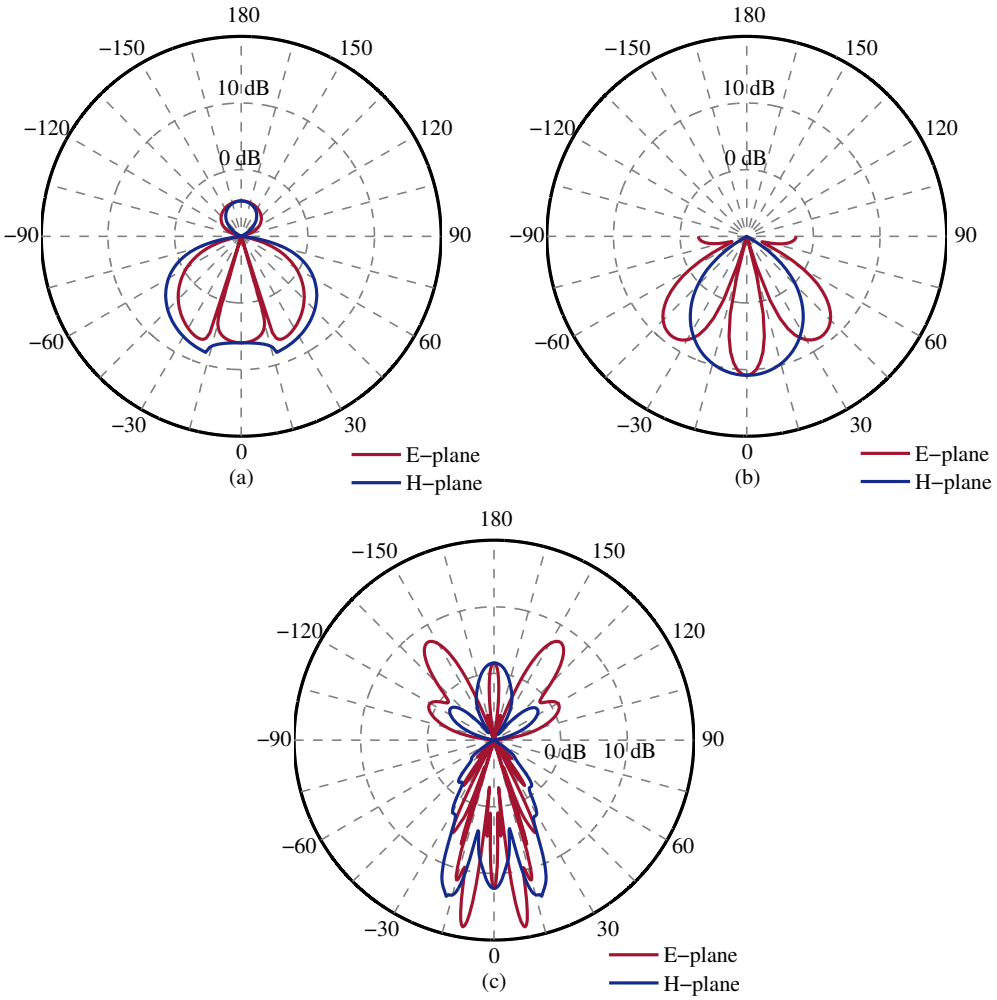

Figure 5.12 Radiation pattern in the principal planes of the antenna printed at the interface of silicon-air half-spaces for (a) resonant half-wavelength dipole, (b) array, and (c) self-complementary bow-tie with arm length of 2.5 mm.

far-field [197]. Fig. 5.12b shows the array pattern at the principal planes. It presents a behavior similar to the resonant dipole, but it is more directive due to the larger electrical size of the array. To illuminate a lens, reducing the H-plane beamwidth would be preferred to get a symmetric pattern. It could be accomplished by including more elements along this plane to obtain, for instance, a 3×2 array. Alternatively, the E-plane pitch could be reduced. One can also observe from the simulated E-plane patterns that the phases of the electric field for the main lobe and side-lobes are in quadrature (not shown here). This is better than the π phase difference observed in other antennas, such as long-wire antennas when considering them as feeds since they produce a more uniform illumination [193]. Finally, regarding the bow-tie pattern, it peaks off-broadside, also noted in [181, Fig. 8], which makes it less attractive as a feed [181]. In particular, and depending on the extension length of the extended hemispherical lens, rays in the direction of the main lobes could be totally reflected and trapped by the lens

[195].

Next, we will examine the patterns when the array is integrated with an extended hemispherical substrate lens. Such a lens has been widely investigated [198]–[201], and it is not our target to provide an extensive lens optimization but rather to show that our proof-of-concept is suitable as a primary feed. Therefore, we will just present an instance of the structure. In particular, we need to verify that the lens does not image the different antennas of the array independently. Briefly, this occurs when the far-field of the individual elements imaged by the lens do not overlap substantially, given that the antennas are not located in the optical axis [64].

For the structure, we have selected a 500 μm-thick square substrate of 2.5 mm side. The lens diameter is 10 mm [32] with extension length of $l = 1.9$ mm (including the substrate thickness), larger than the hyper hemispherical lens extension length ($l = r/n = 1.4$ mm) [198] because it provides a more directive beam and lower side-lobes. In addition, we have added a $\lambda/4$ (100 GHz) anti-reflection coating conformal to the lens to reduce reflections at the silicon-air interface. Fig. 5.13a shows the pattern of the array in the principal planes, and Fig. 5.13b shows the corresponding for the self-complementary bow-tie. They have been obtained with the FEM solver of HFSS and a perfect magnetic conductor (PMC) symmetry plane to reduce the computation volume by a factor of 2. For the array, the directivity is 17.0 dBi and more than 80% of the power is contained in the main lobe. The E-plane shows sidelobes at -10 dB, which are attributed to the primary fields of the array (see Fig. 5.12b). The side-lobe level could be improved by introducing more elements in this direction, for instance. For the bow-tie, the directivity is 18.0 dBi, and the power contained in the main lobe amounts to about 75%, which is comparable to the array. The side-lobes at -8 dB for the H-plane are attributed to the primary fields of the bow-tie (see Fig. 5.12c).

It is worth pointing out that we have used the metric given by (5.5) to determine and compare the power radiated. A rigorous analysis would require a more in-depth examination of the patterns than the one carried out in this section. Pertinent methods for lens optimization and analysis were explained in [195], [198]–[201]. However, these aspects are beyond the scope of this chapter, intended to demonstrate a novel matching method.

5.4 Practical Considerations for the Array Assembly

In this section, we comment on a possible assembly of the 2×2 array, as shown in Fig. 5.14.

The first aspect is the optical excitation of the photodiodes. It could be achieved by illuminating the optical waveguide input with a lensed fiber, one at each side, as shown in the inset of Fig. 5.14. Next, the optical waveguide would be split by a multimode interference coupler and directed towards the two PDs by an S-bend. In [161], such a structure was reported, with measured insertion losses of about $3-4$ dB. This small loss could be easily compensated by an optical amplifier that should be included in any case to achieve the required optical

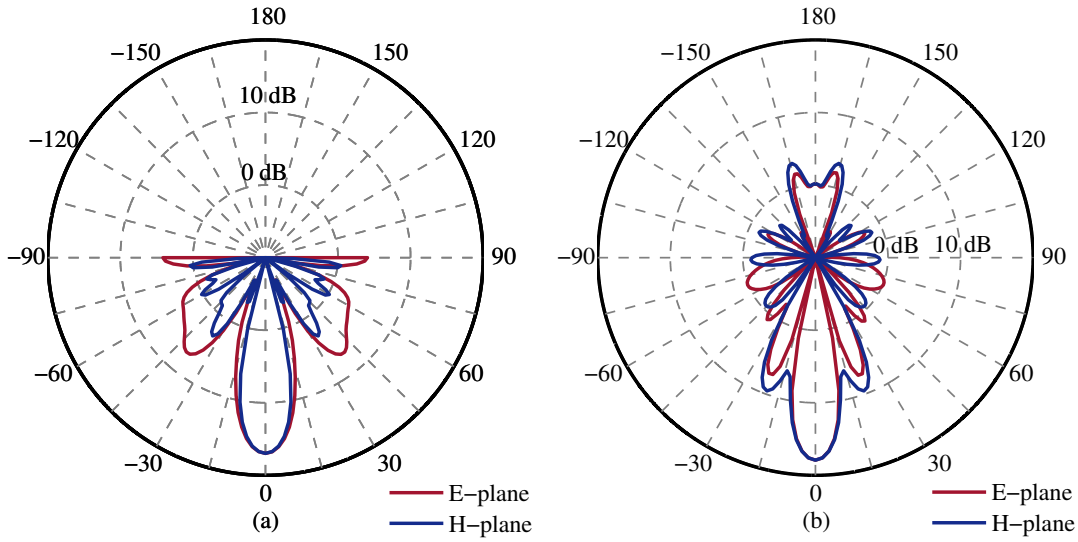

Figure 5.13 Radiation pattern in the principal planes for the antenna integrated with the anti-reflection coated silicon lens. (a) array, and (b) self-complementary bow-tie.

power per photodiode ($\approx 20-60$ mW). The fact that there is one lensed fiber per side instead of two is advantageous to integrate and to optimize the illumination. Besides, it would allow us to get rid of two optical time delays to control the phase at each fiber [64].

The reflector could be either a ground plane or a closely spaced grid that resembles a ground plane printed on a quartz substrate using photolithography and metal lift-off. In the latter case, it would be partially transparent for alignment and/or inspection. To control the reflector height a spacer (see gray blocks in Fig. 5.14) should be included. It could be realized in silicon and fixed to the lens with SU8 epoxy. The critical metric for the spacer would be its height, in our example a tolerance of $\pm 5\,\mu$m would be required. To obtain the desired one, the silicon wafer could be gradually etched or polished. Its height would be monitored with, for instance, a scanning electron microscope (SEM), or an interferometer-based method whose accuracy is better than $0.2\,\mu$m [202], until the height difference to the array chip corresponded to h. Using the height difference for the spacer instead of h would avoid integrating a thin ($h < 60\,\mu$m) silicon membrane more challenging to fabricate and handle.

5.5 Conclusions of the Chapter

In this chapter, we have developed an array design that aims at enhancing the power emitted by a mm-wave photonic transmitter. The review of the state-of-the-art points at two possible directions to reach this goal: one is to integrate several antennas in an array configuration, and the other consists in increasing the matching efficiency between the UTC-PD and the antenna. Our approach constitutes a hybrid of the two previous ones: a design method for an array of antennas efficiently matched to UTC-PD.

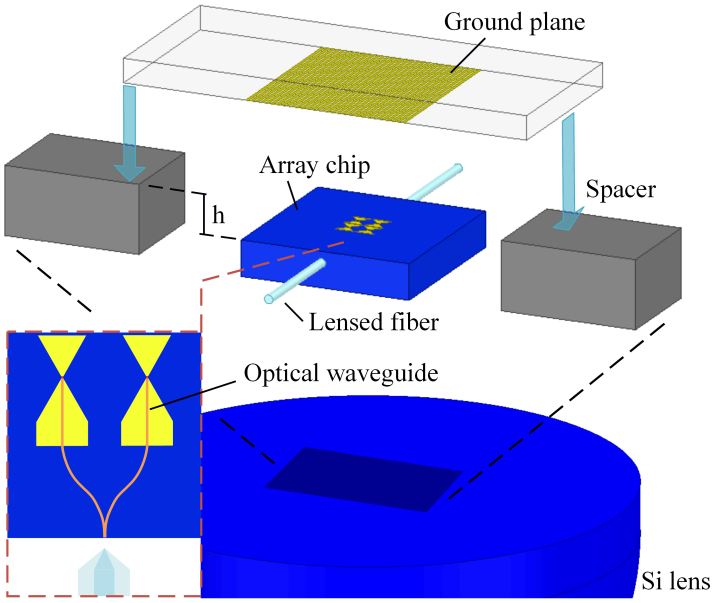

Figure 5.14 Schematic with the proposed integration of the different elements.

To accomplish it, first, we have used the infinite array approach to show how a ground plane placed close to the antenna array contributes inductively to the antenna impedance, also decreasing the radiation resistance. Next, we have used a circuit equivalent to predict accurately the array radiated power, and we have optimized the distance of the array to the ground plane. Then, we have moved to a 2×2 array architecture, and we have maximized the radiated power. Finally, we have shown the radiation patterns when the array was integrated with a silicon substrate lens, and we have presented a possible solution for the array assembly. Compared with classical self-complementary antennas, the array enables more than an 11 dB peak increase in the radiated power, whereas the matching method performance offers more potential than others reported in the bibliography (shorted-stub matching circuit or resonant antennas). While the design shows promising results, we acknowledge that a fabrication run can take substantial time, as well as being costly. Therefore, we are currently looking for funding, hoping that this research line can move soon to the fabrication and testing stages.

Before a fabrication run, a more sophisticated array design should couple the optimization of the radiation patterns and radiated power (e.g., using the fields calculator functionality in HFSS). In this proof-of-concept, the array pitch, number of elements, or the inclusion of an RF choke are degrees of freedom not explored yet, and they could further improve the array performance.

Last, it is worth pointing out that even if the method offers more bandwidth than the other techniques, the matching efficiency improvement comes at the cost of reduced bandwidth. Nevertheless, the system could find applications in many of the demonstrations that focus on a particular frequency range for spectroscopic studies or imaging, as in[43], [128], [163], to

mention a few. Besides, the matching bandwidth is wide enough for telecommunications, so it could be used to remove the problem of alignment of fixed links, given that the array also offers the possibility of beam steering. The steering capabilities would be enhanced by replacing the silicon substrate lens by an array of dielectric rod waveguides (DRW), with one DRW coupled to each antenna [203]. The silicon lens tends to produce a collimated beam parallel to the optical axis, therefore, it counteracts beamsteering. This effect would not occur if each antenna was integrated with a DRW, ultimately resulting in better beamsteering performance.

The main original contribution of this chapter is the method to obtain near conjugate matching to UTC-PDs using a closely placed reflector. In addition, the equivalent circuit presented in Section 5.2 to synthesize the infinite array is original and stems from our previous analysis on infinite arrays of dipoles in an earlier chapter. The circuit is similar to others used in the bibliography but it is also valid for dipoles whose length is comparable to the resonant length.

6

Photonic Tx Based on a Leaky-Wave Antenna for 1-D Beam Steering in Reconfigurable Wireless Links

In the previous chapters, we have considered array theory and, in particular, how to achieve efficient impedance matching in antenna arrays integrated with UTC-PDs. In this chapter and the next one, we adopt a more pragmatic approach designing and prototyping antenna arrays integrated with available chips of PDs for beam steering. In the context of wireless communications, we have seen that this feature would be instrumental for overcoming some of the limitations arising from line-of-sight (LoS) links, such as reconfigurability, tracking, or fine-alignment. The main part of this work was carried out during a 6-month stay at University Carlos III de Madrid (UC3M), and it is based on [i], [iii], and [viii] from the List of Publications.

In summary, we report one of the first leaky-wave antenna (LWA) arrays integrated with photodiodes at mm-/sub-mm-wave frequencies. The designed LWA array is manufactured in printed circuit board (PCB) technology and works at the E-band (from 75 to 85 GHz). The antenna element consists of a microstrip line periodically loaded with stubs, and it has been designed employing a hybrid approach combining full-wave simulations and transmission line theory. This approach enables period optimization when the open-stopband of the LWA is mitigated or removed at the frequency of broadside emission. The antenna provides a directive beam of about 18 dBi with a frequency scanning span of 22°, but it was truncated after four periods due to experimental constraints. The LWA composed of 19 periods featured a simulated half-power beamwidth as narrow as 4°. First, the fabricated prototype was tested using a ground signal ground (GSG) probe, and the measured return loss and radiation patterns were in good agreement with full-wave simulations. Then, the LWA array was integrated with the photomixer chip. Measurements of the radiated power yielded a maximum of 120 μW at 80.5 GHz for a 9.8 mA photocurrent. Finally, the antenna was used in a 25 cm wireless link, obtaining a 2.15 Gbps error-free data rate and demonstrating live transmission of HD video (1.5 Gbps).

6.1 Introduction

Mm-wave systems based on photonic technologies benefit from reusing reliable and cost-effective optical components such as Erbium-doped fiber amplifiers (EDFAs), semiconductor optical amplifiers (SOAs), switches, or time delay lines. It is relatively simple to develop a homodyne detection system where the same beat note is split by an optical coupler to emit and detect the mm-wave signal. Examples exploiting these features include the all-photonic systems of [45], [204]. Besides, due to the seamless integration with fiber optics, photonically-excited antennas are commonly used in wireless links at terahertz and mm-wave frequencies with multi-Gbps data throughput [30], [102], [205], [206]. Photonic transmitters typically use on-chip antennas [207] as reviewed in Chapter 5, horns [208], horns as feeds of quasi-optical (QO) systems [168], [209], and, less commonly, alternatives such as tapered slot antennas [205], or the monolithically integrated transverse electromagnetic horn, also reviewed in Chapter 5 [210]. In general, these antennas present a challenging escalation towards arrays [62], [211]. We will examine later the types most commonly used in wireless links.

The difficulty of integrating several photodiode-excited antennas has obstructed the development of arrays with beam steering capabilities, and just a few demonstrations can be found in the open literature [61], [63], [64], [212]. Beam steering would extend the range of applications of this kind of antenna. Among possible use cases, to name a few, one can find imaging systems, fine beam alignment to compensate mast misalignment or twist and sways from mounting structures [57], reconfigurable wireless links in data centers [213], or even a radar system [204].

The development of photomixer-excited antennas with beam steering could unlock the use of the E-band (71-76 GHz, 81-86 GHz), which presents several advantages. It offers a little licensed 2 × 5 GHz bandwidth, adequate for tens of Gbps of data transmission; it does not feature the absorption peak of oxygen compared to the 60-GHz band, and the FSL is lower than at higher sub-mm-wave frequencies.

The availability of low-loss, thin, inexpensive substrates well adapted to this frequency range makes printed circuit board (PCB) technology a promising approach to develop photonic transmitters/receivers (Tx/Rx). Active components with complex polarization networks can be integrated with passive components in a single multilayered board, as in [214].

To the best of our knowledge, the work presented in this chapter is the first realization of a leaky-wave antenna (LWA) integrated with photodiodes as a simple means to steer the beam with frequency in 1-D at mm-wave frequencies. The LWA is printed using PCB technology following a similar integration process as [205]. It works at the upper window of the E-band, and it could find applications in some of the cases cited above. In particular, automatic alignment in LoS mm-wave links will be discussed in more detail here. The realized design features a fairly broad relative bandwidth (>10%) and allows a scanning range of 22°, including broadside. Moreover, the scalability of the presented layout is beneficial with respect to classical mm-wave antennas to combine several emitters and increase emitted power and or

directivity.

Section 6.2 describes antennas commonly used in wireless links and their limitations. In section 6.3, we describe the design of the LWA. The integration of the photodiode chip with the PCB is discussed in Section 6.4. Sections 6.5 and 6.6 present measurement results and a potential application, respectively. Finally, conclusions are drawn in Section 6.7.

6.2 Photonic Transmitters for Wireless Links

A module integrating a photodiode with a waveguide output is one of the main approaches to develop a photonic transmitter. An example has been shown in Fig. 4.7c,d. Fig. 6.1a shows another example. The modular architecture allows the addition of more waveguide modules such as an orthomode transducer (OMT) so that an antenna can transmit and receive in different polarizations [216]. To extend the upper-frequency range, the transition structure between the photodiode output and the waveguide suppresses higher-order modes [128]. The −3 dB power bandwidth achieved is between 15 – 35%, sufficient for many applications. This approach has been widely investigated and demonstrations range between 65 GHz up to 350 GHz [156], [168], [172]. Besides, the modules can include the matching circuit presented in Chapter 5 and an amplifier [168], [172]. It is also possible to include two photodiodes for power combining [172], [173].

In telecommunications, photonic transmitters of the waveguide type are the workhorse, typically combined with horn antennas, or with horns and QO systems for enhanced directivity [206], [216], [217]. In [168], the photodiode module with a horn antenna is assembled with a dielectric lens, referred to as Gaussian optics antenna (GOA), as shown in Fig. 6.1a. Gains of 37.1 dBi and 52.3 dBi are reported. These values of gain (>25 dBi) are required to compensate FSL in long-distance wireless links (> 100 m), as detailed before in Chapter 3. Alternatively, the horn illuminates a 54 dBi gain parabolic reflector to avoid lens dielectric loss [209].

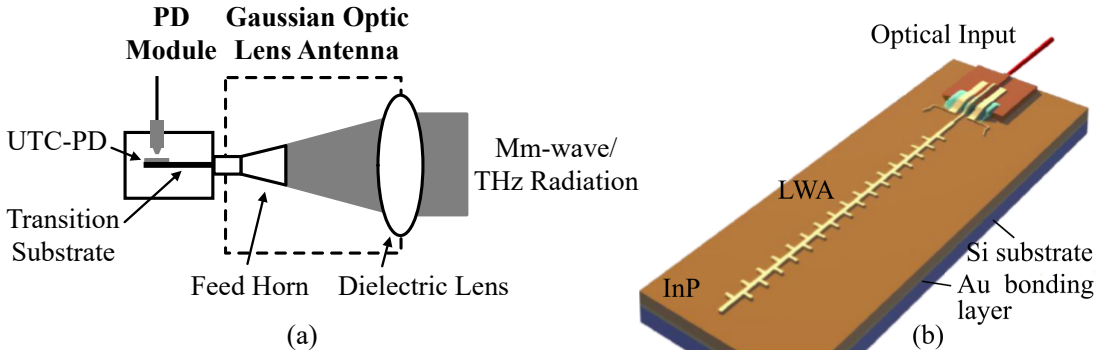

Figure 6.1 (a) Photonic transmitter of the waveguide type and Gaussian optics antenna, from [168]. (b) Terahertz LWA for monolithic integration with photodiodes, from [218].

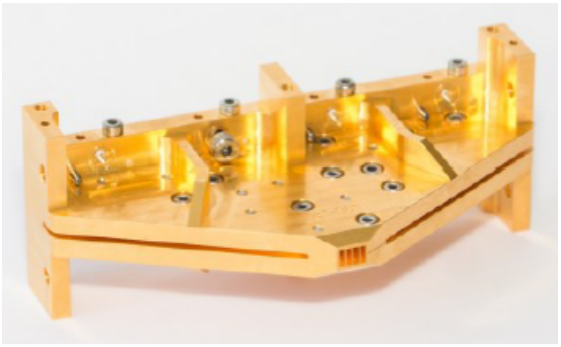

Figure 6.2 1 × 4 horn array for a phased array at 300 GHz, from [211].

The waveguide module features many advantages: it is rugged and modular, is a mature technology, and can be combined with QO systems, as commented above. Nevertheless, beam steering with this approach presents some issues. The first one is escalation since the waveguide size limits the minimal space between antennas. Fig. 6.2 shows a 1 × 4 array of pyramidal horns [211]. Due to the horn size and the required wall thickness for proper manufacturing, the array suffers from high sidelobes (at about −2 dB at 20° scan). To minimize the spacing the horn can be reduced to an open-ended waveguide. However, the gain of an open-ended waveguide is about 7.3 dBi, and it would be necessary to combine many elements (>10) to obtain a gain > 25 dBi. The second aspect is that the system complexity/cost would increase proportionally to the number of elements.

Alternatively, one finds well-known leaky-wave structures characterized by frequency-selective beam steering. Fig. 6.1b shows one instance of a LWA for monolithic integration with photodiodes. Since beam steering is achieved by sweeping the frequency, leaky-wave structures do not require beamforming networks. In addition, the structure can be designed several wavelengths long to obtain high directivities. For photonically-excited antennas, one photodiode suffices to steer the beam through a change in the laser emission wavelength. The speed of this tuning is 100 GHz/s [45]. In [219], a leaky-wave structure was used as a demultiplexer to separate two channels at 265 GHz and 320 GHz in a wireless transmission experiment. Another example includes the photonics-based radar system of [220] (also demonstrated in a wireless communications link). The characteristic feature of leaky-wave structures makes them an attractive candidate for applications where a steerable beam is of more importance than the data rate, such as to separate channels in the example above, for flexible interconnects, or radar systems [204], [219], [220].

In the remaining part of the chapter, we describe a LWA integrated with photodiodes for 1-D beam steering at mm-wave frequencies.

6.3 Leaky-Wave Antenna Array

The antenna design is motivated by the necessity of increasing the emitted power by a scalable layout, with beam steering capabilities, and a 10% relative bandwidth around the center frequency (81 GHz). One of the simplest beam steering methods is frequency steering with a 1-D periodic LWA. In this configuration, a traveling wave encounters periodic perturbations in one direction, so that it leaks progressively. If the electrical path between successive perturbations is such that the traveling wave encounters them in phase, the antenna will radiate a beam at or near broadside, as is clear from the array factor. Conversely, as frequency increases, the electrical path between elements will also increase, and the array factor will produce a beam moving from the backward to the forward quadrant [221].

Fig. 6.3 shows a top view of the proposed antenna, its different parts, and the unit-cell of the radiating section, all described in detail hereinafter. The geometrical features were printed on a grounded Duroid 5880 substrate ($\epsilon_r = 2.24$, $\tan\delta = 0.004$ at 60 GHz), suitable for high-frequency applications. At mm-wave frequencies, these values are a more exact determination of the relative permittivity than the typical values used ($\epsilon_r = 2.20$, $\tan\delta = 0.0009$ at 10 GHz) [222]. The chosen thickness is the minimum among the standards (127 μm) to minimize the radiation loss and the power lost to surface-waves of the different printed structures [223]. The antenna is excited by a 2 × 1 array of UTC-PD on InP. Each UTC-PD presents a 50-Ω grounded coplanar waveguide (G-CPW) output and feeds two rows of the array. They will be described in Section 6.4.1. The length of each row is truncated by a matched patch, where a longer row will feature a more directive beam. Additionally, this design is scalable in the direction perpendicular to the rows, so that more rows can be added. By controlling the number of rows and their length, one can easily accomplish symmetrical patterns (at E- and H-planes) or increase the directivity or the emitted power. In this respect, the proposed structure is advantageous to other classical mm/sub-mm wave antennas, such as horns or on-chip antennas with silicon substrate lenses, which are more challenging to escalate. The antenna was designed using a full-wave simulator (ANSYS HFSS, version 19.0.0 [91]) and equivalent network modeling for fast and preliminary layouts.

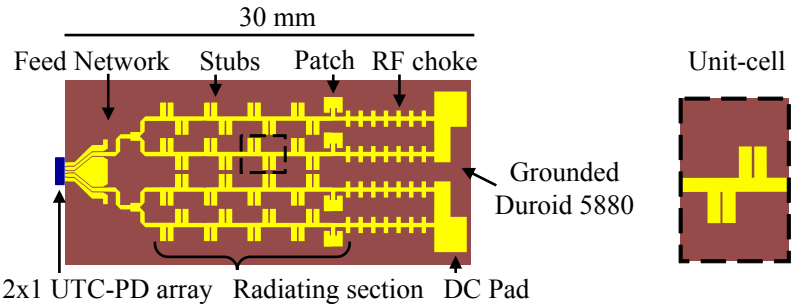

Figure 6.3 Layout of the designed antenna with the different sections indicated, and unit-cell of the radiating section.

6.3.1 Feed Network

The antenna feed network comprises the section between the photodiode chip and the rows. It is composed of a tapered transition to adapt the width difference between the photodiode output and the 50-Ω G-CPW on the Duroid 5880 substrate (as detailed in Fig. 6.11b). After this transition, a section follows in which the two G-CPWs separate to conform to the row separation. Finally, the last section is a transition to a microstrip transmission line (TL) and a symmetric corporate feed network for the array rows. It was designed with a full-wave simulator to minimize the reflection coefficient, cross-talk between photodiodes, and the radiation loss that could degrade the patterns.

6.3.2 RF Choke

Antennas integrated with photodiodes often require a polarization network to increase the built-in electric field and diminish saturation effects. Therefore, one must include an RF choke at the end of each row to separate the radiating section from the pads used to polarize the UTC-PD. The choke is developed in a 50-Ω microstrip, and it features a simulated RF isolation better than 35 dB within the array operating frequency band. It consists of seven cascaded identical sections, as shown in Fig. 6.4a. Each section is T-shaped, and the horizontal bar is composed of two parallel, $\lambda/4$ open-ended stubs. The stubs create a short-circuit, resulting in an RF choke. Besides, the length of the T's vertical bar, L, is chosen to translate the shorted microstrip to a large inductive load, so that it presents high input impedance, and this effect is reinforced, cascading them. Fig. 6.4c,d represent simulated and calculated isolation, $|S_{21}|$, depending on the number of sections as well as the magnitude of the reflection coefficient, $|S_{11}|$, for the 7-section choke, which is better than -0.85 dB in the whole band. In practice, the stubs do not create an exact short-circuit, and several sections need to be cascaded. Calculations are performed retrieving the ABCD matrix of the parallel stubs from full-wave simulations, taking the vertical bar as a section of transmission line of length L, and cascading the sections. The network equivalent used in the calculations is shown in Fig. 6.4b.

6.3.3 Periodic Radiating Section

The radiating section of the array comprises four identical rows. Every row consists of a microstrip line periodically loaded by groups of four stubs plus a patch that truncates it, as shown in Fig. 6.3. The design of the periodic structure is crucial to obtain low values of $|S_{11}|$, as explained below.

One of the difficulties encountered while designing a 1-D periodic LWA is the scan through broadside. At this point, all reflections from the perturbations add in phase back to the source. This can create a bandgap in the $k-\beta$ diagram; in this case the wave does not propagate into the structure and is completely reflected, degrading the input impedance matching. Following the discussion in [221], the perturbations of the periodic structure are modeled in a simplified

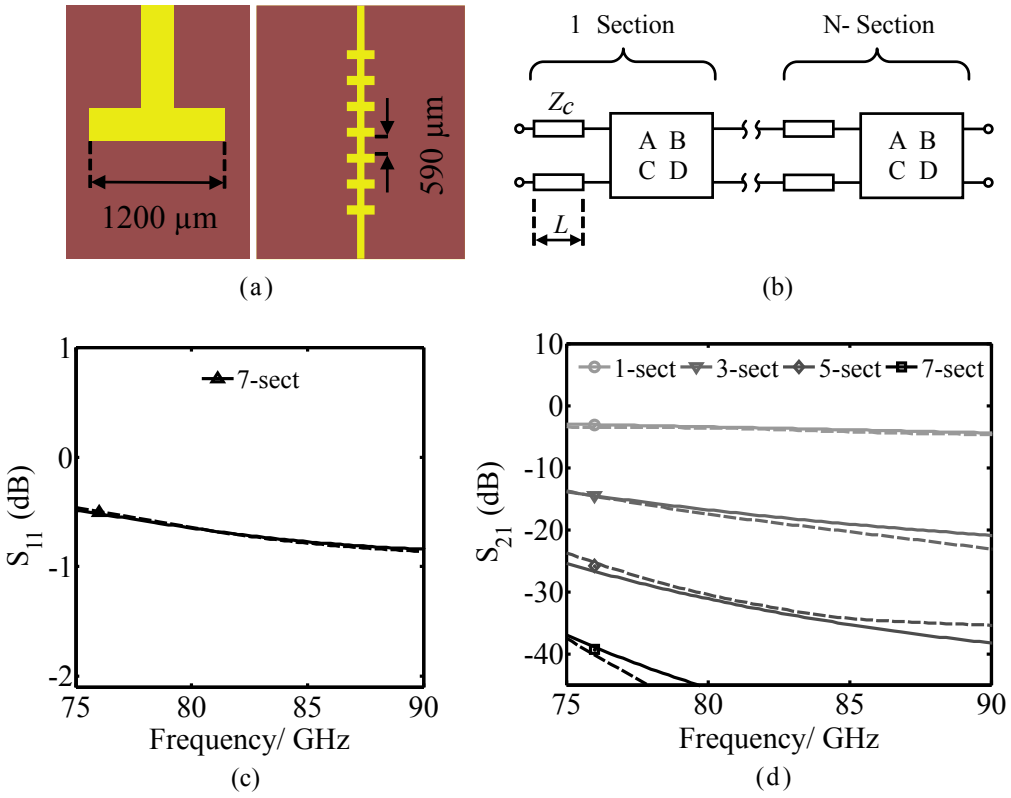

Figure 6.4 (a) View of the choke, (b) network used to compute the S-parameters (Z_c = Characteristic impedance of the TL), (c) magnitude of the reflection coefficient, $|S_{11}|$, for a 7-section choke, and (d) magnitude of isolation, $|S_{21}|$, for a choke composed of 1, 3, 5, and 7 sections. Continuous line: calculated by a transmission line equivalent. Dashed line: full-wave simulation.

network by shunt impedances connected by segments of TL. At broadside emission, the wave impinges the perturbations in phase, and the equivalent network is a shunt of infinite loads, which produces a short-circuit and the structure reflects the wave completely. However, if substantial losses are introduced by each perturbation, the current will progressively decay, effectively breaking the infinite periodicity, and a short-circuit will not be achieved. Hence, the latter case will present better matching characteristics.

The analysis of the periodic radiating section is carried out from two perspectives. First, as a cascade of identical two-port networks (unit-cells). This analysis enables the optimization of the input impedance matching at the frequency of broadside emission. Next, the dispersion diagram of the unit-cell is computed to assess the stop-band reduction of the optimized solution.

Design from a Cascaded Two-Port Network Perspective

In practice, each perturbation introduces losses and reflections to some degree. They have to be traded-off to obtain the desired radiation and impedance matching characteristics. Since

the full-wave simulation of electrically large structures can be a computationally intensive task, it is preferable to use approximate criteria to optimize the period of the structure at the frequency of broadside radiation. To that end, the periodic radiating section is first analyzed as a cascade of identical two-port networks. It is assumed that coupling among periods and surface-wave generation are negligible. In [224] it was shown that a spacing larger than 0.1 λ_g leads to tolerable coupling effects between stubs in a loaded microstrip, where λ_g is the guided wavelength in the microstrip TL.

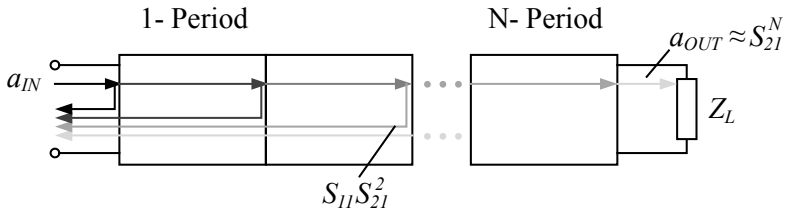

Figure 6.5 Schematic of the approximate calculation of the scattering parameters for the complete periodic structure.

The procedure consists of computing the S-parameters of an N-periods network (S_{Tot}), from the scattering matrix of a network with just one, retrieved from full-wave simulations. The structure is assumed to be terminated in a matched load, and only the first bounce is considered for reflections, whereas for transmission no bounces are summed up. This is true only if $|S_{21}| \gg |S_{11}|$. The schematic of the calculation is shown in Fig. 6.5. In this manner, the following calculation yields expressions that can be readily computed and used for optimization:

$$S_{11}^{Tot} \approx S_{11} \sum_{n=0}^{N-1} S_{21}^{2n}, \tag{6.1}$$

$$S_{21}^{Tot} \approx S_{21}^{N}. \tag{6.2}$$

The results from (6.1) and (6.2), along with the exact computations, are shown in Fig. 6.6 for a 10% and a 20% loss per pass ($|S_{21}| = \sqrt{0.9}$, $\sqrt{0.8}$, respectively). A symmetric unit-cell with $S_{11} = S_{22}$ was assumed to compute the exact values. $|S_{11}|$ is taken proportional to $|S_{21}|$ so that the infinite periodic structure presents S_{11}^{Tot} equal to -10 dB (and the bandgap can be considered effectively removed in terms of impedance matching). Fig. 6.6 shows the largest deviation between exact and approximate curves. It occurs when the phase of S_{11} equals π. Second and higher-order even bounces add in phase with the traveling wave, yielding lower transmission losses than the approximate calculation. Additionally, third and higher-order odd bounces add in phase with the first bounce so that S_{11} is underestimated in the approximate curves. As $|S_{11}^{Tot}|$ decreases, the agreement is better, while it degrades the other way around. In the latter case, the effects of stationary waves should be included computing multiple bounces. Finally, it is worth mentioning that as the losses per pass increase, $|S_{11}|$ can be proportionally

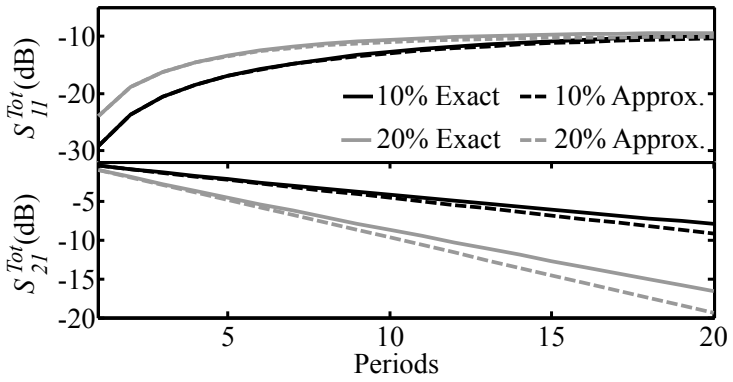

Figure 6.6 *S*-parameters as a function of the number of periods in the structure. Continuous line: exact calculation. Dashed line: approximate calculation from (6.1) and (6.2). The percentage indicates the power loss per pass of one period of the structure.

larger to $|S_{21}|$ to achieve the same S_{11}^{Tot} threshold (the sum in (6.1) approaches 1). Hence, increasing the losses per period relaxes the demand on S_{11} for adequate input impedance matching, in line with the earlier discussion. Note also that truncating the structure helps to decrease the reflection coefficient. Finally, for frequencies other than that of broadside directed emission, (6.1) and (6.2) are valid as long as the phase change per period is accounted for in S_{21}.

As an example of the usefulness of (6.1) and (6.2), we simulated the unit-cell reported in [225, Fig. 10] that removed the bandgap at broadside. The structure can be well described by a traveling wave, following our assumptions. S_{11}^{Tot} , S_{21}^{Tot} were computed for N = 32 and the approximate calculations yielded a return loss of 14.5 dB and a transmission loss of 16.3 dB, whereas the full-wave simulation of the complete structure (using waveports at both ends) yielded 15.1 dB and 18.5 dB, respectively, with a CPU simulation time 18 times larger than the single unit-cell. This indicates that (6.1) and (6.2) constitute a useful tool for preliminary optimization of this kind of structure.

Once the optimization procedure has been explained, we now explain the designed periodic radiating section. The unit-cell used in our design was first reported in [224], and it is shown in Fig. 6.7a. The stub length (l) is approximately $\lambda/2$, presenting high input impedance, to introduce a small perturbation in the TL, whereas its width (w) controls the amount of radiated power [224]. In turn, the stubs form groups of four: two towards the right and two towards the left, equispaced at distance s. This configuration allows one to increase the return loss if $\Delta\arg(S_{21})$ per stub plus inner separation is approximately $\pi/2$. In addition, it introduces more losses per period, so that the design can be made more compact. Nevertheless, the stubs do not radiate in phase but in quadrature. This results in a pattern that points off-broadside in the plane perpendicular to the row; this effect is conveniently eliminated by the array factor of the complete four-row structure. The simulated and calculated *S*-parameters using (6.1) and (6.2) are shown in Fig. 6.7b for broadside emission. The periodic structure presents $S_{11}^{\mathrm{Tot}} < -12$ dB, and the calculated curve is in agreement with the simulated values. The calculated values

for S_{21}^{Tot} are slightly overestimated due to the exclusion of the higher-order bounces in the calculation, as also occurred in Fig. 6.6. Once the group of four stubs is optimized (Fig. 6.7b), a four-period structure is simulated. When several periods are simulated, the length of TL in the unit-cell needs to be re-tuned. Its final value changes by about 4%. Hence, effects associated with surface waves and coupling introduce only a small perturbation.

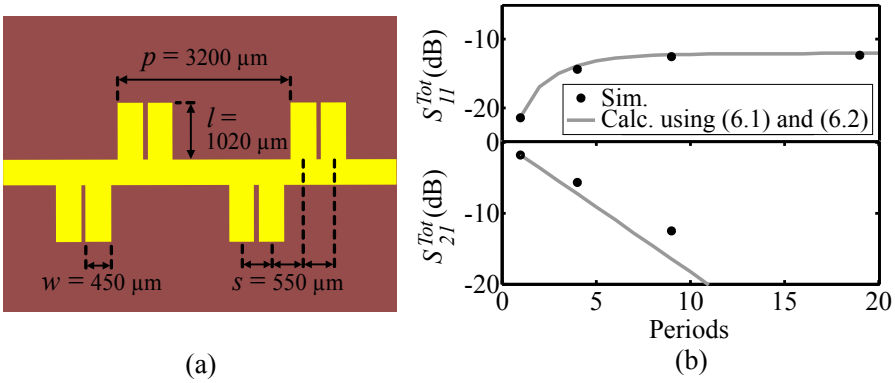

Figure 6.7 (a) Two consecutive periods along with representative geometrical parameters. (b) Optimized $|S_{11}^{\text{Tot}}|$ and $|S_{21}^{\text{Tot}}|$ for broadside emission as a function of the number of elements in the periodic structure (lines), and simulated values (dots).

Analysis from the Perspective of a 1-D Periodic Structure

To show the suppression of the open-stopband, Fig. 6.8 represents the dispersion diagram and attenuation constant of the optimized unit-cell within the band of interest (solid black line), as calculated from [226, Eq. 8.7], [227]. Dispersion and attenuation are also plotted for the same unit-cell geometry with $w = 50$ μm (solid grey line), and for a unit-cell with just a 50 μm wide stub (dashed grey line). In the latter cases, p is tuned to obtain $\Delta\arg(S_{21})$ equaling 2π approximately at 81 GHz. The unit-cell with one stub features the typical open-stopband behavior around the frequency of broadside emission ($\beta_{-1}p\pi = 0$) [221]. For $\beta_{-1}p\pi$ equal exactly to 0, the wave is not radiated (α/k_0 equals 0), and it is totally reflected ($S_{11}^{\text{Tot}} > -1$ dB in the stop-band frequencies when a sufficiently large structure is simulated). For the four-stub unit-cell with $w = 50$ μm, the previous behavior is mitigated since the reflections from the stubs compensate to some degree, but it is still observed (in this case, $S_{11}^{\text{Tot}} = -3$ dB). Finally, for the designed unit-cell optimized using the approach explained before, the curves present a much smoother behavior, and the stopband effect is largely mitigated $S_{11}^{\text{Tot}} < -12$ dB.

6.3.4 Complete Antenna Array

Since the antenna will be tested in a wireless link with a QO parabolic mirror of 10.16 cm focal length, its phase center should remain constant over the operation band. Therefore, a compact design (far-field at 10.5 cm), with broadside directed radiation (for simpler alignment) was targeted. For that purpose, the row is truncated after four periods in a patch that radiates

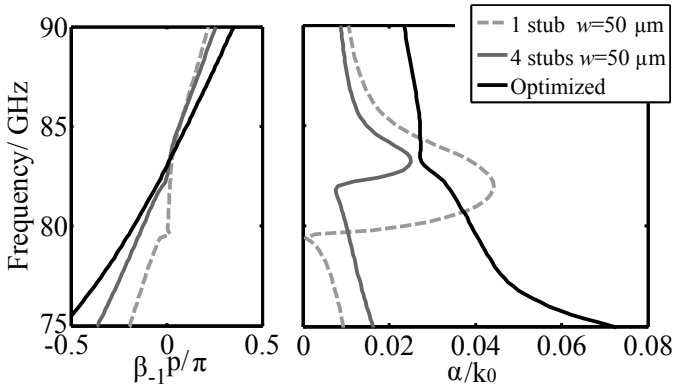

Figure 6.8 Dispersion diagram and attenuation constant for three structures: the optimized one shown in Fig. 6.7(a) with 4 stubs per unit-cell and $w = 450\,\mu$m (solid black lines), a 4-stub structure with $w = 50\,\mu$m (solid grey lines), and a structure with a single stub per unit-cell with $w = 50\,\mu$m (dashed grey lines).

the remaining power, between 10% and 25%. The resonance frequency of the patch is fixed to 85 GHz, slightly higher than the central frequency (81 GHz), to compensate for the lower losses at the higher end of the operation band. It is worth mentioning that the patch used to truncate the antenna and make it compact degrades the patterns beyond its resonance frequency, and thus, it limits the antenna bandwidth. In line with the application discussed in Section 6.6, by including more periods in the row, the bandwidth upper limit would be increased, the side-lobes would be decreased, and also it would help to obtain a narrower beam for more pointing resolution. Indeed, for a single row of 19 periods, the HPBW is only 4° and the gain is 18.5 dBi at broadside emission.

The above-described row is used to obtain the final planar array comprised of four rows. First, the row is duplicated to get a 2 × 1 array. Second, this 2 × 1 array is mirrored and excited in phase opposition, which leads to a significant reduction of the cross-polarization level and an E-plane pattern pointing at broadside. The final structure consists of an approximately square array with a simulated directivity between 18.5 and 20.0 dBi, side-lobe level (SLL) < -9 dB, a HPBW $< 13°$, and a radiation efficiency better than 75% in the 75-86 GHz frequency range. Fig. 6.9a shows the *S*-parameters of the whole structure, and Fig. 6.9b depicts the E- and H-plane cuts at broadside (81 GHz). The UTC-PDs are included as 50-Ω lumped ports, which corresponds to the characteristic impedance of the output G-CPW of the photodiodes. In the future, one could envisage integration of the UTC-PD with a matching network, as in [51], whose output impedance is also 50 Ω.

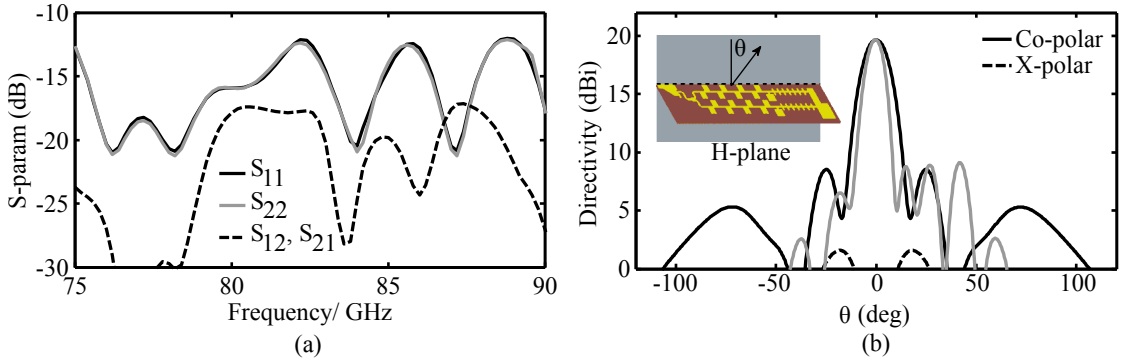

Figure 6.9 (a) Simulated magnitude of the reflection coefficient and cross-talk for the complete array. (b) Simulated E-plane (black) and H-plane (grey) cuts of the radiation pattern for broadside emission at 81 GHz.

6.4 Antenna and Photodiode Integration

In this section, we describe the photodiode chip and the integration with the antenna.

6.4.1 Description of the UTC-PD Used

The UTC-PD that will be integrated with the LWA antenna array was fabricated by III-V labs [161]. Additional details of the device have been reported in [154], [162]. It consist of a waveguide-fed, evanescently coupled UTC-PD. Fig. 6.10a details the layer structure. As it can be seen, values are among the typical ones used in the bibliography. The dielectric waveguide is detailed in Fig. 6.10b. It is a ridge waveguide where the core is made of InGaAsP, with dimensions 3 μm wide × 0.3 μm thick. The cladding (top and bottom) are developed on InP. It is important to note that, in this case, the optical coupling to the dielectric waveguide is dependent on the polarization of the light, therefore, it requires the use of a polarization controller in the experiments. Relevant characteristics of the UTC-PD are listed in Table 6.1.

Parameter	Value	Comment
Dimensions	15 μm × 3 μm × 2.5 μm	Length × width × thickness
Responsivity	0.35 A/W	3 μm spot size illum.
3 dB bandwidth	120 GHz	50 Ω load
Saturation P_{out}	1 dBm	110 GHz, 12 mA photocurr., −3 V bias

Table 6.1 Relevant parameters of the UTC-PD used [161].

Fig. 6.10c shows the available chips. They consist of two UTC-PDs per chip on an InP substrate. They are already mounted on an Aluminum Nitride (AlN) block for mechanical support, handling, and heat dissipation (shown later). The separation between UTC-PDs is 500 μm, and each photodiode is integrated with a 50-Ω G-CPW. The PDs can be illuminated by an array of lensed fibers with the same pitch, or just with a single lensed fiber to feed them

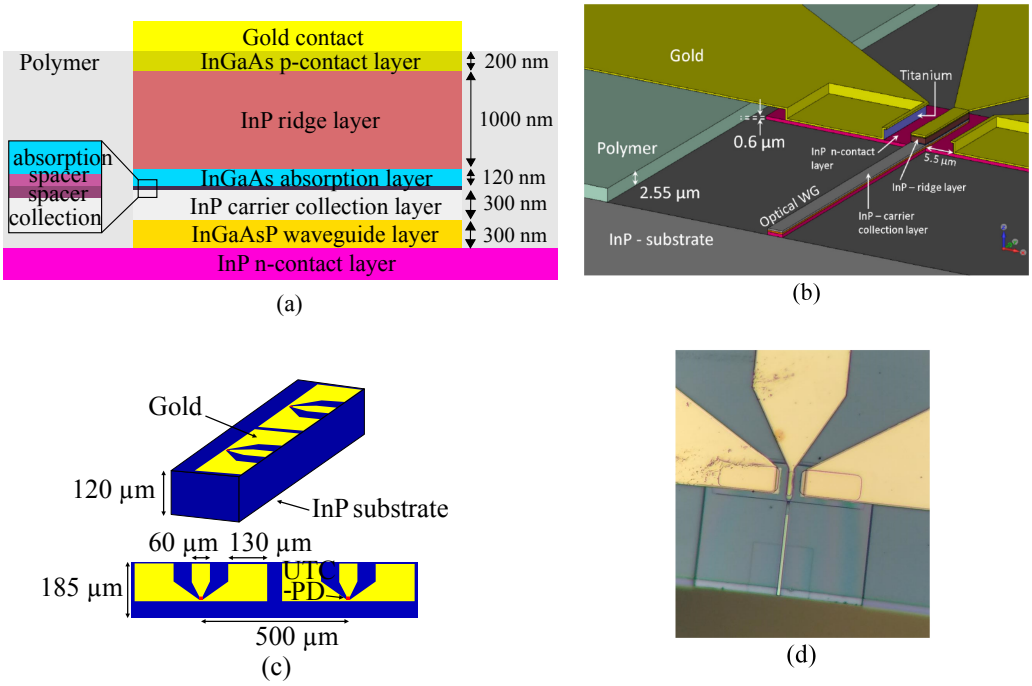

Figure 6.10 Views of the UTC-PD used. (a) layer structure, (b) zoom to PD region (from [154]). (c) Layout of the 2× UTC-PD chip, and (d) photograph of the PD region with its optical waveguide.

individually. In the latter case, light is more efficiently coupled since tolerances in the fiber array manufacturing make it difficult to illuminate both simultaneously while keeping the $\Re$ optimal [228]. Finally, Fig. 6.10d shows a zoom to one PD and its optical waveguide. The sharp border finish is achieved cleaving the chips along a crystallographic plane of the substrate.

6.4.2 Integration

Prior assembly, an aluminum housing to provide support for the AlN block and the PCB is fabricated. The housing features a groove where the AlN block is placed, with a depth such that the top metal of the PCB and the G-CPWs of the chip are at the same height ($\pm 50\,\mu$m). It also includes pins to perform electrical connections and bias the UTC-PD, as can be seen in Fig. 6.11a. A zoom on the antenna feed is shown in Fig. 6.11b, where lensed fibers are also included. They illuminate the UTC-PD by the optical waveguide input at the back edge (not shown).

In the first step of the integration process, the AlN block is positioned parallel to the PCB in such a way that the G-CPW of the chip is aligned to the G-CPW of the PCB. It is thereafter glued to the housing using a UV curable glue (BLUFIXX MGS), as shown in Fig. 6.11c. For positioning and maintaining in place the AlN block while applying the glue, a probe plus micropositioner (SUSS Microtech PH100) are used (Fig. 6.11d). In addition, the edge of the PCB where the feed is located is glued in a similar fashion to the housing (not shown). This avoids the PCB from

bends while curing the bonds.

Once both parts are aligned and fixed to the housing, the last step is to bond the UTC-PDs to the G-CPW lines on the PCB. To do so, a silver-based conductive epoxy is used (EPO-TEK). To perform the bonds, the same micropositioner and probe are used. A $\approx 60\,\mu$m diameter thread is picked by the probe and deposited in place with the aid of the micropositioner. Trials on $100\,\mu$m-wide lines are shown in Fig. 6.11e, while the inset shows the probe tip with an epoxy thread ready to bond. Finally, Fig. 6.11f shows the UTC-PDs bonded to the PCB as well as a lensed fiber used for illumination. After bonding, the epoxy requires curing at 80 °C for 4 h. The whole process is assisted by an optical microscope.

The reason to use the bonding method presented above and not the more common ball-wire bonding is because the gold pads of the chip lie on a Benzocyclobutene (BCB) layer. While in the former negligible pressure is applied to do the bond, the combination of temperature ($\approx 100\,$°C), ultrasound, and pressure to create the weld in the wire bonding process, can result in fatal structural damage to the chip. In addition, the conductive epoxy thread results in a thick connection. Compared to wire bonding, it reduces the self-inductance of the wire, yielding a better electrical connection. This has been evaluated by bonding two sections of G-CPW on Duroid 5880 separated by $150\,\mu$m. The insertion loss (IL) obtained for ball wire bonding at 67 GHz are 1.4 dB higher than the IL using conductive epoxy.

Out of the three chips that were available, unfortunately, it was not possible to get both UTC-PDs functioning well simultaneously. Most commonly, one of them had the input of the optical waveguide damaged to some extent. This impeded us to realize measurements with both PDs working and we were restricted to perform measurements with only one PD active. In particular, power combining and wireless link demonstrations with both active PDs could not be demonstrated. SEM images of damaged chips can be seen in Fig. 6.12.

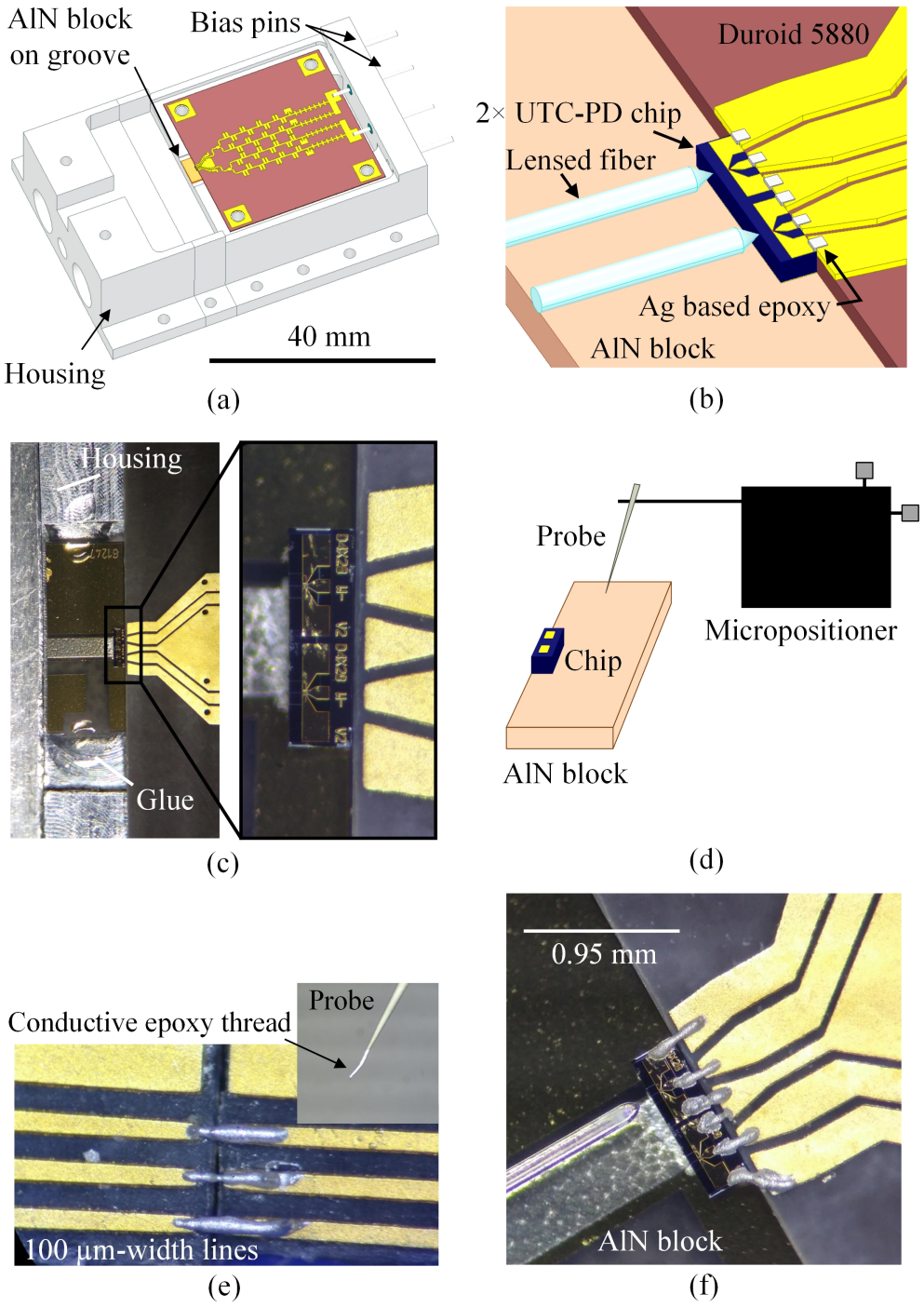

Figure 6.11 Images of the integration process: (a) designed housing, (b) G-CPW transition, (c) AlN block aligned to PCB and glued to the housing, (d) schematic of AlN block fixed in place by a micropositioner, (e) practice of thread bonding on 100 μm-wide dummy lines, inset: probe and epoxy thread ready to deposit. (f) detail of thread bonding and fiber used to excite the UTC-PD.

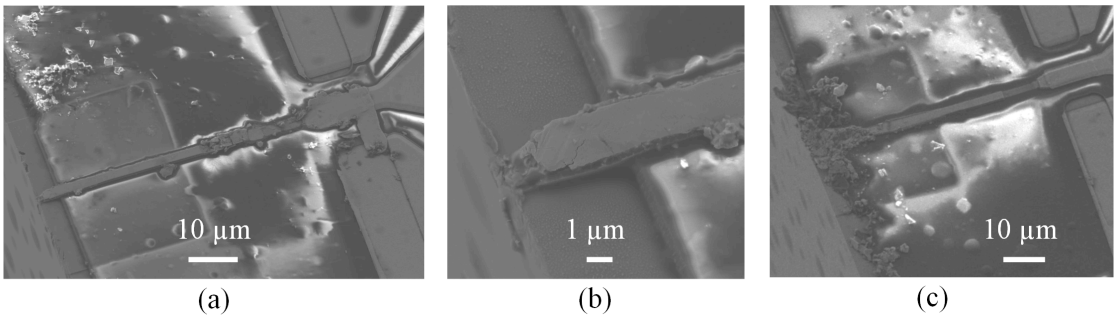

Figure 6.12 SEM images of damaged chips: (a) photodiode and optical waveguide damaged, (b) zoom to the damaged optical waveguide input, and (c) healthy photodiode with a severely damaged optical waveguide input.

6.5 Transmitter Characterization

Two different sets of measurements were carried out to evaluate the performance of the designed antenna: electronic measurements to determine return loss and radiation pattern, and photonic measurements to examine the power radiated and its performance in a wireless transmission link.

6.5.1 Electronic Measurements

The set of electronic measurements was performed on a two-row array prototype with a GSG probe (Form Factor ACP 110-T), and an Agilent N5242A vector network analyzer (VNA) with a mm-wave extension head (OML V10VNA2). The set-up and measurement methods will be presented in detail in Appendix D. The prototype included a tapered interconnection to adapt the pitch of the GSG pads (150 μm) to the G-CPW in the PCB, as shown in Fig. 6.13a.

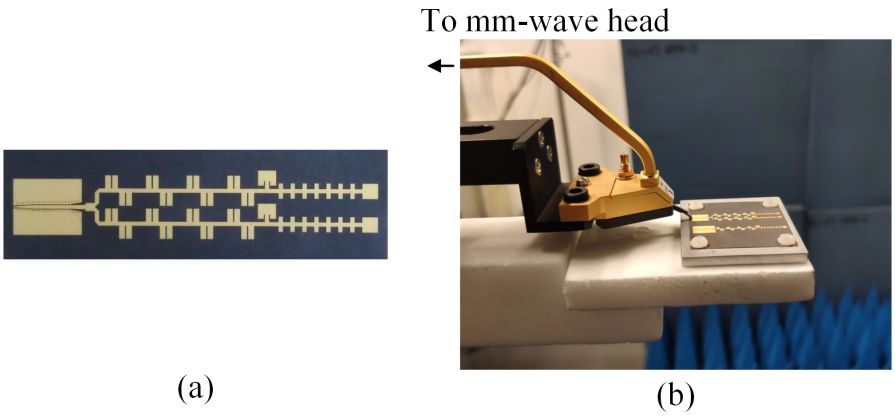

Figure 6.13 (a) Layout of the two-column array adapted for GSG probe measurements, and (b) detail of the GSG probe exciting the antenna.

In the reflection coefficient measurements, it was necessary to de-embed the probe and interconnection. For this purpose, the procedure described in Appendix D was employed. Measurement results are shown in Fig. 6.14. The antenna was well adapted through the operation band and did not present an increased reflection coefficient at the frequency of broadside emission (81 GHz). The disagreement between simulation and measurement around 78 GHz could be attributed to an inexact value of the relative permittivity of the substrate used in the simulation, and to errors associated with the electrical connection between the probe and the PCB. Finally, tolerances in the fabrication of the PCB could also have impacted the performance. More precisely, VIA holes were positioned with an accuracy of ± 25 μm, which is comparable to the VIA-center to edge distance (150 μm).

For pattern measurements, a spherical 3D scanner and a receiving horn were additionally used. This is also explained in detail in Appendix D. Fig. 6.15a shows the normalized co-polar directivity of the two-row array at different frequencies. A frequency-scanning range of 22° was achieved. Note that the cross-polarization component, emitted largely off the scanning range of the array, vanished in the complete structure (Fig. 6.9b). Additionally, the SLL of the two-row array was higher than in the complete structure (Fig. 6.9b) because the patterns were optimized for the prototype excited photonically. The SLL could be improved by including more periods in the row. Fig. 6.15b shows the simulated and the measured peak gain for the two-row prototype adapted for probe measurements. The largest deviation between simulated and measured data equaled 1.4 dB, which was acceptable considering the method used to excite the antenna. This value of measured gain was also consistent with the simulated radiation efficiency (77% at broadside). In the measurements, a standard gain horn was first characterized as a reference to retrieve absolute values of gain. Note the antenna did not present degraded gain at the frequency of broadside emission due to the good input matching observed in Fig. 6.14. Therefore, the operation range was extended from the backward quadrant ($\theta < 0°$) to the broadside and the forward quadrant.

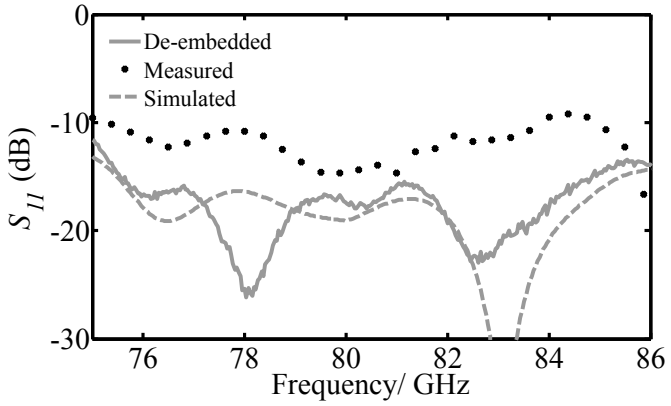

Figure 6.14 Magnitude of the reflection coefficient for the two-row prototype adapted for probe measurements. The black dots represent the measurement taken directly from the VNA, whereas the grey continuous curve represents the measurement after de-embedding the probe and the interconnection.

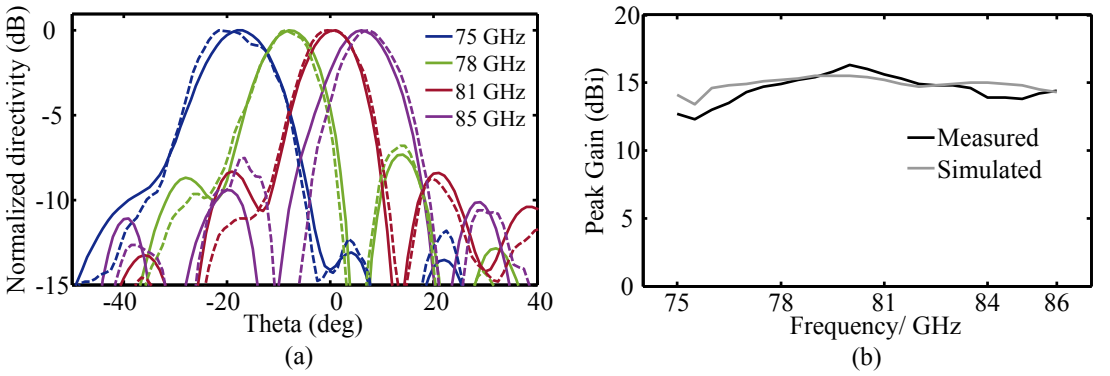

Figure 6.15 (a) Normalized co-polar directivity at H-plane at different frequencies for the two-row prototype adapted for probe measurements. Continuous line: simulation, dashed line: measurements. (b) Simulated and measured peak gain.

6.5.2 Photonic Measurements

For photonic measurements, the antenna integrated with the PD as described in Section 6.4, was used to measure photodiode I-V curves, the performance in a wireless link, and the output power, with one active UTC-PD. It was optically fed by a 4 μm spot-diameter lensed fiber (OZ Optics). The fiber was mounted on a 3-axis stage (Thorlabs MBT616D) to align it to the PD optical input, as shown in Fig. 6.16, and Fig. 6.11f.

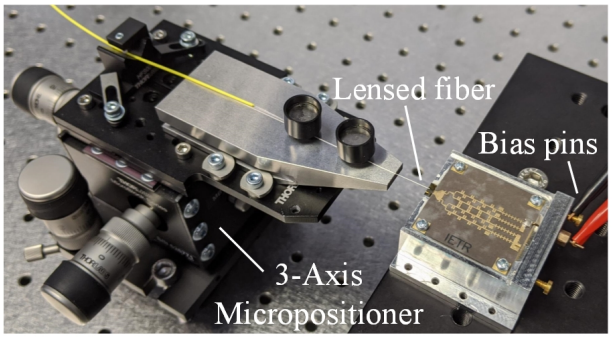

Figure 6.16 Photonic excitation of the antenna.

I-V Curve and Responsivity

Fig. 6.17 shows the characterized DC response of the UTC-PD. To preserve the lifespan of the devices, the reverse bias voltage was limited to -2.5 V and the photocurrent to 11 mA in all experiments (unless the PDs were damaged, in that case we diverted ourselves). The DC voltage was applied by a DC power supply, the photocurrent was measured by a workbench precision current meter (Keysight B2980A), and the optical power was measured with an optical power meter (Thorlabs S154C). The left graph shows the I-V curve at dark (it was measured on a PD with a damaged waveguide). The response follows the classical curve of a

p-n junction. At forward bias, the slope of the curve is defined by the series resistance of the PD, calculated to be 60 Ω, including also the resistance due to PD bonding in the assembled prototype. At reverse bias, the dark current is in the order of hundreds of nA (indicating a high resistance of the depletion region), until $V = -8$ V, where the electric field is high enough so that Zenner or avalanche effects increase the dark current. Fig. 6.17b shows the (reverse) photocurrent versus optical power at two different bias voltages. For $V = 0$ V, the onset of saturation is observed, whereas it is not observed at −2.5 V. Responsivity is 0.2 A/W, and is slightly lower than that reported elsewhere [161] because we used a lensed fiber with a larger spot. The cut in the abscissa for the $V = -2.5$ V curve is about 0.4 mA, whereas the dark current of the photodiode is in the range of nA [160]. This offset indicates that integration in this prototype has introduced a parasitic shunt resistance of about 5 kΩ when the PD chip was assembled. The shunt resistance leaves the value of a 50 Ω load practically the same, but the offset must be removed from the photocurrent if RF output power versus photocurrent is considered.

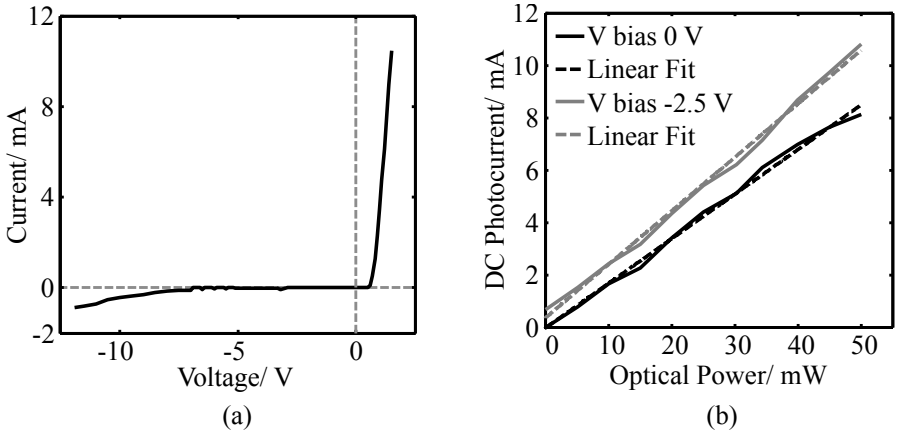

Figure 6.17 Measure of the DC response of the UTC-PD used in this work. (a) response at dark, (b) DC photocurrent versus optical power at two different bias.

Performance in a Wireless Link

The wireless link set-up is shown in Fig. 6.18a. A standard photonic approach [30], [174] was used to generate and modulate two optical tones of two distributed feedback lasers (Toptica Photonics DFB pro BFY), with a spacing in frequency equal to that of the mm-wave carrier. After modulation using on–off keying (OOK), the signal was amplified (EDFA), monitored in an optical spectrum analyzer (OSA), and coupled to the UTC-PD input optical dielectric waveguide by a lensed fiber. Subsequently, a QO system was employed to collimate the radiation. Note that the antenna radiates perpendicularly to the PCB plane (Fig. 6.18b,c). Hence, it is placed at the focal point of a parabolic mirror that collimates radiation horizontally, as is most convenient for the QO link. On the receiving side, a 10 cm diameter Teflon lens focuses the radiation onto a Zero bias Schottky Barrier Diode detector (ZSBD) [229]. After the mm-wave carrier is detected, the signal, in baseband, is filtered and amplified (LNA amplifier + limiting

amplifier). Finally, the detected signal is compared to the original using a BER tester (Anritsu MP2100A). The link parameters are summarized in Table 6.2, and Fig. 6.18d shows the corresponding eye-diagram for 2.15 Gbps error-free transmission. At higher data-rates, variations of the antenna phase center with frequency create jitter, distorting the communication.

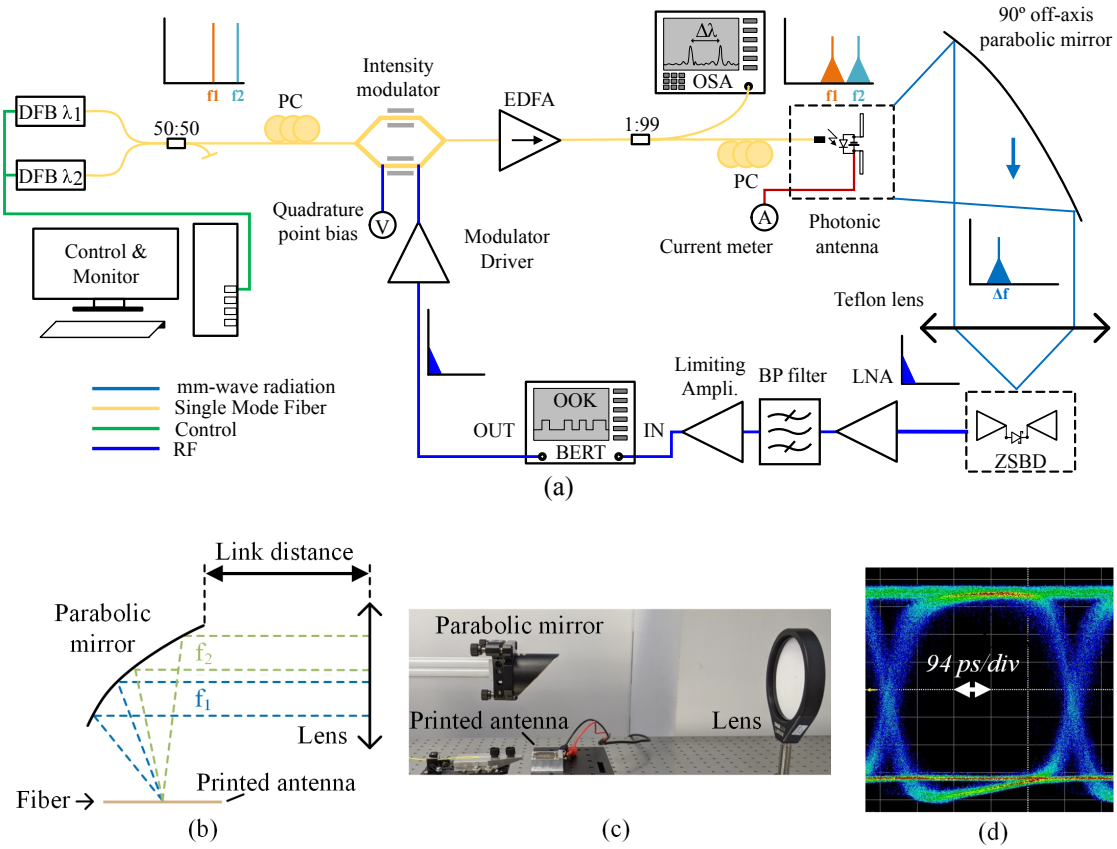

Figure 6.18 (a) Schematic of the set-up utilized for the wireless link (PC = polarization controller, BP = bandpass, LNA = low noise amplifier). (b) and (c) QO system. (d) Eye diagram for the error-free transmission at 2.15 Gbps.

In addition, the wireless link was used to transmit the HD screen of a laptop computer (data rate of 1.5 Gbps) to a second screen, as it can be seen in Fig. 6.19. To do so, the HDMI port of the laptop was connected to an HDMI to Serial Digital Interface (SDI) converter, which serializes the video output with OOK modulation. In turn the converter was directly connected to the modulator driver input. After the amplification stage on the receiving chain of the link, an SDI to HDMI converter changed back the modulation of the transmitted video, and was connected to the second screen. Except for the BER tester, which was removed, the rest of the link elements remained the same, including distance, photocurrent, and carrier frequency.

Parameter	Value
Data Rate	2.15 Gbps
RF Carrier	80 GHz
Modulation	OOK
Link Distance	25 cm
Bit Error Rate	$< 10^{-12}$
Photocurrent	7.0 mA

Table 6.2 Wireless link with one active PD: summary of main parameters.

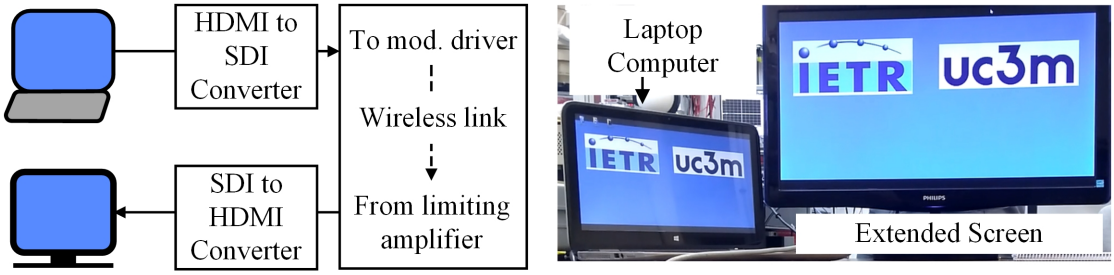

Figure 6.19 Live transmission of an HD laptop computer screen to a second screen through the wireless link.

Radiated Power

Power measurements of the photonic prototype with a UTC-PD excited were performed on a similar set-up as the transmission link shown on Fig. 6.20. The Teflon lens, ZSBD, and receiving chain were replaced by a THz absolute power meter (Thomas Keating Instruments). Additionally, the modulator was substituted by a fiber-coupled free-space collimator plus a chopper to enable lock-in detection. Since the broadband detector presented a large window in which pressure variations due to thermal heating were measured, external stimuli could alter measurements (Fig. 6.21a). Therefore, the dependence $P \propto I^2$ was checked before power measurements, P being the detected RF power and I the DC photocurrent. This is of utmost importance if an end-fire antenna is measured. In this case, some light, which was chopped at the same lock-in frequency, could couple and destroy the measurements. In this case, however, the previous relationship would be linear and it could be easily noted. Fig. 6.21b shows the frequency dependence of the detected power. It featured a 3 dB bandwidth of 11 GHz (74 GHz to 85 GHz), with a maximum of 120 μW at 80.5 GHz, for 45 mW input optical power at -2.5 V bias voltage (9.8 mA photocurrent). This was in agreement with the photodiode output power [161] when bonding losses (4-5 dB) and antenna radiation efficiency (77%) were accounted for. For frequencies out of the operation band, the mirror did not capture all the emitted radiation, emitted largely off-boresight, and the detected power decreased. This could be solved using a mirror with lower F-number or placing the power meter window horizontally, with the appropriate support and alignment structure. Nevertheless, these frequencies are not within the range of interest and were not measured in the present work.

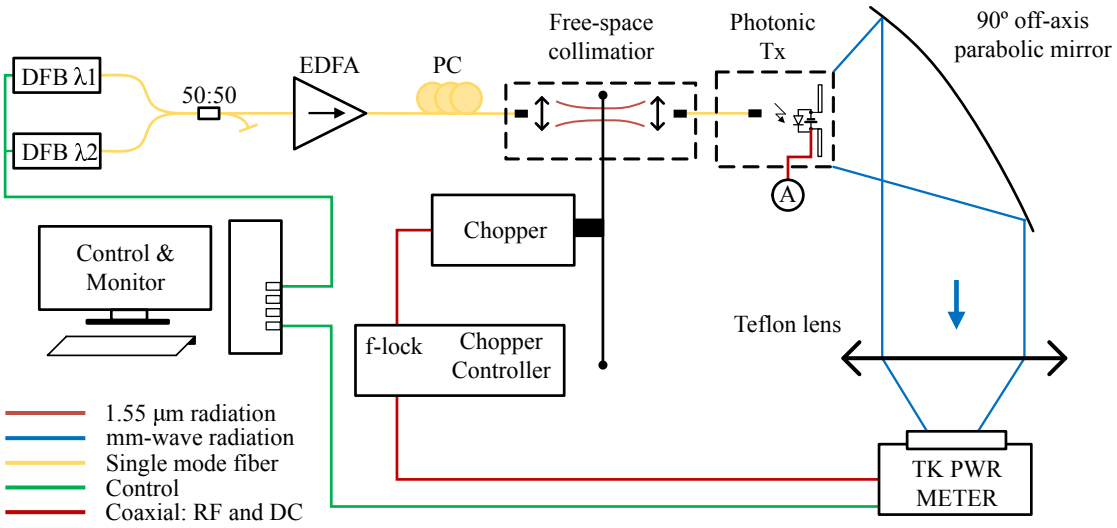

Figure 6.20 Schematic of the set-up utilized for radiated power measurements (TK PWR METER = Tomas Keating power meter).

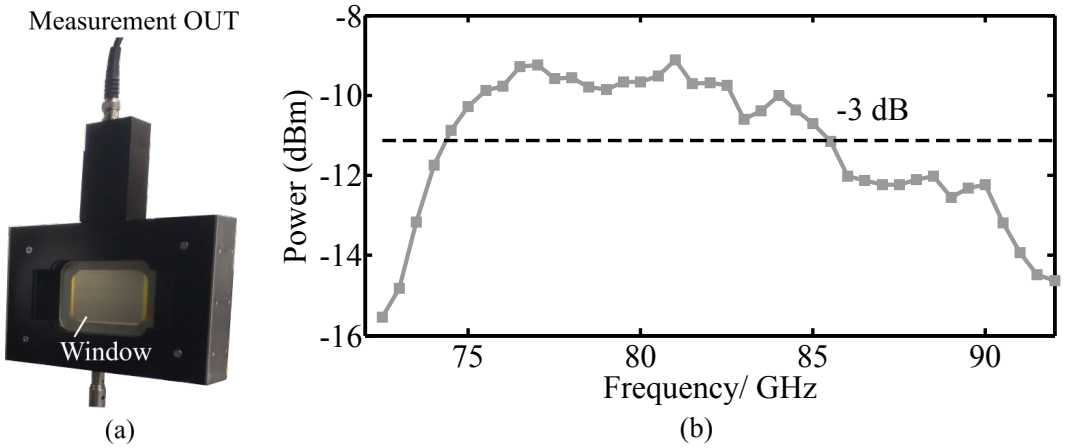

Figure 6.21 (a) Measurement head of the power meter, and (b) detected power after the QO system.

6.6 Featured Application

In a potential scenario, we discuss the application of the LWA for beam alignment in wireless data center interconnections. Wireless interconnections in data centers were proposed in [119] to provide scalability and reconfigurability, which are difficult to achieve by fiber interconnected nodes as the number of servers increases. Mm-wave links at 60 GHz or sub-THz frequencies, better suited for tens of Gbps data rates, could provide a flexible alternative to an all-fiber scenario.

Fig. 6.22a depicts a simplified data center node structure with server racks distributed in a hexagonal lattice. The servers form sub-groups that are interconnected by fiber, whereas the wireless links provide flexible interconnection between them, thus forming a hybrid

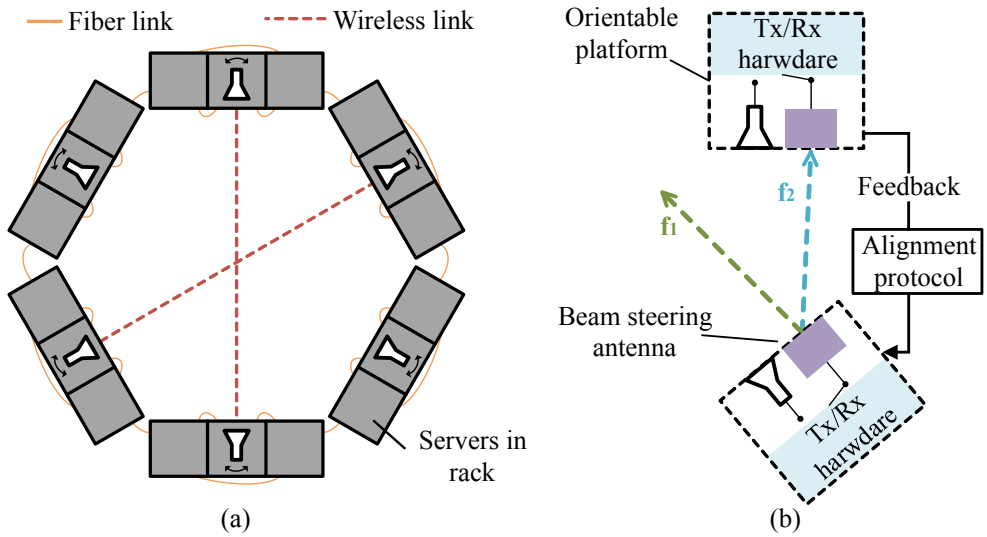

Figure 6.22 (a) Hybrid interconnections in a data center; the continuous yellow lines represent wired fiber links whereas the dashed red lines illustrate reconfigurable wireless LoS links. (b) LWA set-up, co-located with the wireless transceivers, to enable alignment in a LoS link.

architecture. More details on hybrid architectures can be found in [119].

Electronic beam steering with phased arrays is frequently proposed in the literature as a means to align the different LoS links [119], [213]. However, mechanical alignment is more affordable, given the cost and energy consumption of many active elements required in a high gain phased array. As discussed next, these high-frequency data links feature high directivity and narrow beamwidth, which require dedicated hardware, as well as the corresponding protocol to control the stringent alignment.

In the previous sections we have reported on the LWA that produces a beam squint with frequency, which is one of the simplest forms to steer the beam. It shows a medium directivity of about 18–20 dBi, points within the 22° scan range, and works at the E-band (from 75 GHz to 85 GHz). Owing to the antenna scalability, these characteristics can be easily adapted for a lower HPBW and enhanced pointing resolution. Indeed, we have already commented that the row composed of 19 periods presents an HPBW of 4° (18.5 dBi gain for one row), while maintaining good input impedance matching. Besides, the same concept can likewise be employed at other frequencies [230]. In this use case, the LWA would be co-located with the transceivers on top of the racks in a structure that would offer in-plane mechanical rotation, as shown in Fig. 6.22b. After, the LWA could be used to establish optimum alignment between transceivers in the link. During alignment, a signal with reduced bandwidth or lock-in detection could be employed, lowering the demand for highly directive antennas and eluding a dedicated QO system. For instance, for a detector NEP of 2 $\text{pW}/\sqrt{\text{Hz}}$ [231], and a signal bandwidth of 1 MHz, it suffices with 21 dBi directive antennas to obtain an SNR = 10 dB (0 dBm noiseless radiated power, 10 m distance, f = 75 GHz, and D = G for the Rx antenna). For 10 GHz, the required directivity would increase to 31 dBi.

This solution would offer a fast and simple option to set-up the wireless links in reconfigurable data centers. Additionally, the transceiver hardware, represented in blue in Fig. 6.22b, could be partially reused. For instance, it would suffice with an optical switch for a photonically generated signal to select either of the antennas. Therefore, this solution would play little role in the overall system cost or size. The PCB in which the antenna has been fabricated is 30 mm by 30 mm, with an approximate packaging footprint of around 5-10 cm^3.

6.7 Conclusions of the Chapter

In this chapter, we have reported the design, photonic integration, and characterization of a premier leaky-wave antenna array integrated with photodiodes at mm-/sub-mm-wave frequencies. The designed antenna exhibited beam steering with frequency with a scalable layout and was fabricated in PCB technology. Measurements of the radiation pattern were performed on a two-row array, adapted for excitation with a GSG probe. A 22° scan range, including broadside, has been shown across the frequency of operation of the antenna (75 GHz to 85 GHz), which was in agreement with full-wave simulations. Measurements of return loss were also in good agreement with simulations. In this respect, a novel method to de-embed the probe plus interconnection will be described in Appendix D. To the best of our knowledge, this was one of the few realizations of periodic 1-D structures in which the complete periodic structure shows adequate matching characteristics ($S_{11} < -12$ dB) at broadside. This was due to increased losses per period, which also helped to obtain a compact structure and higher radiation efficiency and to enlarge the scanning range of the antenna from the backward quadrant to broadside and the forward quadrant. Furthermore, the antenna was tested in a wireless communications system, demonstrating error-free transmission at 2.15 Gbps as well as HD live video retransmission (1.5 Gbps) for a 25 cm link distance. Finally, the application of the LWA antenna as a simple means to align mm-wave LoS links was outlined.

As for simulations of the photonic prototype, the structure shown in Fig. 6.11a (without housing) was considered. The feed structure was detailed in Fig. 6.11b where the UTC-PDs were simulated as 50-Ω lumped ports. For the rest of the simulations comprising the choke, the design of the unit-cell, and the two-column prototype for excitation with a GSG probe, waveports were utilized to excite directly the microstrip line or the G-CPW line. For the complete prototype, a full-wave simulation was also carried out in CST (Ver. 2018)[228] with the frequency-domain solver to cross-check results.

As for the different aspects of the experimental work of this chapter, the housing was manufactured by X. Morvan at IETR workshop with a high-precision milling machine. The PCB was manufactured by CONTAG AG, and the UTC-PD chips on an AlN block were provided by G. Carpintero (UC3M) prior approval of F. van Dijk (III-V Labs Thales-Alcatel). The SEM images of damaged chips were taken by O. de Sagazan at Nano-Rennes cleanroom (UR1), whereas the set of electronic measurements were taken at LEAT (Université Côte d'Azur) with the guidance of L. Brochier, and F. Ferrero. Prototype assembly and photonic measurements

were carried out at the Electronics Lab of Professors G. Carpintero and L. E. García-Muñoz at UC3M. It is worth mentioning that a similar integration, and notably the bonding process, had already been carried out, for instance, in [205]. Also, the wireless link set-up was already available, and it was only necessary to adapt the QO system shown in Fig. 6.18b. All the integration process and measurements were taken by the author except for the bonding of the UTC-PDs to the PCB. Bonding was performed by fellow Ph.D. student M. Ali (UC3M). The rest of the work herein presented was carried out by the author under the supervision of D. González-Ovejero, R. Sauleau, and L. E. García-Muñoz.

7

Photonic-Enabled Beam Switching With a Mm-Wave Antenna Array for Telecommunications

In the previous chapter, we have shown a photonic transmitter based on a leaky-wave antenna array as a simple means to steer the beam in 1-D by frequency-selective beamsteering. In this chapter, we present the second and last realization of a mm-wave photonic transmitter which is based on beam switching. One of the particular characteristics of mm-wave photonic transmitters is the difficulty of integrating more than a few active elements (approximately four), as we have seen in the SotA of the preceding chapters. Therefore, an alternative to more traditional approaches based on phased arrays is required to obtain, simultaneously, a highly directive and steerable beam. In this chapter, we apply the technique of beam switching to an array of mm-wave photonic transmitters to accomplish such beam characteristics. The work presented in this chapter is based on , [v-vii] from the List of Publications.

In summary, we present in this chapter the last original contribution of the thesis: a photonic-enabled antenna array at E-band for scanning and beam alignment by beam switching in wireless links. First, we discuss the trade-offs between beam switching and beam steering for photonic (sub)millimeter-wave transmitters. Next, we present the proposed solution; it consists of two sub-arrays of stacked patches as primary feeds of a PTFE lens, with one photodiode feeding each sub-array. To validate the assembly, the return loss and radiation patterns have been measured for one of the sub-arrays excited with a coplanar probe. In turn, the lens illuminated by one of the sub-arrays yields a directivity of 27 dBi. The radiation patterns measured for the transmitter module (including the lens) are in very good agreement with full-wave simulations, and they show that excitation of one of either sub-arrays allows beam switching between $\pm 2.7^{\circ}$ with a beam crossing at -3 dB. Finally, we will test the transmitter in a 0.6 m wireless link. Depending on the position of the detector and on which sub-array is excited, we expect to accomplish error-free transmission at several Gpbs using on-off-keying modulation and direct detection. The system constitutes an initial proof of photonic-assisted beam switching for mm-wave transmitters enabling broadband operation with a directive and

switchable beam.

7.1 Introduction

The increasing demand for data traffic in wireless systems will require the deployment of high capacity cellular networks. Millimeter- (mm-) and sub-millimeter (sub-mm) waves have been widely accepted as the most suitable spectral regions to provide enough bandwidth for multi-Gbps data throughput [9], [56], [102]. In particular, the E-band (71-76 and 81-86 GHz) constitutes one of the most promising bands. It has been already allocated for fixed cellular backhaul links [107]. The E-band offers a 2×5 GHz bandwidth not intensively licensed so far [113] and lies within a relatively low atmospheric absorption window of approximately 0.5 dB/km [232].

In other respects, intense research efforts carried out over the past decades have put the photonic generation of mm- and sub-mm waves in the spotlight. Specifically, the possibility of seamless integration of photonic transmitters (Tx) with fiber optics has led to numerous point-to-point wireless links demonstrations [59], [108], [150], [233]. The photonic approach is advantageous in terms of antenna remoting, centralization of signal processing with flexible modulation formats, wavelength division multiplexing for multichannel wireless links, and compatibility with already deployed and forthcoming optical access networks. With a bandwidth spanning over 4 THz, photonic generation and analog signal processing of mm-waves can benefit from ultra-broadband, reliable, and cost-effective commercial components such as Er-doped fiber amplifiers (EDFAs), which are nearly insensitive to the mm-wave frequency. However, photonic Tx provide lower source power than their electronic counterparts, suffering from a large down-conversion loss at the O/E converter (usually a high-speed photodiode). This shortcoming, in addition to a high free space loss at mm-waves, requires the use of line-of-sight links and highly directive antennas.

An additional challenge is to provide photonic-enabled mm-wave transmitters with beam steering capabilities. This feature is also crucial to enable high data rate wireless links in realistic scenarios [4], [19], [31], [234]. Some relevant use cases include: fine alignment of highly directive beams [108], compensation from twists and sways from mounting structures [57], [235], and reconfigurable links [118], [234].

Despite the numerous demonstrations of photonic-enabled wireless links, experimental realizations of photonic Tx featuring beamsteering at E-band frequencies or beyond are relatively uncommon. Only in recent years the number has started to grow [61], [63]–[65], [236], [237], although the performance assessment in a wireless link still has received little attention [61]. Several of the previous examples on photonic Tx featuring beamsteering have been shown in the preceding chapters, and we will cover next the remainder ones. Other than leaky-wave antennas, all the previous realizations use in common a phased array to steer the beam, but with a small number of active elements, up to four. The reason is that it is complicated to integrate a large number of photodiodes (PDs) with the antennas, while

maintaining optimal PD illumination. This issue has hindered the development of wireless links using high gain antennas featuring beam steering simultaneously.

Instead of using a phased array, an approach that combines an antenna array with quasi-optical (QO) elements to obtain the required gain enhancement can be a plausible solution to the problem above. In particular, we propose in this contribution photonic-assisted beam switching with a mm-wave antenna array integrated with uni-travelling-carrier photodiodes (UTC-PDs). By using a lens, the Tx features a highly directive and switchable beam, while a low number of active components need to be integrated. The system constitutes a proof-of-concept towards photonic-enabled mm- or sub-mm wave Tx featuring broadband operation with a directive and steerable beam.

The remainder of the chapter is organized as follows: Section 7.2 describes the SotA on arrays of photonic transmitters for beamsteering. Section 7.3 analyzes the advantages and drawbacks of photonic-enabled beam switching and phased arrays to obtain a high gain and a steerable beam simultaneously. Next, Section 7.4 describes the design, assembly, and characterization of a 2×1 antenna array used as a lens primary feed for beam switching. After, in Section 7.5 we describe the experimental characterization of photonic beam switching. Last, Section 7.6 presents the system in a wireless data transmission experiment. We conclude the chapter with future work guidelines and conclusions in Sections 7.7 and 7.8, respectively.

7.2 Arrays of Photonic Transmitters for Beamsteering

In the preceding chapters, we have commented on some of the most relevant realizations of photonic transmitters for beamsteering at E-band frequencies or beyond. In particular, Fig. 5.2d shows an array of on-chip log-spiral antennas with 2×2 active elements. Fig. 5.3b,c shows also two on-chip antenna arrays with three and two active elements, respectively. The former uses an on-chip antenna that radiates towards a silicon substrate lens, which tends to collimate the beam and produces an early onset of grating lobes ($\pm 5.2°$ before the sidelobes became more powerful than the main beam). The two instances in Fig. 5.3b,c radiate towards free-space, enabling a large scan range ($\approx \pm 30°$), but with a reduced directivity due to the half-power beamwidths of around $30° - 40°$. In addition, Fig. 6.1b shows a leaky-wave antenna for frequency-selective beamsteering, and Fig. 6.2 shows a 1×4 waveguide-fed horn array. The horn array features a gain of 18 dBi, but it may be challenging to scale to obtain a gain > 25 dBi since the structure is fed by waveguides. Additionally, the LWA features a simple means to steer the beam by frequency-selective beamsteering, but at the same time this property precludes the use of a LWA in a wireless link over a large bandwidth.

Finally, one can observe in Fig. 7.1 the two last relevant realizations of photonic Tx for beamsteering at E-band frequencies of beyond. In the first case (Fig. 7.1a) [61], [238], the antenna concept is similar to the 1×4 waveguide-fed horn array shown in Fig. 6.2. In this case, the operation frequency is around 80-90 GHz, so it is fed by W-band coaxial connectors instead of waveguides. The system is, to the best of our knowledge, the only realization wherein the

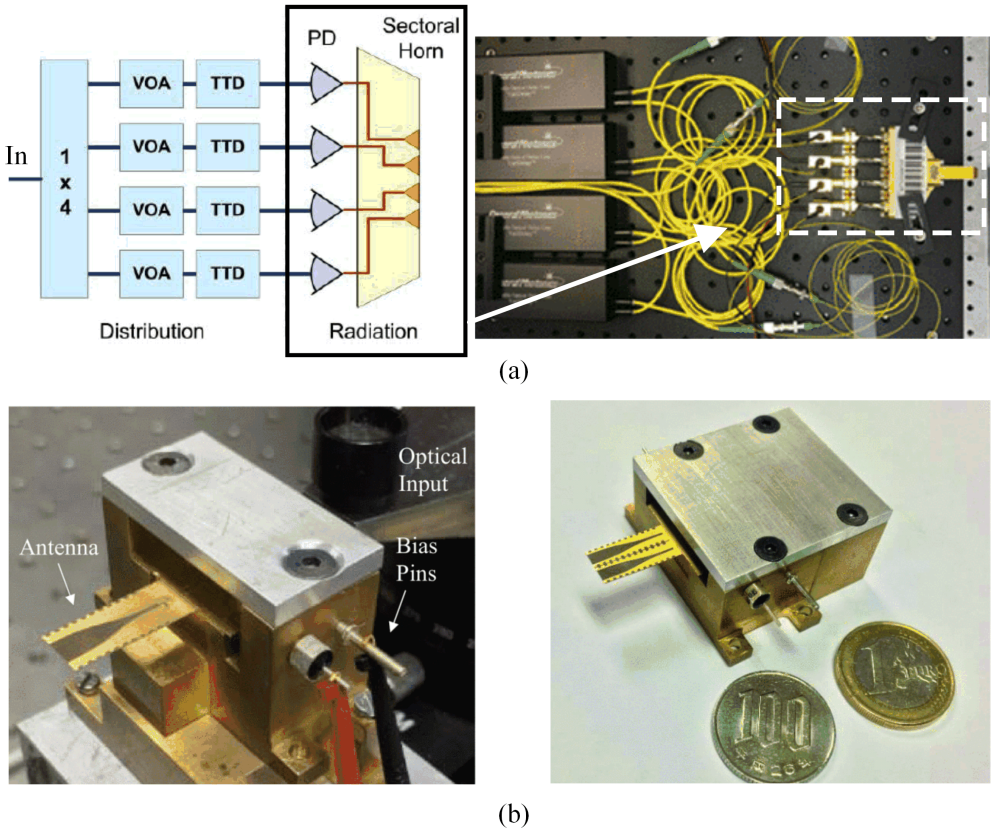

Figure 7.1 Demonstrations of photonic transmitters for beamsteering: (a) sectorial horn fed by an array of 1×4 photodiodes [61], [238]. (b) Left: tapered slot antenna (TSA) and right: two-element TSA array [240], [241].

performance in a wireless link is also assessed. The baudrate is 2.5 Gbaud and, by using 16-QAM modulation, the aggregate data rate is 10 Gbps. They also demonstrate the error-free performance of the link for $\pm 35°$. However, the approach presents several drawbacks: first, the antenna is fed by commercial off-the-self photodiodes with a price tag > 15 kEuro each [239]. Second, the antenna features a gain of 18 dBi but it may be difficult to scale and achieve 25-30 dBi to extend the link distance. Besides, the phased array beamforming network (denoted as distribution in Fig. 7.1a) is substantially bulkier than the antenna.

Fig. 7.1b shows the mm-wave photonic transmitter developed by our colleagues at UC3M for a single antenna (left) and for a two-element array (right). This transmitter is based on PCB technology, and the experimental realizations presented in this thesis have inherited the integration process of the UTC-PDs with the antennas on the PCB. The existence of low-loss, thin PCB substrates allows a cheap and flexible integration framework that can in principle benefit from the possibility of including RF components such as amplifiers or matching networks. Besides, multilayered boards can also be employed to accommodate complex bias networks. PCB technology is also compatible with array antennas, and substrate modes are less important than in on-chip antennas due to a lower dielectric permittivity of typical high-

frequency substrates ($\epsilon_r = 2.2$ for Duroid 5880). Thus, the antennas can radiate directly to free space or to an adapted QO sytem, providing more design flexibility. In Fig. 7.1b left one can observe the the single element transmitter consisting in a wideband a tapered slot antenna (TSA) [240], whereas Fig. 7.1b right shows a 2×1 TSA array. The TSA presents a gain of around 15 dBi and a wideband performance of nearly an octave, enabling a large bandwidth. However, the antenna size constrains the separation between elements in the array configuration to λ_0, which makes it complicated to steer the beam while avoiding grating lobes. Finally, in common with other realizations, the difficulty of integrating sufficient elements (in this case two), results in a directivity below 20 dBi.

The previous discussion indicates that obtaining a directivity > 25 dBi with a photonic-enabled phased array can be challenging at mm-wave frequencies. Instead of using such an approach, a combination of an antenna array with quasi-optical elements to obtain the required directivity enhancement can be a pragmatic solution. Therefore, in this contribution we propose photonic-assisted beam switching. This technique has been used with electronics-based transmitters before but the huge potential that beam switching offers to photonic-enabled transmitters has not been explored yet.

7.3 Beam Switching Versus Phased Arrays

In this section, we compare photonic beam switching against photonic beamforming with a phased array in a mm-wave Tx. Fig. 7.2a shows a typical block diagram of a photonic-enabled phased array transmitter [61], whereas Fig. 7.2b shows the equivalent beam switching alternative adopted in this chapter. In phased arrays, the optical tones modulated according to a data string are carried by an optical fiber (yellow line). The optical input is then divided among the N elements of the array. For a phased array, it is compulsory to control the amplitude and phase of the signal driving each array element. This is accomplished in the optical domain with a variable optical attenuator (VOA) or amplifier, and an optical time delay (OTD), in practice a true time delay. After the VOA-OTD chain, the light illuminates the photodiodes, in turn coupled (blue line) to the antennas that will radiate the modulated mm-wave carrier in the desired direction (in red). Alternatively, for photonic beam switching, N antennas are located at the back focal plane of a lens with focal length f. For an antenna placed at a distance s out of the optical axis, the beam tilt is given from geometrical optics by

$$\tan\theta = \pm s/f, \tag{7.1}$$

where θ is the angle measured respect to broadside, and the sign depends on the clockwise direction of θ. In this case, only one antenna is active at a time, and the beam can be switched among N different directions governed by (7.1). Finally, it is also possible for both approaches to integrate a HEMT amplifier after the photodiode to enhance the emitted power, as in [108].

Compared with a phased array, beam switching presents several trade-offs that make it

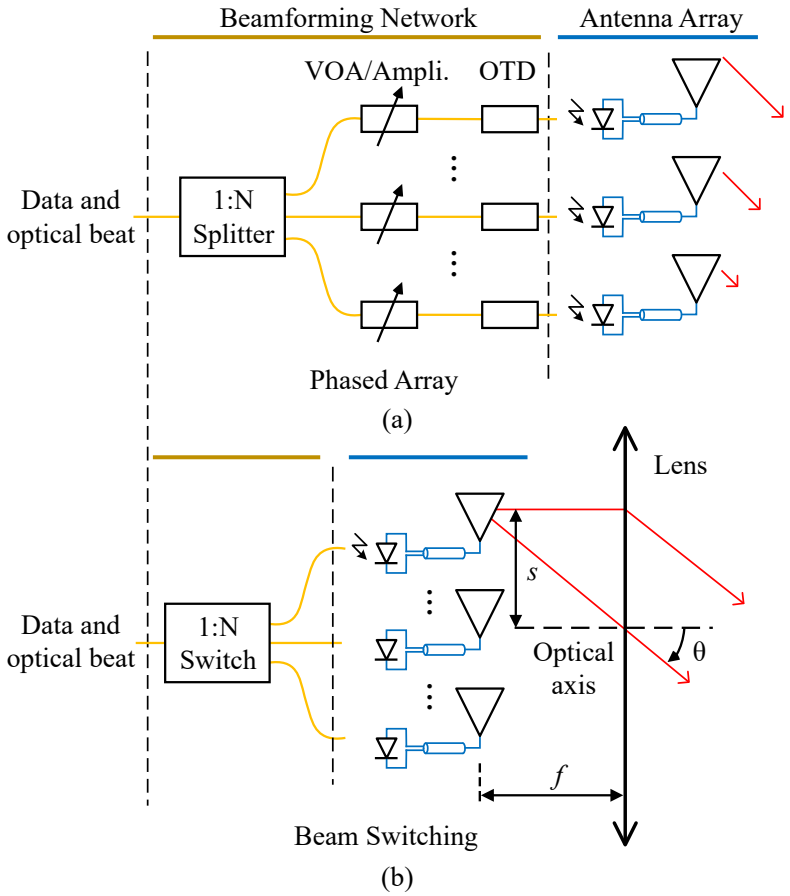

Figure 7.2 Architectures of mm-wave antennas excited photonically for (a) a phased array, and (b) a beam switching array.

an extremely interesting route to explore. First, beam switching can achieve a high directivity (measured > 32 dBi) [107], [242] due to the lens, and not depending on the number of elements, N. Even if beam switching allows discrete scanning directions only, the element separation can be chosen to obtain a beam crossing at −3 dB for quasi-continuous coverage. Conversely, for a uniformly excited planar phased array with a pitch of $\lambda_0/2$, the array directivity is 14 dBi and 20 dBi for 25 and 100 elements, respectively. The overall directivity can be enhanced by about 12.5 dBi using directive elements such as dielectric rod waveguide antennas [203], [243], however, the number of required elements to reach the 30 dBi mark remains high, which makes the array integration difficult.

Another option is the combination of the phased array with a quasi-optical element. Following the discussion of [244], for a confocal dual reflector system with a magnification M, the directivity increase would be M^2 at the cost of a scan range decreased by M. This would imply a huge reduction for values of $M \approx$ 10-20.

Regarding beam switching, the beamforming network (BFN) is largely simplified respect to that of a phased array. In the former, the BFN can be realized using just an optical switch with

low insertion loss (2 dB for the 1 × 4 Agiltron NanoSpeed switch) and low power consumption. For a phased array, the BFN can be substantially bulkier (compare its size with the 4 × 1 array in Fig. 7.1a). Although integrated photonics are reporting more and more promising results [150], [245], the integration of many photodiodes with the BFN and the antennas in a 2-D lattice can prove a challenging task.

However, beam switching does not provide power combining unlike a phased array. This implies that, to achieve the same level of emitted power, the HEMT amplifier after the photodiode in beam switching must feature more gain than that of a phased array. However, given that a photonic Tx is more power-hungry than one based on MMIC technology [108], it can become an advantage when considering the system power consumption. The power consumption in a phased array could be reduced using lower levels of optical intensity to illuminate the PDs. However, the optical to electrical conversion efficiency of a PD is proportional to the optical power squared, and the system efficiency would then be reduced.

Finally, it is to be observed that the reduced number of elements in beam switching will imply having less fibers to align with the PDs, thus simplifying assembly. Besides, III-V components are costly [4], so it is desirable to use as few of them as possible to fulfill the system requirements.

7.4 Antenna Array

In this section, we describe the design and assembly of the antenna array used as primary feed of a dielectric lens. For validation, we also show measurements of the radiation pattern and return loss of a prototype excited with a ground-signal-ground (GSG) probe. Similar to the leaky-wave antenna reported in Chapter 6, the array has been fabricated using printed circuit board (PCB) technology on a 127 μm-thick, high-frequency Duroid 5880 laminate ($\epsilon_r = 2.24$, $\tan\delta = 0.004$ at 60 GHz) [222].

7.4.1 Design

The design of the transmitter has been carried out with High Frequency Structure Simulator (ANSYS HFSS, release 19.0.0) [91] and starts with the optimization of the array element. The array element should feature large impedance and gain bandwidth to provide the desired channel capacity. Radiation should be directed towards one half-space, and the element should be sufficiently small to enable the array configuration.

Microstrip stacked patch antennas are good candidates to fulfill the aforementioned requirements [246], [247]. This approach usually consists in using a driven patch and a coupled parasitic patch with similar dimensions placed at a certain height h from the driven patch, as shown in Fig. 7.3a. The overall structure presents two close resonances, thereby enhancing the impedance bandwidth of the single microstrip patch. Besides, the extended

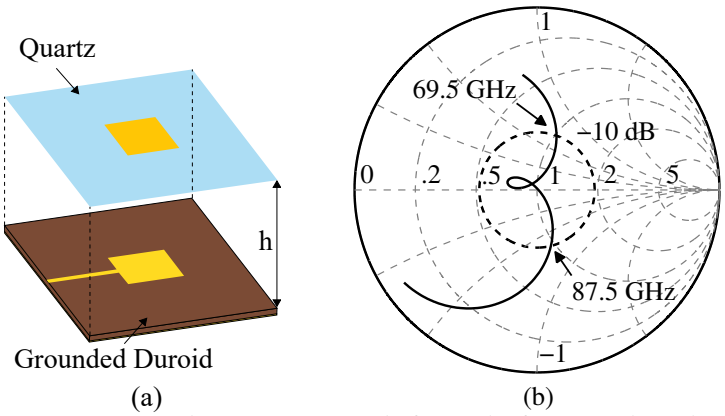

Figure 7.3 (a) Primary array element composed of a stack of two patches. (b) Corresponding input impedance.

coupled cavity in the vertical direction does not increase the area of the element and preserves the symmetry of the structure. Hence, it maintains a fairly symmetric radiation pattern and the phase center, which are desirable characteristics for array configurations used as primary feed in a QO system.

In this case, the bottom patch is directly printed on the PCB whereas the top patch is printed on the bottom side of a 112 μm-thick quartz superstrate layer. Quartz exhibits low loss ($\tan\delta < 0.0004$ at 30 GHz [248]), relatively low ϵ_r (≈ 3.80), and is optically transparent. Therefore, alignment marks on both the PCB and the quartz enable an accurate alignment of the layers. The distance h between the top and the bottom patches is controlled by a silicon spacer (shown later), which can be polished until the desired height. For an optimum h of 300 μm, a proper balance of coupling between patches is achieved. The relative bandwidth is 23% for a reflection coefficient below −10 dB, as shown in Fig. 7.3b. The bottom patch is excited by an 80 Ω microstrip line, since it allows better matching characteristics. Finally, for our design, we have not found a significant improvement in the use of an inset fed patch.

Once the stacked patch has been designed, it is replicated to form two 2 × 2 sub-arrays, as observed in Fig. 7.4. For each sub-array, a feed network divides the incoming signal from the 50-Ohm microstrip line into the four 80-Ohm microstrip lines that feed each of the patches. The 2 × 2 sub-array features a more directive beam, and the patch spacing has been selected to obtain symmetrical patterns along the E- and H-planes. The separation between sub-arrays is 5 mm as is most convenient for beam switching (explained later). The main dimensions of the structure are given in Fig. 7.4.

The next design step is the the feed network between the antenna array and the source. In this case, the antenna array is excited by a 2 × 1 UTC-PD chip on InP [161],[149, Fig. 6]. Each UTC-PD feeds independently one of the sub-arrays.

Regarding the feed network connecting the photodiodes with the antenna, a tapered

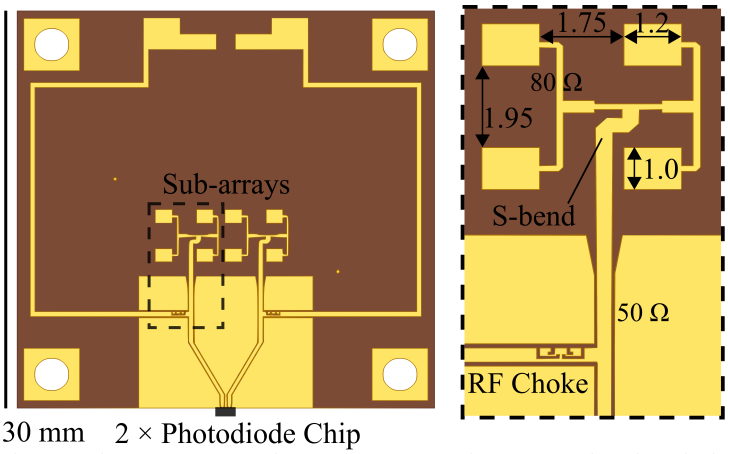

Figure 7.4 Left: designed PCB on Duroid 5880 (VIAS not shown). Right: detailed view of one of the sub-arrays (dimensions in mm). The width and length of the top patches are 1.2 mm and 1.075 mm, respectively.

transition is first used to adapt the coplanar waveguide (CPW) output from the photodiodes grown on InP to the Grounded-CPW (GCPW) on Duroid. Next, both signal lines separate to reach the distance required to feed the 2 × 2 sub-arrays. Perpendicular to the signal lines, one can also observe in Fig. 7.4 the RF chokes made of split-ring resonators as in [249], and the DC interconnections used to bias the photodiodes. These chokes feature an isolation higher than 20 dB on the whole E-band. Last, transitions from GCPW to microstrip line are used to excite the corporate feed network of each sub-array.

7.4.2 Assembly

To assemble the structure, an aluminum housing as shown in Fig. 7.5 is used. It holds the PCB and quartz superstrate, provides a groove to place the UTC-PDs chip, and enables DC electrical connections.

The first step of the assembly is gluing the thin PCB to the housing using an Ag-based epoxy (EPO-TEK). This avoids the PCB from bending due to temperature changes, which could impact the bonding of the UTC-PDs. Next, the silicon spacer and quartz superstrate are positioned, as detailed in the exploded view of Fig. 7.5. The silicon spacer is laser-cut from a standard wafer of thickness 306 μm, which is close enough to the nominal value and it does not require to be polished. As for the top patches and alignment marks on quartz, they are formed using photolithography by a 1 μm-thick gold layer plus a 50 nm Ti adhesion layer. To position the quartz precisely, a micropositioner is used to align the marks in the PCB and quartz layers. Next, the two lateral clamps are fixed to hold the structure in place. The lateral accuracy achieved is better than 20 μm whereas the in-plane alignment tolerance estimated from full-wave simulations is around ±150 μm. For reference, one can observe on the right of Fig. 7.5 the alignment marks on the PCB and quartz superstrate before final alignment.

Finally, the last step of the assembly consists in bonding the UTC-PDs electrical output to

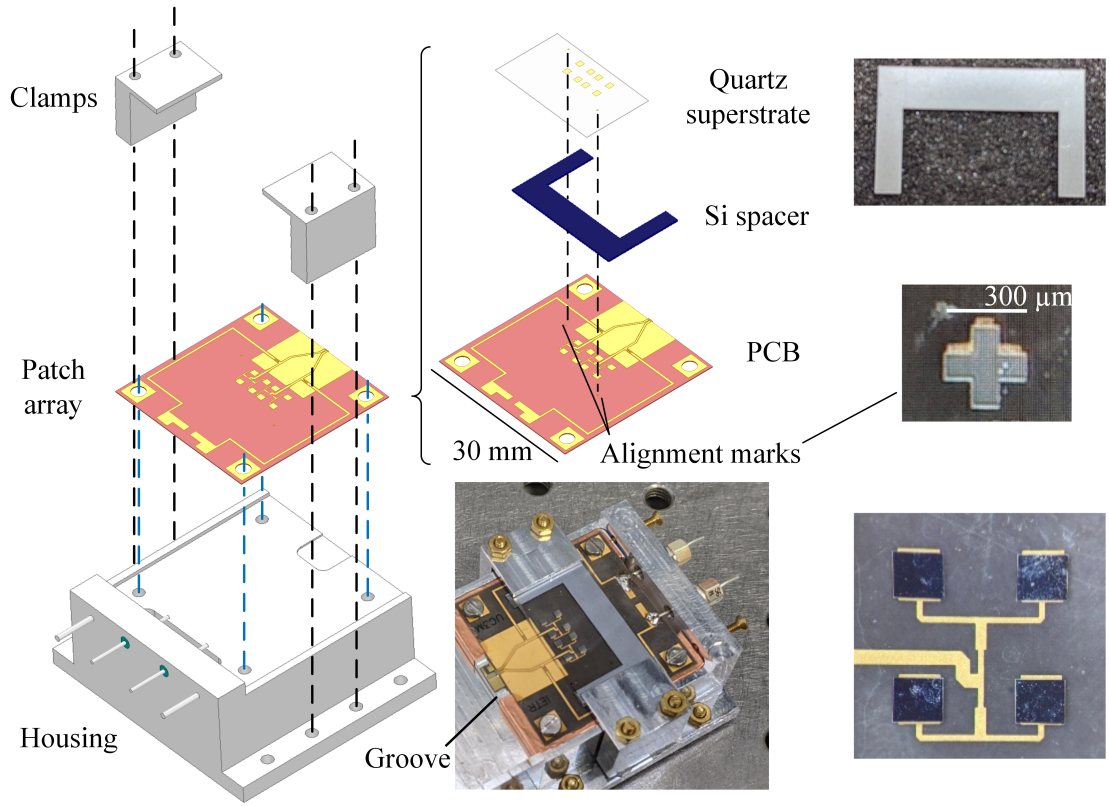

Figure 7.5 Exploded view of the assembled prototype with the different parts detailed.

the PCB. The PD chip is fixed to an AlN block for simpler handling and heat dissipation. In turn, the AlN block is positioned on the housing groove so that the electrical lines of the CPW on InP and the GCPW on Duroid are aligned. It is then fixed to the housing with a UV-curable glue (Blufixx MGS). Next, to perform the bonding, an Ag-based conductive epoxy thread is used. It results in a thick thread ($\approx 60\,\mu$m diameter), reducing the bond inductance as compared to wire bonding [149]. The process was demonstrated and explained in more detail in Section 6.3 and in [149], [250]. The assembled structure is shown on the bottom-right of Fig. 7.5. The grey color of the patches on quartz is due to the titanium layer.

7.4.3 Characterization

To validate the prototype, we have measured the return loss and radiation pattern of a single 2×2 sub-array excited by a coplanar GSG probe (Form Factor ACP 110-T), as shown in Fig. 7.6. The GSG probe was connected to a W-band (75 GHz to 110 GHz) extension head (OML V10VNA2), in turn connected to a Vectorial Network Analyzer (Agilent N5242A).

Fig. 7.7a shows the measured and simulated values of the reflection coefficient of the structure shown in Fig. 7.6. The continuous grey line corresponds to the VNA measurement, calibrated at the output waveguide of the probe. The continuous black line corresponds to the measurement when the probe is de-embedded using the procedure described in Appendix D.

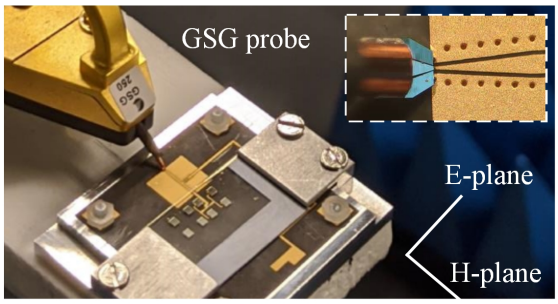

Figure 7.6 Detail of the assembled prototype for excitation with a coplanar GSG probe.

In a nutshell, the procedure consists in measuring S_{11} with the probe for an open, short, and a $\lambda/4$-translated short, all in GCPW, using the same interconnection between the probe and the antenna (shown in the inset of Fig. 7.6), and on the same PCB substrate as the antenna. After, the transmission matrix of the probe plus its interconnection with the antenna is de-embedded from the measurement. The measured reflection coefficient shows a reasonably good agreement with the simulated values in the frequency range that can be tested with the available W-band mm-wave extension head and probe. Discrepancies between simulated and de-embedded curves are mainly attributed to an inaccurate determination of PCB substrate parameters: ϵ_r and thickness. In particular, an inaccurate determination of ϵ_r by 0.02 could explain the horizontal shift near 84 GHz between the simulated and de-embedded curves, in addition, the substrate thickness can vary within 10% [251], which impacts the return loss for low values of S_{11}. For the antenna integrated with the UTC-PDs, the simulated values of $|S_{11}|$ are close to the ones obtained for the single sub-array prototype, below -10 dB between $70.1-84.7$ GHz with a maximum of crosstalk of -15 dB (the UTC-PDs are simulated as lumped sources of 50 Ω impedance, with the structure detailed in [149]).

To measure the radiation pattern, a receiving horn connected to a second W-band extension head, and a 3-D spherical scanner were used. Fig. 7.7b shows the measured and simulated normalized directivity at 80 GHz. At other frequencies, the radiation patterns of the simulated and measured curves present a similar agreement. The relatively high side-lobe at $-50°$ occurs due to the S-bend of the 50-Ω microstrip line that feeds the sub-array (visible in Fig. 7.4), and the side-lobe level stays below -10 dB up to 83 GHz. In the measurements, the ripples in the curves are due to the interference coming from the probe tip. Also, it is not possible to measure beyond 45° in the H-plane because the probe and mm-wave head block the movement of the 3-D scanner. Finally, the measured cross-polarization levels are < -15 dB at broadside. Using the procedure reported in [149], it is also possible to obtain the antenna gain, and the measured and simulated results are shown in Fig. 7.8. A maximum deviation of 0.8 dB with respect to full-wave simulations is obtained, with measured gain values of 12.3 ± 0.7 dB between 75-87 GHz. The gain decrease in the upper end of the frequency window is due to an increased return loss (see Fig. 7.7). The estimated radiation efficiency is > 75 % at E-band frequencies.

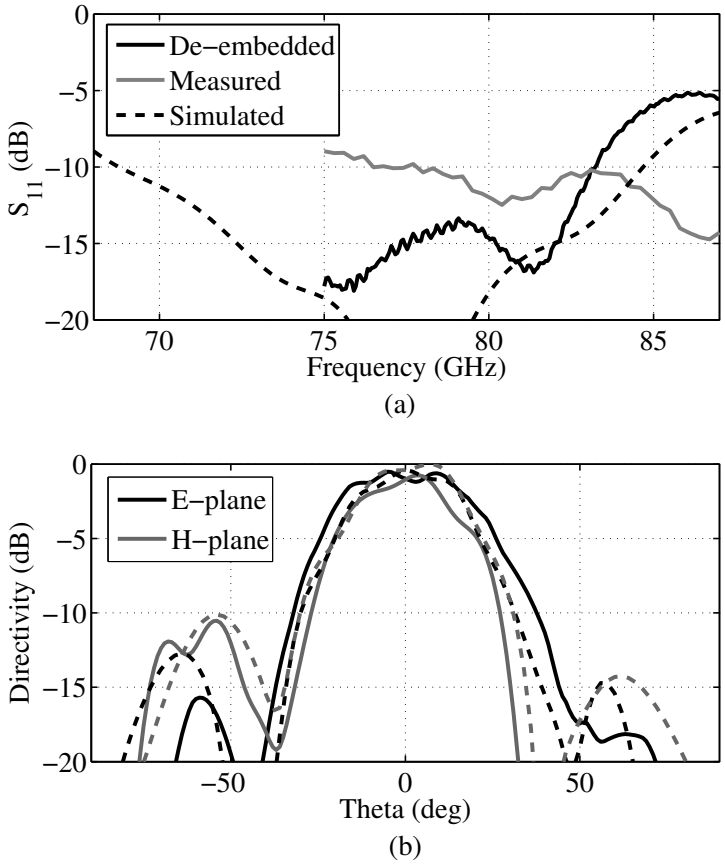

Figure 7.7 (a) Magnitude of the reflection coefficient of the prototype. Dashed line: simulated values, continuous grey line: measured directly from the VNA, and continuous black line: measured after de-embedding the GSG probe with the procedure outlined in [149]. (b) Normalized directivity at the E- and H-planes for 80 GHz. Continuous line: measured values, and dashed line: simulated values.

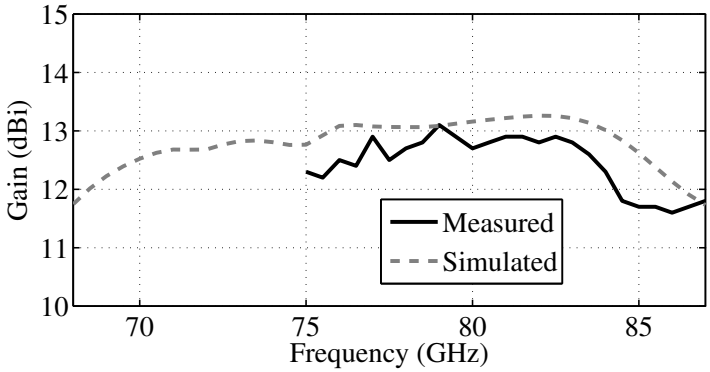

Figure 7.8 Simulated and measured gain of the prototype.

7.5 Photonic Beam Switching

To realize photonic beam switching, the antenna array is placed at the focal plane of a PTFE lens (Thorlabs LAT075) with a back focal length (bfl) of 53 mm and a diameter of 5 cm. The two sub-arrays lie symmetrically $s = 2.5$ mm above and below the optical axis. From (7.1),

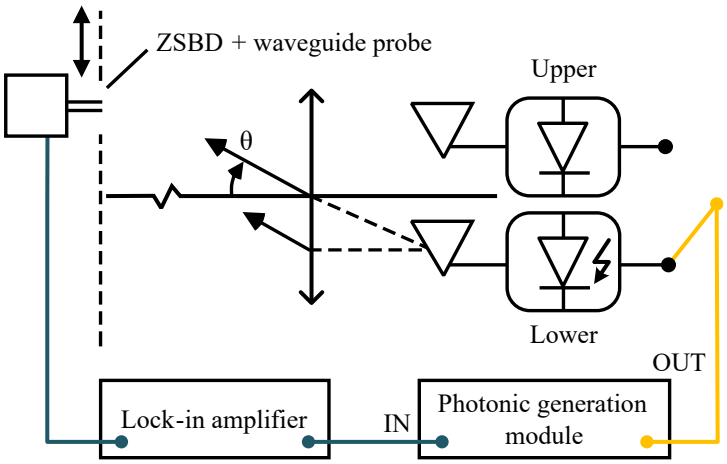

Figure 7.9 Schematic of the set-up used to characterize beam switching. Dark blue line: RF and yellow line: optical fiber.

excitation of one of either photodiodes produces a tilted beam at an angle $\theta = \pm 2.7°$.

Fig. 7.9 shows the set-up schematic to characterize beam switching, and Fig. 7.10a shows the set-up mounted on an optical table. In enables radiation pattern measurements along a vertical cut. At the background of Fig. 7.10a, one observes the photonic generation module which is detailed in Appendix E. It contains the blocks used for a standard approach of mm-wave generation with two free-running lasers [149]. The module output consists of two amplitude modulated, $\approx 1.55\,\mu$m optical tones whose separation is the desired mm-wave frequency. The module input is an RF signal that modulates the output beatnote. For the beam switching experiment, the RF input corresponds to a sinusoidal waveform from a lock-in amplifier (SRS SR830). The module output is directed by a fiber patchcord (depicted in yellow in Fig. 7.9) to a lensed fiber (OZ optics) that illuminates one of the two UTC-PDs in the chip. Precise alignment of the fiber to the optical input of the PD is enabled by a 3-axis micropositioner (Thorlabs Nanomax 313D). A distance corresponding to bfl from the antenna, the lens is placed and aligned with another positioner, as shown in Fig. 7.10c. The receiving side consists of a WR-10 waveguide probe (shown in Fig. 7.10b), in turn connected to a zero bias Schottky barrier diode detector (ZSBD) from VDI [252]. The ZSBD is mounted on a linear translation stage (Thorlabs LTS300) which enables a 30 cm travel range. To avoid undesired reflections and standing waves, the optical table, translation stage, and receiving module are covered with absorber. Finally, to close the loop, the RF output of the ZSBD is extracted with a bias-tee connected to the lock-in amplifier input, and the detected relative amplitude is measured. Lock-in amplification is used because the small electrical aperture of the waveguide probe captures little power. The measurement distance (waveguide probe tip to lens) is $d = 60.5\,$cm, which is a trade-off between angular coverage allowed by the translation range, signal level, and lens far-field (1.15 m). The angular resolution of this detection scheme is 0.12°.

The simulation results of the antenna plus lens (including the annular lens mount) using

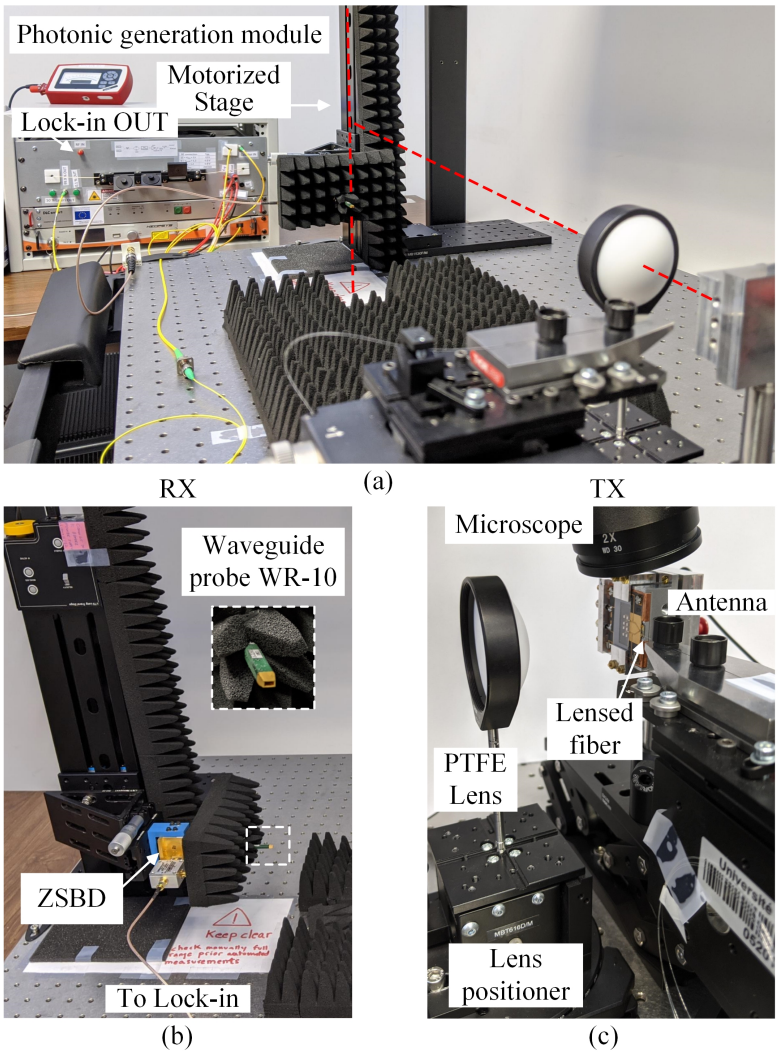

Figure 7.10 Set-up used to characterize beam switching.

ANSYS HFSS' Finite Element-Boundary Integral (FE-BI) boundary conditions are shown in Fig. 7.11a for 75 GHz and in Fig. 7.11b for 85 GHz. The figures also show the measured values. The half-power beamwidths are 5.2° and 4.8°, respectively, and the simulated directivities are 27.5 dBi and 27.9 dBi, respectively (the system does not allow directivity measurements but is expected to be in this range given that the curves are in very good agreement). For a separation between sub-arrays of 5 mm, the beam crossing occurs approximately at −3 dB, as can be observed in Fig. 7.11. Furthermore, the pointing direction is stable within ±0.1° across the E-band.

7.6 Wireless Link Demonstrations

Last, the photonic transmitter is tested in a wireless link. The experimental set-up is is based on the mm-wave wireless link explained in Appendix E and it is similar to that shown in Fig. 7.10. In

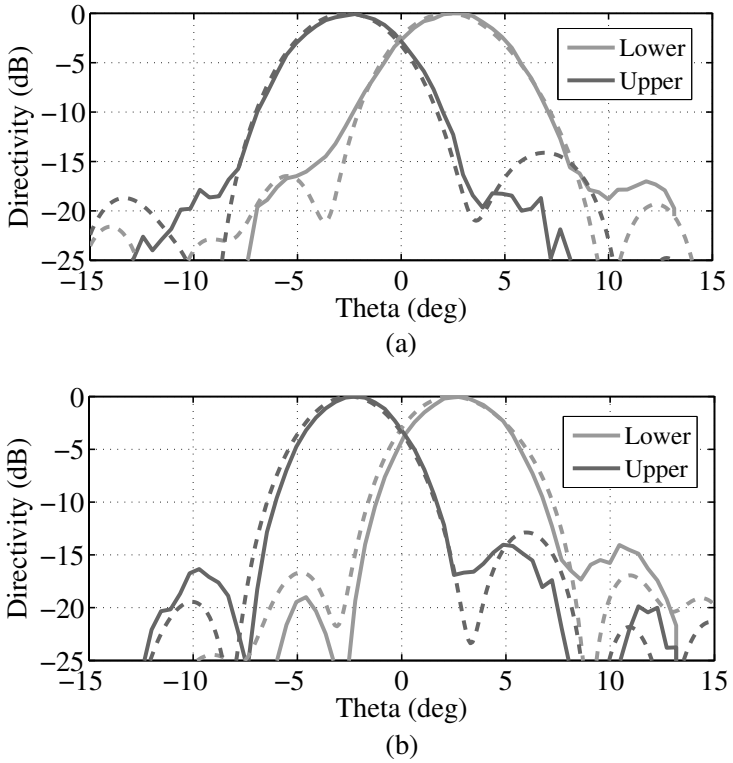

Figure 7.11 Measured (continuous line) and simulated (dashed line) normalized radiation patterns versus elevation angle for the experimental characterization of photonic beam switching for (a) 75 GHz, and (b) 85 GHz. Lower and Upper refer to the sub-array position respect to the optical axis.

this case, the waveguide probe is substituted by a waveguide horn and another 5 cm diameter PTFE lens. At the output of the ZSBD, a 42 dB gain amplifier (Wenteq ABL0300004030) plus a 10 dB gain block (Minicircuits ZX60-14012L-S+) are connected. Finally, the lock-in detector is replaced by an Anritsu MP1763C/1764C bit-error rate tester (BERT).

Fig. 7.12(a) shows the BER versus the detector elevation angle when the upper or lower sub-arrays are active for a carrier in the lower frequency window of the E-band. In turn, Fig. 7.12(b) depicts the same curves but for a carrier in the E-band higher frequency window. Fig. 7.12(c) shows the eye diagram for optimum BER = 10^{-11}. The photocurrent is kept at 3.7 mA and the link distance is also d = 60.5 cm. On-off keying modulation and direct detection are used with a data rate of 5 Gbps, which is limited by the amplifier bandwidth (3 GHz). Still, the link baud rate (5 Gbaud/s) is double of that reported in [61] (2.5 Gbaud/s) using a phased array and 16-QAM modulation with a link distance of 50 cm. The curves in Fig. 7.12(a) and (b) show that, for both E-band windows, link operation is accomplished (BER < 10^{-3}) over an angular range approximately twice as wide with respect to a fixed beam. Thus, the developed Tx yields a system more tolerant to misalignment.

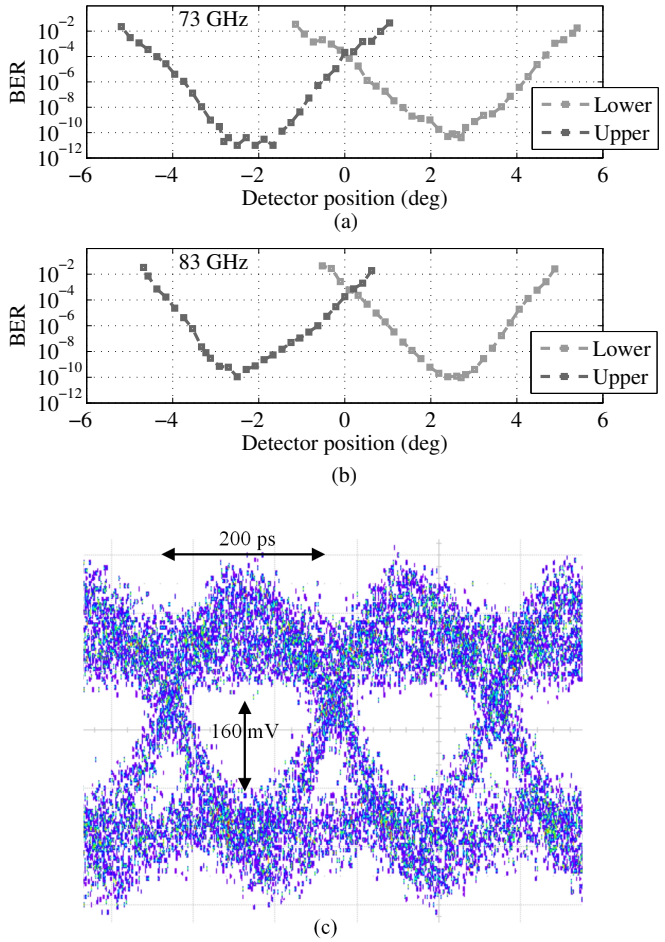

Figure 7.12 (a) and (b): BER versus detector elevation angle for the upper and lower sub-arrays at the two windows of the E-band. (c) Eye diagram for BER= 10^{-11} with a 73 GHz carrier.

7.7 Future Work

In the previous sections, we have shown a realization of photonic beam switching. However, this work presents only an initial demonstration as well as an experimental basis to develop more sophisticated photonic Tx. In particular, future research efforts could be directed towards the following aspects:

- To enlarge the field-of-view using more than two active elements. It is important to mention that the antenna could be mirrored and scaled N-times in 1-D so that switching among 2 × N directions would be possible. Furthermore, previous works on photonic-enabled transmitters in the literature indicate that it is possible to integrate four PDs [61], [64], [65], [236]. Additionally, successful performance in an operator's network field test using a 2 × 2-active element integrated lens antenna (ILA) and an electronic approach for mm-wave generation was accomplished in [242]. The switchable beam eased alignment and allowed deflection compensation of the mounting structure. For a

photonic-enabled ILA transmitter, in addition to compensation, it would be possible to feed the antenna remotely and combine it with the existing fiber-optic network.

- Integrate the UTC-PDs with the fiber. This has been also reported before [172], [173], and it would enable faster beam switching using an optical switch. Currently, the fiber is aligned with a micropositioner to the optical input of each PD, which involves manual work. Hence, this addition would be required by practical applications or a field trial outside a lab environment. In addition, an 1×4 optical switch (Agiltron NanoSpeed) outperforms an RF equivalent (Triquint Semicondudcot TGS4306-FC) in terms of insertion loss (2 versus 3-4 dB), as well as in bandwidth and return loss. Importantly, the losses in the optical domain can be relatively simply compensated by an optical amplifier so that the RF power does not get affected.

- Finally, for the demonstration we have used a commercial lens. A more advanced transmitter would require the optimization and integration of the array together with the optical system. This would result in an ILA with photonic-enabled switchable beams. ILAs with switchable beams have been demonstrated to provide a gain > 33 dBi, including 7-9 dB losses from the feed network, of which 3-4 dB correspond to the RF switch [242]. Such a level of gain approaches the European Telecommunications Standards Institute (ETSI) minimum requirement of 38 dBi for E-band backhauling[113].

7.8 Conclusions of the Chapter

We have demonstrated a broadband solution for beam switching with a photonic Tx at E-band for telecommunications. First, we have discussed the trade-offs and potential advantages of beam switching over beam steering with phased arrays for photonic transmitters at mm- and sub-mm waves. Notably, a simpler BFN and the possibility of obtaining a high directivity while integrating a reduced number of elements. Next, we have presented the design, assembly, and validation of an antenna consisting of two 2×2 sub-arrays of stacked patches fed independently by two UTC-PDs. When the antenna is placed at the focal plane of a PTFE lens, excitation of one of either sub-arrays allows 1-D beam switching between $\pm 2.7^\circ$ with a simulated directivity > 27 dBi. The measured normalized radiation pattern of the transmitter are in very good agreement with full-wave simulations. Finally, by the time of the defense we expect to test the transmitter in a wireless link. Depending on which sub-array is active and on the receiver position, error-free live data transmission at several Gbps should be achieved for a ≈ 60.5 cm link distance. The presented work sets the basis to develop more advanced designs of broadband photonic transmitters with a highly directive and switchable beam.

A number of people have been involved to accomplish the work presented in this chapter, and the different contributions can be summarized as follows: the antenna housing and some fixtures in the beam switching set-up were manufactured by X. Morvan at IETR workshop with a high-precision milling machine and a 3-D printer. The silicon spacer was laser-cut from a wafer by C. Guitton, also at IETR workshop. The PCB was manufactured by CONTAG AG,

and the photolithography of patches on the quartz superstrate was done by O. de Sagazan at Nano-Rennes cleanroom (UR1). For the experiments, we used two chips of photodiodes due to availability. The first chip was lent by B. Globish (HHI Fraunhofer) and it was used for the pattern measurements in beam switching. Integration of this chip to the housing was done by T. Batté at Nano-Rennes cleanroom (INSA) using a pick-and-place machine for stamping, and performing the electrical connections by wire bonds. A second prototype included the same 2×1 UTC-PD chip on an AlN substrate as in Chapter 6, and it was used to investigate the transmitter performance in the wireless link. In this case, the chip was provided by G. Carpintero (UC3M) prior approval of F. van Dijk (III-V Labs Thales-Alcatel), and it was integrated with the transmitter by M. Ali. The set of electronic measurements was taken at LEAT (Université Côte d'Azur) with the guidance of L. Brochier, and F. Ferrero. The rest of the work, including the transmitter design, antenna assembly, and conception of the set-up and measurements was done by the author under the supervision of L. E. García-Muñoz, R. Sauleau, and D. González-Ovejero.

Concluding Remarks

This thesis is the result of the first efforts carried out at IETR towards consolidating a research line in photonic-enabled continuous-wave radiation in the mm-wave range. In a bit over three years, we identified the advantages and drawbacks of the photonic generation of mm-waves, proposed solutions to overcome some of the identified hurdles, and experimentally demonstrated some of them. Nevertheless, the novelty of this topic in our laboratory has also required additional effort. In particular, we had to explore a broader SotA, assess the viability of the proposed solutions, and develop the characterization platform described in Appendix E.

The photonic generation of CW mm-wave radiation through photomixing is no exempt from drawbacks, such as a relatively low emitted power compared to other generation methods. Nevertheless, its advantages outnumber the downsides. The most important benefits include integrated components that provide wideband operation at room temperature, seamless integration with fiber-optic communication networks, and compact systems with coherent detection for spectroscopy and imaging. The previous features have prompted over the last years numerous research works and even commercial systems that use photomixing for high data-rate communications, spectroscopy, and imaging [10], [30], [36], [45], [164], to cite a few. The potential of photomixing has also motivated our research, focused on the study of mm-wave photonic transmitters from an antenna engineering perspective.

Research is uncertain by nature, and a novel circuit model to study the scan impedance of infinite phased arrays of dipoles stemmed from our investigation of photomixing antenna arrays. Although not strictly adhering to our target, our research has provided new insight into a topic widely studied before. Importantly, we have shown that it is possible to spot new knowledge if one devotes himself to a topic thoroughly and passionately enough. The fact that we have not treated a single subject but rather investigated those offering the most potential has had implications in the structure of this manuscript. It has not been straightforward to report and contextualize in a single document the different matters treated. However, we have tried our best efforts to present the contents coherently.

Next, we will again review the thesis main contributions by chapter, comment on the research impact, and discuss future research lines of an exciting project we hope has only got off the ground.

Contributions of the Thesis

Chapter 2 describes the first contribution of the thesis: "An asymptotic approach to analyze the scan impedance in infinite phased arrays of dipoles." Despite the many previous works on infinite phased arrays of dipoles, some of which are seminal papers [73], [79], [93], we have proposed a novel derivation. It is based on the boundary conditions met by the propagating Floquet mode and on an asymptotic approximation for the current along the dipoles. Generally, the model results in equivalent circuits, and it yields original equations and new perspectives to understand this canonical type of antenna. Among the alternative derivations and new expressions in this chapter, one finds: the formulas for the intensity radiated towards each half-space in (2.13) and (2.14), the current distribution in (2.33) (which accounts for arbitrary dipole end load and scan angle in the principal planes), and the scan reactance in E-plane for connected dipoles in (2.38). The developed model provides insight into the physics of the problem, so it is more prone to interpretation than numerical methods or the results of a full-wave simulation. For instance, the model will be very useful for establishing rules of thumb, design guidelines, or quantifying the effect of the main array variables on the scan impedance. However, one has to admit that numerical methods are more accurate than our model. Therefore, the antenna engineer will obtain the most benefit by combining both approaches. The findings on this chapter have been reported in a paper accepted for publication in the IEEE Transactions on Antennas and Propagation ([ii] in the List of Publications).

The next original contribution of this thesis is presented in Chapter 5: "A method for on-chip antenna arrays efficiently matched to UTC-PDs." In this chapter, we have proposed a continuous-wave mm-wave photonic transmitter concept with high emitted power. Currently, a measurement for spectroscopy or imaging takes from several minutes to even some hours. An increase in the emitted power would result in a reduction of the required integration time, thus leading to a faster measurement and enabling widespread use of CW photonic Tx in these applications and even for industrial purposes [10]. To increase the emitted power, we have developed a method to efficiently match an antenna array with photodiode sources using some of the results of Chapter 2. Subsequently, we discussed a practical 2×2 realization. The simulated increase in the emitted power compared to a classical self-complementary antenna was twofold due to the use of four elements with $\times 4$ matching efficiency enhancement. A total of 11 dB peak emitted power increase was obtained when the radiation efficiency was also considered, with a 30% relative impedance bandwidth (-3 dB). Since we did not investigate some additional possibilities (e.g., the inclusion of an RF choke, array pitch, or lens shape), we believe there is still room for improvement. Nevertheless, the presented proof-of-concept already enabled a relevant increase in the radiated power, while the matching method offered more potential than others reported in the bibliography. For instance, the obtained improvement in the matching efficiency is $\times 2$ higher than with the shorted-stub matching circuit in [51], while the latter offered a slightly lower relative impedance bandwidth of 25%. Concerning resonant antennas [179], we obtained a similar increase in the radiated power per antenna (5 dB compared to three to four times in resonant antennas), but the latter feature a

narrower relative impedance bandwidth of 15%.

The rest of the thesis was devoted to the design, fabrication, and testing of antennas with beamsteering capabilities, as required by some applications of current and future mobile networks (5G and B5G). In particular, we have developed and measured two prototypes at E-band, one suited for reconfigurable links and the other one suited to ease alignment and overcome twists and sways from mounting structures in wireless backhauling. In the first case, we used a leaky-wave antenna (LWA) array integrated with photodiodes (Chapter 6), which constitutes one of the first demonstrations at mm-wave or THz frequencies. Due to the frequency-selective scan properties of an LWA, beamsteering is accomplished in one dimension by tuning the emission frequency. Also, the scan range spanned from the backward to the forward quadrants (mitigating the open stop-band effect to include broadside direction) owing to an optimized structure. In addition, the array layout featured scalability. Unfortunately, we could not prove this because we could not get a fully functional photonic Tx with both photodiodes active due to damage of the available chip. We believe that demonstrating a scalable layout with increased emitted power would have added additional value to this contribution, increasing the impact of our work. However, one assumes this sort of risk when different technologies must be combined in interdisciplinary hardware developments. While LWAs present a simple mechanism for beamsteering, as shown, for instance, in the all-photonic radar in [204], the fact that the beam angle changes with frequency is detrimental for high data-rate wireless links. Therefore an application to assist in the reconfigurability of wireless links using a reduced bandwidth was envisaged. The results obtained for this LWA array and the discussion on possible application scenarios were reported in Applied Science ([i] in the List of Publications).

With the second prototype (Chapter 7), we proposed and demonstrated photonic-enabled beam switching at mm-waves. Doing so, it was possible to overcome the drawbacks of a photonic-enabled phased array. For instance, it is possible to obtain a discrete number of directive beams in different directions, while integrating a reduced number of photodiodes. As the SotA revealed, the integration of more than four photodiodes with the antennas is challenging, which makes it difficult to obtain a high gain (>25 dBi) phased array as required in practical applications to overcome the free space loss and attenuation. Besides, power consumption is lower in beam switching with a beamforming network considerably simplified with respect to that of a phased array. To demonstrate the technique, we assembled a prototype consisting of two sub-arrays of stacked patches each fed independently by a UTC-PD. The prototype presented an approximate relative bandwidth of 20% and was placed at the back focal plane of a PTFE lens to enhance the directivity to >27 dBi. Photonic-enabled beam switching was then validated experimentally with a developed ad hoc set-up, where the beam switched between $\pm 2.7°$ depending on which photodiode was excited. The beam crossing was at -3 dB for quasi-continuous coverage. Besides, we expect measurements of the performance in a wireless data link by the time of the defense. To conclude, with this prototype, we have set a framework to develop more advanced photonic transmitters. Potentially the method could resolve one of the biggest problems the approach of photonic generation is facing: to obtain

the high gain required by regulators [113] and practical applications while providing more flexibility with a steerable (switchable) beam.

For completeness, five appendices and two introductory chapters have accompanied the original contributions in the thesis. As mentioned above, these contributions have resulted in several works reported in renowned journals and conferences as listed in the List of Publications. We would like to mention that two papers have been already published in peer-reviewed journals (Applied Sciences and IEEE Transactions on Antennas and Propagation), and a third paper on the photonic-enabled beam-switching will be submitted shortly. Finally, we would like to mention that our work on beamforming will be included in a joint chapter with our colleagues at UC3M in a book edited by leading scientists in the field.

Future Work

We envisage two main future lines of research. The first one is to refine the matching method for on-chip antenna arrays and work towards a practical structure. It would be necessary to add an RF choke in the structure to bias the photodiodes, which could potentially result in more degrees of freedom to further improve the impedance matching. Also, it would be necessary to optimize the radiation patterns and shape of the silicon substrate lens. For that purpose, a method based on physical optics could be used [198]. However, one can also devise different alternatives to the silicon lens, such as dielectric rod waveguides (DRWs) or a transmit array. The DRWs would couple the radiation to free space for each antenna individually. Therefore, beamsteering could be accomplished more simply than with a silicon lens, which tends to collimate the beam parallel to the optical axis. With respect to a transmitarray, it could be a multilayer structure placed at the bottom of the silicon substrate. The transmitarray would enable design flexibility to efficiently couple radiation to free space with an optimized pattern to, e.g., illuminate a parabolic reflector in a spectroscopic system. Finally, it would be necessary to review the aspects related to the assembly and fabrication. Currently, we are seeking funding and partners. Indeed fabricating an on-chip antenna array fed by ultra-fast photodiodes requires highly specialized know-how and funding to support the fabrication runs.

The second research direction is to continue exploring the realizations of mm-wave photonic transmitters, which also entails improvements in the characterization platform. For the mm-wave link set-up, in the short-term, we are aiming to include coherent detection. For that purpose, it would be necessary to substitute the Schottky detector with a mixer and a local oscillator (using, for instance, a signal generator) and the Mach-Zender modulator with a QPSK one. Additionally, with an ongoing project with Institut Photon, we will substitute the two free-running lasers with a bi-frequency laser that presents higher stability and lower phase noise. These parameters are critical for a link with coherent detection, and we expect to achieve data-rates in the order of tens of Gbps with the previous upgrades.

Concerning photonic-enabled beam switching, the presented prototype constitutes only

an experimental basis for more advanced designs. Some works on beam switching with integrated lens antennas that use electronic means for switching and signal generation indicate that reaching high performance is possible with this approach [107], [242]. Besides, we pointed out in Chapter 7 that an optical switch outperforms the RF equivalent in terms of insertion loss and bandwidth. Therefore, there is still great potential in photonic-enabled beam switching that should be investigated. In particular, several options could be explored. The first one is to develop an optimization algorithm to design the lens. In Chapter 7, we used a commercial one, but optimizing an integrated lens antenna would enable us to obtain the high values of gain (>35 dBi) required by practical applications and regulations [107], [113]. Another option would be to integrate the fiber with the photodiodes, as in [172], [173]. This feature would be required for fast switching using an optical switch and for demonstrations in field-trials outside a lab environment. Finally, the last option would be to integrate more active elements to extend the transmitter field-of-view and achieve 2-D beam switching.

A

Detailed Plane Wave Expansion

In this appendix, we detail the steps of the plane wave expansion that relates the electric far-field of an interfacial Hertzian dipole given by (2.1), with the electric field of the infinite phased array of dipoles given by (2.4). Through the appendix, we follow a procedure similar to that in [87, Ch. 4]. We express the field of the array as a double infinite sum of plane waves making use of Poisson's sum formula. For convenience, the geometry is shown again in Fig. A.1a, and we also rewrite (2.1):

$$dE_i = \frac{\mathrm{j}k_0 n_i I \Delta l}{2\pi} Z_0 f_i(\theta,\phi) \frac{\mathrm{e}^{-\mathrm{j}n_i k_0 r}}{r}, \tag{A.1}$$

where the polarization superscripts have been omitted, and the variables have been defined in Section 2.2. Let us now replicate the Hertizan dipole to form a double infinite array of elements in a rectangular lattice with uniform current amplitude and uniform phase progression, as in Figure Fig. A.1b. The element periodicity in the x and y directions is given by p_x and p_y, respectively. Recall that the current for the (q,s) element is given by $I_{qs} = I_{00}\mathrm{e}^{-\mathrm{j}q\Delta\alpha}\mathrm{e}^{-\mathrm{j}s\Delta\beta}$, with I_{00} the current of the $(0,0)$ element located at the origin of coordinates. For clarity in the following development, we note that q and s represent index related to the position of the element in space, whereas s_x and s_y are components of a vector representing the propagation direction of a plane wave. Adding the contributions of the elements along the q row yields

$$dE_i^q = \frac{\mathrm{j}k_0 n_i I_{00} \Delta l}{2\pi} Z_0 f_i(\theta,\phi)\mathrm{e}^{-\mathrm{j}q\Delta\alpha} \sum_{s=-\infty}^{+\infty} \mathrm{e}^{-\mathrm{j}s\Delta\beta} \frac{\mathrm{e}^{-\mathrm{j}n_i k_0 r_{qs}}}{r_{qs}}. \tag{A.2}$$

r_{qs} is the distance of the (q,s) element to the observation point r, that is: $r_{qs}^2 = z^2 + (qp_x - x)^2 + (sp_y - y)^2$. For convenience, it is rewritten as $r_{qs}^2 = a^2 + (sp_y - y)^2$. In the far-field, the θ and ϕ components are orthogonal and the angles are equal for all elements, then, the addition is simply given by a scalar sum in (A.2). We now make use of Poisson's sum formula:

$$\sum_{s=-\infty}^{+\infty} \mathrm{e}^{-\mathrm{j}s\omega_0 t} F(s\omega_0) = T \sum_{\nu=-\infty}^{+\infty} f(t+\nu T), \tag{A.3}$$

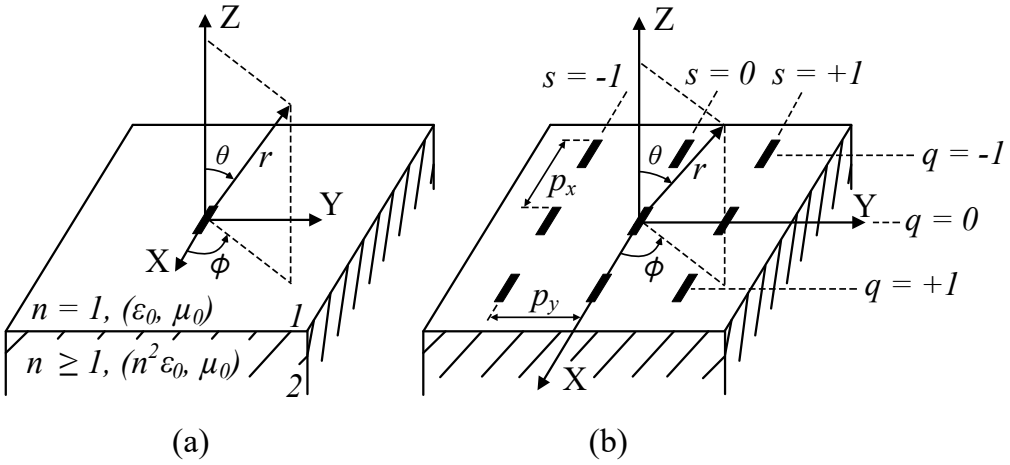

Figure A.1 (a) Hertzian dipole printed on a semi-infinite interface. Medium 1 (z > 0) is characterized by $n = 1$ and medium 2 (z < 0) is characterized by $n \geq 1$. (b) 3 × 3 cut of the infinite array of Hertzian dipoles in a rectangular lattice.

with ω_0 and t denoting variables, $T = 2\pi/\omega_0$, and $F(\omega) = \mathscr{F}\left[f(t)\right]$ ($\mathscr{F}$ denotes the Fourier transform). If we compare the left-hand side of (A.3) with the sum in (A.2), we have $\omega_0 t = \Delta\beta$, and

$$F(s\omega_0) = \frac{\mathrm{e}^{-\mathrm{j}k_i\sqrt{a^2+(sp_y-y)^2}}}{\sqrt{a^2+(sp_y-y)^2}}. \tag{A.4}$$

It is important to recall that $\Delta\beta = k_1 s_y p_y$. k_1 appears in the definition because medium 1 was chosen to define the phase progression of the array elements in Section 2.2 (the phase progression determines the direction of the main beam in medium 1). In addition, since $n_1 = 1$, then $k_1 = k_0$. From the previous, we identify $\omega_0 = p_y$. Hence, $t = s_y k_0$, and $T = 2\pi/p_y$. To find a suitable Fourier transform pair, we have that:

$$\frac{\mathrm{e}^{-\mathrm{j}k_i\sqrt{a^2+(\omega-\omega_1)^2}}}{\sqrt{a^2+(\omega-\omega_1)^2}} = \mathscr{F}\left[\frac{\mathrm{e}^{-\mathrm{j}\omega_1 t}}{2\mathrm{j}} H_0^{(2)}\left(a\sqrt{k_i^2-t^2}\right)\right], \tag{A.5}$$

with $H_0^{(2)}$ the Hankel function of the second kind and zeroth order. After identifying $\omega_1 = y$, it is possible to rewrite (A.2) according to the previous transformation as

$$dE_i^q = \frac{\mathrm{j}k_0 n_i I_{00}\Delta l}{2\pi} Z_0 f_i(\theta,\phi)\mathrm{e}^{-\mathrm{j}q\Delta\alpha}\frac{1}{2j}\frac{2\pi}{p_y}\sum_{\nu=-\infty}^{+\infty}\mathrm{e}^{-\mathrm{j}y\left(s_y k_0+\nu\frac{2\pi}{p_y}\right)} H_0^{(2)}\left(a\sqrt{k_i^2-\left(s_y k_0+\nu\frac{2\pi}{p_y}\right)^2}\right). \tag{A.6}$$

Next, we define $r_\rho = \sqrt{1-\left(s_y/n_i+\nu\lambda_0/\left(n_i p_y\right)\right)^2}$ and rewrite (A.6) as:

$$dE_i^q = \frac{k_0 n_i I_{00}\Delta l}{2p_y} Z_0 f_i(\theta,\phi)\mathrm{e}^{-\mathrm{j}q\Delta\alpha}\sum_{\nu=-\infty}^{+\infty}\mathrm{e}^{-\mathrm{j}y\left(s_y k_0+\nu\frac{2\pi}{p_y}\right)} H_0^{(2)}\left(ak_i r_\rho\right). \tag{A.7}$$

In turn, now we add the contribution of the infinite q rows of the array to obtain the total electric field. Using $\Delta\alpha$ defined in (2.3) as $\Delta\alpha = k_0 p_x s_x$, we obtain:

$$\begin{aligned} dE_i^{\text{array}} &= \sum_{q=-\infty}^{+\infty} dE_i^q \\ &= \frac{k_0 n_i I_{00} \Delta l}{2p_y} Z_0 f_i(\theta,\phi) \sum_{v=-\infty}^{+\infty} \mathrm{e}^{-\mathrm{j}y\left(s_y k_0 + v\frac{2\pi}{p_y}\right)} \sum_{q=-\infty}^{+\infty} \mathrm{e}^{-\mathrm{j}q k_0 p_x s_x} H_0^{(2)}\left(a k_i r_\rho\right). \end{aligned} \tag{A.8}$$

Let us examine Poisson's sum formula in (A.3) with q instead of s and u instead of v, and compare it with the sum in q in (A.8). We can identify:

$$F(q\omega_0) = H_0^{(2)}(a k_i r_\rho), \tag{A.9}$$

and $\omega_0 t = k_0 p_x s_x$. In the right-hand side of (A.9) only a depends on q as $a^2 = z^2 + (q p_x - x)^2$. Then, $\omega_0 = p_x$, $t = k_0 s_x$, and $T = 2\pi/p_x$. The Fourier transform pair that relates $F(\omega) = \mathscr{F}\left[f(t)\right]$ is given by:

$$H_0^2\left(k_i r_\rho \sqrt{z^2 + (\omega - \omega_2)^2}\right) = \mathscr{F}\left[\mathrm{e}^{-\mathrm{j}\omega_2 t} \frac{\mathrm{e}^{-\mathrm{j}z\sqrt{(k_i r_\rho)^2 - t^2}}}{\pi\sqrt{(k_i r_\rho)^2 - t^2}}\right]. \tag{A.10}$$

Furthermore, we identify $\omega_2 = x$. Applying Poisson's sum with the transform pair above in (A.8) gives

$$dE_i^{\text{array}} = \frac{k_0 n_i I_{00} \Delta l}{p_x p_y} Z_0 f_i(\theta,\phi) \sum_{v=-\infty}^{+\infty} \mathrm{e}^{-\mathrm{j}y\left(s_y k_0 + v\frac{2\pi}{p_y}\right)} \sum_{u=-\infty}^{+\infty} \mathrm{e}^{-\mathrm{j}x\left(k_0 s_x + u\frac{2\pi}{p_x}\right)} \frac{\mathrm{e}^{-\mathrm{j}z\sqrt{(k_i r_\rho)^2 - \left(k_0 s_x + u\frac{2\pi}{p_x}\right)^2}}}{\sqrt{(k_i r_\rho)^2 - \left(k_0 s_x + u\frac{2\pi}{p_x}\right)^2}}. \tag{A.11}$$

We have $(k_i r_\rho)^2 = k_i^2\left(1 - \left(s_y/n_i + v\frac{\lambda_0}{p_y n_i}\right)^2\right)$, then, we define:

$$s_z = \sqrt{1 - \left(\frac{s_x}{n_i} + u\frac{\lambda_i}{p_x}\right)^2 - \left(\frac{s_y}{n_i} + v\frac{\lambda_i}{p_y}\right)^2}. \tag{A.12}$$

Equation (A.11) is written in compact form using (A.12) as

$$dE_i^{\text{array}} = \frac{I_{00}\Delta l}{p_x p_y} Z_0 f_i(\theta,\phi) \sum_{u=-\infty}^{+\infty} \sum_{v=-\infty}^{+\infty} \mathrm{e}^{-\mathrm{j}k_0 x\left(s_x + u\frac{\lambda_0}{p_x}\right)} \mathrm{e}^{-\mathrm{j}k_0 y\left(s_y + v\frac{\lambda_0}{p_y}\right)} \frac{\mathrm{e}^{\pm\mathrm{j}z k_i s_z}}{s_z}, \qquad z \lessgtr 0, \tag{A.13}$$

The $\pm$ sign in the last exponential arises when the physical propagation of the modes in medium i away of the interface is considered. It is also to be observed that $f_i(\theta,\phi)$ depends on the propagation directions of the mode.

If the central Hertzian dipole is not located at the origin of coordinates but in $(x_0, 0, 0)$,

it suffices to make the change $x \rightarrow x - x_0$ in (A.13). Considering this, if the dipole is not infinitesimal but has a non-infinitesimal length l, and the current flows in its longitudinal axis, one has to integrate (A.13) over the dipole length to obtain the field from the array of dipoles. The resultant expression for centered-fed dipoles is given by (2.4) and also shown below. It is further discussed and used in Section 2.2 to derive the boundary conditions of the radiated fields.

$$E_i = \frac{Z_0}{p_x p_y} \sum_{u=-\infty}^{+\infty} \sum_{v=-\infty}^{+\infty} \frac{f_i(\theta,\phi)}{s_z} \mathrm{e}^{\pm \mathrm{j} k_i z s_z} \mathrm{e}^{-\mathrm{j} k_0 x \left(s_x + u\left(\frac{\lambda_0}{p_x}\right)\right)} \mathrm{e}^{-\mathrm{j} k_0 y \left(s_y + v\left(\frac{\lambda_0}{p_y}\right)\right)} \int_{-l/2}^{l/2} I(x') \mathrm{e}^{\mathrm{j} k_0 x' \left(s_x + u\left(\frac{\lambda_0}{p_x}\right)\right)} dx'. \tag{A.14}$$

B

The Scan Resistance when Grating Lobes Appear

Section 2.3 of Chapter 2 (Array on a Dielectric Interface), deals with the scan resistance derived from the boundary conditions. The approach is exact and, using a similar analysis, it can be extended to the case where grating lobes are present. In particular, it can be used to examine how the radiation resistance changes at the onset of a grating lobe.

Let us analyze the array shown in Fig. 2.1b. For simplicity, let us consider the case of the array standing in free-space, scanning at the θ direction in the E- or H-plane. The element periodicity is such that a grating lobe lies inside the visible space. Furthermore, an ideal current generator creates a finite current, $I(0)$, at the dipole input terminals.

The total power radiated by each element equals the power radiated by the main and grating lobe modes in the element's apparent allocated area. This area is defined as the projection of the area allocated for an array element in the mode's propagation direction. Then, the radiation resistance can be written as

$$R_r = \frac{1}{|I(0)|^2}\frac{2p_x p_y}{Z_0}\left(|E_{\mathrm{M}}|^2\cos\theta_{\mathrm{M}} + |E_{\mathrm{GL}}|^2\cos\theta_{\mathrm{GL}}\right). \tag{B.1}$$

The subscripts M and GL stand for main beam and grating lobe, respectively. From (2.4), the fields are:

$$E_M = \frac{Z_0}{p_x p_y}\frac{f(\theta_{\mathrm{M}},\phi_{\mathrm{M}})\mathrm{e}^{-\mathrm{j}k_0\vec{r}\vec{s}_{\mathrm{M}}}}{\cos\theta_M}\int_{-l/2}^{l/2} I(x')\mathrm{e}^{\mathrm{j}k_0 x' s_x}\,dx', \tag{B.2}$$

$$E_{\mathrm{GL}} = \frac{Z_0}{p_x p_y}\frac{f(\theta_{\mathrm{GL}},\phi_{\mathrm{GL}})\mathrm{e}^{-\mathrm{j}k_0\vec{r}\vec{s}_{\mathrm{GL}}}}{\sqrt{1-\left(s_x+u\frac{\lambda_0}{p_x}\right)^2-\left(s_y+v\frac{\lambda_0}{p_y}\right)^2}}\int_{-l/2}^{l/2} I(x')\mathrm{e}^{\mathrm{j}k_0 x'(s_x+u\frac{\lambda_0}{p_y})}\,dx'. \tag{B.3}$$

The grating lobe corresponds to the $(\pm 1, 0)$ Floquet mode for E-plane scan and to the $(0, \pm 1)$ mode for H-plane scan. We will take for instance the plus sign. Substitution of $E_{\mathrm{M}}, E_{\mathrm{GL}}$ from the equations above in (B.1), gives:

$$R_r = \frac{1}{|I(0)|^2} \frac{2Z_0}{p_x p_y} \left(\frac{|f(\theta_{\mathrm{M}}, \phi_{\mathrm{M}})|^2}{\cos\theta_{\mathrm{M}}} \left| \int_{-l/2}^{l/2} I(x') \mathrm{e}^{\mathrm{j}k_0 x' s_x} dx' \right|^2 + \right.$$
$$\left. + \frac{|f(\theta_{\mathrm{GL}}, \phi_{\mathrm{GL}})|^2}{\cos\theta_{\mathrm{GL}}} \left| \int_{-l/2}^{l/2} I(x') \mathrm{e}^{\mathrm{j}k_0 x' \left(s_x + \frac{\lambda_0}{p_x} \right)} dx' \right|^2 \right). \tag{B.4}$$

Where $\cos\theta_{\mathrm{GL}}$ is real since the grating lobe lies in the visible space, and $\sin\theta_{\mathrm{GL}} = s_j + \lambda_0 / p_j$, $j = x, y$. From the pattern functions in (2.2) we have $f_1^{\phi} = -1/2$, $f_1^{\theta} = 0$ for H-plane scan ($\phi = 90°$), and $f_1^{\phi} = 0$, $f_1^{\theta} = -\cos\theta/2$ for E-plane scan ($\phi = 0°$).

If the term due to the grating lobe is not present, expression (B.4) reduces to those derived previously ((2.11) at broadside and (2.12a), (2.12b) for the principal planes). In general, this procedure enables to determine the dipole scan resistance in infinite interfacial arrays and it is based on computing the Poynting vector of the propagating modes times the element's apparent allocated area in their corresponding propagation direction.

Let us focus now on the second term corresponding to the grating lobe in (B.4). At its onset, $\cos\theta_{\mathrm{GL}}$ equals zero except if the radiation pattern is exactly zero, which occurs only for E-plane scan. From this, we conclude that R_r presents a singularity when a grating lobe emerges in the H-plane but not in the E-plane. Fig. B.1 shows simulated and calculated results for the scan resistance at different scan angles in the principal planes. The array pitch is $p_x = p_y = 0.6\lambda_0$, and according to (2.6), the onset of the grating lobe occurs at $\theta = 41.8°$. For the calculations, the asymptotic current approximation given by the special case of (2.33) for disconnected dipoles has been inserted in (B.4). At intermediate scan planes, the pattern function is $0 \leq |f_1| \leq 1/2$, therefore, grating lobes will generate an intermediate transition between the two previous. This phenomenon is deeply related to the radiation pattern of the Hertzian element and will occur similarly in connected, disconnected or loaded dipoles. Finally, examination of (2.4) indicates that the step will also be present if the array is located at an interface. These results are also in agreement with the conclusions of [74], [75].

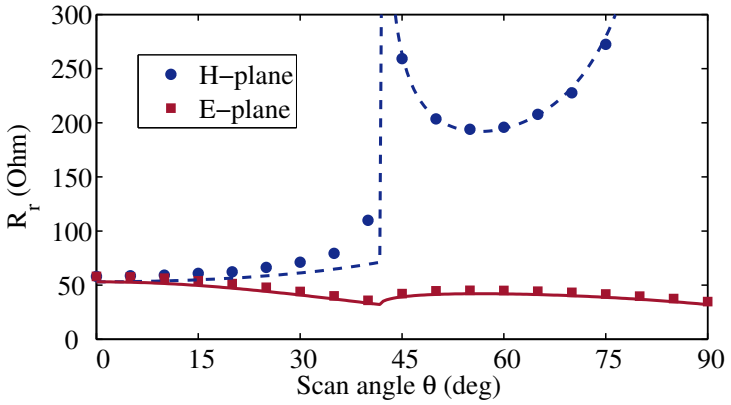

Figure B.1 Variation of the scan resistance with the scan angle for the E-plane (calculated: continuous red line; simulated: red squares) and for the H-plane (calculated: dashed blue line; simulated: blue dots). The array is in free-space, the spacing is $p_x = p_y = 0.6\lambda_0$, $w = \lambda_0/1000$, and $l = \lambda_0/2$. The vertical dashed line corresponds to the onset of a grating lobe.

C

Propagation Properties at Mm-wave and THz Frequencies

Any application of mm- or THz waves will, almost inexorably, involve wave propagation to some extent in a guided or unguided medium. Wave propagation is closely related to interference and diffraction, absorption, reflection, and scattering, all phenomena dependent on frequency. Every spectral region is rich in propagation phenomena associated with its wavelength, and the mm-wave/THz bands are no exception. In this appendix, we describe effects concerning wave propagation in the atmosphere that impose constraints to the main applications of mm-wave/THz science: spectroscopy, imaging, and telecommunications. Comparisons to optical and microwave frequencies are done where pertinent. Also, some propagation properties on general media are given. Guided propagation in dielectric waveguides is not covered, and the reader is referred to [253], [254].

C.1 Free Space Loss

Free space loss (FSL) arises from wave propagation in an unbounded loss-less scenario. It is related to the Friis transmission formula [1, Eq. 2-117], which links the power transmitted by an antenna, P_{tr}, to the power received by another antenna, P_{rec}. The receiving antenna is a distance r in the far-field. Assuming that the transmitted wave is monochromatic of frequency f, and both antennas transmit and receive in the same polarization, Friis equation reads as

$$\frac{P_{\text{rec}}}{P_{\text{tr}}} = G_{\text{Tx}}(\theta,\phi)G_{\text{Rx}}(\theta,\phi)\left(\frac{c}{4\pi r f}\right)^2. \tag{C.1}$$

G represents the gain of the Tx and Rx antenna. To receive maximum power, the antennas are aligned in the direction of maximum gain over the solid angle, in which case the (θ,ϕ)

Frequency (GHz)	λ (mm)	d = 1 m FSL (dB)	G (dBi)	d = 100 m FSL (dB)	G (dBi)
1	300	32.4	1.2	72.4	21.2
100	3	72.4	21.2	112.4	41.2
1000	0.3	92.4	31.2	132.4	51.2

Table C.1 FSL and required antenna gain ($G = G_{\text{Tx}} = G_{\text{Rx}}$) for a loss of 30 dB.

dependence is dropped and G refers to the maximum gain. Expressed in dB, it reads:

$$P_{\text{rec}} - P_{\text{tr}} = G_{\text{Tx}} + G_{\text{Rx}} - 20\log\left(\frac{4\pi r f}{c}\right). \tag{C.2}$$

The last factor in (C.2), without the minus sign, is denoted as FSL. It can be interpreted as the power loss when both antennas radiate isotropically. Since no other losses have been included, it presents the upper limit of the received power. As f or r increases, it amounts to 20 dB per decade (6 dB/octave). Table C.1 shows the FSL at several frequencies and two distances, one characteristic of laboratory experiments, and the other related to outdoors wireless communications. Assuming $G_{\text{Tx}} = G_{\text{Rx}}$, the antenna gain is calculated using (C.2) for a loss of 30 dB.

In general, the allowed loss will depend on the detector sensitivity, the radiated power, system margin, sources of noise, and additional loss. Specifically, link budgets have been discussed in the context of telecommunications in Chapter 3. As frequency increases, FSL compensation requires a higher antenna gain. An antenna with a pencil beam and a high gain of 30 dBi features an HPBW of around $6° - 7°$ [255]. Consequently, high-gain antennas require line-of-sight (LoS) links.

Finally, the gain and effective area, A, of an antenna are related by:

$$G = \frac{4\pi A}{\lambda^2}. \tag{C.3}$$

For a fixed effective area, gain increases with frequency squared. In other words, as frequency increases, high-gain antennas (or QO systems) that would be otherwise prohibitively large to use are more feasible. For instance, [209] uses a pair of 12-in (30.5 cm) reflectors at 300 GHz to achieve a gain of 54 dBi per reflector in a 100 m wireless link.

C.2 Atmospheric Attenuation

In addition to the FSL, the propagation of a wave in the atmosphere will inevitably suffer from attenuation. Attenuation includes both absorption and scattering due to the media present in

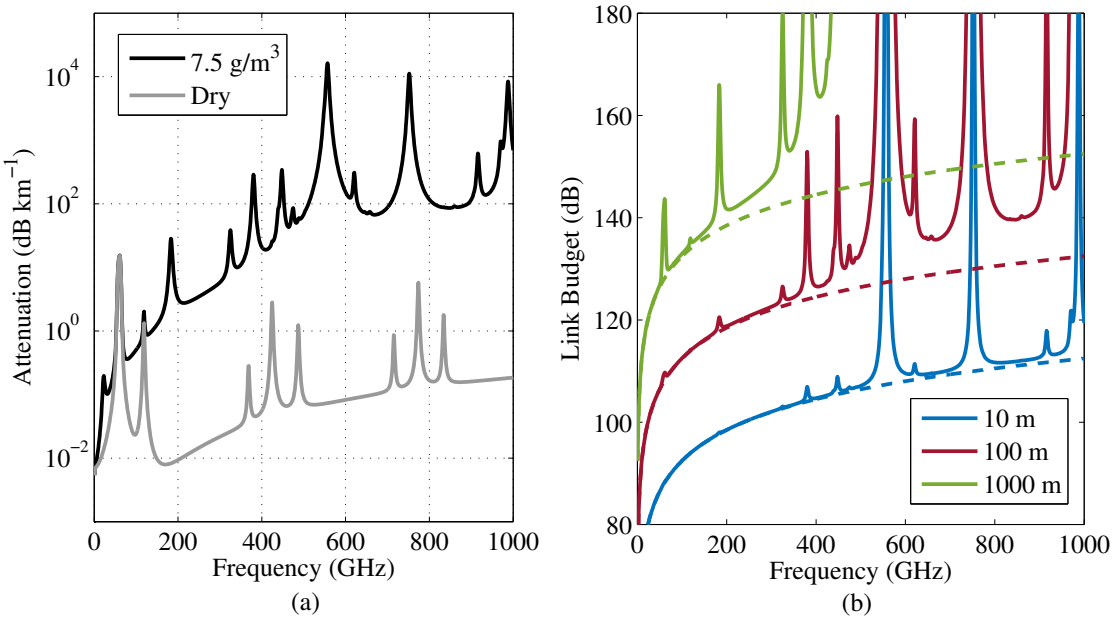

Figure C.1 (a) Atmospheric attenuation for a dry and a standard atmosphere calculated from [232]. (b) Link budget under standard conditions and several propagation distances ($G = 0$).

the atmosphere. In [111], the attenuation due to Mie scattering by spherical airborne particles was calculated (Rayleigh scattering is orders of magnitude smaller) and will not be covered here. In general, attenuation can be characterized by a frequency-dependent loss per unit length, α. A modified Friis equation to account for attenuation in a homogeneous atmosphere reads:

$$P_{\text{rec}} - P_{\text{tr}} = G_{\text{Tx}} + G_{\text{Rx}} - 20\log\left(\frac{4\pi r f}{c}\right) - \alpha r. \tag{C.4}$$

The last two factors (without the minus signs) correspond to the link budget for a link with Tx and Rx antennas with $G = 0$ dBi.

Attenuation by atmospheric gases in the mm-wave/THz ranges is due to oxygen, water vapor, and nitrogen [232]. Fig. C.1a shows the atmospheric attenuation calculated from [232] for a homogeneous atmosphere under standard conditions ($T = 15\,°\text{C}$, $P = 101300$ Pa, and water vapor density $7.5\,\text{g/m}^3$ -59% relative humidity-). The curve for the same T, P conditions but with a dry atmosphere is also calculated. Attenuation due to atmospheric gases at frequencies above 100 GHz is much higher than that in the microwave frequency band. In fact, beyond 1 THz the absorption lines appear almost as a continuum, ruling out long-distance sensing and telecommunications [37]. In Fig. C.1b, the link budget for three different distances is given. Below 0.5 THz, attenuation is dominated by the relatively narrow absorption lines, for instance, O_2 at 60 GHz, or H_2O around 170 GHz. Then, this spectral region offers frequency windows useful for sensing or wireless telecommunications for the

short (< 500 GHz and 10-100 m), medium (< 350 GHz and 100-1000 m), or long-ranges (< 100-150 GHz and 1-10 km) [37]. At visible wavelengths, the atmosphere presents a transmission window with attenuation below 0.1 dB/km [9]. In principle, this makes visible wavelengths more attractive for free space communications, but it will be seen next that other effects play against them more strongly.

Finally, other agents in the atmosphere, such as fog, rain, snow, or dust and smoke particles, further contribute to attenuation. Fog and rain attenuation can be calculated from the ITU recommendations [256] and [257], respectively. Table C.2 summarizes attenuation due to a heavy, 25 mm/h rain and fog with 50 m visibility for microwaves, terahertz, and IR and visible frequencies.

Frequency (THz)	Rain (25 mm/h)	Fog (50 m visibility)
0.01	0.5	<0.01
0.1	11	0.5
1	10	5
100-1000	9	200

Table C.2 Atmospheric attenuation (dB/km) due to fog and rain, extracted from [9].

With respect to microwaves, attenuation from the table above in the mm-wave/THz range is higher but moderate, amounting to less than 20 dB/km, approximately the attenuation in the standard atmosphere for frequencies ≈ 400 GHz. In addition, these contributions are lower than the FSL for a 1 km link (145 dB). When all the effects are combined, they reinforce the need for high-gain antennas. At IR and visible wavelengths, attenuation under foggy conditions is considerably higher, and this gives an advantage to links operating at mm-/THz waves.

C.3 Other Propagation Considerations

Aside from FSL and atmospheric attenuation, other relevant propagation effects of mm- and THz waves include wave-matter interaction in general media, important to spectroscopy and imaging, and susceptibility to scintillation, relevant for telecommunications. Several other effects include quasi-optical propagation, transmission through building materials as wood, brick, or glass, as well as scattering, reflection, and dispersion by rough surfaces. These effects are discussed in [10].

In order to provide some general data to support the chapters before, Table C.3 summarizes the dielectric index and absorption at 1 THz on usual media. Generally, THz waves are highly absorbed (and reflected) by water beyond 1 THz. Mm- and THz waves are also highly reflected by metals, and to a lower extent, by semiconductors. The photon energy at these frequencies is not enough to produce transitions in semiconductors, so they penetrate them. Conversely, the photon energy is comparable to vibration transitions of polar gases and transitions in other

media (explosives, organic molecules), as discussed in Chapter 3 in the context of spectroscopy. Last, plastics are largely transparent, which is useful feature to inspect packaged materials.

Material Type	Optical property	at 1 THz
Liquid water	high absorption	$\alpha \approx 250$ cm^{-1}
Metal	high reflectivity	$> 99.5\%$
Plastic	low absorption	$\alpha < 0.5$ cm^{-1}
	low refractive index	$n \approx 1.5$
Semiconductor	low absorption	$\alpha < 1$ cm^{-1}
	high refractive index	$n \sim 3-4$

Table C.3 Some condensed matter properties at 1 THz, from [125].

Finally, the last effect discussed in this appendix is scintillation. Together with attenuation under foggy conditions, it is one of the reasons why mm- and THz waves are potentially better suited to wireless links than free space optics [258]. While absorption is associated with the imaginary part of the refractive index, scintillation is due to fluctuations in the real part of the refractive index, a cumulative effect caused by spatial and temporal variations of temperature, pressure, or humidity [111]. Fig. C.2 shows schematically the scintillation effect. Following the discussion of [111], under favorable weather conditions, i.e., only water vapor in the atmosphere, $\Delta n_{\mathrm{mmW}} \approx \Delta n_{\mathrm{IR}} = \Delta n$. mmW denotes frequencies in the mm-wave range up to a few hundred GHz, and IR denotes wavelengths around 1.55 μm (193.5 THz). That is, the fluctuations in n are comparable. The phase difference arising from a fluctuation of length, L, is $\Delta\phi = 2\pi\Delta nLf/c$. Thus, mmW are much less susceptible to variations in the refractive index than IR frequencies. These variations cause scintillation for the IR, distorting a flat wavefront to a non-uniform beam with a speckle-like pattern with local and temporal intensity variations. It constitutes the main cause of link length limitation under favorable weather conditions [111].

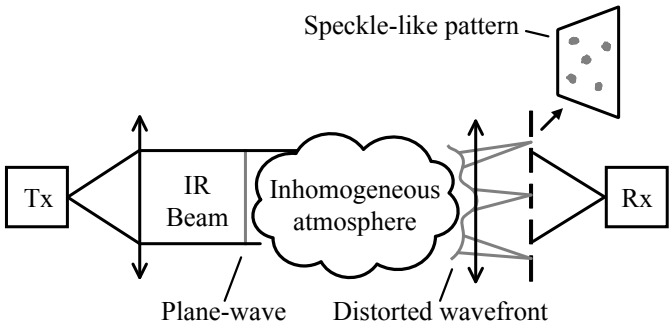

Figure C.2 Scintillation due to spatial variations of the real part of the refractive index, from [111].

D

Electronic Measurements with Coplanar Probes

The electronic characterization of the prototypes presented in Section 6.5.1 (LWA) and Section 7.4 (patch array) was carried out using a VNA with mm-wave extension heads and a coplanar GSG probe (it was the only one available). It enabled measuring the return loss. It also enabled measuring the radiation patterns and gain using an additional 3-D scanner and a receiving horn. However, these measurements comprise the challenge of de-embedding the probe and the interconnection. The interconnection is required to adapt the pitch of the GSG probe (150 μm) to the separation between ground and signal lines of the G-CPW that feeds the device under test (DUT). Indeed, the interconnection, as well as the probe itself, can introduce a relevant contribution to the overall measurement. Therefore, this effect must be removed for accurate device characterization.

In this appendix, we describe an original procedure to de-embed the probe and the interconnection from S_{11} measurements. It is useful to characterize one-port components requiring just one probe, but it can be extended to N-ports provided that the interaction among probes is negligible. Latter, we apply it to determine the return loss and the gain of a sample antenna. A version of the method was presented in work [i] from the List of Publications. The procedure was developed by the author, whereas measurements were carried out at LEAT (Université Côte d'Azur) under the supervision of L. Brochier and F. Ferrero.

D.1 Method for Probe plus Interconnection De-Embedding

The difficulty to fabricate 50-Ω loads at mm-wave frequencies in the same substrate as the DUT makes the use of the standard short-open-load-through (SOLT) calibration impractical [259]. Another of the standard methods, the through-reflection-line (TRL), requires the use of two probes. Alternatively, one finds the open-short or the short-open methods, which include the modeling of parasitic lumped elements introduced by the probe plus interconnection. These methods, however, rely on the specific probe plus interconnection, and it was shown in

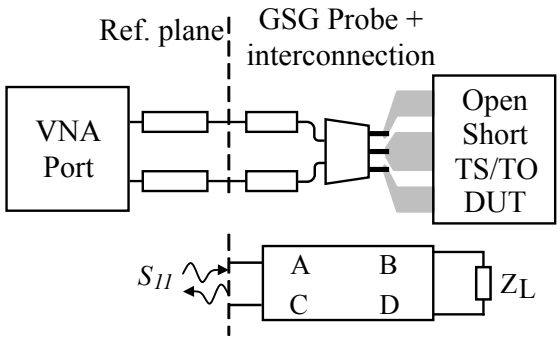

Figure D.1 Schematic used for 1-port S_{11} measurements with different loads: open, short, translated short (TS), translated open (TO), and device under test (DUT), as well as the corresponding network equivalent.

[259] that beyond 30 GHz substantial discrepancies existed between both for a reverse-biased Schottky diode on a silicon substrate.

The method presented herein is a variant from [259] based on simulation and measurements. Since the probe plus interconnection are in general not symmetrical, instead of imposing $S_{11} = S_{22}$, as in [259], an additional load is measured to obtain another equation. The de-embedding method consists of a set of three measurements on test loads whose values are assumed, also enforcing reciprocity. It yields four relations to retrieve analytically the ABCD parameters of the probe plus interconnection. It is assumed that the ABCD matrix of the probing structure is maintained through measurements. It implies that the same interconnect has to be used, in addition to landing the probes at the same positions. Fig. D.1 shows the measurement schematic.

The S_{11} parameter at a calibrated reference plane of an arbitrary structure plus load, Z_L, is given by (D.1), where A, B, C, and D are the ABCD-matrix elements of the structure between the load and the reference plane:

$$S_{11} = -\frac{Z_c Z_L C + Z_c D - A Z_L - B}{Z_c Z_L C + Z_c D + A Z_L + B}. \tag{D.1}$$

A short-circuit (S) and an open circuit (O) are loads that can be relatively simply manufactured in the same conditions as the DUT. Substituting in (D.1), the corresponding relations are found for S and O:

$$D = \frac{B\left(1 - S_{11}^S\right)}{Z_c\left(1 + S_{11}^S\right)}, \tag{D.2}$$

$$C = \frac{A\left(1 - S_{11}^O\right)}{Z_c\left(1 + S_{11}^O\right)}. \tag{D.3}$$

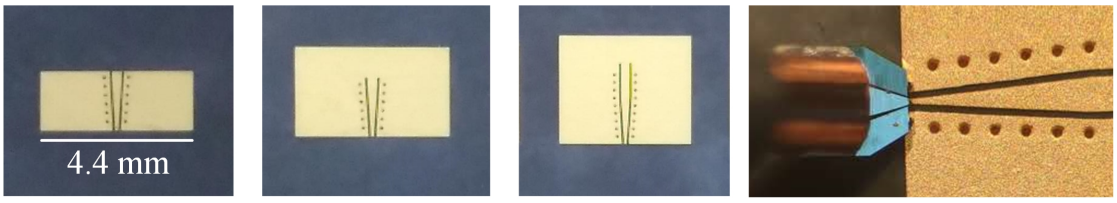

Figure D.2 Different structures measured for probe plus interconnection de-embedding: (a) open-circuit, (b) short-circuit, (c) translated short. (d) Detail of the probe tip and tapered interconnection shared among measurements.

If the probe plus interconnect structure are composed of passive, isotropic materials, one can enforce reciprocity and obtain the following relation:

$$AD - BC = 1. \tag{D.4}$$

Finally, a third load is measured to obtain from (D.1) the fourth relation. It consists of a translated short (TS) or translated open (TO). The characteristic impedance of the transmission line, Z_c, and the propagation constant, are obtained from full-wave simulations. These parameters are simulated easily for standard low-loss 50-Ω transmission lines. The translated length of the load is chosen as $\lambda/8$ to distribute the three loads evenly on the Smith Chart. If broadband measurements were performed, different windows of frequencies would require different translated lengths. It is important to mention that the sign of A (or any other unknown, depending on the procedure) has to be chosen to solve the system of equations. Nevertheless, the choice does not affect the determination of S_{11}.

Fig. D.2a–c shows the manufactured O, S, and TS. To minimize the effect of the GSG pads, and to adapt the probe pitch to the width of the G-CPW, a tapered interconnection is optimized (Fig. D.2d). Additionally, the short and open structures are optimized using full-wave simulations to obtain nominal S_{11} parameters. The same interconnect geometry is used among measurements, and redundant samples are taken to ensure that assuming the ABCD matrix constant is a valid supposition.

Fine Correction and Numerical Check

The above-described method enables retrieving the ABCD parameters of a reciprocal probing structure by solving a system of equations analytically. Nevertheless, (D.2) and (D.3) assume a nominal short and open, respectively. In practice, a realized short will feature mainly an inductive impedance, whereas a realized open, like the one in Fig. D.2a, will feature an impedance mainly capacitive. This assumption can be mitigated by solving the system of equations with the simulated values for the loads, which are closer to the real ones. To do so, a system of equations is built using (D.1) for the three measured loads as well as the

reciprocity condition in (D.4). The system is then solved with a nonlinear solver with the ABCD parameters retrieved before as the initial guess.

The method and fine correction were implemented in a MATLAB code. It was first checked numerically with several $\pi-$networks. In all cases, the ABCD parameters were retrieved successfully. Fig. D.3 shows the retrieved values for the method and the fine correction. The test values correspond to the ABCD matrix of a network composed of a length of TL ($Z_c = 50\,\Omega$, length = 5 mm) and a shunt inductor of 0.1 nH. Since the same values of load impedance, propagation constant, and characteristic impedance are used to generate numerically S_{11} data for the test, it is not surprising that the algorithm recovers exactly the test values (to numerical error precision) when the system of equations is solved using the fine correction.

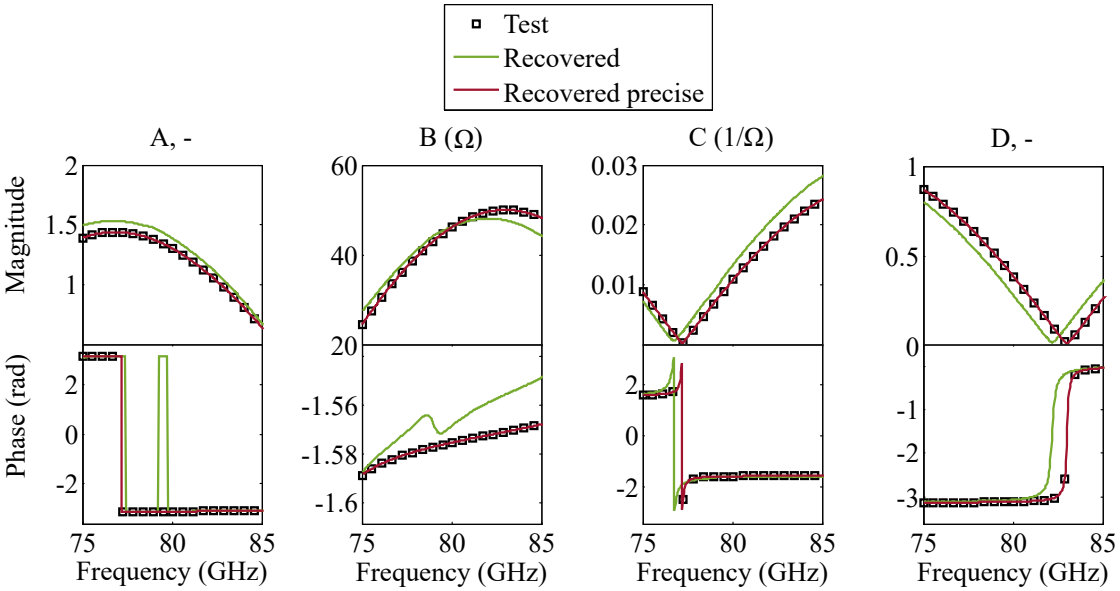

Figure D.3 Retrieved ABCD parameters from a numerical test. Squares = test. Solid green = recovered using the de-embedding method, and solid red = recovered using the precise de-embedding method.

D.2 Measurements of Return Loss

Once the ABCD matrix of the probe plus interconnection is obtained using the method above, it is a simple matter to retrieve the de-embedded S_{11} of the DUT. It suffices to perform an S_{11} measurement on the DUT (S_{11}^{M}), and then to solve for Z_L in (D.1), obtaining:

$$Z_L = \frac{Z_c D\left(1+S_{11}^{\mathrm{M}}\right) - B\left(1-S_{11}^{\mathrm{M}}\right)}{-Z_c C\left(1+S_{11}^{\mathrm{M}}\right) + A\left(1-S_{11}^{\mathrm{M}}\right)}. \tag{D.5}$$

The de-embedded value of S_{11} is finally obtained from the definition: $S_{11} = (Z_L - Z_c)/(Z_L + Z_c)$ for a normalizing impedance Z_c. Fig. D.4 shows the magnitude and phase of the reflection coefficient for the one-row LWA array for directly measured, de-embedded, and simulated data. The fast variations of the argument in the curve of measured data are due to the waveguide

that interconnects the probe with the mm-wave head, around 10 cm long (see Fig. 6.13b).

Even if the method successfully de-embedded the reflection coefficient for the prototypes tested, it could be improved. In particular, the argument of S_{11} in Figure D.4 suggests some deviation between the relative permittivity of the PCB substrate, and that used in the method and simulations. In particular, the value used is provided in [222] for 60 GHz, which already differs substantially from that provided by the manufacturer at 10 GHz (refer to Section 6.5.1). An accurate characterization of the relative permittivity of the substrate could improve the agreement between simulated and de-embedded data. Additional sources of disagreement have been discussed in Sections 6.5.1 and 7.4.3.

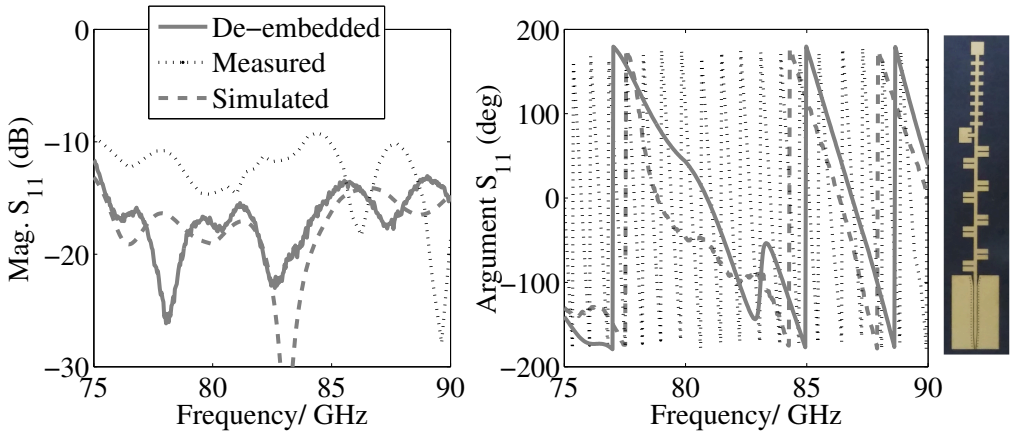

Figure D.4 Reflection coefficient for the one-row LWA prototype adapted for probe measurements. Inset: view of the prototype.

D.3 Measurements of Radiation Pattern and Gain

Measurements of the radiation pattern are performed with an additional 3-D scanner and a receiving horn, as shown in Figure D.5. To measure the directivity, it suffices to record the detected intensity around a sphere whose center is coincident with the antenna. Since the probe and mm-wave head block a substantial part of the solid angle (refer to Fig. 6.13 or Fig. D.5), it is not possible to retrieve the total radiated power reliably. Hence, the directivity curves shown in Fig. 6.15a for the LWA, and in Fig. 7.6 for the patch array, are normalized at each frequency. Nevertheless, it is possible to measure the absolute gain of the antenna using a reference horn. The procedure is as follows:

The (maximum) absolute gain for an antenna is defined as [1, Eq. 2-49b]:

$$G = \left(1 - |S_{11}|^2\right) \frac{4\pi U}{P_{\text{in}}}, \tag{D.6}$$

where U is the maximum radiation intensity and P_{in} is the incident power on the antenna. To proceed with the measurement, first, the intensity of a horn of known absolute gain (G^h) is

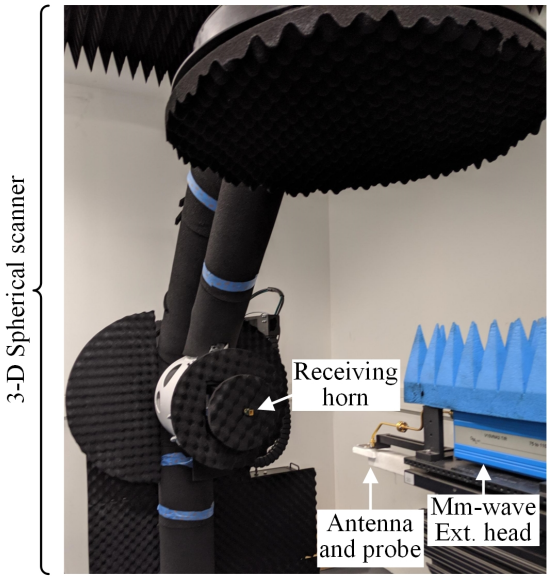

Figure D.5 Detail of the set-up used for radiation pattern and gain measurements (Ext. = extension). The receiving horn is detecting the end-fire amplitude radiated by the antenna.

measured. From (D.6), we obtain:

$$U^h = \frac{P_{\text{in}} G^h}{4\pi\alpha\left(1-|S_{11}^h|^2\right)}, \tag{D.7}$$

where α includes losses due to the receiving part of the experiment. Next, a measurement on the DUT is performed maintaining the sphere radius:

$$U^M = \frac{P_{\text{in}} G^M}{4\pi\alpha\left(1-|S_{11}^M|^2\right)}. \tag{D.8}$$

From the ratio of intensities we can retrieve the measured value of gain for the DUT:

$$G^M = \frac{U^M\left(1-|S_{11}^M|^2\right)}{U^h\left(1-|S_{11}^h|^2\right)} G^h. \tag{D.9}$$

To remove the effect of the probe plus interconnection it is necessary to recalculate the incident power on the antenna, P_{in}^A, and latter use: $G^A/G^M = P_{\text{in}}/P_{\text{in}}^A$ (G^A is the gain of the antenna that we want to determine). The incident power is given from the standard definition of voltages and currents in a two-port network, e.g., [226, Figure 4.11a]:

$$P_{\text{in}} = \frac{|V_1|^2}{2Z_c|1+S_{11}^M|^2}, \qquad P_{\text{in}}^A = \frac{|V_2|^2}{2Z_c|1+S_{11}|^2}. \tag{D.10}$$

V_1 and V_2 correspond respectively to the input and output voltages of the two-port network given by the probe plus interconnection. S_{11} is the de-embedded reflection coefficient of the antenna as calculated in the preceding section. Also, we have that $V_1 = V_2(A + B/Z_L)$ with Z_L the input impedance of the antenna. Thus, the ratio of incident powers is given by:

$$\frac{P_{\text{in}}^A}{P_{\text{in}}} = \frac{1}{|A + B/Z_L|^2} \frac{|1 + S_{11}^M|^2}{|1 + S_{11}|^2}, \tag{D.11}$$

where A and B are the parameters of the ABCD matrix of the probing structure determined before. Since the probe and the tested antennas are approximately well matched to 50 Ω ($S_{11} \lessapprox -10$ dB), the ratio of incident power is roughly given by the insertion loss of the probing structure, $|S_{21}|^2$. Indeed, (D.11) reduces to $|S_{21}|^2$ when the antenna is matched to the output impedance of the probing structure. The insertion loss are estimated around 1.8 dB. For perspective, the loss of the probe given by the manufacturer are 1.5 dB [260]. Results and discussion of gain measurements employing this procedure are found in Section 6.5.1 for the LWA, and Section 7.4 for the patch array.

E

Mm-Wave Wireless Link

The performance indicators of data transmission in a mm-wave wireless link have been investigated as part of the prototype characterization in Chapters 6 and 7. Although the set-up of Professors Carpintero and García-Muñoz at UC3M was used for the LWA in Chapter 6, we have established an experimental platform at IETR for future projects under this new research line. For the set-up, we targeted real-time 10 Gbps data transmission at E-band with commercial off-the-shelf components. The set-up for the wireless link shares many features with the architectures of other experiments. Examples of these others include live retransmission of a screen to a second screen, as described in Section 6.5, or the experimental investigation of photonic beam switching in Section 7.5. For the latter, we additionally used a computer-controlled motorized linear stage onto which we mounted the detector, as shown in Fig. 7.10, and it will not be shown here.

To avoid redundancy with other parts of the manuscript, in this appendix, we will mainly focus on the practical aspects of the set-up. Fig. E.1 top shows the block diagram, and Fig. E.1 bottom shows the set-up deployed for measurements carried out at CNRS's Persyst platform in ENSSAT, Lannion. The link follows a standard approach of mm-wave photonic generation and amplitude modulation with direct detection [261]–[263] using a zero-bias Schottky barrier diode detector (ZSBD) [252]. The set-up is composed of four modules to ease transportation and interchangeability and to potentially enable the characterization of outdoor links. The four modules listed below are detailed in the following sections:

1. Photonic generation of the mm-wave carrier and modulation, including also the photonic Tx.
2. Detection and baseband electronics.
3. A quasi-optical rail system, in which there are mounted:
   (a) A photomixing antenna on the transmitter side.
   (b) A zero-bias Schottky diode detector on the receiver side.

4. Software for computer control.

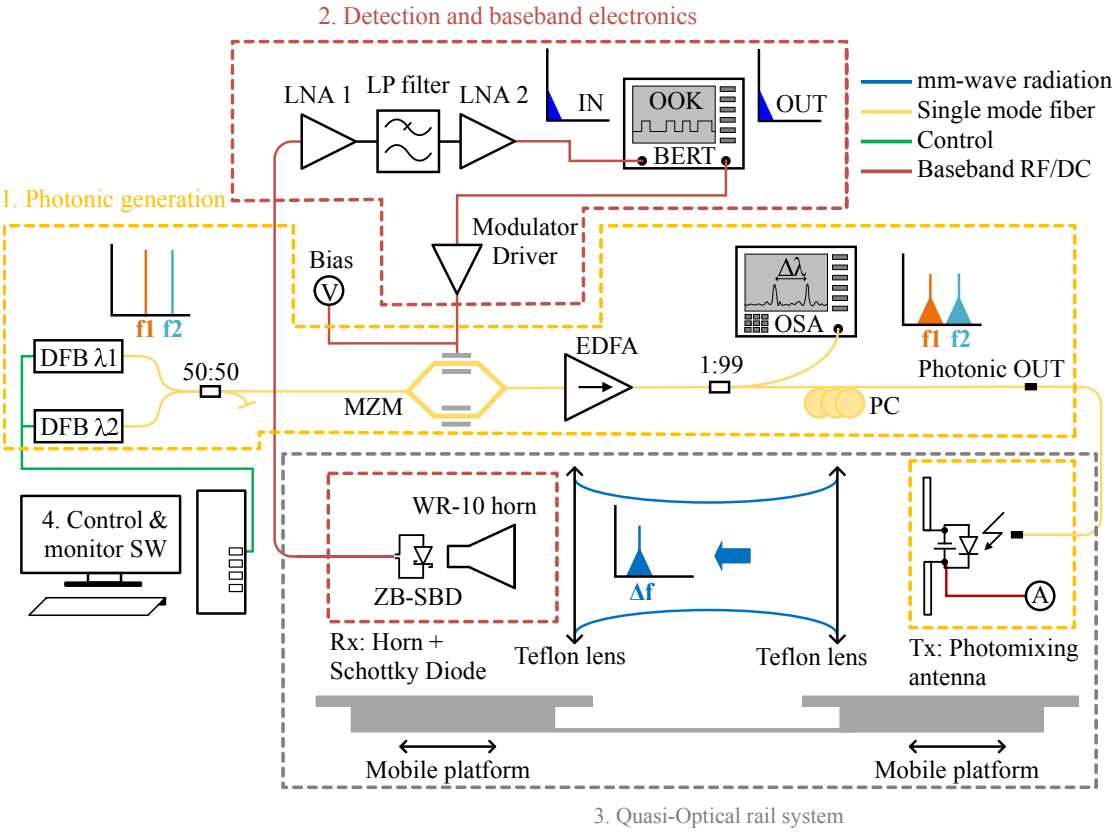

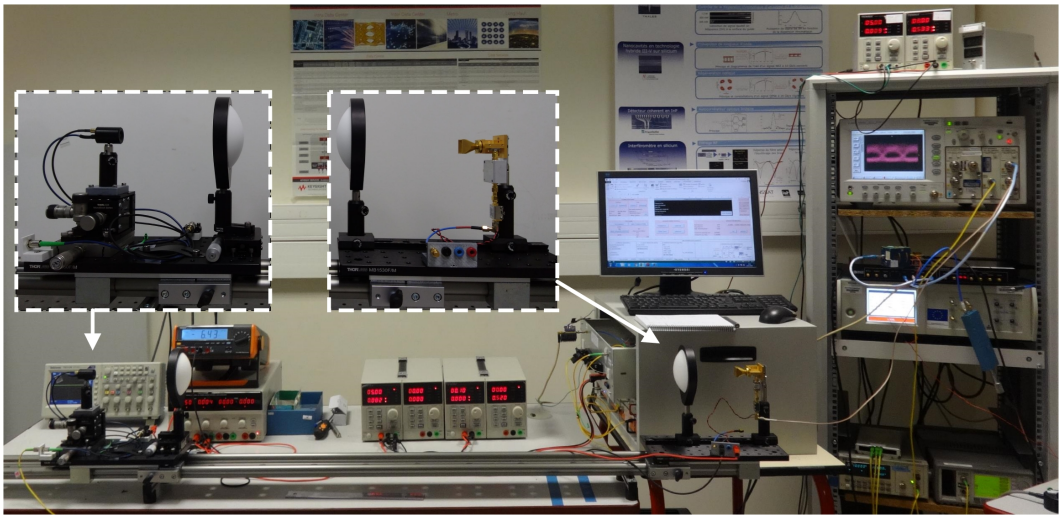

Figure E.1 Top: schematic of the mm-wave wireless link, including photonic generation and data modulation for the optical sub-carriers, the quasi-optical system, and the electronic detection using a ZSBD. Bottom: photo of the set-up mounted at ENSSAT in Lannion according to the schematic above. The rack on the right-hand side of the picture contains the BER tester from Persyst platform.

E.1 Module for Photonic Generation

The module of photonic generation and mm-wave photonic Tx constitutes one of the main blocks of the experimental set-up. It is schematically encircled in yellow in Fig. E.1 top.

In a nutshell, optical heterodyning is used to generate a mm-wave signal. The two optical tones or sub-carriers are generated by two frequency-tunable, distributed feedback laser diodes operating at C-band (Toptica Photonics DFB Pro BFY [32]). The lasers are accompanied by a control unit (Toptica DLC Smart) that sets the temperature and current of the lasers so that they emit equal output power (±0.5 dB) and maintain a fixed difference frequency (f_{RF}) defined by the user.

There are two possible schemes for amplitude modulation; the first one is double optical sub-carrier modulation, where both tones are modulated, and the other is a single tone modulation where just one sub-carrier is modulated. We have selected the former since it offers a higher SNR [110].

Amplitude modulation of optical frequencies can be carried out with a Mach-Zehnder modulator (MZM). The transfer function of such a modulator under pull-push operation for the electric field is given by $\cos(\pi V/(2V_\pi))$ [264], where V is the voltage driving the modulator. In general, V is composed of a DC term plus the RF signal that we want to transmit, for instance, a 5 Gbps non-return to zero pseudo-random binary sequence (PRBS). V_π is the required V to change from maximum to zero power transmission. If the arms of the MZM are of unequal length, the transfer function presents a phase shift that can be overcome with the DC bias. When both optical sub-carriers are intensity-modulated, following (4.3), the current generated by the photodiode in the Tx reads as

$$I \propto P\left(1+\cos(2\pi f_{RF}t+\phi)\right)\cos^2(\pi V/(2V_\pi))\,. \tag{E.1}$$

We recall that P corresponds to the average incident optical power, and the RF power corresponds to I squared. Since the characteristic frequencies of V are $\ll f_{RF}$, only the component $\cos(2\pi f_{RF}t+\phi)\cos^2(\pi V/(2V_\pi))$ in (E.1) is radiated and detected. Thus, for a power detector where the readout voltage is proportional to the power of the incident signal (such as a ZSBD), we have:

$$V_{\mathrm{readout}} \propto 1/2\cos^4(\pi V/(2V_\pi))\,, \tag{E.2}$$

where variations with f_{RF} have been averaged. If the MZM is DC biased at its quadrature point Q (where the power transfer equals 1/2) with positive slope, its power transfer function is approximately linear: $\cos^2(\pi V/(2V_\pi)) \approx 1/2+\pi V_{AC}/(2V_\pi)$ for $|V_{AC}| < V_\pi/2$. V_{AC} corresponds to the RF signal driving the modulator, and we have denoted it in this way to avoid confusion with the carrier frequency f_{RF}.

Since the readout voltage is not linear with V_{AC} but with its square, double sub-carrier modulation is compatible with on-off keying (OOK) but not with higher multilevel modulation formats (such as PAM4). Finally, for the maximum level difference in (E.2) between the 0 and 1 symbols, the peak-to-peak amplitude of the AC signal equals V_{π}.

Once the modulation and detection scheme has been clarified, we continue explaining the photonic generation module. In this module, first, the optical sub-carriers are combined and intensity-modulated (OOK) using an MZM from IXBlue (MX-LN-20-PD) [265]. The operating bias point of the modulator is set to the quadrature point by a bias controller (IXBlue MBC-DG-LAB-A1), but it could also be set manually after characterization of the transmission-DC voltage curve of the MZM. Next, the optical power is amplified by an Er-Doped fiber amplifier EDFA CEFA-C-PB-HP from Keopsys [266] to approximately 14 dBm. After, part of the optical signal is monitored with an OSA (Yokogawa AQ6370D [267]), and the rest goes through a fiber polarization controller (PC) whose output drives the photonic transmitter. A PC is required because the optical input of the UTC-PD is a dielectric waveguide sensitive to the polarization of the incident light.

All of the previous components but the OSA and photonic Tx have been put assembled in a rack box, as shown in Fig. E.2. This assembly helps to improve portability of the experimental set-up when medium-/long-range link measurements have to be carried out in halls or outdoor environments. Furthermore, more modules can be added to the rack box. In particular, in a future project with Institute Photon, we will investigate the employment of a low phase noise, high stability, bi-frequency laser in a coherent communication link. This laser source will substitute the present free-running lasers since it has been shown that their performance deteriorates the BER in coherent communications [30], [110]. The bi-frequency laser would be included in a 1U-rack, only needing to switch a few connections to re-establish the module operation.

The rack box also includes the modulator driver (IXBlue DR-DG-20-MO). It is used to adapt the amplitude of a non-return to zero PRBS from the BERT (0.8 Vpp) to the RF input of the MZM (6 Vpp). The RF data from the BERT is directly fed to the "RF In" port shown in Fig. E.2. The rack box also includes several required DC connections. Finally, the "Photonic Out" port with the two modulated optical sub-carriers is connected by fiber to the mm-wave photonic Tx.

The last part of the photonic generation module is the Tx. In the example of Fig. E.1, it corresponds to a commercial one from Toptica Photonics based on a high-speed InGaAs photodiode integrated with a bow-tie antenna [34]. The transmitter is placed at the focal point of a 10 cm diameter Teflon lens that collimates the beam. They are both mounted on a movable platform, as explained after.

The main advantage of photonic generation and signal modulation is that the mm-wave carrier frequency is tunable over a wide bandwidth ($\approx$ 50 GHz to 1 THz). Besides, the optical components (couplers, modulators, polarization controllers) are extremely broadband,

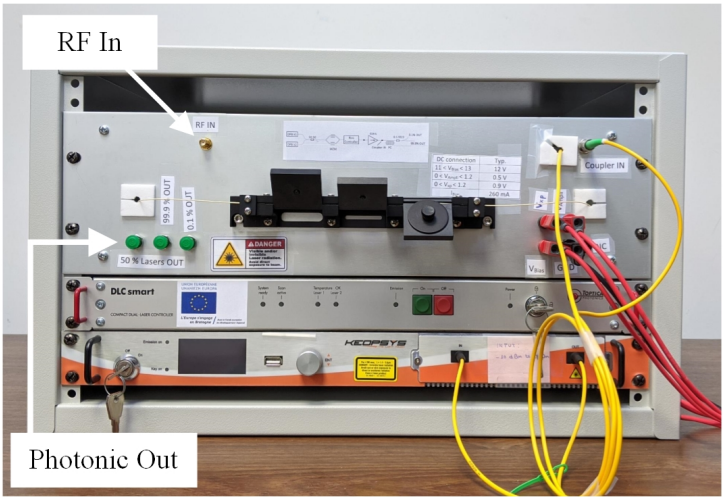

Figure E.2 Rack box used to arrange the components required for photonic generation and modulation of the optical tones (except for the mm-wave photonic Tx and OSA).

covering most, or the complete C-band (4 THz). Therefore, the photonic part of the set-up is almost independent of the mm-wave frequency used. Moreover, readily available commercial off-the-shelf components can be used, such as the EDFA. Finally, it becomes possible to establish a seamless connection between the 1.55 μm data flow guided in optical fiber and mm-wave radio.

E.2 Module for Detection and Baseband Electronics

The module of detection and baseband electronics is encircled in dark red in Figure E.1. The receiver consists of a horn antenna (WR-10 waveguide) placed at the focal point of the second 10-cm diameter Teflon lens, and a zero bias Schottky diode detector from Virginia Diodes (WR10ZBD-F [252]). For low input powers (< -25 dBm), the ZSBD produces a current (or voltage in a load) proportional to the incident power. The output of the ZSBD is amplified by an LNA (RF-lambda RLNA01M10GC [268]). Optionally, a low-pass (LP) filter and another amplifier (LNA2) can be added to the receiving chain to optimize the BERT input voltage. In particular, the latter requires an input amplitude $> 0.25\,V_{pp}$.

Among the RF components, the LNA bandwidth is found to have the most impact on the targeted link speed of 10 Gbaud. A MATLAB code was developed to examine the eye diagram after the detection chain and determine the optimum characteristics among the commercially available LNAs. It was found that an amplifier with an electrical bandwidth of 10 GHz did not substantially distort the eye diagram, whereas the lower frequency cutoff significantly reduced the vertical eye-opening. Increasing the lower frequency cutoff from DC to 50 MHz reduced the vertical eye-opening by 50%, and for a 10 MHz cutoff, the eye opening was reduced by 10%. The RLNA01M10GC, with lower and higher frequency cutoffs of 10 MHz and 10 GHz, respectively, was found to best suit our needs.

Finally, the BER tester is the first and last part of the communications link. It is composed of a pulse-pattern generator (Anritsu MP1763C) that outputs a non-return to zero PRBS. On the input, an error detector (Anritsu 1764C) compares the input with the pattern generator output to calculate the BER.

E.3 Quasi-Optical Rail System

The rail system can be observed in the lower part of Fig. E.1. It comprises a 2-m-long rail with anti-vibration Sorbothane feet and two movable platforms where the Tx/Rx plus Teflon lenses that form the quasi-optical link are mounted. The platforms are shown in the insets of Fig. E.1 bottom; left: photonic Tx, and right: Rx composed of the horn, ZSBD, and LNA1. The rail configuration enables indoor measurements to characterize the antenna performance in a short-range communications link. It also simplifies the investigation of BER variations with link distance. Besides, since this measurement might not be carried out in-house in the future, the rail configuration eases module alignment if they are not placed on an optical table or if they are directly placed on different surfaces.

E.4 Software for Computer Control

The last part of the set-up is the software for computer control. It controls the emission wavelength of the lasers through a VBA code implemented in an Excel workbook. The software communicates with Toptica's control unit (DLC smart) via established remote commands to directly set the lasers frequency difference. No further action is required from the user. Similarly, the workbook communicates with the OSA to monitor the spacing and power of the optical tones, and it also controls the position of the motorized linear stage for the measurements of beam switching. A screenshot of the program interface is shown in Fig. E.3. The worksheet also contains a template in the lower part to store relevant experimental data. The rest of the link aspects, such as the EDFA amplification, current meter, or voltage control of the LNA amplifier are controlled manually, but it would be possible to adapt the computer program to control them remotely too, if required.

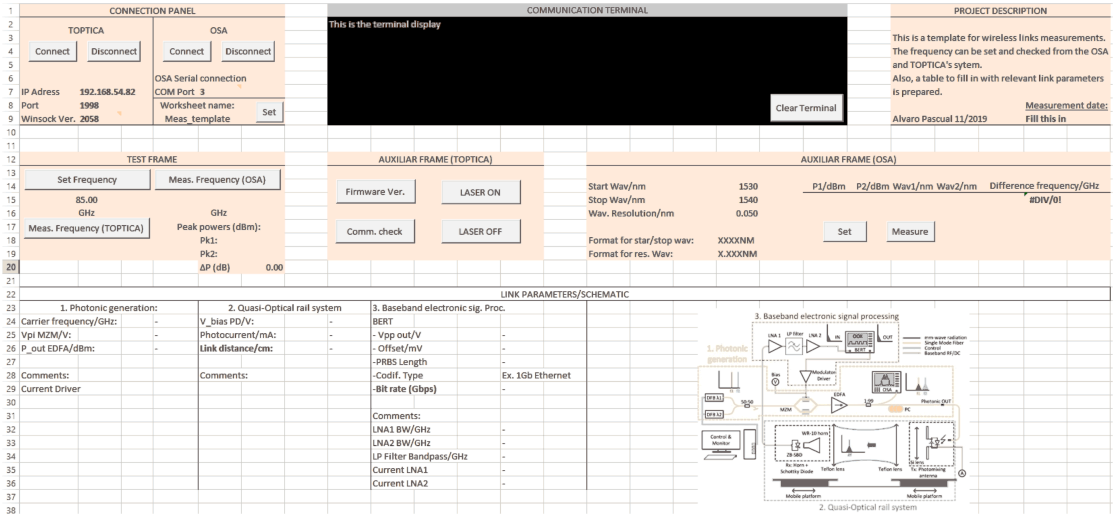

Figure E.3 Excel workbook used to control and record data in the wireless data transmission experiment.

List of Publications

Journal Papers

[i] A. J. Pascual, M. Ali, G. Carpintero, F. Ferrero, L. Brochier, R. Sauleau, L. E. García-Muñoz, and D. González-Ovejero, "A photonically-excited leaky-wave antenna array at E-band for 1-D beam steering," *Appl. Sci.*, vol. 10, no. 10, May 2020.

[ii] A. J. Pascual, R. Sauleau, and D. González-Ovejero, "An asymptotic approach for the scan impedance in infinite phased arrays of dipoles," *Accepted for publication in IEEE Trans. Antennas Propag.*, In press.

International Conference Papers

[iii] A. J. Pascual, M Ali, L. E. García-Muñoz, G. Carpintero, F. van Dijk, D. González-Ovejero, and R. Sauleau, "A scalable photomixing array for increased emitted power," *2019 44th Int. Conf. Infrared, Millimeter, Terahertz Waves (IRMMW-THz)*, Paris, France, Sep. 2019.

[iv] A. J. Pascual, L. E. García-Muñoz, R. Sauleau, and D. González-Ovejero, "Unit-cell design for antenna arrays efficiently matched to uni-traveling-carrier photodiodes," *2019 44th Int. Conf. Infrared, Millimeter, Terahertz Waves (IRMMW-THz)*, Paris, France, Sep. 2019.

[v] A. J. Pascual, M. Ali, L. E. García-Muñoz, G. Carpintero, D. González-Ovejero, and R. Sauleau, "A photonic beam-steerable mm-wave antenna array for radio over fiber applications," *14th European Conf. Antennas Propagation (EuCAP)*, Copenhagen, Sweden, March 2020.

[vi] A. J. Pascual, T. Batté, O. de Sagazan, G. Carpintero, R. Sauleau, and D. González-Ovejero, "A photonic transmitter for beam switching in mm-wave wireless links," *2020 45th Int. Conf. Infrared, Millimeter, Terahertz Waves (IRMMW-THz)*, Buffalo, US, Nov. 2020.

[vii] A. J. Pascual, F. Ferrero, L. Brochier, T. Batté, O. de Sagazan, G. Carpintero, R. Sauleau, and D. González-Ovejero, "An antenna array for photonic beam switching in mm-wave wireless communications," *15th European Conf. Antennas Propagation (EuCAP)*, Düsseldorf, Germany, March 2021.

National Conference Papers

[viii] A. J. Pascual, M. Ali, L. E. García-Muñoz, G. Carpintero, F. van Dijk, D. González-Ovejero, and R. Sauleau, "Antenna array on PCB compatible with photomixing technology," *Journée du Club Optique Micro-Ondes*, Brest, France, Jun. 2019.

Bibliography

[1] C. A. Balanis, *Antenna theory: analysis and design*, 3rd ed. Hoboken, NJ: John Wiley, 2005, 1117 pp.

[2] S. Preu, G. H. Döhler, S. Malzer, A. Stöhr, V. Rymanov, T. Göbel, *et al.*, "Principles of THz generation," in *Semiconductor Terahertz Technology*, G. Carpintero, L. E. García Muñoz, H. L. Hartnagel, S. Preu, and A. V. Räisänen, Eds., Chichester, UK: John Wiley & Sons, Ltd, 2015, pp. 3–68.

[3] T. Nagatsuma, H. Ito, and T. Ishibashi, "High-power RF photodiodes and their applications," *Laser & Photon. Rev.*, vol. 3, no. 1, pp. 123–137, Feb. 24, 2009.

[4] K. Sengupta, T. Nagatsuma, and D. M. Mittleman, "Terahertz integrated electronic and hybrid electronic-photonic systems," *Nat. Electron.*, vol. 1, pp. 622–635, 2018.

[5] P. Chevalier *et al.*, "Widely tunable compact terahertz gas lasers," *Science*, vol. 366, no. 6467, pp. 856–860, Nov. 15, 2019.

[6] J. H. Booske *et al.*, "Vacuum electronic high power terahertz sources," *IEEE Trans. THz Sci. Technol.*, vol. 1, no. 1, pp. 54–75, 2011.

[7] P. Siegel, "Terahertz technology," *IEEE Trans. Microw. Theory Techn.*, vol. 50, no. 3, pp. 910–928, Mar. 2002.

[8] M. Tonouchi, "Cutting-edge terahertz technology," *Nat. Photon.*, vol. 1, pp. 97–105, 2007.

[9] H. Elayan, O. Amin, B. Shihada, R. M. Shubair, and M. .-. Alouini, "Terahertz band: The last piece of RF spectrum puzzle for communication systems," *IEEE Open J. Commun. Soc.*, vol. 1, pp. 1–32, 2020.

[10] H.-J. Song and T. Nagatsuma, Eds., *Handbook of terahertz technologies: devices and applications*. Singapore: Pan Stanford Publishing, 2015, 593 pp.

[11] D. M. Mittleman, "Perspective: Terahertz science and technology," *J. Appl. Phys.*, vol. 122, no. 23, p. 230 901, 2017.

[12] S. S. Dhillon *et al.*, "The 2017 terahertz science and technology roadmap," *J. Phys. D*, vol. 50, no. 4, p. 043 001, Jan. 2017.

[13] L. A. Samoska, "An overview of solid-state integrated circuit amplifiers in the submillimeter-wave and thz regime," *IEEE Trans. THz Sci. Technol.*, vol. 1, no. 1, pp. 9–24, 2011.

[14] M. Asada and S. Suzuki, "Resonant tunneling diodes for terahertz sources," in *Handbook of Terahertz Technologies*, H.-J. Song and T. Nagatsuma, Eds. Pan Stanford Publishing Pte. Ltd., 2015, pp. 151–185.

[15] M. Urteaga, Z. Griffith, M. Seo, J. Hacker, and M. J. W. Rodwell, "InP HBT technologies for THz integrated circuits," *Proc. IEEE*, vol. 105, no. 6, pp. 1051–1067, 2017.

[16] T. Kim, J. A. del Alamo, K.Seo, B. Brar, and D. Kim, "III-V High-electron-mobility transistors toward terahertz operation," in *Handbook of Terahertz Technologies*, H.-J. Song and T. Nagatsuma, Eds. Pan Stanford Publishing Pte. Ltd., 2015, pp. 133–185.

[17] M. Kawashima, T. Seki, A. Hirata, and T. Kosugi, "Millimeter-wave/terahertz circuits and transceivers for broadband wireless systems," in *2011 IEEE 54th Int. Midwest Symp. Circuits and Systems (MWSCAS)*, 2011, pp. 1–4.

[18] N. J. Kolias, "MMIC pioneers: A historical review of MMIC development at Raytheon," in *2009 IEEE MTT-S Int. Microwave Symp. Digest*, 2009, pp. 1405–1408.

[19] A. Hirata *et al.*, "Transmission trial of television broadcast materials using 120-GHz-band wireless link," NTT Microsystem Integration Laboratories, Atsugi-shi, Japan, Technical Review, 2009.

[20] J. Hesler, "Terahertz Schottky diode technology," in *Handbook of Terahertz Technologies*, H.-J. Song and T. Nagatsuma, Eds. Pan Stanford Publishing Pte. Ltd., 2015, pp. 101–131.

[21] I. Hosako and H. Yasuda, "Quantum cascade lasers as terahertz wave source," in *Handbook of Terahertz Technologies*, H.-J. Song and T. Nagatsuma, Eds. Pan Stanford Publishing Pte. Ltd., 2015, pp. 77–99.

[22] Y.-S. Lee, "Continuous-wave terahertz sources and detectors," in *Principles of Terahertz Science and Technology*, Boston, MA: Springer US, 2009, pp. 1–41.

[23] C. Armstrong, "The truth about terahertz," *IEEE Spectrum*, vol. 49, no. 9, pp. 36–41, Sep. 2012.

[24] S. Matsuura and H. Ito, "Generation of CW terahertz radiation with photomixing," in *Terahertz Optoelectronics*, K. Sakai, Ed., vol. 97, Series Title: Topics in Applied Physics, Berlin/Heidelberg: Springer-Verlag, 2005, pp. 157–202.

[25] M. Nagai, "Nonlinear crystal for broadband terahertz pulse generation and detection," in *Handbook of Terahertz Technologies*, H.-J. Song and T. Nagatsuma, Eds. Pan Stanford Publishing Pte. Ltd., 2015, pp. 37–55.

[26] J. Neu and C. A. Schmuttenmaer, "Tutorial: An introduction to terahertz time domain spectroscopy (THz-TDS)," *J. Appl. Phys.*, vol. 124, no. 23, p. 231 101, Dec. 21, 2018.

[27] S. Preu, G. H. Döhler, S. Malzer, L. J. Wang, and A. C. Gossard, "Tunable, continuous-wave terahertz photomixer sources and applications," *J. Appl. Phys.*, vol. 109, no. 6, p. 061 301, Mar. 15, 2011.

[28] S. Nellen *et al.*, "Experimental comparison of UTC- and PIN- photodiodes for continuous-wave Terahertz emission," *J. Infrared Milli. THz Waves*, vol. 41, pp. 343–354, 2020.

[29] P. Latzel *et al.*, "Generation of mW level in the 300-GHz band using resonant-cavity-enhanced unitraveling carrier photodiodes," *IEEE Trans. THz Sci. Technol.*, vol. 7, no. 6, pp. 800–807, 2017.

[30] T. Nagatsuma *et al.*, "Millimeter-wave and terahertz-wave applications enabled by photonics," *IEEE J. Quantum Electron.*, vol. 52, no. 1, pp. 1–12, Jan. 2016.

[31] A. J. Seeds, H. Shams, M. J. Fice, and C. C. Renaud, "Terahertz photonics for wireless communications," *J. Lightw. Technol.*, vol. 33, no. 3, pp. 579–587, 2015.

[32] TOPTICA Photonics. "Terahertz systems." (n.d.), [Online]. Available: https://www.toptica.com/products/terahertz-systems/. [Accessed: Jun. 2, 2020].

[33] E. R. Brown, "Thz photomixing," in *LEOS 2007 - IEEE Lasers and Electro-Optics Society Annu. Meeting Conf. Proc.*, 2007, pp. 790–791.

[34] TOPTICA Photonics. "GaAs and InGaAs photomixers." (n.d.), [Online]. Available: https://www.toptica.com/products/terahertz-systems/frequency-domain/gaas-and-ingaas-photomixers/. [Accessed: Aug. 21, 2020].

[35] I. C. Mayorga, A. Schmitz, T. Klein, C. Leinz, and R. Gusten, "First in-field application of a full photonic local oscillator to terahertz astronomy," *IEEE Trans. THz Sci. Technol.*, vol. 2, no. 4, pp. 393–399, 2012.

[36] B. Shillue *et al.*, "The ALMA photonic local oscillator system," in *Millimeter, Submillimeter, and Far-Infrared Detectors and Instrumentation for Astronomy VI*, W. S. Holland, Ed., Int. Soc. Optics and Photonics, vol. 8452, SPIE, 2012, pp. 320–325.

[37] T. Nagatsuma, G. Ducournau, and C. C. Renaud, "Advances in terahertz communications accelerated by photonics," *Nat. Photon.*, vol. 10, no. 6, pp. 371–379, Jun. 2016.

[38] A. Wakatsuki, Y. Muramoto, and T. Ishibashi, "Development of a terahertz-wave photomixer module using a uni-traveling-carrier photodiode," NTT Photonics Laboratories, Technical Review, 2012.

[39] G. Carpintero, L. E. García-Muñoz, H. L. Hartnagel, S. Preu, and A. V. Raïsänen, Eds., *Semiconductor terahertz technology: devices and systems at room temperature operation*, Hoboken: John Wiley & Sons, Inc, 2015.

[40] S. Daryoosh, Ed., *Handbook of terahertz technology for imaging, sensing and communications*, Woodhead publishing series in electronic and optical materials, Oxford, England ; Philadelphia, Pennsylvania: WP, Woodhead Publishing, 2013, 662 pp.

[41] Y.-S. Lee, *Principles of terahertz science and technology*. New York, NY: Springer, 2009, 340 pp.

[42] P. Chen *et al.*, "Spectroscopic applications and frequency locking of THz photomixing with distributed-bragg-reflector diode lasers in low-temperature-grown GaAs," *Appl. Phys. Lett.*, vol. 71, no. 12, pp. 1601–1603, Sep. 22, 1997.

[43] M. Yahyapour, N. Vieweg, A. Roggenbuck, F. Rettich, O. Cojocari, and A. Deninger, "A flexible phase-insensitive system for broadband CW-terahertz spectroscopy and imaging," *IEEE Trans. THz Sci. Technol.*, vol. 6, no. 5, pp. 670–673, Sep. 2016.

[44] B. Sartorius *et al.*, "All-fiber terahertz time-domain spectrometer operating at 1.5 µm telecom wavelengths," *Opt. Express*, vol. 16, no. 13, p. 9565, Jun. 23, 2008.

[45] TOPTICA Photonics. "TeraFlash TD system." (n.d.), [Online]. Available: https://www.toptica.com/products/terahertz-systems/frequency-domain/terascan/. [Accessed: Jun. 4, 2020].

[46] H.-J. Song and T. Nagatsuma, "Low-coherence terahertz signal sources and their applications," in *Handbook of Terahertz Technologies*, H.-J. Song and T. Nagatsuma, Eds. Pan Stanford Publishing Pte. Ltd., 2015, pp. 375–393.

[47] I. S. Gregory *et al.*, "Continuous-wave terahertz system with a 60 dB dynamic range," *Appl. Phys. Lett.*, vol. 86, no. 20, p. 204 104, May 16, 2005.

[48] J.-Y. Kim, H.-J. Song, K. Ajito, M. Yaita, and N. Kukutsu, "Continuous-wave THz homodyne spectroscopy and imaging system with electro-optical phase modulation for high dynamic range," *IEEE Trans. THz Sci. Technol.*, vol. 3, no. 2, pp. 158–164, Mar. 2013.

[49] H. Song, S. Hwang, H. An, H.-J. Song, and J.-I. Song, "Continuous-wave THz vector imaging system utilizing two-tone signal generation and self-mixing detection," *Opt. Express*, vol. 25, no. 17, p. 20 718, Aug. 21, 2017.

[50] *Lock-in amplifier user manual (model SR810)*, version 1.8, Stanford Research Systems, 2005, Jan, 2005.

[51] A. Hirata *et al.*, "High-power photonic millimetre wave generation at 100 GHz using matching-circuit-integrated uni-travelling-carrier photodiodes," *IEE Proc. - Optoelectron.*, vol. 150, no. 2, pp. 138–142, Apr. 1, 2003.

[52] M. Natrella *et al.*, "Accurate equivalent circuit model for millimetre-wave UTC photodiodes," *Opt. Express*, vol. 24, no. 5, pp. 4698–4713, Mar. 2016.

[53] M. Chiani and F. Callegati, "Open issues and beyond 5G," in *5G Italy Conf.*, Rome, Italy, 2018, pp. 1–1.

[54] Terranova Consortium. "Wireless terahertz system applications for networks beyond 5G." (2019), [Online]. Available: https://ict-terranova.eu/wp-content/uploads/2019/04/TERRANOVA-Applications-for-Networks-Beyond-5G-v1.0.pdf. [Accessed: Jan. 20, 2021].

[55] T. Kürner, *IEEE P802.15 Working group for wireless personal area networks (WPANs)*, Presentation, 2013.

[56] J. G. Andrews *et al.*, "What will 5G be?" *IEEE J. Sel. Areas Commun.*, vol. 32, no. 6, pp. 1065–1082, 2014.

[57] R. Kalimulin, A. Artemenko, R. Maslennikov, J. Putkonen, and J. Salmelin, "Impact of mounting structures twists and sways on point-to-point millimeter-wave backhaul links," in *2015 IEEE Int. Conf. Communication Workshop (ICCW)*, London, United Kingdom: IEEE, Jun. 2015, pp. 19–24.

[58] M. F. Hermelo, P.-T. Shih, M. Steeg, A. Ng'oma, and A. Stöhr, "Spectral efficient 64-QAM-OFDM terahertz communication link," *Opt. Express*, vol. 25, no. 16, pp. 19 360–19 370, Aug. 2017.

[59] J. A. Altabas *et al.*, "Nonorthogonal multiple access and carrierless amplitude phase modulation for flexible multiuser provisioning in 5G mobile networks," *J. Lightw. Technol.*, vol. 35, no. 24, pp. 5456–5463, 2017.

[60] A. Kanno *et al.*, "20-Gb/s QPSK W-band (75-110GHz) wireless link in free space using radio-over-fiber technique," *IEICE Electron. Express*, vol. 8, no. 8, pp. 612–617, 2011.

[61] T. P. McKenna, J. A. Nanzer, and T. R. Clark, "Photonic beamsteering of a millimeter-wave array with 10-Gb/s data transmission," *IEEE Photon. Technol. Lett.*, vol. 26, no. 14, pp. 1407–1410, 2014.

[62] S. T. Bauerschmidt, G. H. Döhler, H. Lu, A. C. Gossard, S. Malzer, and S. Preu, "Arrayed free space continuous-wave terahertz photomixers," *Opt. Lett.*, vol. 38, no. 18, p. 3673, Sep. 15, 2013.

[63] N. Shimizu and T. Nagatsuma, "Photodiode-integrated microstrip antenna array for subterahertz radiation," *IEEE Photon. Technol. Lett.*, vol. 18, no. 6, pp. 743–745, Mar. 2006.

[64] S. Preu *et al.*, "Fiber-coupled 2-D n-i-pn-i-p superlattice photomixer array," *IEEE Trans. Antennas Propag.*, vol. 65, no. 7, pp. 3474–3480, 2017.

[65] M. Che, Y. Matsuo, H. Kanaya, H. Ito, T. Ishibashi, and K. Kato, "Optoelectronic THz-wave beam steering by arrayed photomixers with integrated antennas," *IEEE Photon. Technol. Lett.*, vol. 32, no. 16, 2020.

[66] R. C. Hansen, *Phased Array Antennas*, 2nd ed. Wiley, 2009.

[67] A. K. Bhattacharyya, *Phased Array Antennas: Floquet Analysis, Synthesis, BFNs and Active Array Systems*. Wiley-Interscience, 2006.

[68] C. Craeye and D. González-Ovejero, "A review on array mutual coupling analysis," *Radio Sci.*, vol. 46, no. 02, pp. 1–25, 2011.

[69] M. Jones and J. Rawnick, "A new approach to broadband array design using tightly coupled elements," in *MILCOM 2007 - IEEE Mil. Commun. Conf.*, Oct. 2007, pp. 1–7.

[70] S. S. Holland and M. N. Vouvakis, "The planar ultrawideband modular antenna (PUMA) array," *IEEE Trans. Antennas Propag.*, vol. 60, no. 1, pp. 130–140, Jan. 2012.

[71] D. Cavallo and A. Neto, "A connected array of slots supporting broadband leaky waves," *IEEE Trans. Antennas Propag.*, vol. 61, no. 4, pp. 1986–1994, Apr. 2013.

[72] D. Pozar, "Analysis of finite phased arrays of printed dipoles," *IEEE Trans. Antennas Propag.*, vol. 33, no. 10, pp. 1045–1053, Oct. 1985.

[73] H. Wheeler, "Simple relations derived fom a phased-array antenna made of an infinite current sheet," *IEEE Trans. Antennas Propag.*, vol. 13, no. 4, pp. 506–514, Jul. 1965.

[74] D. Pozar, "General relations for a phased array of printed antennas derived from infinite current sheets," *IEEE Trans. Antennas Propag.*, vol. 33, no. 5, pp. 498–504, May 1985.

[75] L. Stark, "Radiation impedance of a dipole in an infinite planar phased array," *Radio Sci.*, vol. 1, no. 3, pp. 361–377, Mar. 1966.

[76] B. L. Diamond, "A generalized approach to the analysis of infinite planar array antennas," *Proc. IEEE*, vol. 56, no. 11, pp. 1837–1851, Nov. 1968.

[77] R. C. Hansen, *Microwave Scanning Antennas, Vol. II: Array Theory and Practice*. New York: Academic, 1966.

[78] V. W. H. Chang, "Infinite phased dipole array," *Proc. IEEE*, vol. 56, no. 11, pp. 1892–1900, Nov. 1968.

[79] M. Kominami, D. Pozar, and D. Schaubert, "Dipole and slot elements and arrays on semi-infinite substrates," *IEEE Trans. Antennas Propag.*, vol. 33, no. 6, pp. 600–607, Jun. 1985.

[80] R. C. Hansen, "Non-Foster and connected planar arrays," *Radio Sci.*, vol. 39, no. 4, pp. 1–14, Aug. 2004.

[81] C. Mias and A. Freni, "Application of Wait's formulation to connected array antennas," *IEEE Antennas Wireless Propag. Lett.*, vol. 12, pp. 1535–1538, 2013.

[82] A. Neto, D. Cavallo, G. Gerini, and G. Toso, "Scanning performances of wideband connected arrays in the presence of a backing reflector," *IEEE Trans. Antennas Propag.*, vol. 57, no. 10, pp. 3092–3102, Oct. 2009.

[83] D. Cavallo, A. Neto, and G. Gerini, "Green's function based equivalent circuits for connected arrays in transmission and in reception," *IEEE Trans. Antennas Propag.*, vol. 59, no. 5, pp. 1535–1545, May 2011.

[84] ——, "Analytical description and design of printed dipole arrays for wideband wide-scan applications," *IEEE Trans. Antennas Propag.*, vol. 60, no. 12, pp. 6027–6031, Dec. 2012.

[85] E. A. Alwan, K. Sertel, and J. L. Volakis, "Circuit model based optimization of ultra-wideband arrays," in *Proc. 2012 IEEE Int. Symp. Antennas and Propagation*, Jul. 2012, pp. 1–2.

[86] Y. Zhou *et al.*, "Tightly coupled array antennas for ultra-wideband wireless systems," *IEEE Access*, vol. 6, pp. 61 851–61 866, 2018.

[87] B. A. Munk, *Frequency Selective Surfaces: Theory and Design*. Wiley-Blackwell, 2000.

[88] ——, *Finite Antenna Arrays and FSS*. Wiley-Interscience, 2003.

[89] S. N. Makarov, A. Puzella, and V. Iyer, "Scan impedance for an infinite dipole array: Accurate theoretical model compared to numerical software," *IEEE Antennas Propag. Mag.*, vol. 50, no. 6, pp. 132–149, 2008.

[90] N. Engheta, C. H. Papas, and C. Elachi, "Radiation patterns of interfacial dipole antennas," *Radio Sci.*, vol. 17, no. 06, pp. 1557–1566, Nov. 1982.

[91] ANSYS, *High Frequency Structure Simulator*, Ver. 19.0.0, 2019.

[92] O. Luukkonen *et al.*, "Simple and accurate analytical model of planar grids and high-impedance surfaces comprising metal strips or patches," *IEEE Trans. Antennas Propag.*, vol. 56, no. 6, pp. 1624–1632, Jun. 2008.

[93] D. Pozar and D. Schaubert, "Scan blindness in infinite phased arrays of printed dipoles," *IEEE Trans. Antennas Propag.*, vol. 32, no. 6, pp. 602–610, Jun. 1984.

[94] G. D. Alley, "Interdigital capacitors and their application to lumped-element microwave integrated circuits," *IEEE Trans. Microw. Theory Techn.*, vol. 18, no. 12, pp. 1028–1033, 1970.

[95] S. A. Schelkunoff and H. T. Friis, "Antenna current," in *Antennas: Theory and Practice*, Wiley, 1952.

[96] Computer Simulation Technology, *CST Studio Suite*, Ver. 2018.

[97] R. Hansen, "Linear connected arrays [coupled dipole arrays]," *IEEE Antennas Wireless Propag. Lett.*, vol. 3, pp. 154–156, 2004.

[98] L. B. Whitbourn and R. C. Compton, "Equivalent-circuit formulas for metal grid reflectors at a dielectric boundary," *Appl. Opt.*, vol. 24, no. 2, pp. 217–220, Jan. 1985.

[99] S. Tretyakov, "Periodical structures, arrays and meshes," in *Analytical Modelling in Applied Electromagnetics*, Artech House, 2003.

[100] G. G. Macfarlane, "Quasi-stationary field theory and its application to diaphragms and junctions in transmission lines and wave guides," *J. IEE - Part IIIA: Radiolocation*, vol. 93, no. 4, pp. 703–719, 1946.

[101] B. Riviere, H. Jeuland, and S. Bolioli, "New equivalent circuit model for a broadband optimization of dipole arrays," *IEEE Antennas Wireless Propag. Lett.*, vol. 13, pp. 1300–1304, 2014.

[102] T. Nagatsuma and G. Carpintero, "Recent progress and future prospect of photonics-enabled terahertz communications research," *IEICE Trans. Electron.*, vol. E98.C, no. 12, pp. 1060–1070, 2015.

[103] Ericsson. "Mobile data traffic oulook (June 2019)." (2019), [Online]. Available: https://www.ericsson.com/en/mobility-report/reports. [Accessed: Sep. 15, 2020].

[104] IEEE 5G initiative. "5G and beyond technology roadmap white paper (2017)." (2017), [Online]. Available: https://futurenetworks.ieee.org/images/files/pdf/ieee-5groadmap-%20white-paper.pdf. [Accessed: Sep. 15, 2020].

[105] IWPC. "Evolutionary and disruptive visions towards ultra high capacity networks." (2014), [Online]. Available: https://www.keysight.com/upload/cmc_upload/All/IWPC_UltraHighCapacityNetworks_Whitepaper_v1-1.pdf. [Accessed: Jan. 20, 2021].

[106] T. Sowlati *et al.*, "A 60-GHz 144-element phased-array transceiver for backhaul application," *IEEE J. Solid-State Circuits*, vol. 53, no. 12, pp. 3640–3659, 2018.

[107] J. Ala-Laurinaho *et al.*, "2-D beam-steerable integrated lens antenna system for 5G E-band access and backhaul," *IEEE Trans. Microw. Theory Techn.*, vol. 64, no. 7, pp. 2244–2255, 2016.

[108] A. Hirata *et al.*, "120-GHz-band wireless link technologies for outdoor 10-Gbit/s data transmission," *IEEE Trans. Microw. Theory Techn.*, vol. 60, no. 3, pp. 881–895, 2012.

[109] EU H2020 Project. "Terranova." (2017), [Online]. Available: https://ict-terranova.eu/. [Accessed: Jan. 20, 2021].

[110] T. Nagatsuma *et al.*, "Terahertz wireless communications based on photonics technologies," *Opt. Express*, vol. 21, no. 20, pp. 23 736–23 747, Oct. 2013.

[111] J. F. Federici, "Terahertz wireless communications," in *Handbook of Terahertz Technology for Imaging, Sensing and Communications*, D. Saeedkia, Ed., Woodhead Publishing Series in Electronic and Optical Materials, Elsevier, 2013, pp. 156–214.

[112] Facebook connectivity. "Terragraph." (2017), [Online]. Available: https://terragraph.com/. [Accessed: Jan. 20, 2021].

[113] M. Frecassetti, "E-band and V-band -survey on status of worldwide regulation," *ETSI white paper*, no. 9, pp. 3495–3501, 2015.

[114] T. Nagatsuma, "Breakthroughs in photonics 2013: THz communications based on photonics," *IEEE Photon. J.*, vol. 6, no. 2, pp. 1–5, 2014.

[115] HHI- Fraunhofer. "Frauhofer HHI and IAF demonstrate wireless terahetz transmission over a distance of one kilometer." (2019), [Online]. Available: https://www.hhi.fraunhofer.de/en/press-media/news/2019/fraunhofer-hhi-and-iaf-demonstrate-wireless-terahertz-transmission-over-a-distance-of-one-kilometer.html. [Accessed: Oct. 19, 2020].

[116] H.-J. Song, S. Priebe, and T. Kürner, "Terahertz Wireless Communications," in *Handbook of Terahertz Technologies*, H.-J. Song and T. Nagatsuma, Eds. Pan Stanford Publishing Pte. Ltd., 2015, pp. 495–526.

[117] H. Schrank and K. Praba, "Optimal aperture for maximum edge-of-coverage (EOC) directivity," *IEEE Antennas Propag. Mag.*, vol. 36, no. 3, pp. 72–74, 1994.

[118] S. Rommel, T. R. Raddo, U. Johannsen, C. Okonkwo, and I. T. Monroy, "Beyond 5G - wireless data center connectivity," in *Broadband Access Communication Technologies XIII*, B. B. Dingel, K. Tsukamoto, and S. Mikroulis, Eds., Int. Soc. Optics and Photonics, SPIE, 2019, pp. 125–133.

[119] H. Vardhan, N. Thomas, S.-R. Ryu, B. Banerjee, and R. Prakash, "Wireless data center with millimeter wave network," in *2010 IEEE Global Telecommunications Conf. GLOBECOM 2010*, Miami, FL, USA: IEEE, Dec. 2010, pp. 1–6.

[120] T. Schneider, A. Wiatrek, S. Preussler, M. Grigat, and R. Braun, "Link budget analysis for terahertz fixed wireless links," *IEEE Trans. THz Sci. Technol.*, vol. 2, no. 2, pp. 250–256, 2012.

[121] Y.-S. Lee, "Terahertz spectroscopy of atoms and molecules," in *Principles of Terahertz Science and Technology*, Boston, MA: Springer US, 2009, pp. 215–258.

[122] A. Deninger, "State-of-the-art in terahertz continuous-wave photomixer systems," in *Handbook of Terahertz Technology for Imaging, Sensing and Communications*, D. Saeedkia, Ed., Woodhead Publishing Series in Electronic and Optical Materials, Elsevier, 2013, pp. 327–373.

[123] HITRAN. "The HITRAN Database." (n.d.), [Online]. Available: https://hitran.org/. [Accessed: Jun. 2, 2020].

[124] Z. Wang, T. Chang, and H. Cui, "Review of active millimeter wave imaging techniques for personnel security screening," *IEEE Access*, vol. 7, pp. 148 336–148 350, 2019.

[125] Y.-S. Lee, "Introduction," in *Principles of Terahertz Science and Technology*, Boston, MA: Springer US, 2009, pp. 1–9.

[126] R. Gente and M. Koch, "Monitoring leaf water content with THz and sub-THz waves," *Plant Methods*, vol. 11, no. 1, p. 15, 2015.

[127] S. Dülme *et al.*, "Compact optoelectronic THz frequency domain spectroscopy system for refractive index determination based on Fabry-Perot effect," in *2018 1st Int. Workshop Mobile Terahertz Systems (IWMTS)*, 2018, pp. 1–5.

[128] N. Shimizu, A. Wakatsuki, K. Kikuchi, S. Kohjiro, T. Ikari, R. Fukasawa, *et al.*, "Terahertz remote gas sensing system," in *Handbook of Terahertz Technologies*, H.-J. Song and T. Nagatsuma, Eds. Pan Stanford Publishing Pte. Ltd., 2015, pp. 527–562.

[129] M. Naftaly, N. Vieweg, and A.Deninger, "Industrial applications of terahertz sensing: State of play," *Sensors*, vol. 19, no. 19, p. 4203, Sep. 27, 2019.

[130] MENLO Systems. "Terahertz time domain solutions." (2020), [Online]. Available: https://www.menlosystems.com/products/thz-time-domain-solutions/. [Accessed: Jun. 2, 2020].

[131] LUNA. "Terametrix - Terahertz solutions." (2020), [Online]. Available: https://lunainc.com/market/time-domain-terahertz-td-thz/. [Accessed: Jun. 2, 2020].

[132] B. Sartorius *et al.*, "Continuous wave terahertz systems exploiting 1.5 µm telecom technologies," *Opt. Express*, vol. 17, no. 17, p. 15 001, Aug. 17, 2009.

[133] E. Castro-Camus, K. Wiesauer, R. Gente, and M. Koch, "Industrial applications of terahertz waves," in *Handbook of Terahertz Technologies*, H.-J. Song and T. Nagatsuma, Eds. Pan Stanford Publishing Pte. Ltd., 2015, pp. 451–494.

[134] E. R. Brown and D. Segovia-Vargas, "Principles of THz direct detection," in *Semiconductor Terahertz Technology*, G. Carpintero, L. E. García Muñoz, H. L. Hartnagel, S. Preu, and A. V. Räisänen, Eds., Chichester, UK: John Wiley & Sons, Ltd, 2015, pp. 212–253.

[135] A. J. Deninger, A. Roggenbuck, S. Schindler, and S. Preu, "2.75 THz tuning with a triple-DFB laser system at 1550 nm and InGaAs photomixers," *J. Infrared Milli. THz Waves*, vol. 36, no. 3, pp. 269–277, Mar. 2015.

[136] Toptica Photonics, "Production and quality control datasheet TeraScan 1550," unpublished.

[137] D. W. Vogt, M. Erkintalo, and R. Leonhardt, "Terahertz frequency domain spectroscopy using Hilbert transformation," in *2019 Conf. Lasers and Electro-Optics Europe and European Quantum Electronics Conf.*, OSA Tech. Dig., 2019.

[138] F. Simoens, "Terahertz cameras," in *Handbook of Terahertz Technologies*, H.-J. Song and T. Nagatsuma, Eds. Pan Stanford Publishing Pte. Ltd., 2015, pp. 395–428.

[139] Y.-S. Lee, "T-ray imaging," in *Principles of Terahertz Science and Technology*, Boston, MA: Springer US, 2009, pp. 259–294.

[140] D. M. Mittleman, R. H. Jacobsen, and M. C. Nuss, "T-ray imaging," *IEEE J. Sel. Topics Quantum Electron.*, vol. 2, no. 3, pp. 679–692, 1996.

[141] Y. Ueno and K. Ajito, "Terahertz chemical spectroscopy," in *Handbook of Terahertz Technologies*, H.-J. Song and T. Nagatsuma, Eds. Pan Stanford Publishing Pte. Ltd., 2015, pp. 429–449.

[142] J. Meilhan *et al.*, "Active THz imaging and explosive detection with uncooled antenna-coupled microbolometer arrays," in *Terahertz Physics, Devices, and Systems V: Advance Applications in Industry and Defense*, M. Anwar, N. K. Dhar, and T. W. Crowe, Eds., Int. Soc. Optics and Photonics, vol. 8023, SPIE, 2011, pp. 82–94.

[143] D. M. Mittleman, "Twenty years of terahertz imaging [invited]," *Opt. Express*, vol. 26, no. 8, p. 9417, Apr. 16, 2018.

[144] B. B. Hu and M. C. Nuss, "Imaging with terahertz waves," *Opt. Lett.*, vol. 20, no. 16, p. 1716, Aug. 15, 1995.

[145] H. Guerboukha, K. Nallappan, and M. Skorobogatiy, "Toward real-time terahertz imaging," *Adv. Opt. Photon.*, vol. 10, no. 4, p. 843, Dec. 31, 2018.

[146] C. Henry, "Phase noise in semiconductor lasers," *J. Lightw. Technol.*, vol. 4, no. 3, pp. 298–311, 1986.

[147] P. Gallion, F. J. Mendieta, and R. Leconte, "Single-frequency laser phase-noise limitation in single-mode optical-fiber coherent-detection systems with correlated fields," *J. Opt. Soc. Am.*, vol. 72, no. 9, pp. 1167–1170, Sep. 1982.

[148] D. Stanze, A. Deninger, A. Roggenbuck, S. Schindler, M. Schlak, and B. Sartorius, "Compact cw terahertz spectrometer pumped at 1.5 um wavelength," *J. Infrared Milli. THz Waves*, vol. 32, pp. 225–232, 2011.

[149] A. J. Pascual *et al.*, "A photonically-excited leaky-wave antenna array at E-Band for 1-D beam steering," *Appl. Sci.*, vol. 10, no. 10, 2020.

[150] G. Carpintero *et al.*, "Microwave photonic integrated circuits for millimeter-wave wireless communications," *J. Lightw. Technol.*, vol. 32, no. 20, pp. 3495–3501, 2014.

[151] H. Ito, S. Kodama, Y. Muramoto, T. Furuta, T. Nagatsuma, and T. Ishibashi, "High-speed and high-output InP-InGaAs unitraveling-carrier photodiodes," *IEEE J. Sel. Topics Quantum Electon.*, vol. 10, no. 4, pp. 709–727, 2004.

[152] E. Rouvalis, C. C. Renaud, D. G. Moodie, M. J. Robertson, and A. J. Seeds, "Travelling-wave uni-traveling carrier photodiodes for continuous wave THz generation," *Opt. Express*, vol. 18, no. 11, pp. 11 105–11 110, May 2010.

[153] H. Ito, T. Furuta, F. Nakajima, K. Yoshino, and T. Ishibashi, "Photonic generation of continuous THz wave using uni-traveling-carrier photodiode," *J. Lightw. Technol.*, vol. 23, no. 12, pp. 4016–4021, 2005.

[154] M. Natrella *et al.*, "Modelling and measurement of the absolute level of power radiated by antenna integrated THz UTC photodiodes," *Opt. Express*, vol. 24, no. 11, pp. 11 793–11 807, May 2016.

[155] T. Ishibashi *et al.*, "InP/InGaAs uni-traveling-carrier photodiodes," *IEICE Trans. Electon.*, vol. 83, pp. 938–949, 2000.

[156] T. Ishibashi, "Ultrafast photodiodes," in *Handbook of Terahertz Technologies*, H.-J. Song and T. Nagatsuma, Eds. Pan Stanford Publishing Pte. Ltd., 2015, pp. 58–75.

[157] P. Bhattacharya, Ed., *Properties of lattice-matched and strained Indium Gallium Arsenide*. UK: INSPEC, the Institution of Electrical Engineers, 1994, 702 pp.

[158] T. Ishibashi, S. Kodama, N. Shimizu, and T. Furuta, "High-speed response of uni-traveling-carrier photodiodes," *Jpn J. Appl. Phys.*, vol. 36, no. Part 1, No. 10, pp. 6263–6268, Oct. 1997.

[159] Y. Li *et al.*, "Characterization and comparison of GaAs/AlGaAs uni-traveling carrier and separated-transport-recombination photodiode based high-power sub-THz photonic transmitters," *IEEE J. Quantum Electron.*, vol. 46, no. 1, pp. 19–27, 2010.

[160] A. Jankowski, "Photonic integrated circuits on InP for high power signals generation in the millimeter wave range," PhD Thesis, Institute of Microelectronics, Electromagnetism and Photonics (IMEP-LAHC)- U. Grenoble Alpes, 2016.

[161] E. Rouvalis *et al.*, "High-speed photodiodes for InP-based photonic integrated circuits," *Opt. Express*, vol. 20, no. 8, pp. 9172–9177, Apr. 2012.

[162] C. C. Renaud *et al.*, "A high responsivity, broadband waveguide uni-travelling carrier photodiode," in *Millimeter-Wave and Terahertz Photonics*, D. Jäger and A. Stöhr, Eds., Int. Soc. Optics and Photonics, vol. 6194, SPIE, 2006, pp. 87–94.

[163] T. Nagatsuma, "Generating millimeter and terahertz waves," *IEEE Microw. Mag.*, vol. 10, no. 4, pp. 64–74, Jun. 2009.

[164] NTT Electronics. "UTC-PD photomixer module." (n.d.), [Online]. Available: https://www.ntt-electronics.com/en/products/gas_sensing/utc-pd.html. [Accessed: Jan. 25, 2021].

[165] C. R. Brewitt-Taylor, D. J. Gunton, and H. D. Rees, "Planar antennas on a dielectric surface," *Electronics Lett.*, vol. 17, no. 20, pp. 729–731, 1981.

[166] K. Park, K. Moon, H. Ryu, N. Kim, and S. Han, "Photoconductive Antenna vs. Photomixer for Broadband Terahertz Wave Generation and Detection," in *Handbook of Terahertz Technologies*, H.-J. Song and T. Nagatsuma, Eds. Pan Stanford Publishing Pte. Ltd., 2015, pp. 1–35.

[167] J. Montero-de-Paz, E. Ugarte-Muñoz, L. E. García-Muñoz, I. C. Mayorga, and D. Segovia-Vargas, "Meander dipole antenna to increase cw thz photomixing emitted power," *IEEE Trans. Antennas Propag.*, vol. 62, no. 9, pp. 4868–4872, 2014.

[168] A. Hirata, T. Kosugi, N. Meisl, T. Shibata, and T. Nagatsuma, "High-directivity photonic emitter using photodiode module integrated with HEMT amplifier for 10-Gbit/s wireless link," *IEEE Trans. Microw. Theory Techn.*, vol. 52, no. 8, pp. 1843–1850, Aug. 2004.

[169] T. Nagatsuma and H. Ito, "High-power RF uni-traveling-carrier photodiodes (UTC-PDs) and their applications," in *Advances in Photodiodes*, G. F. D. Betta, Ed., INTECH, 2011, pp. 291–314.

[170] H. Ito *et al.*, "Photonic millimetre-wave emission at 300 GHz using an antenna-integrated uni-travelling-carrier photodiode," *Electon. Lett.*, vol. 38, no. 17, pp. 989–990, 2002.

[171] OZ Optics. "Tapered and lensed fibers." (2020), [Online]. Available: https://www.ozoptics.com/ALLNEW_PDF/DTS0080.pdf. [Accessed: Jan. 25, 2021].

[172] B. Khani, S. Makhlouf, A. G. Steffan, J. Honecker, and A. Stöhr, "Planar 0.05–1.1 THz laminate-based transition designs for integrating high-frequency photodiodes with rectangular waveguides," *J. Lightw. Technol.*, vol. 37, no. 3, pp. 1037–1044, 2019.

[173] H. Song, K. Ajito, Y. Muramoto, A. Wakatsuki, T. Nagatsuma, and N. Kukutsu, "Uni-travelling-carrier photodiode module generating 300 GHz power greater than 1 mW," *IEEE Microw. Wireless Compon. Lett.*, vol. 22, no. 7, pp. 363–365, 2012.

[174] E. García-Muñoz *et al.*, "Photonic-based integrated sources and antenna arrays for broadband wireless links in terahertz communications," *Semicond. Sci. Technol.*, vol. 34, no. 5, p. 054 001, May 1, 2019.

[175] Thorlabs. "Microlens arrays." (2021), [Online]. Available: https://www.thorlabs.com/newgrouppage9.cfm?objectgroup_id=2861. [Accessed: Jan. 25, 2021].

[176] E. R. Brown, A. C. Young, J. Zimmerman, H. Kazerni, and A. C. Gossard, "Advances in Schottky rectifier performance," *IEEE Microw. Mag.*, vol. 8, no. 3, pp. 54–59, 2007.

[177] T. Ishibashi and H. Ito, "Uni-traveling-carrier photodiodes," *J. Appl. Phys.*, vol. 127, no. 3, p. 031 101, 2020.

[178] Y. Mushiake, "Self-complementary antennas," *IEEE Antennas Propag. Mag.*, vol. 34, no. 6, pp. 23–29, 1992.

[179] F. Nakajima, T. Furuta, and H. Ito, "High-power continuous-terahertz-wave generation using resonant-antenna-integrated uni-travelling-carrier photodiode," *Electon. Lett.*, vol. 40, no. 20, pp. 1297–1298, 2004.

[180] G. Ducournau *et al.*, "Ultrawide-bandwidth single-channel 0.4-THz wireless link combining broadband quasi-optic photomixer and coherent detection," *IEEE Trans. THz Sci. Technol.*, vol. 4, no. 3, pp. 328–337, 2014.

[181] R. Compton, R. McPhedran, Z. Popovic, G. Rebeiz, P. Tong, and D. Rutledge, "Bow-tie antennas on a dielectric half-space: Theory and experiment," *IEEE Trans. Antennas Propag.*, vol. 35, no. 6, pp. 622–631, 1987.

[182] M. Hamid and R. Hamid, "Equivalent circuit of dipole antenna of arbitrary length," *IEEE Trans. Antennas Propag.*, vol. 45, no. 11, pp. 1695–1696, 1997.

[183] H. Kanaya, M. Koga, K. Tsugami, G. C. Eu, and K. Kato, "4x4 planar array antenna on indium phosphide substrate for 0.3-THz band application," in *Terahertz, RF, Millimeter, and Submillimeter-Wave Technology and Applications X*, L. P. Sadwick and T. Yang, Eds., Int. Society Optics Photonics, vol. 10103, SPIE, 2017, pp. 251–256.

[184] E. A. Alwan, K. Sertel, and J. L. Volakis, "A simple equivalent circuit model for ultrawideband coupled arrays," *IEEE Antennas Wireless Propag. Lett.*, vol. 11, pp. 117–120, 2012.

[185] S. Shi *et al.*, "Ultrawideband optically fed tightly coupled phased array," *J. Lightw. Technol.*, vol. 33, no. 23, pp. 4781–4790, Dec. 2015.

[186] M. R. Konkol *et al.*, "High-power photodiode-integrated-connected array antenna," *J. Lightw. Technol.*, vol. 35, no. 10, pp. 2010–2016, May 2017.

[187] M. R. Konkol, D. D. Ross, S. Shi, C. E. Harrity, A. A. Wright, C. A. Schuetz, *et al.*, "Photonic tightly coupled array," *IEEE Trans. Microw. Theory Tech.*, vol. 66, no. 5, pp. 2570–2578, 2018.

[188] X. Yang, X. Liu, S. Yu, L. Gan, J. Zhou, and Y. Zeng, "Permittivity of undoped silicon in the millimeter wave range," *Electronics*, vol. 8, no. 8, p. 886, Aug. 10, 2019.

[189] S. M. Duffy, S. Verghese, A. McIntosh, A. Jackson, A. C. Gossard, and S. Matsuura, "Accurate modeling of dual dipole and slot elements used with photomixers for coherent terahertz output power," *IEEE Trans. Microw. Theory Techn.*, vol. 49, no. 6, pp. 1032–1038, Jun. 2001.

[190] I. S. Gregory *et al.*, "Optimization of photomixers and antennas for continuous-wave terahertz emission," *IEEE J. Quantum Electron.*, vol. 41, no. 5, pp. 717–728, 2005.

[191] R. C. Hansen, "Fano limits on matching bandwidth," *IEEE Antennas Propag. Mag.*, vol. 47, no. 3, pp. 89–90, 2005.

[192] J. P. Doane, K. Sertel, and J. L. Volakis, "Bandwidth limits for lossless planar arrays over ground plane," *Electron. Lett.*, vol. 48, no. 10, pp. 540–542, 2012.

[193] D. Rutledge and M. Muha, "Imaging antenna arrays," *IEEE Trans. Antennas Propag.*, vol. 30, no. 4, pp. 535–540, 1982.

[194] D. Rutledge, D. Neikirk, and D. Kasilingam, "Integrated circuit antennas," 1983.

[195] L. E. García Muñoz, S. Preu, S. Malzer, G. H. Döhler, J. Montero-de-Paz, R. Gonzalo, *et al.*, "Principles of emission of THz waves," in *Semiconductor Terahertz Technology*, G. Carpintero, L. E. García Muñoz, H. L. Hartnagel, S. Preu, and A. V. Räisänen, Eds., Chichester, UK: John Wiley & Sons, Ltd, 2015, pp. 69–159.

[196] L. E. García Muñoz, "Comments on "THz time-domain sensing: The antenna dispersion problem and a possible solution"," *IEEE Trans THz Sci. Technol.*, vol. 4, no. 1, pp. 125–126, 2014.

[197] L. E. Garcia-Munoz, E. Ugarte-Munoz, J. Montero-de-Paz, A. Rivera-Lavado, and D. Segovia-Vargas, "Anomalous behavior in the radiation patterns," *IEEE Trans. Antennas Propag.*, vol. 61, no. 2, pp. 973–976, 2013.

[198] D. F. Filipovic, S. S. Gearhart, and G. M. Rebeiz, "Double-slot antennas on extended hemispherical and elliptical silicon dielectric lenses," *IEEE Trans. Microw. Theory Techn.*, vol. 41, no. 10, pp. 1738–1749, 1993.

[199] A. Karttunen, J. Ala-Laurinaho, R. Sauleau, and A. V. Räisänen, "A study of extended hemispherical lenses for a high-gain beam-steering antenna," in *Proc. 4th European Conf. Antennas and Propagation*, 2010, pp. 1–5.

[200] A. Neto, S. Maci, and P. J. I. De Maagt, "Reflections inside an elliptical dielectric lens antenna," *IEE Proc. Microw. Antennas Propag.*, vol. 145, no. 3, pp. 243–247, 1998.

[201] G. Godi, R. Sauleau, and D. Thouroude, "Performance of reduced size substrate lens antennas for millimeter-wave communications," *IEEE Trans. Antennas Propag.*, vol. 53, no. 4, pp. 1278–1286, 2005.

[202] Polytec. "Optical wafer thickness microgauge." (2020), [Online]. Available: https://www.polytec.com/int/. [Accessed: Dec. 14, 2020].

[203] A. Rivera-Lavado *et al.*, "Dielectric rod waveguide antenna as THz emitter for photomixing devices," *IEEE Trans. Antennas Propag.*, vol. 63, no. 3, pp. 882–890, 2015.

[204] M. Steeg, A. A. Assad, and A. Stöhr, "All photonic radar system based on laser frequency sweeping and leaky-wave antennas," in *2018 Int. Topical Meeting Microwave Photonics (MWP)*, 2018, pp. 1–4.

[205] M. Ali *et al.*, "Photonics-based compact broadband transmitter module for E-band wireless communications," in *2019 49th European Microwave Conf. (EuMC)*, Paris, France: IEEE, Oct. 2019, pp. 808–811.

[206] S. Koenig *et al.*, "Wireless sub-THz communication system with high data rate," *Nat. Photon.*, vol. 7, no. 12, pp. 977–981, Dec. 2013.

[207] A. Hirata, H. Ishii, and T. Nagatsuma, "Design and characterization of a 120-GHz millimeter-wave antenna for integrated photonic transmitters," *IEEE Trans. Microw. Theory Techn.*, vol. 49, no. 11, pp. 2157–2162, 2001.

[208] X. Li and J. Yu, "Over 100 Gb/s ultrabroadband MIMO wireless signal delivery system at the D-band," *IEEE Photon. J.*, vol. 8, no. 5, pp. 1–10, Oct. 2016.

[209] T. Nagatsuma *et al.*, "300-GHz-band wireless transmission at 50 Gbit/s over 100 meters," in *2016 41st Int. Conf. Infrared, Millimeter, and Terahertz waves (IRMMW-THz)*, Copenhagen, Denmark: IEEE, Sep. 2016, pp. 1–2.

[210] E. Peytavit *et al.*, "Continuous terahertz-wave generation using a monolithically integrated horn antenna," *Appl. Phys. Lett.*, vol. 93, no. 11, p. 111 108, Sep. 15, 2008.

[211] S. Rey, T. Merkle, A. Tessmann, and T. Kürner, "A phased array antenna with horn elements for 300 GHz communications," in *2016 Int. Symp. Antennas and Propagation (ISAP)*, Okinawa, 2016, pp. 122–123.

[212] M. Ali, R. C. Guzmán, F. v. Dijk, L. E. García-Muñoz, and G. Carpintero, "An antenna-integrated UTC-PD based photonic emitter array," in *2019 Int. Topical Meeting Microwave Photonics (MWP)*, 2019, pp. 1–4.

[213] Y. Katayama, K. Takano, Y. Kohda, N. Ohba, and D. Nakano, "Wireless data center networking with steered-beam mmWave links," in *2011 IEEE Wireless Communications and Networking Conf.*, Cancun, Mexico: IEEE, Mar. 2011, pp. 2179–2184.

[214] B. Rupakula, A. Nafe, S. Zihir, Y. Wang, T.-W. Lin, and G. Rebeiz, "63.5–65.5-GHz transmit/receive phased-array communication link with 0.5–2 Gb/s at 100–800 m and ± 50° scan angles," *IEEE Trans. Microw. Theory Techn.*, vol. 66, no. 9, pp. 4108–4120, Sep. 2018.

[215] A. Pascual *et al.*, "A scalable photomixing array for increased emitted power," in *2019 44th Int. Conf. Infrared, Millimeter, and Terahertz Waves (IRMMW-THz)*, Paris, France: IEEE, Sep. 2019, pp. 1–2.

[216] J. Takeuchi, A. Hirata, H. Takahashi, and N. Kukutsu, "10-Gbit/s bi-directional wireless data transmission system using 120-GHz-band ortho-mode transducers," in *2012 IEEE Radio and Wireless Symp.*, 2012, pp. 63–66.

[217] X. Pang *et al.*, "100 Gbit/s hybrid optical fiber-wireless link in the W-band (75–110 GHz)," *Opt. Express*, vol. 19, no. 25, pp. 24 944–24 949, Dec. 2011.

[218] P. Lu *et al.*, "InP-based THz beam steering leaky-wave antenna," *IEEE Trans. THz Sci. Technol.*, pp. 1–1, 2020.

[219] J. Ma, N. J. Karl, S. Bretin, G. Ducournau, and D. M. Mittleman, "Frequency-division multiplexer and demultiplexer for terahertz wireless links," *Nat. Commun.*, vol. 8, no. 1, p. 729, Dec. 2017.

[220] M. Steeg, F. Exner, J. Tebart, A. Czylwik, and A. Stöhr, "OFDM joint communication–radar with leaky-wave antennas," *Electron. Lett.*, vol. 56, no. 21, pp. 1139–1141, 2020.

[221] D. R. Jackon and A. A. Oliner, "Leaky-wave antennas," in *Modern Antenna Handbook*, C. A. Balanis, Ed., 1st ed. Hoboken, NJ: John Wiley & Sons, Ltd., 2007, pp. 325–367.

[222] O. Lafond and M. Himdi, "Printed millimeter antennas– multilayer technologies," in *Advanced Millimeter-Wave Technologies*, D. Liu, B. Gaucher, U. Pfeiffer, and J. Grzyb, Eds., Chichester, UK: John Wiley & Sons, Ltd, 2009, pp. 163–232.

[223] J. R. James, P. S. Hall, and C. Wood, *Microstrip antenna: theory and design*, ser. IEE electromagnetic waves series 12. London: Peregrinus on behalf of the Institution of Electrical Engineers, 2015, 290 pp.

[224] J. James and P. Hall, "Microstrip antennas and arrays. Part 2: New array-design technique," *IEE J. Microw. Opt. Acoust. UK*, vol. 1, no. 5, p. 175, 1977.

[225] S. Paulotto, P. Baccarelli, F. Frezza, and D. R. Jackson, "A novel technique for open-stopband suppression in 1-D periodic printed leaky-wave antennas," *IEEE Trans. Antennas Propag.*, vol. 57, no. 7, pp. 1894–1906, Jul. 2009.

[226] D. M. Pozar, *Microwave Engineering*, 4th ed. Hoboken, NJ: Wiley, 2012.

[227] F. Mesa, R. Rodríguez-Berral, and F. Medina, "On the computation of the dispersion diagram of symmetric one-dimensionally periodic structures," *Symmetry*, vol. 10, no. 8, p. 307, Aug. 1, 2018.

[228] M. Ali, private communication, Feb. 3, 2020.

[229] M. Ali *et al.*, "Quasi-optical Schottky barrier diode detector for mmWave/sub-THz wireless communication," in *2018 25th Int. Conf. Telecommunications (ICT)*, St. Malo: IEEE, Jun. 2018, pp. 279–282.

[230] A. Mahmoud *et al.*, "High gain constrained lens antenna on BCB substrate for 300-GHz applications," in *2019 IEEE Int. Symp. Antennas and Propagation and USNC-URSI Radio Science Meeting*, Atlanta, GA, USA: IEEE, Jul. 2019, pp. 507–508.

[231] J. Hesler and T. Crowe, "NEP and responsivity of THz zero-bias Schottky diode detectors," in *2007 Joint 32nd Int. Conf. Infrared and Millimeter Waves and 15th Int. Conf. Terahertz Electronics*, Cardiff: IEEE, Sep. 2007, pp. 844–845.

[232] *Attenuation by atmospheric gases, Rec. ITU-R P.676-8*, International Telecommunications Union, Geneva, Switzerland, Sep. 2009.

[233] S. Jia *et al.*, "120 Gb/s multi-channel THz wireless transmission and THz receiver performance analysis," *IEEE Photon. Technol. Lett.*, vol. 29, no. 3, pp. 310–313, 2017.

[234] D. Headland, Y. Monnai, D. Abbott, C. Fumeaux, and W. Withayachumnankul, "Tutorial: Terahertz beamforming, from concepts to realizations," *APL Photon.*, vol. 3, no. 5, p. 051 101, 2018.

[235] S. Hur, T. Kim, D. J. Love, J. V. Krogmeier, T. A. Thomas, and A. Ghosh, "Millimeter wave beamforming for wireless backhaul and access in small cell networks," *IEEE Trans. Commun.*, vol. 61, no. 10, pp. 4391–4403, 2013.

[236] Y. Zhou, G. Sakano, Y. Yamanaka, H. Ito, T. Ishibashi, and K. Kato, "600-GHz-wave beam steering by terahertz-wave combiner," in *2018 Optical Fiber Communications Conf. and Expo. (OFC)*, 2018, pp. 1–3.

[237] M. Steeg, P. Lu, J. Tebart, and A. Stöhr, "2D mm-wave beam steering via optical true-time delay and leaky-wave antennas," in *2019 12th German Microwave Conf. (GeMiC)*, 2019, pp. 158–161.

[238] Y. Liu, B. Isaac, J. Kalkavage, E. Adles, T. Clark, and J. Klamkin, "93-GHz signal beam steering with true time delayed integrated optical beamforming network," in *2019 Optical Fiber Communications Conf. and Exhibition (OFC)*, 2019, pp. 1–3.

[239] Finisar. "Ultra-fast 100 GHz photodetector." (2014), [Online]. Available: https://www.mouser.fr/ProductDetail/Finisar/XPDV4120R-WF-FA?qs=Mv7BduZupUik9xI19lk7lw==. [Accessed: Feb. 23, 2021].

[240] M. Ali, R. C. Guzmán, L. E. García Muñoz, F. Van Dijk, and G. Carpintero, "E-band photonic transmitter employing high-power UTC-PD and broadband antenna," in *2019 12th Global Symp. Millimeter Waves (GSMM)*, 2019, pp. 81–83.

[241] M. Ali, R. Cruzoe-Guzmán, L. E. Garcia-Muñoz, F. van Dijk, and G. Carpintero, "Photonics-enabled millimetre-wave phased-array antenna with true time delay beam-steering," in *2020 50th European Microwave Conf. (EuMC)*, 2021, pp. 316–319.

[242] A. Artemenko, A. Mozharovskiy, A. Sevastyanov, V. Ssorin, and R. Maslennikov, "Electronically beam steerable lens antenna for 71–76/81–86 GHz backhaul applications," in *2015 IEEE MTT-S Int. Microwave Symp.*, 2015, pp. 1–4.

[243] A. Morales, S. Smirnov, D. V. Lioubtchenko, J. Oberhammer, C. Okonkwo, and I. T. Monroy, "Photonic-based beamforming system for sub-THz wireless communications," in *2019 European Microwave Conf. Central Europe (EuMCE)*, 2019, pp. 253–256.

[244] M. Cooley, "Phased array fed reflector (PAFR) antenna architectures for space-based sensors," in *2015 IEEE Aerospace Conf.*, 2015, pp. 1–11.

[245] C. Zhu *et al.*, "Silicon integrated microwave photonic beamformer," *Optica*, vol. 7, no. 9, pp. 1162–1170, Sep. 2020.

[246] D. M. Pozar and D. Schaubert, Eds., *Microstrip antennas: the analysis and design of microstrip antennas and arrays*. Institute of Electrical and Electronics Engineers, 1995.

[247] M. Khalily, R. Tafazolli, P. Xiao, and A. A. Kishk, "Broadband mm-wave microstrip array antenna with improved radiation characteristics for different 5G applications," *IEEE Trans. Antennas Propag.*, vol. 66, no. 9, pp. 4641–4647, 2018.

[248] Heareus Conamic. "Electrical properties of quartz." (2021), [Online]. Available: https://www.heraeus.com/en/hca/fused%5C_silica%5C_quartz%5C_knowledge%5C_base%5C_1/properties%5C_1/properties%5C_hca.html. [Accessed: Feb. 21, 2021].

[249] M. Ali, L. E. García Muñoz, and G. Carpintero, "E-band photonic transmitter with tapered slot antenna for RoF applications," in *2017 Int. Topical Meeting Microwave Photonics (MWP)*, 2017, pp. 1–4.

[250] M. Ali *et al.*, "300 GHz optoelectronic transmitter combinig integrated photonics and electronic multipliers for wireless communication," *Photonics*, vol. 6, no. 35, 2019.

[251] *Product selector guide rev. 3*, Rogers Corp., 2020.

[252] Virginia Diodes. "Zero bias detectors: Model WR10ZBD." (n.d.), [Online]. Available: https://www.vadiodes.com/en/wr10zbd. [Accessed: Aug. 21, 2020].

[253] B. Ung and M. Skorobogatiy, "2 - transmission and propagation of terahertz waves in plastic waveguides," in *Handbook of Terahertz Technology for Imaging, Sensing and Communications*, ser. Woodhead Publishing Series in Electronic and Optical Materials, D. Saeedkia, Ed., Woodhead Publishing, 2013, pp. 28–61.

[254] C. Lai and C. Sun, "Terahertz-wave Plastic Fibers and Their Applications," in *Handbook of Terahertz Technologies*, H.-J. Song and T. Nagatsuma, Eds. Pan Stanford Publishing Pte. Ltd., 2015, pp. 133–185.

[255] H. Song and T. Nagatsuma, "Present and future of Terahertz communications," *IEEE Trans. THz Sci. Technol.*, vol. 1, no. 1, pp. 256–263, 2011.

[256] *Attenuation due to clouds and fog, Rec. ITU-R P.840-4*, International Telecommunications Union, Geneva, Switzerland, Sep. 2009.

[257] *Specific attenuation model for rain for use in prediction methods, Rec. ITU-R P.838-3*, International Telecommunications Union, Geneva, Switzerland, Oct. 2005.

[258] K. Su, L. Moeller, R. B. Barat, and J. F. Federici, "Experimental comparison of performance degradation from terahertz and infrared wireless links in fog," *J. Opt. Soc. Am. A*, vol. 29, no. 2, p. 179, Feb. 1, 2012.

[259] H. Xu and E. Kasper, "A de-embedding procedure for one-port active mm-wave devices," in *2010 Topical Meeting on Silicon Monolithic Integrated Circuits in RF Systems (SiRF)*, New Orleans, LA, USA: IEEE, Jan. 2010, pp. 37–40.

[260] FormFactor. "ACP coaxial pobe." (n.d.), [Online]. Available: https://www.formfactor.com/product/acp-probe-coaxial/. [Accessed: Aug. 21, 2020].

[261] M. Ali *et al.*, "Quasi-optical transmitter and receiver modules enabling next-generation ultra-broadband wireless links at carrier-wave frequencies ranging from 60 to 180 GHz," *J. Infrared Milli. THz Waves*, vol. 40, pp. 688–695, 2019.

[262] T. Kleine-Ostmann and T. Nagatsuma, "A review on Terahertz communications research," *J. Infrared Milli. THz Waves*, vol. 32, pp. 143–171, 2011.

[263] K. Nallappan, H. Guerboukha, C. Nerguizian, and M. Skorobogatiy, "Live streaming of uncompressed HD and 4K videos using terahertz wireless links," *IEEE Access*, vol. 6, pp. 58 030–58 042, 2018.

[264] G. P. Agrawal, "Optical signal generation," in *Lightwave Technology*, John Wiley & Sons, Ltd, 2005, pp. 26–62.

[265] IXBlue. "Photonic products." (2020), [Online]. Available: https://photonics.ixblue.com/. [Accessed: Aug. 21, 2020].

[266] Keopsys. "Erbium-doped fiber amplifier for scientific applications." (n.d.), [Online]. Available: https://www.keopsys.com/portfolio/fiber-amplifier-c-pb-hp-series/. [Accessed: Aug. 21, 2020].

[267] Yokowaga. "Telecom optical spectrum analyzer." (n.d.), [Online]. Available: https://tmi.yokogawa.com/solutions/products/optical-measuring-instruments/optical-spectrum-analyzer/aq6370d-optical-spectrum-analyzer/. [Accessed: Aug. 21, 2020].

[268] RFLambda. “Low noise amplifiers.” (2012), [Online]. Available: https://www.rflambda.com/search_lownoiseamplifier.jsp. [Accessed: Aug. 21, 2020].

About the Author

Álvaro José Pascual-Gracia was born in 1993 in Zaragoza, Spain. He received the B.Sc. degree in Physics from the University of Zaragoza in 2015, and the M.Sc. degree in Photonics (cum laude) from the Polytechnic University of Catalonia (UPC) in 2016. During 2015-2016 he was a research assistant at the Group of Optical Communications at UPC. He was an R&D intern with Aragon Photonics Labs (Zaragoza) in the summer of 2015, and with Melexis Technologies NV (Tessenderlo, Belgium) in the last third of 2016. Since November 2017 he works towards the PhD degree in Electronic Engineering at the Institute of Electronics and numeRical Technologies (IETR) in Rennes, France. In 2019 was a visiting student at the Group of Photonic Technologies and the Radiofrequency and Antennas Group at University Carlos III, Madrid, Spain. His research interests include photonic-enabled mm-wave antenna arrays and phased array antenna theory. Among other journals, Mr. Pascual has served as a reviewer of IEEE Transactions on Antennas and Propagation.

Acknowledgements

I am indebted to my research supervisors David González and Ronan Sauleau, for their guidance and involvement in this exciting project. David, thanks for your friendship and countless technical discussions that proved to be an invaluable piece of advice.

I would also like to express my deep and sincere gratitude to Luis Enrique García-Muñoz and Guillermo Carpintero del Barrio, who kindly hosted my stay at UC3M. Putting at our disposal their experience and facilities undoubtedly boosted the experimental part of the project. Thanks also to Muhsin Ali for revealing the art of photodiode integration.

Special thanks go to our colleagues at LEAT: Fabien Ferrero, Laurent Brochier, and Jean-Yves Dauvignac, for helping us with the antenna measurements.

The permanent personnel at IETR has certainly made the last three years a pleasant journey. Notably, the technicians and secretary personnel have all have been very gentle and professional, and one is thankful for that.

Thank you also to the thesis jury for taking part in the defense and manuscript revision.

On the personal side, I am grateful for having met many people over the years, whom I can call friends. To my friends at hometown, thanks for being there. To those at Novallas, thanks for being just great. To my colleagues at UC3M, thanks for making the visit awesome. And finally, to my colleagues at IETR, thanks for being also my friends and for endless technical, funny, trivial, or existential discussions. Some of the moments we shared have a special place in my heart.

Sincere thanks go to Émilie; for her support and beautiful smile light up my days.

Lastly, my heartfelt goes to my parents and brother: José Ángel, Begoña, and Hugo. I fall short of words when I try to express my gratitude for everything they have done. My parents instilled in me, among others, the sense of hard work and persistence. This thesis is therefore a consequence of the education process they started quite a few years ago, and so, it is dedicated to them.

Álvaro J. Pascual-Gracia

UNIVERSITÉ DE RENNES 1

Titre : Réseaux d'antennes en ondes millimétriques excités par des photodiodes.

Mots clés : ondes millimétriques, photomélange, réseau infinie d'antennes, adaptation d'impédance, antenne leaky, commutation de faisceau.

Résumé : Cette thèse présente des réseaux d'antennes excités par des photodiodes pour la génération en continu d'ondes millimétriques. Les efforts de recherche sur la génération photonique menés au cours des vingt dernières années ont abouti à une méthode à fort potentiel. Le meilleur exemple en est la compatibilité avec les réseaux de communication à fibre optique. Néanmoins, la méthode offre une puissance d'émission plus faible que d'autres technologies. De plus, les antennes photoniques à gain élevé avec un faisceau orientable restent un point critique pour les télécommunications. Ce travail tente de résoudre les deux inconvénients précédents. D'abord, nous proposons une méthode pour augmenter la puissance d'émission en utilisant un réseau d'antennes intégré avec des photodiodes. Un plan de masse placé à proximité des antennes permet une adaptation d'impédance plus efficace, tandis que la configuration du réseau offre une combinaison de puissance. Aussi, nous avons conçu et prototypé deux réseaux d'antennes intégrés avec des photodiodes. Pour le premier, nous utilisons une antenne de type "leaky" pour obtenir une orientation de faisceau sélective avec la fréquence. Pour l'autre, nous proposons et démontrons la commutation de faisceaux photoniques comme un moyen pragmatique d'obtenir un faisceau orientable et hautement directif. À la suite de nos recherches, nous avons également développé un modèle théorique pour analyser l'impédance de balayage (scan impedance) dans des réseaux infinis de dipôles.

Title: Mm-Wave Photonic-Enabled Antenna Arrays.

Keywords: mm-waves, photomixing, infinite array antenna, impedance matching, leaky-wave antenna, beam switching.

Abstract: We present antenna arrays excited by photodiodes for the continuous-wave generation of millimeter-wave radiation using photomixing. Research efforts carried out over the last twenty years have put the photonic generation approach into the spotlight. It offers numerous advantages concerning other methods, and the principal example is seamless compatibility with fiber-optic networks. Nevertheless, photomixing offers a lower emitted power than other technologies. Furthermore, photonic-enabled high-gain and beam-steerable antennas are still a critical point for telecommunications. This work addresses both of the previous drawbacks. First, we propose a method to increase the emitted power using an antenna array integrated with photodiode sources. A ground plane placed close to the antennas enables a more efficient impedance matching, while the array configuration offers power combining. Besides, we have designed and prototyped two antenna arrays integrated with photodiodes. One uses a leaky-wave antenna in a scalable layout to obtain frequency-selective beamsteering. For the other, we propose and demonstrate photonic-enabled beam switching as a pragmatic way to achieve a highly directive, switchable beam with quasi-continuous coverage. Finally, stemming from our investigations, we have also developed a theoretical model to analyze the scan impedance in infinite phased arrays of dipoles.